

Advances in Low-Profile Antennas in Wireless Communications

Guest Editors: Guo Qing Luo, Xiao Ping Chen,
Zhang Cheng Hao, Bing Liu, and Yu Jian Cheng





Advances in Low-Profile Antennas in Wireless Communications

International Journal of Antennas and Propagation

Advances in Low-Profile Antennas in Wireless Communications

Guest Editors: Guo Qing Luo, Xiao Ping Chen,
Zhang Cheng Hao, Bing Liu, and Yu Jian Cheng



Copyright © 2014 Hindawi Publishing Corporation. All rights reserved.

This is a special issue published in "International Journal of Antennas and Propagation." All articles are open access articles distributed under the Creative Commons Attribution License, which permits unrestricted use, distribution, and reproduction in any medium, provided the original work is properly cited.

Editorial Board

Mohammad Ali, USA
Charles Bunting, USA
Felipe Catedra, Spain
Dau-Chyrh Chang, Taiwan
Deb Chatterjee, USA
Z. N. Chen, Singapore
Michael Yan Wah Chia, Singapore
Shyh-Jong Chung, Taiwan
Lorenzo Crocco, Italy
Tayeb A. Denidni, Canada
Karu Esselle, Australia
Francisco Falcone, Spain
Miguel Ferrando, Spain
Vincenzo Galdi, Italy
Wei Hong, China
Tamer S. Ibrahim, USA
Nemai Karmakar, Australia
Se-Yun Kim, Republic of Korea

Ahmed A. Kishk, Canada
Selvan T. Krishnasamy, India
Ju-Hong Lee, Taiwan
Byungje Lee, Republic of Korea
Joshua Le-Wei Li, China
Yilong Lu, Singapore
J.S. Mandeep, Malaysia
Atsushi Mase, Japan
Giuseppe Mazzeola, Italy
Derek McNamara, Canada
C. F. Mecklenbräuker, Austria
Michele Midrio, Italy
Mark Mirotznik, USA
Ananda S. Mohan, Australia
P. Mohanan, India
Pavel Nikitin, USA
A. D. Panagopoulos, Greece
Matteo Pastorino, Italy

Massimiliano Pieraccini, Italy
Sadasiva M. Rao, USA
Sembiam R. Rengarajan, USA
Ahmad Safaai-Jazi, USA
Safieddin Safavi-Naeini, Canada
Magdalena Salazar-Palma, Spain
Stefano Selleri, Italy
Zhongxiang Shen, Singapore
John J. Shynk, USA
Seong-Youp Suh, USA
Parveen Wahid, USA
Yuanxun Ethan Wang, USA
Daniel S. Weile, USA
Tat Soon Yeo, Singapore
Young Joong Yoon, Republic of Korea
Jong-Won Yu, Republic of Korea
Wenhua Yu, USA
Anping Zhao, China

Contents

Advances in Low-Profile Antennas in Wireless Communications, Guo Qing Luo, Xiao Ping Chen, Zhang Cheng Hao, Bing Liu, and Yu Jian Cheng
Volume 2014, Article ID 784685, 2 pages

A 2.4 GHz Cross Rhombic Antenna for a Cube Satellite Application, Jorge Sosa-Pedroza, Sergio Peña Ruiz, and Fabiola Martínez-Zúñiga
Volume 2014, Article ID 268151, 10 pages

Novel Dual Band Microstrip Circular Patch Antennas Loaded with ENG and MNG Metamaterials, Md. Ababil Hossain, Md. Saimoom Ferdous, Shah Mahmud Hasan Chowdhury, and Md. Abdul Matin
Volume 2014, Article ID 904374, 9 pages

Multishorting Pins PIFA Design for Multiband Communications, Muhammad Sajjad Ahmad, C. Y. Kim, and J. G. Park
Volume 2014, Article ID 403871, 10 pages

Multiband Printed Asymmetric Dipole Antenna for LTE/WLAN Applications, Chia-Mei Peng, I-Fong Chen, and Chin-Hao Liu
Volume 2013, Article ID 704847, 6 pages

Microstrip Folded Dipole Antenna for 35 GHz MMW Communication, Guang Hua, Chen Yang, Ping Lu, Hou-Xing Zhou, and Wei Hong
Volume 2013, Article ID 603654, 6 pages

BCB-Si Based Wide Band Millimeter Wave Antenna Fed by Substrate Integrated Waveguide, Hamsakutty Vettikalladi and Majeed A. S. Alkanhal
Volume 2013, Article ID 816050, 4 pages

A Wireless and Real-Time Monitoring System Design for Car Networking Applications, Li Wenjun, Zhong Yiming, and Li Wenbin
Volume 2013, Article ID 298543, 5 pages

A Compact CPW-Fed UWB Antenna with Dual Band-Notched Characteristics, Aiting Wu and Boran Guan
Volume 2013, Article ID 594378, 7 pages

Implementation of Low-Cost UHF RFID Reader Front-Ends with Carrier Leakage Suppression Circuit, Bin You, Bo Yang, Xuan Wen, and Liangyu Qu
Volume 2013, Article ID 135203, 8 pages

Cavity-Backed Dipole Antenna for Intelligent Lock Communication, Bo Yuan, Wen Wang, Xiao Hong Zhang, and Guo Qing Luo
Volume 2013, Article ID 921267, 4 pages

Millimeter Wave on Chip Antenna Using Dogbone Shape Artificial Magnetic Conductor, Guo Qing Luo, Zheng Zheng Song, Xiao Hong Zhang, and Xiao Ping Hu
Volume 2013, Article ID 743649, 5 pages

An AMC Backed Folded Dipole Slot Antenna Based on CMOS Process, Guo Qing Luo, Lin Qi Wu, and Xiao Hong Zhang
Volume 2013, Article ID 351956, 4 pages

Review of Low Profile Substrate Integrated Waveguide Cavity Backed Antennas, Guo Qing Luo, Tian Yang Wang, and Xiao Hong Zhang
Volume 2013, Article ID 746920, 7 pages

Uniplanar Millimeter-Wave Log-Periodic Dipole Array Antenna Fed by Coplanar Waveguide, Guohua Zhai, Yong Cheng, Qiuyan Yin, Shouzheng Zhu, and Jianjun Gao
Volume 2013, Article ID 430618, 5 pages

Design and Implementation of Double-Transmitter-Coil Antenna Used for the Tag Test System, Bin You, Haoling Yue, Xuan Wen, and Liangyu Qu
Volume 2013, Article ID 246831, 5 pages

Simplified Printed Log-Periodic Dipole Array Antenna Fed by CBCPW, Guohua Zhai, Yong Cheng, Qiuyan Yin, Shouzheng Zhu, and Jianjun Gao
Volume 2013, Article ID 548610, 5 pages

Broadband Multilayered Array Antenna with EBG Reflector, P. Chen, X. D. Yang, C. Y. Chen, and Z. H. Ma
Volume 2013, Article ID 250862, 4 pages

A Novel Dual-Shorting Point PIFA (GSM850 to IMT-A) for Mobile Handsets, Pengcheng Li, Jin Pan, Deqiang Yang, and Pingzai Nie
Volume 2013, Article ID 436808, 7 pages

A UWB Band-Pass Antenna with Triple-Notched Band Using Common Direction Rectangular Complementary Split-Ring Resonators, Bo Yan, Di Jiang, Ruimin Xu, and Yuehang Xu
Volume 2013, Article ID 934802, 6 pages

Substrate Integrated Waveguide Fed Cavity Backed Slot Antenna for Circularly Polarized Application, Xiao Hong Zhang, Guo Qing Luo, and Lin Xi Dong
Volume 2013, Article ID 316208, 6 pages

Editorial

Advances in Low-Profile Antennas in Wireless Communications

Guo Qing Luo,¹ Xiao Ping Chen,² Zhang Cheng Hao,³ Bing Liu,⁴ and Yu Jian Cheng⁵

¹ College of Electronic Information, Hangzhou Dianzi University, Hangzhou 310018, China

² Department of Electrical Engineering, Poly-Grames Research Centre, University of Montreal, Montreal, QC, Canada H3T 1J4

³ School of Information Science and Engineering, Southeast University, Nanjing 210096, China

⁴ College of Electronic and Information Engineering, Nanjing University of Aeronautics and Astronautics, Nanjing 210016, China

⁵ School of Electronic Engineering, University of Electronic Science and Technology of China, Chengdu 611731, China

Correspondence should be addressed to Guo Qing Luo; luoguoqing@hdu.edu.cn

Received 6 January 2014; Accepted 6 January 2014; Published 20 February 2014

Copyright © 2014 Guo Qing Luo et al. This is an open access article distributed under the Creative Commons Attribution License, which permits unrestricted use, distribution, and reproduction in any medium, provided the original work is properly cited.

Antenna is a type of device that is adapted to transmit or receive electromagnetic energy. Numerous differing types of antenna structures have been developed, such as reflector antenna, helical antenna, notch antenna, cavity backed antenna, patch antenna, and line antenna. With rapid development of wireless communications, low-profile antenna is in great demand, especially in handheld radios, wireless USB, wireless sensors networks, high speed WPAN, and mobile devices. For the attractive characteristics such as light weight, good conformability, easy integration, and low cost fabrication, low-profile antennas have been extensively studied by researchers both in academia and industry. ISI indexed papers whose titles include the words “low-profile” and “antenna” in the past decades have been counted. From the results shown in Figure 1 it can be found that the research topic on low-profile antenna has become more and more popular.

One low-profile antenna is the patch antenna, which is usually elevated above a large metal plate. Dielectric substrate is used to support the elevated portion of the antenna above the large metal ground plate. The most popular type of patch antenna is microstrip patch antenna, which is manufactured by printed circuit board materials and process. The spacing between the top patch and the bottom metal ground plane is on the order of $1/15$ wavelength and a low physical depth profile can be easily achieved. Main problems of patch antenna include a relatively narrow bandwidth, a high radiation angle above the horizon, and various manufacturing

and fabrication difficulties. Its bandwidth can be increased by adding radiating surfaces and increasing the volume of the antenna, adding an impedance compensating network, placing selected impedance into the radiating surface, and introducing resistances into the radiating surface, thus lowering the Q of the antenna. Its radiation angle can be lowered by using a dielectric structure.

As a low-profile antenna, dipole antenna is also widely used in wireless communication for its vertically polarized radiation performance. The arm length of a dipole is about a half wavelength, which is too long for applications when it operates at a low frequency. Small size antennas such as planar inverted F antenna (PIFA), loop antenna, and table antenna have been presented. The PIFA is a variation of the patch antenna, whose one end of a radiating element disposed on a ground plane is bent so as to be connected to the ground plate. Its edge feeding structure is not easy to flush mounting. It also needs a grounded tuning wire separated from the metal sheet of the radiator. It also suffers from limitations of a narrow bandwidth and a high elevation radiation. A simple loop antenna is constructed by protruding the inner conductor of a coaxial line from one point of the ground plane and its end connects with the ground plane at the other point. A low-profile loop antenna is hard to match for its high capacitive impedance and low radiation resistance. A table antenna constructed by a radiating plate supported by four conductor posts was disposed on the ground plane. A coaxial feed is connected to the central part of the radiating

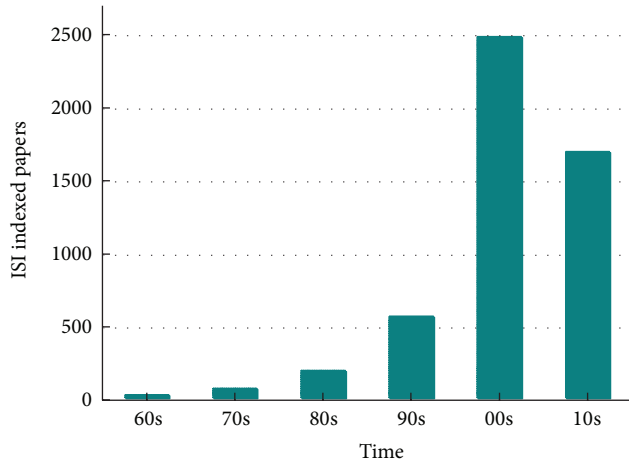


FIGURE 1: ISI indexed papers in the past decades.

element and a broad bandwidth can be achieved. If its height is reduced to get low-profile, the size of its radiating plate must be increased.

In modern wireless communication system, the design considerations of antenna include not only low-profile, high radiation performance, but also compactness, low cost, and easy integration. Recently antennas integrated on board, in package, and on chip have been extensively studied. This special issue presents novel antenna designs, antenna miniaturization and optimization techniques, antenna performance improvement techniques, feeding mechanisms and antenna arrays, and antenna applications.

We hope that through this special issue, the readers will find not only new designs about different low-profile antennas but also their valuable applications.

Guo Qing Luo
Xiao Ping Chen
Zhang Cheng Hao
Bing Liu
Yu Jian Cheng

Research Article

A 2.4 GHz Cross Rhombic Antenna for a Cube Satellite Application

Jorge Sosa-Pedroza, Sergio Peña Ruiz, and Fabiola Martínez-Zúñiga

Unidad Profesional Adolfo López Mateos, Escuela Superior de Ingeniería Mecánica y Eléctrica, Instituto Politécnico Nacional, Edificio Z-4, 3er. Piso, Colonia Lindavista, 07738 Mexico, DF, Mexico

Correspondence should be addressed to Sergio Peña Ruiz; srgpr13@gmail.com

Received 26 August 2013; Revised 22 December 2013; Accepted 23 December 2013; Published 19 February 2014

Academic Editor: Xiao Ping Chen

Copyright © 2014 Jorge Sosa-Pedroza et al. This is an open access article distributed under the Creative Commons Attribution License, which permits unrestricted use, distribution, and reproduction in any medium, provided the original work is properly cited.

We present design and construction results of a 2.4 GHz cross rhombic antenna to be used in a cubesat. Computational design agrees with experimental results after its construction. cross rhombic antenna is a novel planar structure of our own design, presenting circular polarization and medium gain; it is built over a RF60A substrate with $\epsilon_r = 6.15$, decreasing its size to fit the required dimensions of satellite. A special characteristic of this design is the enhancing of operational bandwidth using a technique we have been studying, related to softening the structures with sharp edges. Results show applicability and success of our technique.

1. Introduction

A cube satellite is a very small spacecraft, usually having an area as much as 10 cm^2 and no much longer than 30 cm; its weight should be less than 1 Kg. Most of these small satellites use commercial electronic components. California Polytechnic State University and Stanford University issued the CubeSat specifications in 1999, helping universities to develop the science and space exploration; these specifications are followed by amateur radio satellite builders. It is easy to imagine that the 10 cm^2 satellite area requires an antenna to fit those dimensions. We have been working with planar antennas for long time, developing, designing and constructing our own structures [1]. Some of them have been proposed to be used in different applications. We present in this paper a study of one of those structures: the Cross Rhombic Antenna (CRA). Actually, there are many kinds of planar antennas having different forms. Planar antennas are very popular considering their small dimensions and low cost making them ideal for many applications where small dimensions are needed, as in airplanes, spacecraft, and fixed terrestrial communications taking a great importance in last generation of these systems. Some characteristics to be considered for the antenna design are the following:

(i) high reliability;

- (ii) small size;
- (iii) low weight;
- (iv) high efficiency;
- (v) low cost.

The cubesat dimensions impose as well antenna dimensions, keeping the best behavior. As we show in Section 3, analysis was done in order to get the best behavior for a 10 cm^2 of satellite face. CRA is proposed to be used in Sensat, a cube satellite, working at 2.4 GHz. Sensat is a small educational satellite projected with optical and microwave payloads, developed by several Mexican universities.

2. The Cross Rhombic Antenna

CRA belongs to the family of traveling wave antennas, with circular polarization, medium gain, and a directional field pattern. Antenna is fed in one end and loaded in the other one, to meet expected behavior. The parametric analysis we present takes in account different characteristics of the antenna such as: microstrip width, load impedance, type of substrate and substrate thickness as well as softening of sharp corners. Antenna behavior is related to its gain, field pattern, axial ratio, and 50Ω input coupling; frequency design was

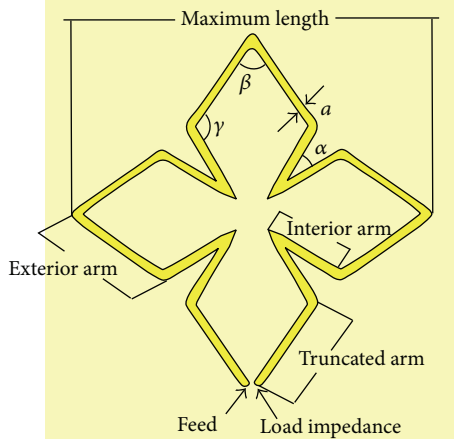


FIGURE 1: Cross rhombic antenna.

2.4 GHz and we use antenna, Computer Simulation Technology (CST) simulator. Modifying structure characteristics using a RF60A substrate with $\epsilon_r = 6.15$, we select the best one to construct an antenna prototype to compare it with simulation results. CRA is an evolution of the antenna proposed by Roederer in 1990 [2]. Antenna is a rhomb shape microstrip over a ground plane as shown in Figure 1. Circular right or left polarization depends on feed and load position. Load impedance could be any value but we have noticed that the best results are obtained using short circuit, open circuit or 50Ω .

3. Parametric Analysis Using RF60A Substrate

In this section, simulation results are presented, modifying physical characteristics of the RF60A substrate structure having $\epsilon_r = 6.15$ and $\lambda = 0.0504$ m at 2.4 GHz. At this frequency, substrate width is $h = \lambda/11$. Original design considers the maximum dimension (Figure 1) as 1.67λ or 8.4 cm, matching the 10 cm^2 area of cube satellite. Physical parameters considered were as follows: microstrip width, load impedance, substrate thickness, and softening of sharp corners.

3.1. Microstrip Line Width. First case of analysis was the microstrip line widths. Table 1 shows the relationship between gain and line width, for the three selected load impedances, while Figures 2, 3, and 4 show the related microstrip line width to return loss parameter for each load.

As seen in Table 1, the best gain results are obtained for $a_3 = 0.033\lambda = 1.7$ mm with open circuit load, but we choose $a_5 = 0.041\lambda = 2.1$ mm, considering the better coupling results of Figure 7; however, as seen in Figure 17, there is a better coupling for a_6 and a_7 but at higher frequencies. Figure 3 shows a better coupling with thicker lines for the 50Ω load, but the gain is lower, as seen in Table 1. For short circuit load, gain is similar to that of open circuit load and better coupling but at higher frequency; to reduce coupling frequency is necessary to increase antenna dimensions which is not desirable. Considering these results, we choose 2.1 mm

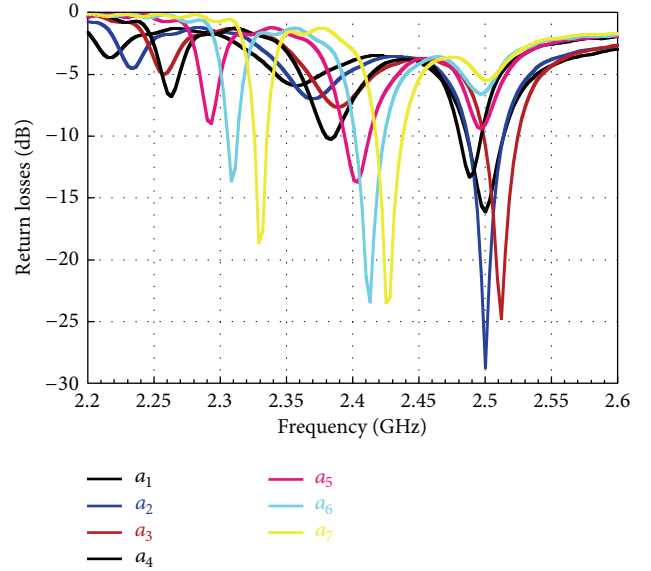
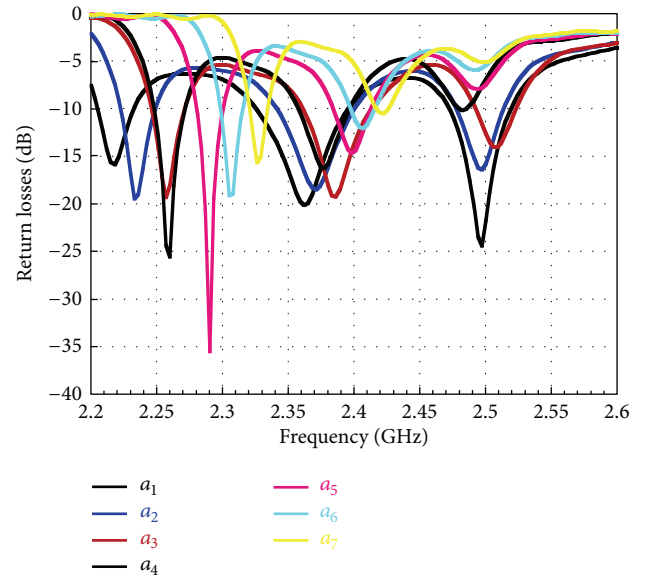


FIGURE 2: Return losses (open load line analysis).

FIGURE 3: Return losses (50Ω load line analysis).

for microstrip line width and open circuit load. Figure 5 shows field patterns ($\phi = 90^\circ$ and $\phi = 180^\circ$) and we can see similarity between all of them, and then they are not a parameter to be used for comparison.

4. Further Size Reduction

We tried a further size reduction of RCA, moving corners to the antenna center, but with little changes in microstrip lines width, as shown in Figure 6. Table 2 shows the final dimensions. To define the new microstrip width, we analyze the effects on gain and coupling; results are shown in Table 3 and Figure 7. Figure 8 depicts the different field patterns for each microstrip width.

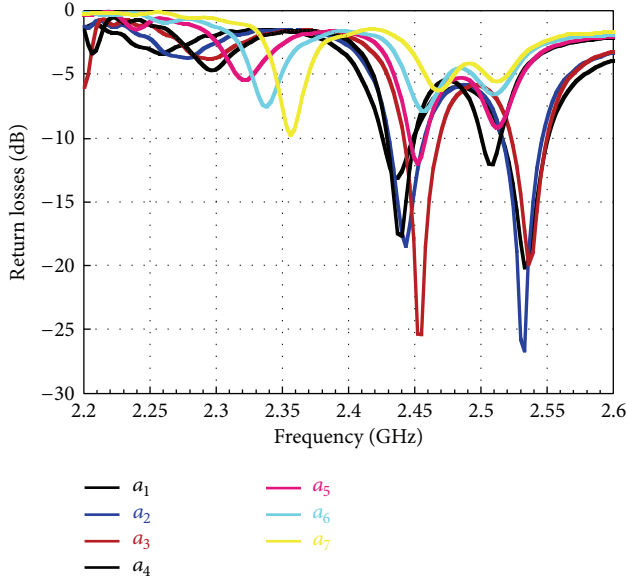


FIGURE 4: Return losses (short load line analysis).

TABLE 1: Line width analysis (RF60A).

| Width (mm) | Width (λ) | Gain open (dBi) | Gain 50 Ω (dBi) | Gain short (dBi) |
|-------------|---------------------|-----------------|------------------------|------------------|
| $a_1 = 1.3$ | 0.025λ | 8.8 | 5.8 | 8.8 |
| $a_2 = 1.5$ | 0.029λ | 8.8 | 5.8 | 8.7 |
| $a_3 = 1.7$ | 0.033λ | 8.9 | 5.7 | 8.7 |
| $a_4 = 1.9$ | 0.037λ | 8.8 | 6.5 | 8.6 |
| $a_5 = 2.1$ | 0.041λ | 8.8 | 6.1 | 8.5 |
| $a_6 = 2.3$ | 0.045λ | 8.6 | 6.0 | 8.4 |
| $a_7 = 2.5$ | 0.049λ | 8.3 | 5.6 | 8.0 |

TABLE 2: Antenna dimensions (RF60A).

| | Original | Modified |
|---|----------------|----------------|
| Maximum length | 1.67λ | 1.62λ |
| Interior arm | 0.32λ | 0.31λ |
| Exterior arm | 0.51λ | 0.49λ |
| Truncated arm | 0.46λ | 0.45λ |
| Angle between interior arms (α) | 31.42° | 31.42° |
| Angle between exterior arms (β) | 69.99° | 69.99° |
| Angle interior-exterior arms (γ) | 115.71° | 115.71° |

5. Substrate Thickness

Although we can make any change in dimensional antenna characteristics in simulation process, a limitation arises if we want to construct it, because commercial substrates have defined thickness dimensions; then we change that dimension in order to know its effects on radiation parameters, taking special attention in results with the materials on hand. Using the best former results, simulation was made for different substrate thicknesses, as Table 4, shows with gain results for each one. Figure 9 depicts the coupling results.

TABLE 3: Antenna gain line analysis.

| Width (mm) | Gain (dBi) |
|-------------|------------|
| $a_1 = 1.5$ | 8.3 |
| $a_2 = 1.6$ | 8.3 |
| $a_3 = 1.7$ | 8.3 |
| $a_4 = 1.8$ | 8.3 |
| $a_5 = 1.9$ | 8.2 |
| $a_6 = 2.0$ | 8.2 |
| $a_7 = 2.1$ | 8.1 |

TABLE 4: Antenna gain substrate thickness analysis.

| Thickness (mm) | Gain open (dBi) |
|-----------------------------|-----------------|
| $h_1 (\lambda/5) = 10$ | 5.4 |
| $h_2 (\lambda/6) = 8.4$ | 5.7 |
| $h_3 (\lambda/7) = 7.2$ | 6.8 |
| $h_4 (\lambda/8) = 6.3$ | 7.7 |
| $h_5 (\lambda/9) = 5.6$ | 8.1 |
| $h_6 (\lambda/10) = 5.04$ | 8.1 |
| $h_7 (\lambda/11) = 4.58$ | 8.2 |
| $h_8 (\lambda/12) = 4.2$ | 8.3 |
| $h_9 (\lambda/13) = 3.8$ | 8.3 |
| $h_{10} (\lambda/14) = 3.6$ | 8.3 |

Figure 9 depicts the coupling results, as seen $h = \lambda/11$ has again the best coupling results, but the commercial thickness of substrate we have is $h = \lambda/9 = 5.6$ mm. We keep the analysis of both the thickness substrates, in the following paragraphs, as a way of comparison.

6. Softening Sharp Edges to Enhance Bandwidth

It can be noticed in S_{11} parameters of former figures that curves are very sharp with small bandwidth, making antenna design and construction with a high dependence on frequency; repeatability could be a problem considering high dependency of antenna parameters of structure dimensions. To avoid this problem, we propose to increase bandwidth softening antenna corners, making it less dependent on frequency [3, 4]; to set those changes we selected the best parameters of the analysis, that is, strip line width $a = 2.0$ mm, substrate thickness $h = \lambda/11$, and open circuit load; antenna modification is shown in Figure 10.

We noticed a small change in frequency coupling after softening edges; to solve this problem, all dimensions were modified and a new substrate thickness analysis was done in order to get a new optimum value for h at the 2.4 GHz resonant frequency; simulation results are presented in Table 5 and Figure 11. Good coupling for $h_4 = \lambda/8$ and $h_5 = \lambda/9$ is noticed, and the last one is precisely the thickness we have to construct; Figures 12 and 13 show field patterns for those thicknesses.

Final optimized dimensions are presented in Table 6. An antenna gain of 8.1 dBi is noticed. Figure 14 depicts the S_{11}

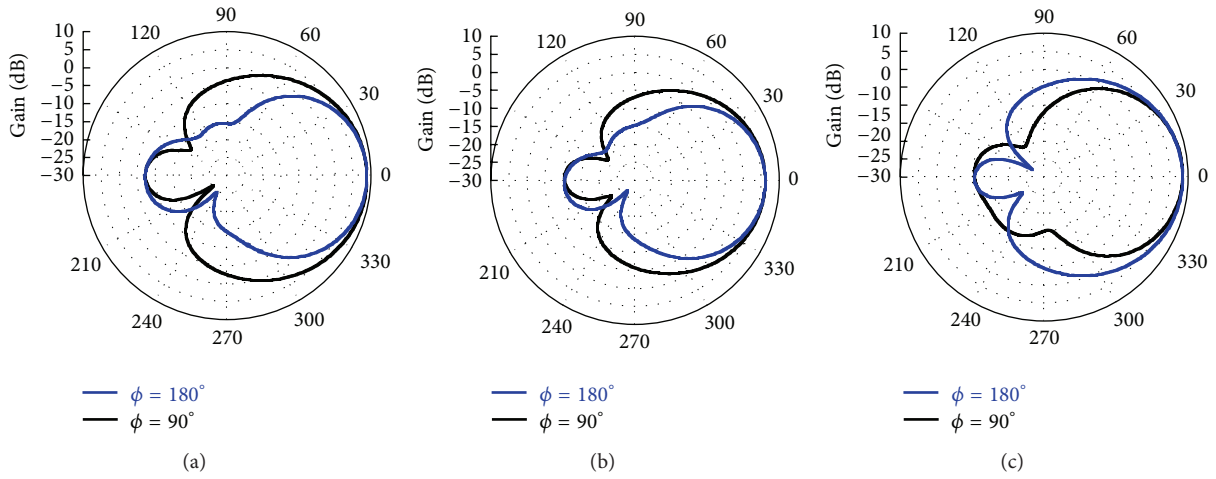


FIGURE 5: Field patterns. (a) Open, (b) 50Ω , and (c) short.

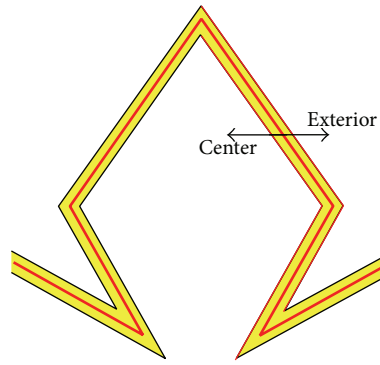


FIGURE 6: CRA modification.

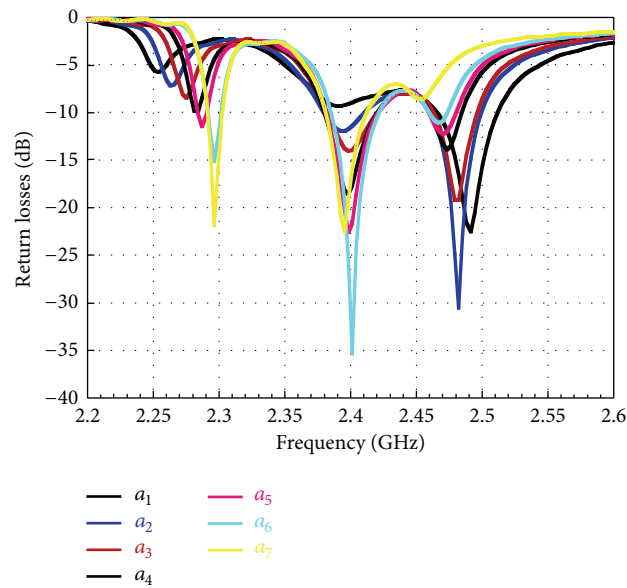


FIGURE 7: Return losses for different line widths.

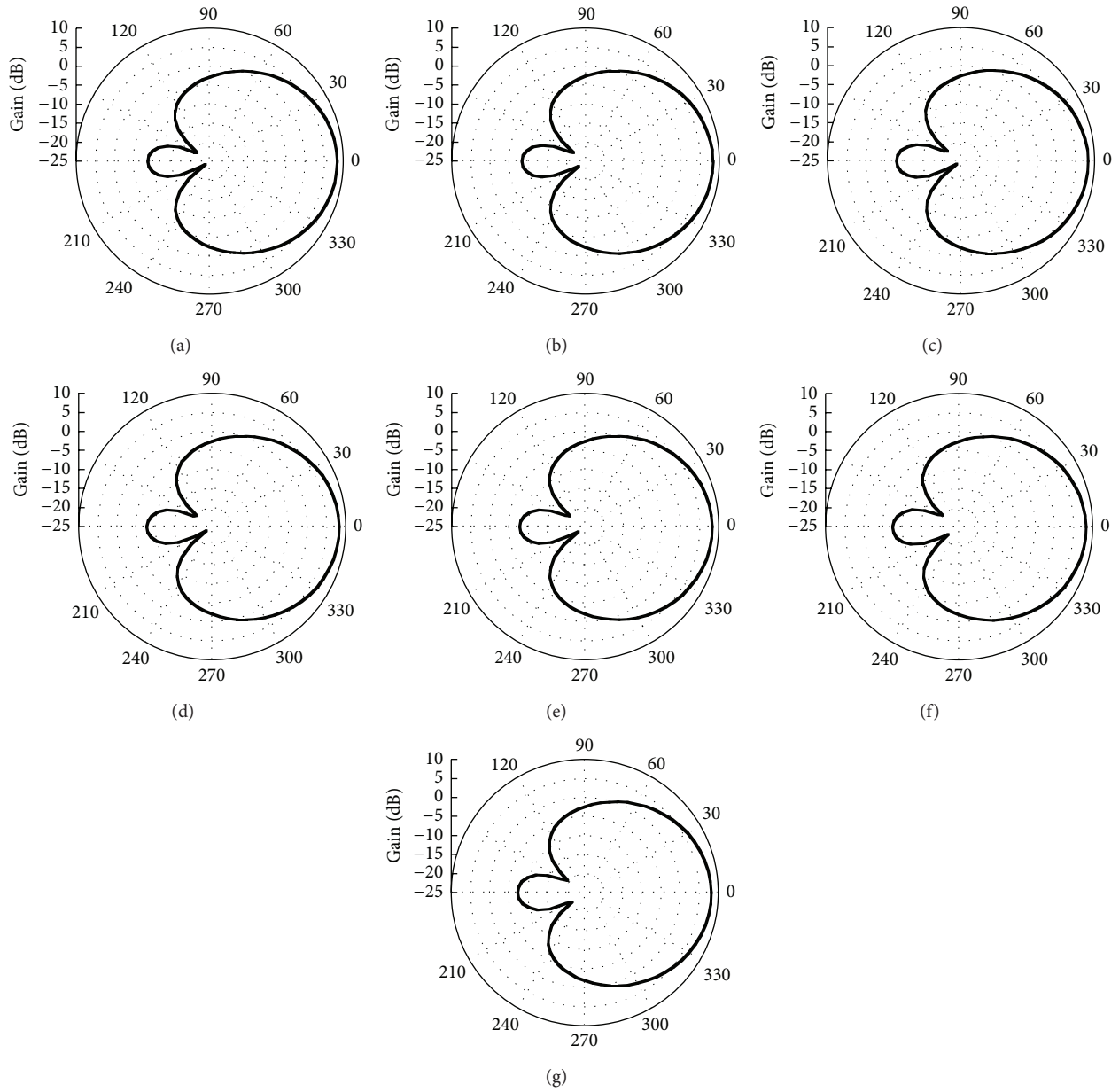


FIGURE 8: Field patterns versus microstrip line widths $\phi = 90^\circ$.

TABLE 5: Antenna gain substrate thickness analysis.

| h | Gain (dBi) |
|------------------|------------|
| $a = \lambda/6$ | 6.1 |
| $b = \lambda/7$ | 7.4 |
| $c = \lambda/8$ | 7.8 |
| $d = \lambda/9$ | 8.1 |
| $e = \lambda/10$ | 8.2 |
| $f = \lambda/11$ | 8.1 |
| $g = \lambda/12$ | 8.2 |

TABLE 6: Optimized antenna dimensions.

| | Optimized | Original |
|---|-----------------|-----------------|
| Total diameter | 1.66λ | 1.62λ |
| Interior arm | 0.32λ | 0.31λ |
| Exterior arm | 0.50λ | 0.49λ |
| Truncated arm | 0.46λ | 0.45λ |
| Line width (a) | 0.042λ | 0.039λ |
| Angle between interior arms (α) | 27.19° | 31.42° |
| Angle between exterior arms (β) | 69.99° | 69.99° |
| Angle interior-exterior arms (γ) | 115.71° | 115.71° |

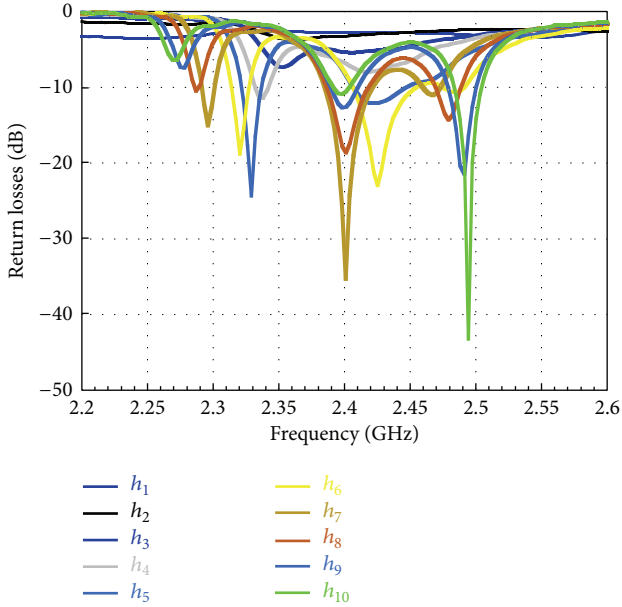


FIGURE 9: Return losses for different substrate thicknesses.

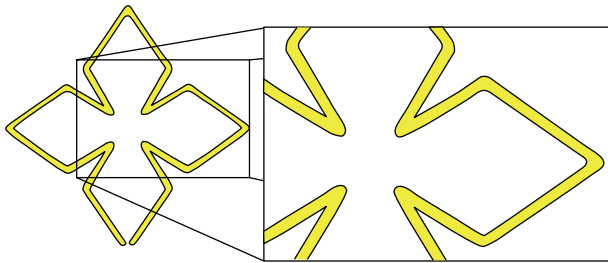


FIGURE 10: Cross rhombic antenna with softened edges.

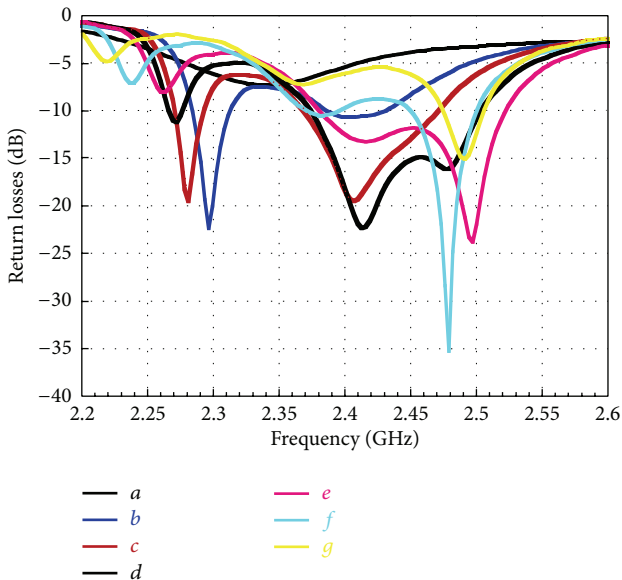


FIGURE 11: Return losses for different substrate thicknesses.

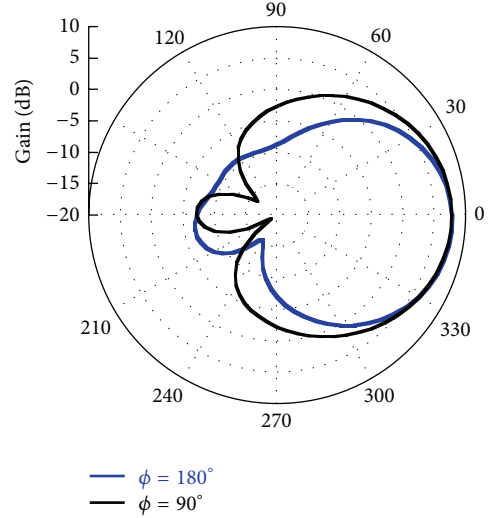


FIGURE 12: Field pattern for $h = \lambda/8$.

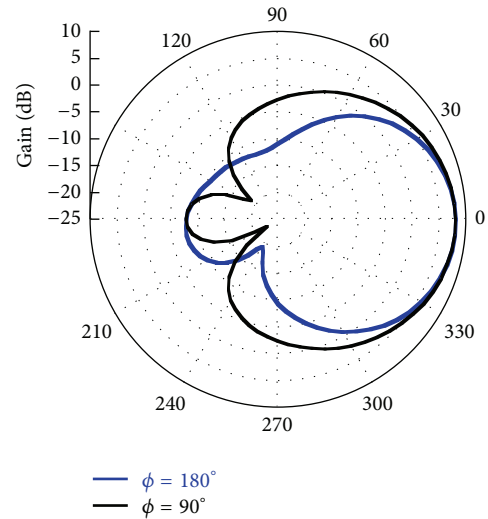


FIGURE 13: Field pattern for $h = \lambda/9$.

parameter response comparison, with and without softening, for $h = \lambda/9$; as it is seen, there are a higher bandwidth and a better response for the optimized antenna. As a way of comparison with other kind of antennas, the rectangular microstrip slot patch presented in [5] has narrower bandwidth and less gain.

7. Construction and Comparison

Two different antennas were constructed, one of them with sharp edges and the other with softened edges. Both antennas are shown in Figure 15, using RF60A substrate with $\epsilon_r = 6.15$ ($\lambda = 5$ cm at 2.4 GHz) and thicknesses of $h_5 = \lambda/9$.

Measurements were done with an Anritsu MS4624B Vector Network Measurement System. Figure 16 shows S_{11} comparison between simulation and construction at $h_5 = \lambda/9$ (real) and $h_7 = \lambda/11$ (optimal); as seen, there is very

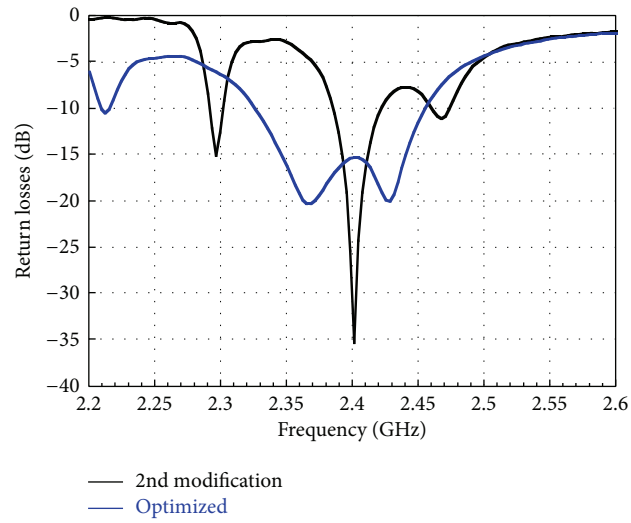


FIGURE 14: Comparison between sharp and softened ends antennas.

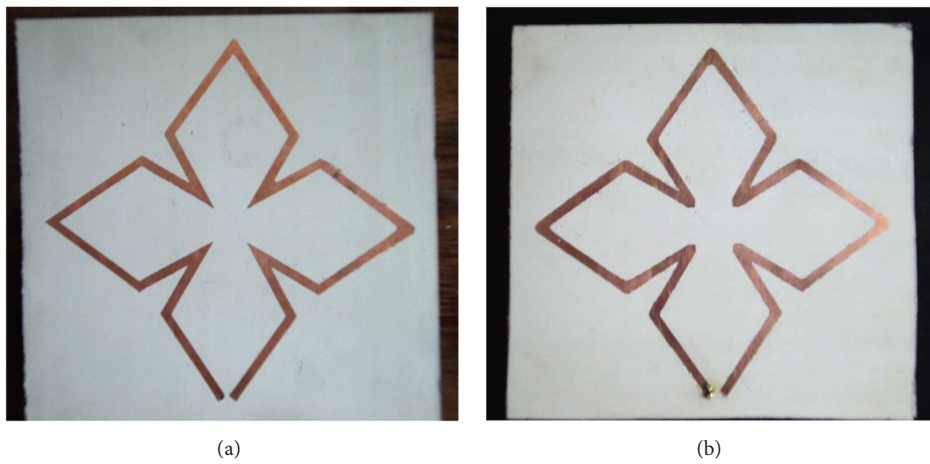


FIGURE 15: Constructed antennas (a) sharp edges and (b) soft edges.

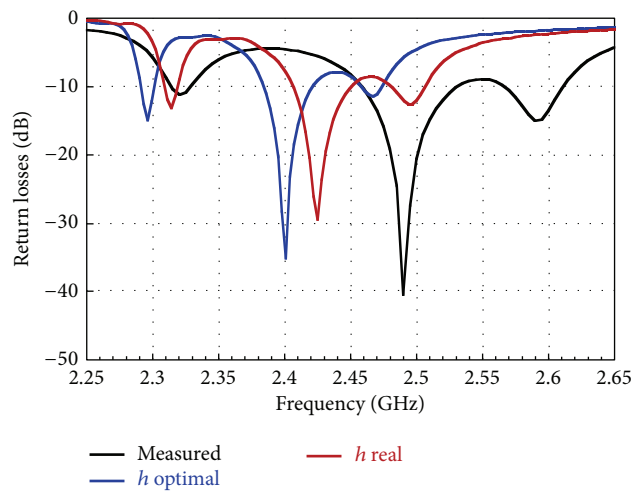


FIGURE 16: Return losses (antenna with sharp edges).

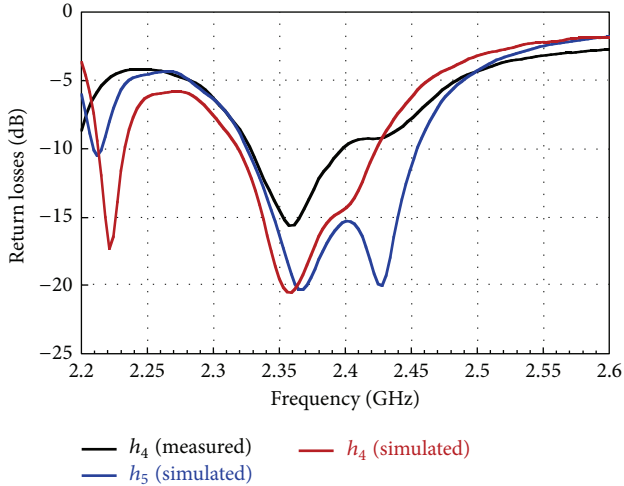


FIGURE 17: Return losses (antenna with softened edges).

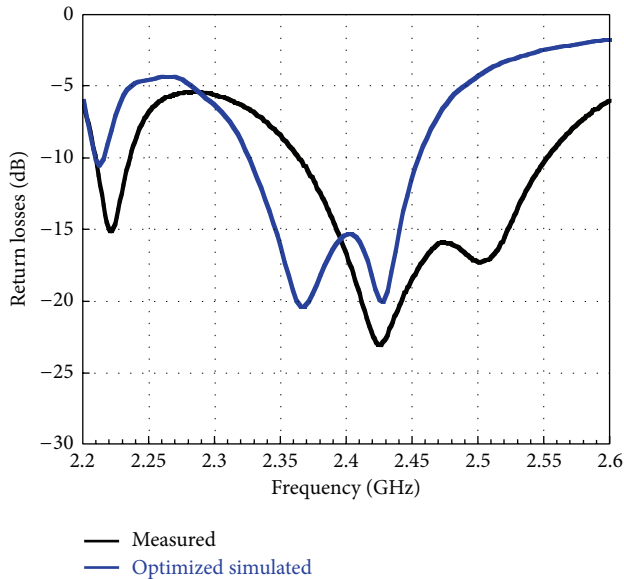


FIGURE 18: Measured return losses (CRA with softened edges).

good similarity between them but with a deviation of about 100 MHz over design frequency.

On the other hand, Figure 17 shows comparison of S_{11} parameters for same antennas but with softened edges; as it is seen, there is a good similitude between all of them. Finally, Figure 18 depicts coupling comparison between simulation and constructed softened edges antennas. We see again a deviation of about 70 MHz between both antennas due to construction problems. Field patterns for constructed and simulation antennas are shown in Figure 19, also with some differences.

Figure 20 shows gain comparison of both antennas, and as seen, there are some differences, with a better response for the simulated one. It is clear that we have to improve our construction methods.

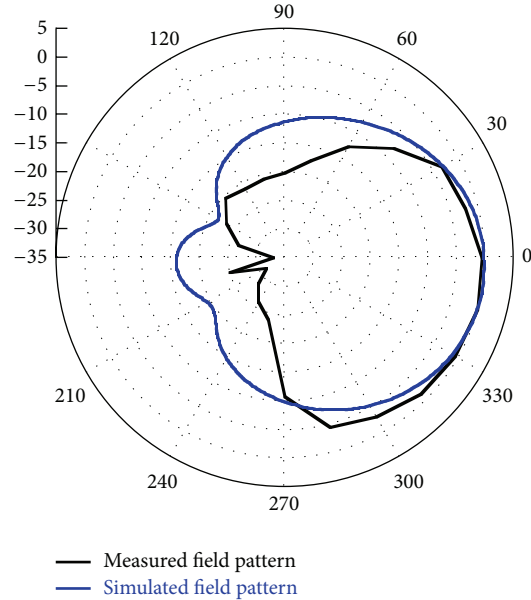


FIGURE 19: Simulation and measured field pattern comparison.

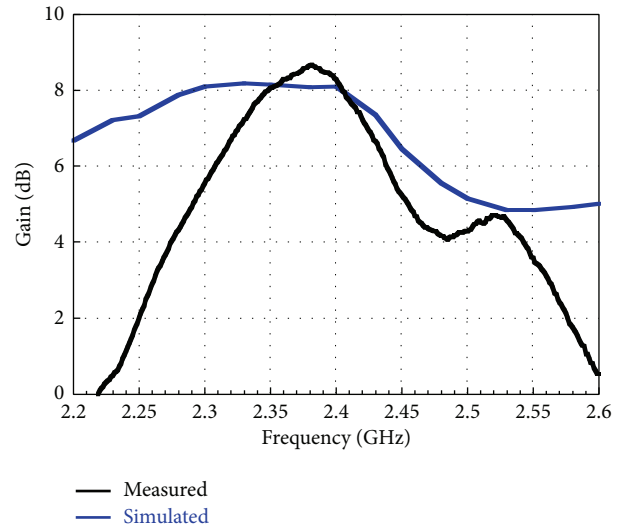


FIGURE 20: Gain comparison.

To characterize circular polarization, we obtained axial ratio, measuring horizontal and vertical field patterns. Both patterns have almost the same magnitude, except in 30° and 285° , probing circular polarization. Figure 21 presents circular polarization measurements; (a) shows measured field patterns and (b) shows axial ratio obtained from subtraction magnitude of both field patterns.

8. Conclusion

We have presented parametric analysis of CRA with results of gain, field pattern, and return losses. Results shown of comparing simulation and constructed structures using RF60A with $\epsilon_r = 6.15$ agree with most of measured parameters

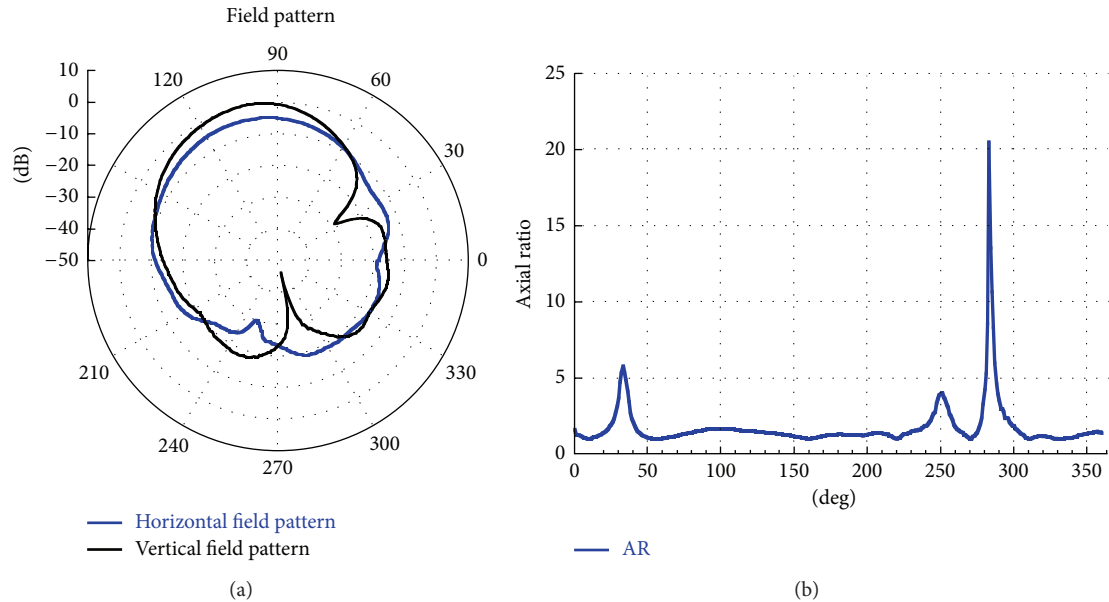


FIGURE 21: Circular polarization (a) field pattern comparison. (b) Axial ratio.

although with a displacement of about 100 MHz, meaning that error in the design frequency is due to manufacturing inaccuracy.

As it is seen from simulation, best configuration is that using open load, getting the best coupling and gain (8.1 dBi in the simulation and 7.9 dBi in measurement). We also analyze the substrate thickness effects on resonant frequency.

A better similarity is obtained for the antenna with softening sharp edges considering its less dependence of frequency. We concluded that the best geometry for CRA is the one with soft edges with better performance and higher bandwidth.

We have proposed CRA for other applications, as those presented in [6, 7], where we designed and constructed air dielectric antennas for GNSS at 1.5 GHz and also an air dielectric antenna for 2.4 GHz with 14.0 dBi gain and bandwidth around 60 MHz, for both of them, are greater than those of rectangular or circular patches presented in [8, 9].

The final dimensions of antenna are $10 \times 10 \times 0.56$ cm with weight of 157 g, and an excess of 1.6 cm over the 8.4 cm of maximum antenna dimension for the ground plane. Those 10 cm per side perfectly fit in the area of Sensat cube satellite.

Conflict of Interests

The authors declare that there is no conflict of interests.

Acknowledgments

The authors wish to thank to Instituto Politécnico Nacional and Consejo Nacional de Ciencia y Tecnología de México for their economic support.

References

- [1] J. S. Pedroza, F. M. Zúñiga, and M. E. Aguilar, "Planar antennas for satellite communications," in *Satellite Communications*, N. Diodato, Ed., pp. 367–394, Sciyo, 2010.
- [2] A. G. Roederer, "The cross antenna: a new low-profile circularly polarized radiator," *IEEE Transactions on Antennas and Propagation*, vol. 38, no. 5, pp. 704–710, 1990.
- [3] E. G. Nolasco, *Optimización de una antena plana para sistemas multiestándar [M.S. thesis]*, Sección de Estudios de Posgrado e Investigación, Escuela Superior de Ingeniería Mecánica y Eléctrica Zacatenco, IPN, Mexico City, Mexico, 2011.
- [4] G. Kumar and K. Ray, *Broadband Microstrip Antennas*, Artech House, Norwood, Mass, USA, 2003.
- [5] M. T. Ali, N. Ramli, M. K. M. Salleh, and M. N. M. Tan, "A design of reconfigurable rectangular microstrip slot patch antennas," in *Proceedings of the IEEE International Conference on System Engineering and Technology (ICSET '11)*, pp. 111–115, Shah Alam, Malaysia, June 2011.
- [6] J. S. Pedroza, L. E. C. Rivera, S. Peña Ruiz, and F. M. Zúñiga, "Análisis de acoplamiento mutuo en arreglos con antenas de cruz rómbica," in *VI Conferencia Internacional en Ingeniería Electromecánica y de Sistemas (CIIES '11)*, November 2011.
- [7] L. C. Rivera, J. S. Pedroza, S. P. Ruiz, and M. A. Mosqueda, "La técnica del patrón del elemento activo para analizar los efectos mutuos en un arreglo lineal de antenas Rómbicas de Cruz," in *XXII Reunión Internacional de Otoño, de Comunicaciones, Computación, Electrónica, Automatización, Robótica y Aplicaciones Industriales y Exposición Industrial*, IEEE, Guerrero, México, December 2011.
- [8] H.-M. Chen, Y.-K. Wang, Y.-F. Lin, C.-Y. Lin, and S.-C. Pan, "Microstrip-fed circularly polarized square-ring patch antenna for GPS applications," *IEEE Transactions on Antennas and Propagation*, vol. 57, no. 4, pp. 1264–1267, 2009.

- [9] H. Li, J. Li, D. Li, and Y. Zhang, "High-gain circular polarization antenna for small satellite data link application," in *Proceedings of the IEEE International Conference on Signal Processing, Communications and Computing (ICSPCC '11)*, Xi'an, China, September 2011.

Research Article

Novel Dual Band Microstrip Circular Patch Antennas Loaded with ENG and MNG Metamaterials

**Md. Ababil Hossain,¹ Md. Saimoom Ferdous,²
Shah Mahmud Hasan Chowdhury,¹ and Md. Abdul Matin¹**

¹ Department of Electrical and Electronic Engineering, BUET, Dhaka 1000, Bangladesh

² Department of ECE, University of British Columbia, Okanagan, BC, Canada

Correspondence should be addressed to Md. Ababil Hossain; ababilh@gmail.com

Received 13 September 2013; Accepted 20 November 2013; Published 11 February 2014

Academic Editor: Guo Qing Luo

Copyright © 2014 Md. Ababil Hossain et al. This is an open access article distributed under the Creative Commons Attribution License, which permits unrestricted use, distribution, and reproduction in any medium, provided the original work is properly cited.

Novel design of a dual band microstrip circular patch antenna loaded with ENG (ϵ negative) metamaterial has been shown in the first section. Using ENG metamaterial instead of the conventional dielectric, unconventional $TM_{\delta 10}$ ($1 < \delta < 2$) mode was produced to yield a dual band performance. Optimized parameters such as permittivity (ϵ_1) and filling ratio (η) of metamaterials were selected with the aid of a MATLAB based parameter optimization algorithm, developed for all these sort of patch antennas. In the second section, a dual band circular patch antenna loaded with MNG (μ negative) metamaterial has been reported. An unconventional modified $TM_{\delta 10}$ ($0 < \delta < 1$) mode has been produced along with conventional TM_{110} mode due to using MNG metamaterial. Here also the optimum values of permeability (μ_1) and filling ratio (η) for these sorts of patch antennas have been calculated from a MATLAB based parameter optimization algorithm. Both the proposed antennas provide good and resonance and satisfactory radiation performances (directivity, radiation efficiency, and gain) with a dual band performance.

1. Introduction

Satellite communications, wireless communications, surveillance, weather, radar, and so forth require highly directive and multiband antennas. In fact, in recent times, highly directive multiband antennas have become a prime concern in satellite communication.

The use of multiband antenna has brought about revolutionary change and dynamism in the trends of communication over the last few decades. However, antenna size miniaturization is also an important factor as far as antenna size is concerned. Therefore, a unique radiating element such as patch antenna which incorporates multiband performance with size miniaturization can further open up a new horizon in telecommunication sector. In [1], a generalized MATLAB based parameter optimization algorithm for designing circular patch antenna loaded with metamaterials has been

developed. On the basis of that design algorithm, in this paper we have presented the design model for dual band antennas loaded with both ENG and MNG metamaterials without the use of any symmetrical slotting which was done in [1, 2].

Wong and Hsieh [2] constructed dual band circular patch antenna by using conventional dielectrics as substrate and by using symmetrical slots where conventional TM_{210} mode was modified to yield dual band performance. In that case the first order mode (TM_{110} mode frequency) and second order mode (TM_{210} mode frequency) were determined by the antenna geometry structure (i.e., radius of the patch). Once the one mode has been selected, the other mode frequency automatically becomes fixed. In that case the designer could only tune any one mode frequency according to his will; he had no control over choosing the other mode frequency as the other mode frequency is determined by antenna radius. In that particular case the degree of freedom was

only one, that is, radius of the patch. So with one degree of freedom designers could choose only one resonant frequency independently, but not both at the same time.

In the first section of this paper, a novel design of dual band ENG metamaterial loaded circular patch antenna has been shown. Its main feature is in the flexibility of choosing both resonant frequencies according to user's will and apart from conventional TM_{110} mode newly produced unconventional $TM_{\delta 10}$ ($1 < \delta < 2$) mode provides high directivity. Our designed antenna has two degrees of freedom (radius of the patch and filling ratio of the metamaterial). In our case, the first band, that is, first order mode, is determined by the patch geometry only. Using ENG metamaterial instead of conventional dielectrics causes resonance in between first and second order mode frequency. For this reason, the biggest advantage here is that the designer can tune the second band almost anywhere in between conventional first and second order mode by just changing the filling ratio of the metamaterial. That is why this design provides a great deal of flexibility in choosing resonant frequency in comparison to other dual band circular patch antennas reported so far.

Alù et al. proposed design method to obtain electrically small rectangular patch antennas using DPS (double positive) ENG metamaterial juxtaposed layer [3]. But such rectangular patches give broadside null radiation pattern at subwavelength regime as illustrated in Figure 2 of [4]. Finally, it was predicted that all these electrically small rectangular antennas loaded with metamaterial can only be good resonators but may not be good radiators. But if the shape is circular [4, 5] or elliptical [6], theoretically it is possible to achieve electrically small size without deterioration of radiation performance. With this concept we developed a proper algorithm in [1], where achieving additional unconventional mode in metamaterial loaded circular patch antenna has been possible. By using the same algorithm, here a dual band ENG metamaterial loaded patch antenna has been designed. Highly directive performance and flexibility in tuning frequency are the two prime criteria of this dual band patch antenna.

In the second section of this paper, by using MNG (μ negative) metamaterial in the inner core as substrate instead of natural dielectric in circular microstrip patch antenna, dual band performance has been achieved with a reduced size antenna. Apart from conventional TM_{110} mode, here unconventional $TM_{\delta 10}$ ($0 < \delta < 1$) mode has been produced. Applying our proposed design algorithm [1], we can achieve broadside radiation at $TM_{\delta 10}$ ($0 < \delta < 1$) mode and hence achieve a dual band performance with a reduced size antenna. In this sort of metamaterial loaded patch antennas, the resonant frequency can be tuned according to designer's will. But it has been shown that electrically small size patch antenna having metamaterial loading is not practicable without degradation of radiation performance [7, 8]. In fact, the gain performances of such electrically small antennas degrade rapidly due to the size reduction. However, nearly 35% size reduction may be possible where gain remains above 0 dB [8]. In our proposed designed antenna based on our developed algorithm, we have obtained around 30% size reduction with a gain of 2.2 dB. Flexibility in tuning resonant

frequency along with size miniaturization has certainly made this dual band patch antenna unique from other dual band antennas reported in current literature.

MNG metamaterial can be fabricated in the laboratory at microwave frequencies by using Split Ring Resonators (SRR) and helices, whereas thin wired structure placed at a periodic distance works as negative Epsilon material when the distance between consecutive wires becomes comparable to the wavelength of the propagating electromagnetic wave. Over the years, a lot of research has been carried out in ENG loaded patch antenna, but ironically the practical implementation of ENG metamaterial at microwave regime using Lorentz model is a tough task [9]. However, recent advancement of ENG medium applications in microwave regime urges its practical implementation. Although the practical application of ENG medium using Lorentz model in microwave regime is really a tough one, the directivity and gain performance of such antennas are attractive with conventional size.

2. Mathematical Modeling of Metamaterial Loaded Circular Microstrip Patch Antenna

The basic magnetization vector equation for a circular patch antenna can be written as

$$A_z^n(\rho, \phi, z) = [A_{mn}J_m(k_{\rho n}\rho) + B_{mn}Y_m(k_{\rho n}\rho)] \times [C_n \cos(m\phi) + D_n \sin(m\phi)] \times [C_3 \cos(k_{zn}z) + D_3 \sin(k_{zn}z)]. \quad (1)$$

But radial component of the electric field can be derived as

$$E_\rho^n = -j \frac{1}{\omega \epsilon_n \mu_n} \frac{\partial^2}{\partial \rho \partial z} (A_z^n). \quad (2)$$

Here, $n = 1$ for region 1 (metamaterial region) and $n = 2$ for region 2 (conventional dielectric region).

From boundary conditions (perfect electric wall assumption of cavity model),

$$\text{at } z = h, E_\rho = 0, \text{ we get } D_3 = 0,$$

$$\text{and at } z = 0, E_\rho = 0, \text{ then we get } C_3 = 1.$$

Therefore,

$$A_z^n(\rho, \phi, z) = [A_{mn}J_m(k_{\rho n}\rho) + B_{mn}Y_m(k_{\rho n}\rho)] \times [C_n \cos(m\phi) + D_n \sin(m\phi)] \times \cos(k_{zn}z), \quad (3)$$

$$E_\rho^n(\rho, \phi, z) = -j \frac{k_{\rho n} k_{zn}}{\omega \epsilon_n \mu_n} \times [A_{mn}J'_m(k_{\rho n}\rho) + B_{mn}Y'_m(k_{\rho n}\rho)] \times [C_n \cos(m\phi) + D_n \sin(m\phi)] \sin(k_{zn}z). \quad (4)$$

Generalized equation for the phi component of the electric field is as follows:

$$E_{\phi}^n = -j \frac{1}{\omega \epsilon_n \mu_n} \frac{1}{\rho} \frac{\partial^2}{\partial \phi \partial z} (A_z^n). \quad (5)$$

By calculation from the equation of A_z^n we get

$$\begin{aligned} E_{\phi}^n(\rho, \phi, z) &= j \frac{k_{zn} m}{\rho \omega \epsilon_n \mu_n} \\ &\times [A_{mn} J_m(k_{\rho n} \rho) + B_{mn} Y_m(k_{\rho n} \rho)] \\ &\times [-C_n \sin(m\phi) + D_n \cos(m\phi)] \sin(k_{zn} z). \end{aligned} \quad (6)$$

Finally, z -component of electric field becomes

$$E_z^n = -\frac{j}{\omega \epsilon_n \mu_n} \left(\frac{\partial^2}{\partial z^2} + k_n^2 \right) A_z^n. \quad (7)$$

Again, calculation from the equation of A_z^n yields

$$\begin{aligned} E_z^n(\rho, \phi, z) &= -j \frac{k_{\rho n}^2}{\omega \epsilon_n \mu_n} [A_{mn} J_m(k_{\rho n} \rho) + B_{mn} Y_m(k_{\rho n} \rho)] \\ &\times [C_n \cos(m\phi) + D_n \sin(m\phi)] \cos(k_{zn} z). \end{aligned} \quad (8)$$

For the magnetic fields component of the cavity, z -component of the magnetic field is 0 everywhere.

So,

$$H_z^n = 0. \quad (9)$$

Again, radial component of the magnetic field is formulated as

$$\begin{aligned} H_{\rho}^n &= \frac{1}{\rho \mu_n} \frac{\partial A_z^n}{\partial \phi} \\ &= \frac{m}{\rho \mu_n} [A_{mn} J_m(k_{\rho n} \rho) + B_{mn} Y_m(k_{\rho n} \rho)] \\ &\times [-C_n \sin(m\phi) + D_n \cos(m\phi)] \cos(k_{zn} z). \end{aligned} \quad (10)$$

Finally,

$$H_{\phi}^n = -\frac{1}{\mu_n} \frac{\partial A_z^n}{\partial \rho}, \quad (11)$$

which gives

$$\begin{aligned} H_{\phi}^n &= -\frac{k_{\rho n}}{\mu_n} [A_{mn} J_m'(k_{\rho n} \rho) + B_{mn} Y_m'(k_{\rho n} \rho)] \\ &\times [C_n \cos(m\phi) + D_n \sin(m\phi)] \cos(k_{zn} z). \end{aligned} \quad (12)$$

For all the above equations, J_m and J_m' are Bessel functions of first kind and its derivative denoted by prime order of

m . Y_m and Y_m' are Bessel functions of second kind and its derivative denoted by prime order of m .

Now applying boundary condition at the interface, that is, at $\rho = b$, $E_z^1 = E_z^2$ we get from electric field equations,

$$\begin{aligned} \left[\frac{k_{\rho 1}^2}{\mu_1 \epsilon_1} J_m(k_{\rho 1} b) \right] A_{m1} - \left[\frac{k_{\rho 2}^2}{\mu_2 \epsilon_2} J_m(k_{\rho 2} b) \right] A_{m2} \\ - \left[\frac{k_{\rho 2}^2}{\mu_2 \epsilon_2} Y_m(k_{\rho 2} b) \right] B_{m2} = 0. \end{aligned} \quad (13)$$

Again, at $\rho = b$, $H_{\phi}^1 = H_{\phi}^2$, we get from magnetic field equations that

$$\begin{aligned} \left[\frac{k_{\rho 1}}{\mu_1} J_m'(k_{\rho 1} b) \right] A_{m1} - \left[\frac{k_{\rho 2}}{\mu_2} J_m'(k_{\rho 2} b) \right] A_{m2} \\ - \frac{k_{\rho 2}}{\mu_2} Y_m'(k_{\rho 2} b) B_{m2} = 0. \end{aligned} \quad (14)$$

Finally, at $\rho = a$, $H_{\phi}^2 = 0$ and then we get similarly

$$\left[\frac{k_{\rho 2}}{\mu_2} J_m'(k_{\rho 2} a) \right] A_{m2} + \left[\frac{k_{\rho 2}}{\mu_2} Y_m'(k_{\rho 2} a) \right] B_{m2} = 0. \quad (15)$$

From the previous three equations, that is, (13), (14), and (15), we see that the right side is zero. So, in order to have solutions, the determinant formed by the corresponding matrix must be equal to 0:

$$\begin{vmatrix} \frac{k_{\rho 1}^2}{\mu_1 \epsilon_1} J_m(k_{\rho 1} b) & -\frac{k_{\rho 2}^2}{\mu_2 \epsilon_2} J_m(k_{\rho 2} b) & -\frac{k_{\rho 2}^2}{\mu_2 \epsilon_2} Y_m(k_{\rho 2} b) \\ \frac{k_{\rho 1}}{\mu_1} J_m'(k_{\rho 1} b) & -\frac{k_{\rho 2}}{\mu_2} J_m'(k_{\rho 2} b) & -\frac{k_{\rho 2}}{\mu_2} Y_m'(k_{\rho 2} b) \\ 0 & \frac{k_{\rho 2}}{\mu_2} J_m'(k_{\rho 2} a) & \frac{k_{\rho 2}}{\mu_2} Y_m'(k_{\rho 2} a) \end{vmatrix} = 0. \quad (16)$$

Solving the above determinant we get

$$\begin{aligned} \frac{k_{\rho 1}}{\epsilon_1} \frac{J_m(k_{\rho 1} b)}{J_m'(k_{\rho 1} b)} \\ = \frac{k_{\rho 2}}{\epsilon_2} \left[\frac{J_m(k_{\rho 2} a) Y_m'(k_{\rho 2} a) - J_m'(k_{\rho 2} a) Y_m(k_{\rho 2} b)}{J_m'(k_{\rho 2} b) Y_m'(k_{\rho 2} a) - J_m'(k_{\rho 2} a) Y_m'(k_{\rho 2} b)} \right]. \end{aligned} \quad (17)$$

Now for ENG metamaterial,

$$k_{\rho 1} \approx k_1 = j\omega \sqrt{\mu_1 |\epsilon_1|}. \quad (18)$$

And for MNG metamaterial,

$$k_{\rho 1} \approx k_1 = j\omega \sqrt{\epsilon_1 |\mu_1|}. \quad (19)$$

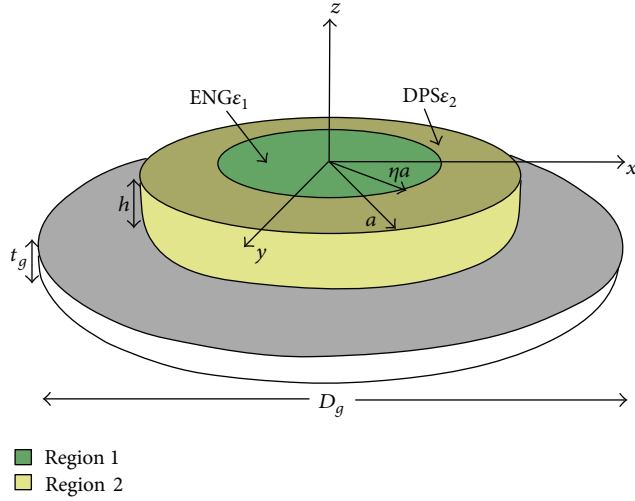


FIGURE 1: Geometry of a circular microstrip patch antenna partially loaded with metamaterial (ENG) substrate and ground plane with parameters $\eta a = (.56)(20 \text{ mm}) = 11.2 \text{ mm}$, $a = 20 \text{ mm}$, $h = 4.3 \text{ mm}$, $t_g = 2 \text{ mm}$, $D_g = 40 \text{ mm}$, $\epsilon_2 = 1.33$, $\epsilon_1 = -1.9$ (at 4.2686 GHz), $\mu_2 = 1$, $\mu_1 = 1$, and feed position from the centre $f_p = 15 \text{ mm}$.

TABLE 1: Selected permittivity and filling ratio for ENG-metamaterial loading in antenna.

| Chosen resonant frequency, f_r (GHz) | ϵ_1 (at f_r) | Filling ratio (η) |
|--|--------------------------|--------------------------|
| 4.2686 | -1.90 | 0.56 |

Putting the above relation, the dispersion relation for ENG metamaterial loaded patch antenna becomes

$$2\sqrt{\frac{\mu_1\epsilon_2}{\mu_2|\epsilon_1|}} \frac{I_m(|k_{\rho 1}b|)}{I_{m-1}(|k_{\rho 1}b|) + I_{m+1}(|k_{\rho 1}b|)} = \frac{J_m(k_{\rho 1}b)Y'_m(k_{\rho 1}a) - J'_m(k_{\rho 1}a)Y'_m(k_{\rho 1}b)}{J'_m(k_{\rho 2}b)Y'_m(k_{\rho 2}a) - J'_m(k_{\rho 2}a)Y'_m(k_{\rho 2}b)} \quad (20)$$

And for MNG metamaterial, the dispersion relation is

$$-2\sqrt{\frac{|\mu_1|\epsilon_2}{\mu_2\epsilon_1}} \frac{I_m(|k_{\rho 1}b|)}{I_{m-1}(|k_{\rho 1}b|) + I_{m+1}(|k_{\rho 1}b|)} = \frac{J_m(k_{\rho 1}b)Y'_m(k_{\rho 1}a) - J'_m(k_{\rho 1}a)Y'_m(k_{\rho 1}b)}{J'_m(k_{\rho 2}b)Y'_m(k_{\rho 2}a) - J'_m(k_{\rho 2}a)Y'_m(k_{\rho 2}b)} \quad (21)$$

By using the above two dispersion relations, a MATLAB based parameter optimization algorithm has been developed in [1]. In that algorithm, the optimized value of metamaterial parameter such as filling ratio, permittivity, and permeability has been calculated for metamaterial loaded circular patch antennas.

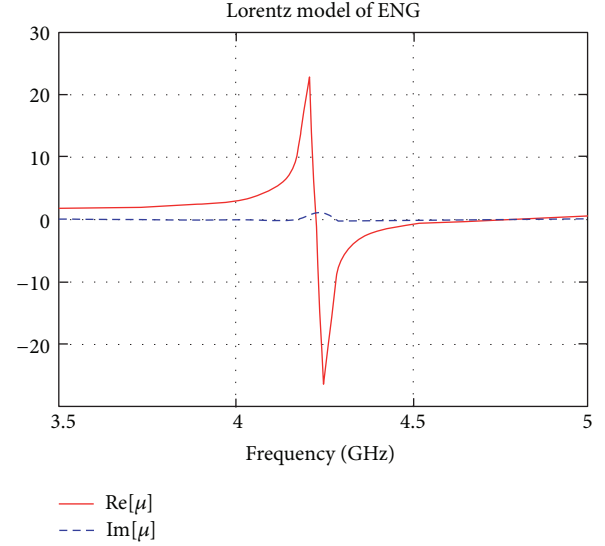


FIGURE 2: Lorentz dispersive model of ENG for proposed antenna.

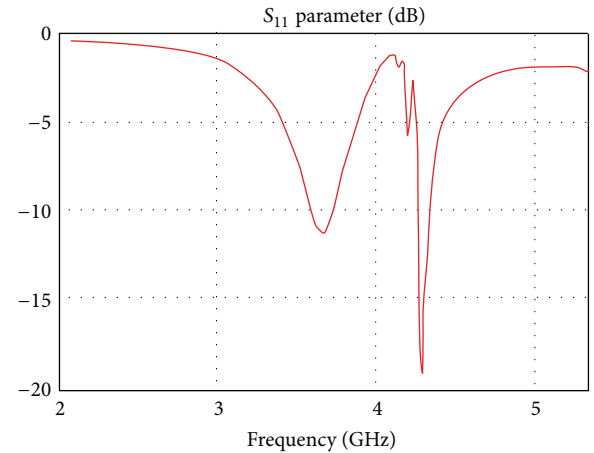


FIGURE 3: S_{11} parameter for 20 mm circular patch antenna using ENG as core material.

3. ENG Metamaterial Loaded Dual Band Circular Patch Antenna

3.1. Antenna Design Structure and Specifications. In circular microstrip patch antenna, by using ENG as a substrate instead of regular dielectric we can achieve dual band performance. Apart from conventional TM_{110} mode unconventional $TM_{\delta 10}$ ($1 < \delta < 2$) mode can be modified.

In designing our proposed antenna, geometry of a circular patch with metamaterial block as shown in Figure 1 has been used. With proper choice of filling ratio (η), ENG metamaterial (ϵ_1) is loaded concentrically with regular dielectric (ϵ_2). In Figure 1 ENG metamaterial is denoted by region 1 (green) and regular dielectric is denoted by region 2 (yellow). The antenna consists of a metallic patch of thickness ($t_p = 1 \text{ mm}$) and radius ($a = 20 \text{ mm}$) at the top. A metallic plate placed at the bottom with radius ($2 \times a = 40 \text{ mm}$) and

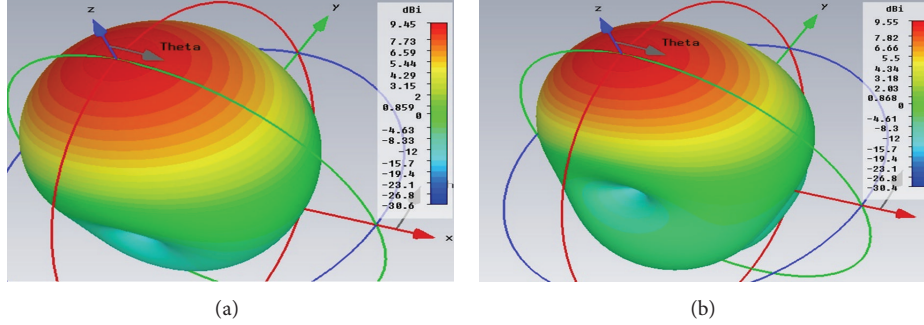


FIGURE 4: 3D view of (a) conventional TM_{110} mode at 3.6665 GHz and (b) unconventional $TM_{\delta 10}$ ($1 < \delta < 2$) mode's radiation pattern at 4.2686 GHz.

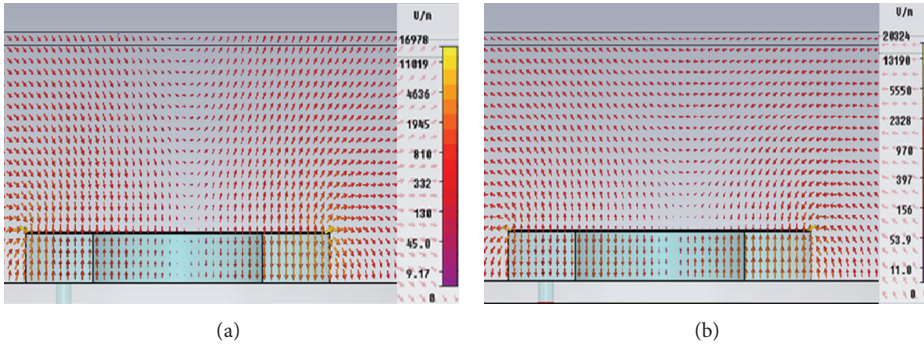


FIGURE 5: Electric field distribution on the $y = 0$ plane at (a) $f_{110} = 3.6665$ GHz and (b) $f_{\delta 10}$ ($1 < \delta < 2$) = 4.2686 GHz.

thickness ($t_g = 2$ mm) acts as ground. This chosen optimum radius and thickness of the ground plate causes maximum reflection from the ground that enhances the directivity. Conductivity of the metal is selected as 0.58 Meg σ . As a feed we have used coaxial cable designed to have $Z_p = 50 \Omega$ characteristic impedance with inner radius of coaxial cable ($r_{in} = 0.4$ mm) and outer radius of coaxial cable ($r_{out} = 1.0456$ mm) and its position is set at $f_p = 15$ mm from the center for achieving good matching properties over operating frequency range. The underneath substrate is filled with concentric dielectrics with ENG metamaterial as the inner core and DPS material as outer core. Dielectric substrate height is $h = 4.3$ mm. Of all the dielectric parameters, $\epsilon_2 = 1.3\epsilon_0$, $\mu_2 = 1.0\mu_0$, and $\mu_1 = 1.0\mu_0$ are chosen as the optimum values for these parameters. However, the rest two controlling parameters, that is, ENG metamaterial's permittivity (ϵ_1) and filling ratio (η) have been calculated by a MATLAB based parameter optimization algorithm [1] and with the aid of dispersive equation (20), developed for ENG metamaterial. In Table 1. those optimum parameters are shown at our desired resonant frequency of 4.26 GHz.

Actually, SNG or DNG metamaterials are inherently dispersive and lossy [10, 11]. So, without using dispersive lossy model the simulated results cannot give proper realistic results. Here we have used Lorentz model for ENG metamaterial dispersive relation:

$$\epsilon(\omega) = \epsilon_{\infty} + \frac{(\epsilon_s - \epsilon_{\infty})\omega_0^2}{\omega_0^2 - \omega^2 - j\omega\delta}, \quad (22)$$

where $\epsilon_{\infty} = 1.0\epsilon_0$, $\epsilon_s = 1.23\epsilon_0$, $\omega_0 = 26.6$ Grad/sec, $f_r = 4.26$ GHz, and damping frequency $\delta = 1$ MHz.

Plugging these parameters into (22) dispersive relation of our desired ENG material should be as in Figure 2.

Using all the above stated material and geometric parameters, CST microwave studio [12] simulation gives the following results: S-parameter, 3D radiation patterns, and electric and current distribution (Figures 3–6).

3.2. Resonance and Radiation Characteristics of the Antenna. From the S_{11} parameter curve of we see that corresponding return losses at 3.66 GHz and 4.2686 GHz frequencies fall well below -10 dB that ensures satisfactory resonance for the antenna structure. But satisfactory resonance does not always guarantee good radiation. So in order to ensure good radiation and thus call it a good radiator, we need to look into its radiation patterns at those particular resonant frequencies also. The radiation patterns obtained at the resonant frequencies indicated at the S_{11} parameter curve of Figure 3 are shown in Figure 4.

From the 3D radiation patterns of the ENG loaded patch antenna (see Figure 4), we see that conventional TM_{110} mode as well as the modified $TM_{\delta 10}$ mode ($1 < \delta < 2$) shows satisfactory z -directed radiation (Figures 4(a) and 4(b)). The conventional TM_{110} mode has the gain of 9.45 dB, whereas the gain of the modified mode $TM_{\delta 10}$ ($1 < \delta < 2$) at frequency 4.2686 GHz is 9.55 dB, which is even higher than the conventional mode.

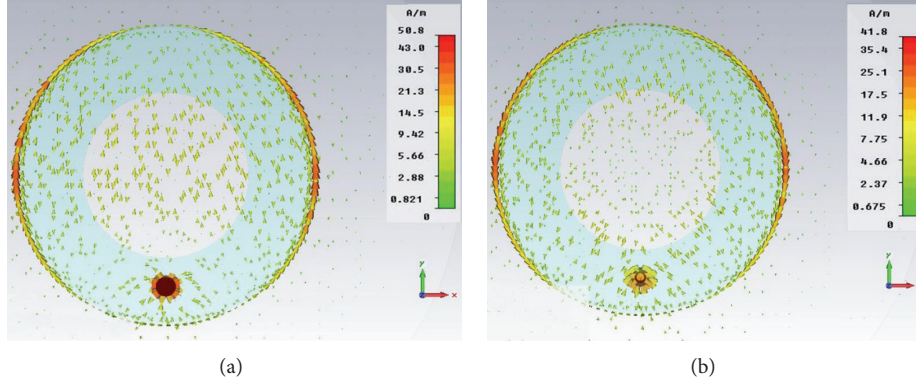


FIGURE 6: Current distribution on the patch at (a) $f_{110} = 3.6665$ GHz and (b) $f_{\delta 10}$ ($1 < \delta < 2$) = 4.2686 GHz.

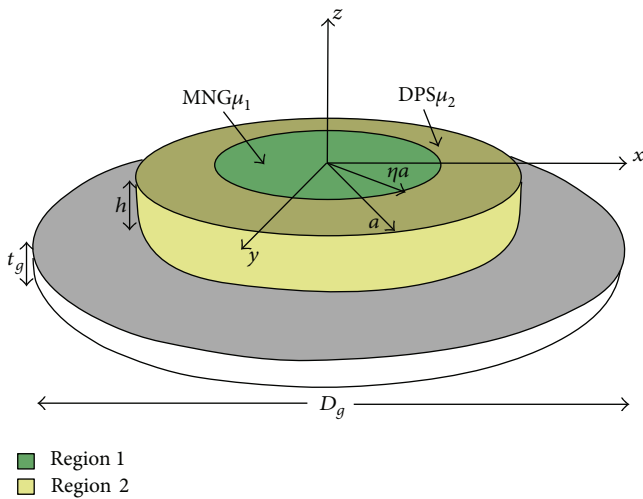


FIGURE 7: Geometry of a circular microstrip patch antenna partially loaded with metamaterial (MNG) substrate and ground plane with parameters: $\eta a = (.56 \text{ mm})(20 \text{ mm}) = 11.2 \text{ mm}$, $a = 20 \text{ mm}$, $h = 5 \text{ mm}$, $t_g = 2 \text{ mm}$, $D_g = 40 \text{ mm}$, $\epsilon_2 = 1.33$, $\epsilon_1 = 1.33$, $\mu_2 = 1$, $\mu_1 = -2.83$ (at 2.56 GHz), and feed position $f_p = 15 \text{ mm}$.

3.3. Electric Field and Current Distribution. From the electric field distribution at the plane $y = 0$, it is apparent that in case of conventional TM_{110} mode electric field flips its sign passing from one side to the other side of the patch, thus satisfying the condition for broadside radiation (Figure 5(a)). But in case of modified $TM_{\delta 10}$ ($1 < \delta < 2$) mode due to using metamaterial, phase change of electric field at the ENG-DPS interface occurs in such a way that the electric field flips from one side to the other side of the patch, as a result of which the electric field distribution of $TM_{\delta 10}$ ($1 < \delta < 2$) mode looks like that of TM_{110} mode, thus also satisfying the condition for broadside radiation (Figure 5(b)).

Microstrip circular patch antenna theory says that if the metallic patch induced current remains in the same phase passing from one side to the other side of the patch, that is, current distribution remains symmetric around y -axis, it must show broadside radiation. At $(x = 0, y = 0, z = 0)$ point magnetic field distribution from the two opposite current

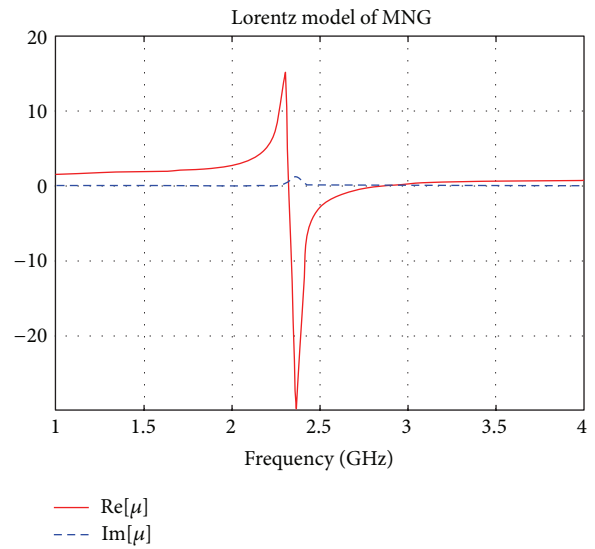


FIGURE 8: Lorentz dispersive model for proposed MNG loaded antenna.

elements reinforce in z direction. That is why TM_{110} mode shows z -directed radiation (Figure 6(a)). But any other mode does not normally show this property. What metamaterial does is that, in our desired frequency, at interface of DPS-ENG, it causes phase change in such a way that the current distribution at that frequency resembles with TM_{110} mode's current distribution. Figure 6(b) shows current distribution of the patch for $TM_{\delta 10}$ ($1 < \delta < 2$) mode that resembles with TM_{110} mode's pattern. It is noticeable that, despite the small dimension of the patch, the current distribution is closed in electrically small resonant loops and it resembles the current distribution of TM_{110} mode.

4. MNG Metamaterial Loaded Dual Band Circular Patch Antenna

4.1. Antenna Design Structure and Specifications. In designing our proposed antenna, geometry of a circular patch with metamaterial block as shown in Figure 7 has been used. It

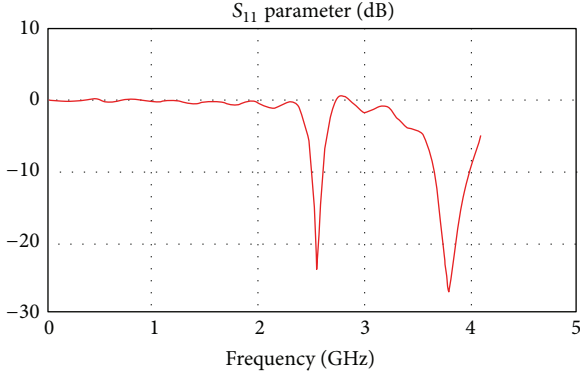


FIGURE 9: S_{11} -parameter for 20 mm radius circular patch antenna using MNG as core material.

is almost similar to the ENG loaded patch structure. It also consists of a metallic patch of thickness ($t_p = 1$ mm) and radius ($a = 20$ mm) at the top. A metallic plate placed at the bottom with radius ($2 \times a = 40$ mm) and thickness ($t_g = 1$ mm) acts as ground. This chosen optimum radius and thickness of the ground plate causes maximum reflection from the ground that enhances the directivity. The metal has a conductivity of $0.58 \text{ Meg}\sigma$. As a feed we have used coaxial cable designed to have $Z_p = 50 \Omega$ characteristic impedance with inner radius of coaxial cable ($r_{in} = 0.4$ mm) and outer radius of coaxial cable ($r_{out} = 1.0351$ mm) and its position is set at $f_p = 12$ mm from the center for achieving good matching properties over operating frequency range. The underneath substrate is filled with concentric dielectrics with MNG metamaterial as the inner core and DPS material as outer core. Dielectric substrate height ($h = 5$ mm) is spacious enough so as to allow realistic hosting of split ring resonator (SRR) to construct MNG material [13]. Of all the dielectric parameters, $\epsilon_2 = 1.3\epsilon_0$, $\mu_2 = 1.0\mu_0$, and $\epsilon_1 = 1.3\epsilon_0$ are chosen as the optimum values for these parameters. However, MNG metamaterial's permeability (μ_1) and filling ratio (η) have been calculated by a MATLAB based parameter optimization algorithm [1] and with the aid of our derived dispersive equation (21) for MNG metamaterial. Calculated optimum permeability and filling ratio are shown in Table 2.

We have used Lorentz model for MNG metamaterial dispersive relation:

$$\mu(\omega) = \mu_{\infty} + \frac{(\mu_s - \mu_{\infty})\omega_0^2}{\omega_0^2 - \omega^2 - j\omega\delta}, \quad (23)$$

where $\mu_{\infty} = 1.0\mu_0$, $\mu_s = 1.5\mu_0$, and $\omega_0 = 14.76 \text{ Grad/sec}$ causes resonance at $f_r = 2.56 \text{ GHz}$ and damping frequency ($\delta = 10 \text{ MHz}$). Putting these values in (3), we get the dispersion curve for MNG as shown in Figure 8.

4.2. Resonance and Radiation Characteristics. Using all the above stated material and geometric parameters, CST microwave studio [12] simulation gives the following results: S-parameter (Figure 9), 3D radiation patterns, and electric field distribution (Figures 10 and 11).

TABLE 2: Selected permeability (μ_1) and filling ratio (η) for MNG loading.

| Chosen resonant frequency, f_r (GHz) | μ_1 (at f_r) | Filling ratio (η) |
|--|---------------------|--------------------------|
| 2.56 | -2.83 | 0.35 |

S_{11} parameter curve, in Figure 9, shows that at frequencies $f_{\delta 10}$ ($0 < \delta < 1$) = 2.56 GHz, $f_{110} = 3.8$ GHz resonance occurs, which causes the corresponding return losses at these frequencies to fall well below -10 dB that ensures satisfactory resonance. Again, from Figure 9, it is also evident that when antenna size is reduced, resonant frequency has to move away from the TM_{110} frequency which eventually causes to lose its z -directed radiation characteristics. So it is not always productive to reduce patch antenna size whimsically. But, in our study, we have found that around 70% size reduction provides us with nearly -9 dB gain, whereas size reduction, that is,

$$\begin{aligned} & \frac{(f_{110} - f_{\delta 10} (0 < \delta < 1))}{f_{110}} \times 100\% \\ &= \frac{(3.66 \text{ GHz} - 2.56 \text{ GHz})}{3.66 \text{ GHz}} \times 100\% \approx 30\%, \end{aligned} \quad (24)$$

provides us 2.2 dB gain which is quite satisfactory for practical antenna operation. This is the maximum allowable limit of size reduction with realizable gain performance that we have found in our study. In fact, antenna size reduction can be extended up to nearly 35% to get gain over 0 dB.

From the 3D radiation patterns of MNG loaded antenna (see Figure 10) we see that conventional TM_{110} mode as well as the modified $TM_{\delta 10}$ mode ($0 < \delta < 1$) shows satisfactory z -directed radiation. The conventional mode TM_{110} has the gain 9.2 dB (Figure 10(b)) at frequency 3.8 GHz, whereas the gain of the modified mode $TM_{\delta 10}$ ($0 < \delta < 1$) at frequency 2.56 GHz is 1.83 dB (Figure 10(a)), which is much lower than the conventional mode. So, this sort of dual band antenna can be a suitable choice where low gain and less directive dual band performance is a prior requirement.

4.3. Electric Field Distribution. From the electric field distribution at the plane $y = 0$, it is apparent that for conventional TM_{110} mode electric field flips its sign passing from one side to the other side of the patch, thus satisfying the condition for broadside radiation (Figure 11(b)). But in case of modified $TM_{\delta 10}$ ($0 < \delta < 1$) mode due to using metamaterial, phase change of electric field at the MNG-DPS interface occurs in such a way that the electric field flips from one side to the other side of the patch, as a result of which the electric field distribution of $TM_{\delta 10}$ ($0 < \delta < 1$) mode looks like that of TM_{110} mode, thus also satisfying the condition for broadside radiation (Figure 11(a)).

5. Conclusions

In the first section of this paper, a novel dual band circular patch antenna with high directivity performance in

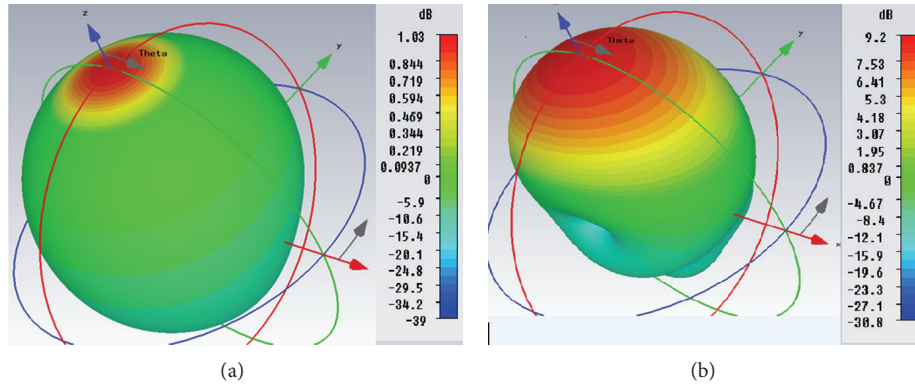


FIGURE 10: 3D view of (a) unconventional $TM_{\delta 10}$ ($0 < \delta < 1$) mode's radiation pattern at 2.56 GHz and (b) conventional TM_{110} mode's radiation pattern at 3.8 GHz.

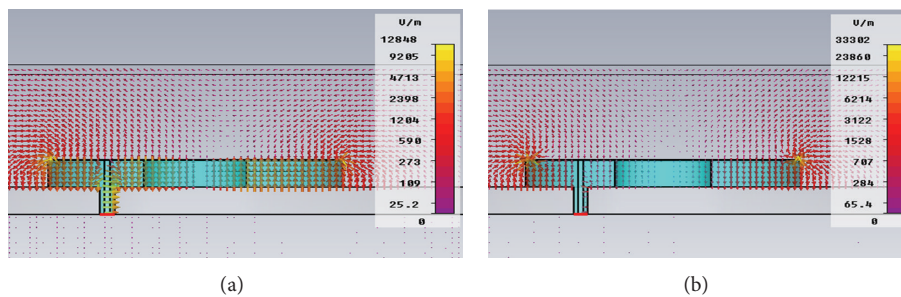


FIGURE 11: Electric field distribution on the $y = 0$ plane on the metallic patch for the antenna of Figure 7 at (a) 2.56 GHz for unconventional $TM_{\delta 10}$ ($0 < \delta < 1$) mode and (b) 3.8 GHz for conventional TM_{110} mode.

both bands has been shown. Inserting ENG metamaterial provides us with an additional modified mode with high gain. By controlling ENG metamaterial's filling ratio different frequency can be tuned in. So, this novel antenna design can be a suitable choice where highly directive gain along with user's flexibility in choosing resonant frequencies for dual band antenna purpose is required. In the second section of this paper, a miniaturized size dual band antenna loaded with MNG metamaterial has been designed. In this sort of antenna, since the unconventional mode yields a much lower gain than the conventional mode, one of its dual bands can be used as a substitute for low-gain antenna. Actually, this sort of antenna can be very effective where the use of less directive and low-gain small antennas is a prime concern. The use of this MNG loaded patch antenna is expected to be conducive for reasonably well signal propagation in some other special areas, such as high multipath interference regions, regions having frequent obstacles between transmitters and receivers, highly dense populated areas, and in spacecraft as a backup to the high-gain antenna.

Conflict of Interests

The authors declare that there is no conflict of interests regarding the publication of this paper.

References

- [1] S. Ferdous, A. Hossain, S. M. H. Chowdhury, M. R. C. Mahdy, and M. Abdul, "Reduced and conventional size multi-band circular patch antennas loaded with metamaterials," *IET Microwaves, Antennas & Propagation*, vol. 7, no. 9, pp. 768–776, 2013.
- [2] K.-L. Wong and G.-B. Hsieh, "Dual-frequency circular microstrip antenna with a pair of arc-shaped slots," *Microwave and Optical Technology Letters*, vol. 19, no. 6, pp. 410–412, 1998.
- [3] A. Alù, F. Bilotti, N. Engheta, and L. Vegni, "Subwavelength, compact, resonant patch antennas loaded with metamaterials," *IEEE Transactions on Antennas and Propagation*, vol. 55, no. 1, pp. 13–25, 2007.
- [4] K. S. Zheng, W. Y. Tam, and D. B. Ge, "Broadside subwavelength microstrip antennas partially loaded with metamaterials," in *Proceedings of the International Workshop on Metamaterials (META '08)*, pp. 39–42, Nanjing, China, November 2008.
- [5] F. Bilotti, A. Alu, and L. Vegni, "Design of miniaturized metamaterial patch antennas with μ -negative loading," *IEEE Transactions on Antennas and Propagation*, vol. 56, no. 6, pp. 1640–1647, 2008.
- [6] P. Y. Chen and A. Alù, "Sub-wavelength elliptical patch antenna loaded with μ -negative metamaterials," *IEEE Transactions on Antennas and Propagation*, vol. 58, no. 9, pp. 2909–2919, 2010.
- [7] J. Pruitt and D. Strickland, "Experimental exploration of metamaterial substrate design for an electrically small patch-like

- antenna,” in *Proceedings of the Antennas and Propagation Society International Symposium (APSURSI '10)*, IEEE, July 2010.
- [8] S. Jahani, J. Rashed-Mohassel, and M. Shahabadi, “Miniaturization of circular patch antennas using MNG metamaterials,” *IEEE Antennas and Wireless Propagation Letters*, vol. 9, pp. 1194–1196, 2010.
- [9] J. Xiong, H. Li, B. Z. Wang, Y. Jin, and S. He, “Theoretical investigation of rectangular patch antenna miniaturization based on the DPS-ENG bi-layer super-slow TM wave,” *Progress in Electromagnetics Research*, vol. 118, pp. 379–396, 2011.
- [10] M. R. C. Mahdy, M. R. A. Zuboraj, A. A. N. Ovi, and M. A. Matin, “An idea of additional modified modes in rectangular patch antennas loaded with metamaterial,” *IEEE Antennas and Wireless Propagation Letters*, vol. 10, pp. 869–872, 2011.
- [11] M. Hassan, M. R. C. Mahdy, G. M. Hasan, and L. Akter, “A novel miniaturized triple-band antenna,” in *Proceedings of the 7th International Conference on Electrical and Computer Engineering (ICECE '12)*, pp. 702–705, Dhaka, Bangladesh, December 2012.
- [12] CST Microwave Studio, CST of America, <http://www.cst.com>.
- [13] S. M. H. Chowdhury, M. A. Hossain, M. S. Ferdous, M. R. Chowdhury Mahdy, and M. A. Matin, “Conceptual and practical realization of reduced size multi-band circular microstrip patch antenna loaded with MNG metamaterial,” in *Proceedings of the 7th International Conference on Electrical and Computer Engineering (ICECE '12)*, pp. 834–837, Dhaka, Bangladesh, December 2012.

Research Article

Multishorting Pins PIFA Design for Multiband Communications

Muhammad Sajjad Ahmad, C. Y. Kim, and J. G. Park

School of Electronics Engineering, Kyungpook National University, 1370 Sankyuk-Dong, Buk-Gu, Daegu 702-701, Republic of Korea

Correspondence should be addressed to C. Y. Kim; cykim@ee.knu.ac.kr

Received 6 October 2013; Revised 16 December 2013; Accepted 17 December 2013; Published 5 February 2014

Academic Editor: Bing Liu

Copyright © 2014 Muhammad Sajjad Ahmad et al. This is an open access article distributed under the Creative Commons Attribution License, which permits unrestricted use, distribution, and reproduction in any medium, provided the original work is properly cited.

A novel PIFA model with multiple shorting pins is proposed for multiband, low profile wireless applications, which has the ability to work in adverse conditions. The proposed model has a planar radiating sheet, a ground plane, and sides covered with PEC boundaries. The substrate inside the *antenna box* is tempered in order to improve the bandwidth and gain. The enhancements applied to the proposed PIFA model show improved characteristics for this PIFA model and make it a versatile candidate for handheld, low profile, and multiband resonant communication devices. Pertinent communication devices are those that work with GSM 850/900, UMTS 850/900/1700/1900/2100, LTE 2300/2500, and ISM 2400 bands used for Bluetooth and WLAN.

1. Introduction

Antennas (electromagnetic waves guiding devices) radiate signals to unbounded mediums. They are frequency dependent devices and are designed to operate at specific frequencies known as the antenna's operating bands. Other than these specific frequency bands, an antenna rejects any signal that is fed to it. Antennas are known for their various properties including gain, directivity, radiation pattern, specific absorption rate (SAR), and Voltage Standing Wave Ratio (VSWR).

In [1–3] modified planar inverted-F antenna (PIFA) models were proposed with compact size, multiple resonant bands, and enhanced bandwidth by changing the width of the shorting and feed pins, adding a parasitic element parallel to the shorting pin at an optimized distance and a planar rectangular monopole top loaded with two rectangular patches with one of them grounded, respectively. In an ordinary PIFA model, when a shorting pin is applied near the feeding point, it allows the design to be reduced in size but narrows the bandwidth at the same time. By applying different schemes and techniques to an ordinary PIFA model, we can enhance not only its bandwidth but also its gain and efficiency as well.

In recent years, the antenna industry has shown a rapid demand for multiband resonant, low profile, and ultrawide

bandwidth antennas [4]. The fact that PIFA has a flexible design and can provide multiband resonant operations makes it a favorable candidate for the antenna industry. Introducing slots in the radiating patch may allow designers to achieve resonant frequencies that are not possible for a conventional PIFA with small dimensions to resonate on. Moreover, with slots in the ground plane of a PIFA model, it is reported in the literature as a bandwidth enhancement method [5]. Such PIFA models, commonly known as a meandered ground plane or meandered radiating patch, have diversified PIFAs for the low profile design industry. Plenty of modified PIFA models have been designed for multiband operations; slotted PIFA, meandered ground plane PIFA, and multiple shorting pins PIFA have been successful among others. In [6, 7], the limitations of electrically small antennas in terms of the gain, bandwidth, and their capacity to produce the desired number of resonant bands along with guidelines to design such antennas based on the parametric analysis of electrically small antennas are discussed.

Antennas are designed and tested in almost ideal environments, but when they are exposed to conducting materials in their surroundings, they do not just shift their resonant frequency but the bandwidth and gain are changed as well. The performance of any conventional antenna is affected severely, in terms of its resonant frequency, gain,

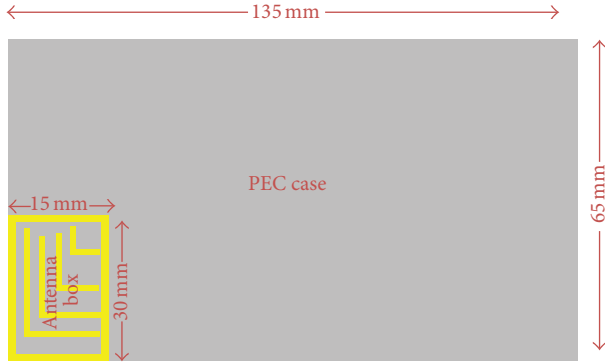


FIGURE 1: Proposed PIFA model *antenna box* and *PEC case*, with PEC boundaries around it.

and bandwidth, in the presence of conducting bodies around the antenna. It is considered a loophole for communication devices working with such antennas. In [8, 9], the impact of metallic surfaces and user's hand on the performance of different antennas are discussed. The efficiency of the antenna is reported to drop from 91% (without the hand's effect) to 41% (with the hand's effect), which might not be acceptable for communication devices which require higher efficiency. Therefore, an exquisite antenna design is needed for today's industry which can cope with such undesired situations and maintain its efficiency even in the worst conditions. Our proposed model has the ability to maintain its performance in such critical conditions. Details of our proposed antenna design are given in the following section.

2. Antenna Design Procedure

The proposed antenna model is shown in Figure 1. It consists of a dielectric material FR-4, which has a dielectric constant of $\epsilon_r = 4.4$ and a thickness of 7 mm, *antenna box*, and *PEC case*. The dielectric material is sandwiched between the radiating patch (top sheet of the *antenna box*) and the ground plane of the *PEC case*. The dimensions of the proposed model are $65 \times 135 \times 7 \text{ mm}^3$. For simplicity the model is divided in two main sections: firstly, the *PEC case* and second the *antenna box*. The dimensions of the *antenna box* are $30 \times 15 \times 7 \text{ mm}^3$. The top sheet of *antenna box* acts as a radiating patch which contains slots around its boundary to maintain the separation between the antenna elements and the *PEC case*. In Figures 2 and 3, a 3D view of the proposed model is shown with special emphasis on the *antenna box* and its components, that is, the radiating patch, parasitic patch, feeding position, and shorting pins. A parametric description for the radiation patch is presented in Figure 4, with detail of the parameters in Table 1. Slots in the radiating patch are used to increase the electrical length of the radiating patch in order to achieve the resonant band at lower frequencies. The sides of the *antenna box* are acting as parasitic patch elements. A prototype of the proposed model is designed and shown in Figure 8.

The proposed model contains three shorting pins, shown in Figure 3, that are connecting the radiating patch to the ground plane at different point. The width of each shorting

TABLE 1: Length of the slots inserted in the radiating patch.

| Slot name | Length (mm) |
|-----------|-------------|
| L_A | 30 |
| L_B | 30 |
| W_A | 15 |
| W_B | 15 |
| L_1 | 6.5 |
| L_2 | 15 |
| L_3 | 18 |
| L_4 | 25 |
| L_5 | 13 |
| L_6 | 5 |
| L_7 | 8 |
| L_8 | 10 |

pin is 1 mm and the height is 7 mm. Thickness of the model is 7 mm. The width of the lumped port feeding sheet is 2 mm and the direction of integration line for the modes excitation is along the z -axis. The distance between consecutive shorting pins can be changed to shift the resonant bands if desired. Multiple shorting pins and a shortening pin are used to add stability to this model and to obtain multiple resonant bands [10, 11]. Because the boundaries are PEC and the PIFA antenna models are known for their narrow band operations, we used the two sides of the *antenna box* as a parasitic patch. In [12, 13], the parasitic patch for microstrip antennas was introduced and a bandwidth enhancement of 25.5% was reported. It was established that multiple parasitic patches can be used for bandwidth enhancement purposes, both in the vertical and horizontal positions. In our model, the parasitic patch is perpendicular to the driving patch and is connected to the ground plane through the shortening pin.

2.1. Slots in the Radiating Patch. Slots are inserted in the radiating patch to increase the electrical length of the radiating patch. The width of the slots in the radiating patch is 0.5 mm and is denoted by s ; the slot lengths were different and are given in Table 1. The slots around the boundary of radiating patch, that is, L_A , L_B , W_A , and W_B , are used to maintain a separation between the antenna elements of the *antenna box* and *PEC case*; their width is fixed to 1 mm. Although the width and length of the slots help us to change the resonant frequency bands, the interslot coupling effect cannot be neglected either. Both the distance between the slots and their width allow us to tune our model to a suitable coupling effect for desired S11 results.

It is known that the small size of a radiating patch has a limit for producing resonant bands at lower frequencies; a well-tuned slotted model can achieve resonant bands at lower frequencies and may improve the performance of the model [14]. Using the fact that inserting a slot in the radiating patch may result in a new resonant frequency, the position and length of the slot to be inserted in the radiating patch for a desired resonant frequency can be approximately predicted [15].

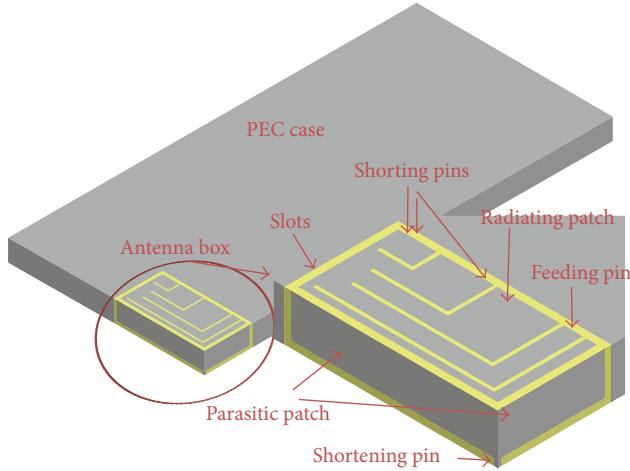


FIGURE 2: A 3D view of the model, parasitic patch, radiating patch, slots, and shortening pin.

2.2. Multiple Shortening Pins. In [16], a dual shortening pin PIFA model was proposed and designed for the dual band operations of mobile handsets. Multiple shortening pins provide different paths and lengths to the antenna for radiating multiple frequencies. Shortening pins provide multiple paths to currents and allow the antenna to radiate at multiple frequencies. In PIFA, the resonant frequency bands depend on both the position and width of the shortening pins used in the model [10]. Multiple shortening pins add stability to the antenna model by allowing it to maintain its performance in adverse situations. Shortening pins, when applied near the feed position, allow designers to reduce the size of the model. In our model, the positions of the shortening pins were chosen carefully to enhance the performance of the antenna at the desired frequency bands and to suppress undesired frequencies.

2.3. Parasitic Patch. A parasitic patch is used to control the directivity and is useful in many ways specially designing low profile antennas. The parasitic patch has a dual effect on S11, when used with the PEC and PMC boundaries. The two sides of the *antenna box* shown in Figure 3 are being used as a parasitic patch to improve the S11 result of our design. Parasitic patches are widely being used in antennas to change the radiating field patterns, steer the beam, and increase the bandwidth [12]. The parasitic patch in our model is used with PEC boundary. Parasitic patch with the PMC boundary may act like a high impedance surface (HIS) [17]. HIS based antennas are extensively being used in vehicular antennas.

2.4. Tempering the Substrate. Dielectric materials like FR-4 are used in antenna designs for many reasons. One aspect is that because it allows miniaturization of the antenna model, and at the same time it is very cheap. However, the problem with using a bulk of dielectric material in communication devices is that it effects the performance of the antenna in terms of efficiency. Because of antenna size limitations (as

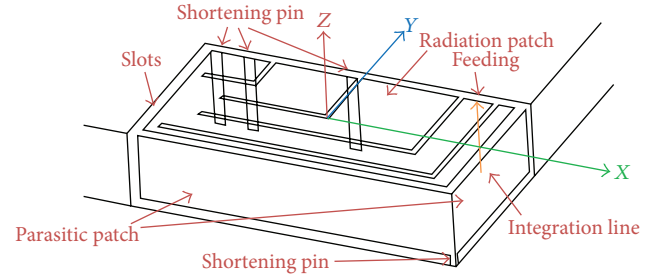


FIGURE 3: A 3D view of the antenna box, radiating patch, parasitic patch, feeding, and shortening pins.

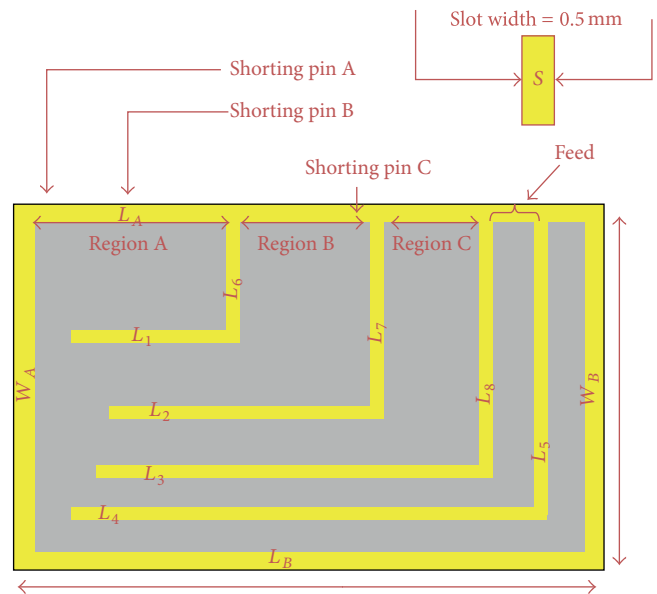


FIGURE 4: Parametric description of the slots in the radiation patch.

we cannot go on increasing the height of our model), it becomes an energy storing device which may be referred to as a lossy device. To deal with this situation, as shown in Figure 5, four vacuum gaps are inserted in the substrate at different positions and the width has been swept for multiple values to ultimately make the proposed model radiate the maximum energy with improved efficiency [18]. The purpose of an antenna is to radiate a signal that is fed to it and not to store it and increase the antenna losses. In [19], substrates are discussed, which can be used in antenna designs. Moreover, the effects of different substrates on the performance of antennas are also highlighted to control the antenna losses.

In our model, we have inserted vacuum gaps inside the FR-4 dielectric material (which we refer to as substrate tempering), for which both the position and width of the vacuum gap affect the S11 results of our model. Moreover, the results show that tempering the substrate material may also improve the gain in the resonant bands of the antenna [20–25].

Because the proposed antenna model is a kind of cavity, the cavity perturbation method can be applied to it. Any increment or decrement in ϵ or μ at any point in the cavity

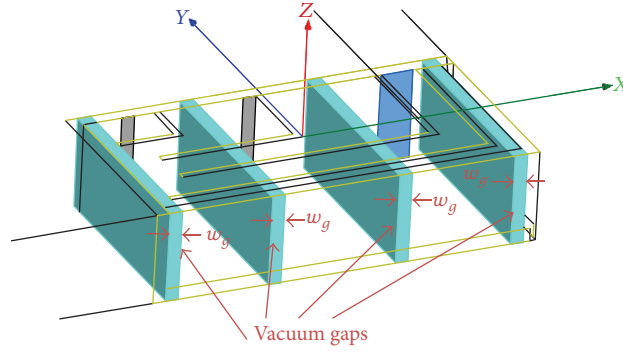


FIGURE 5: Substrate tempering by inserting vacuum gaps in FR-4.

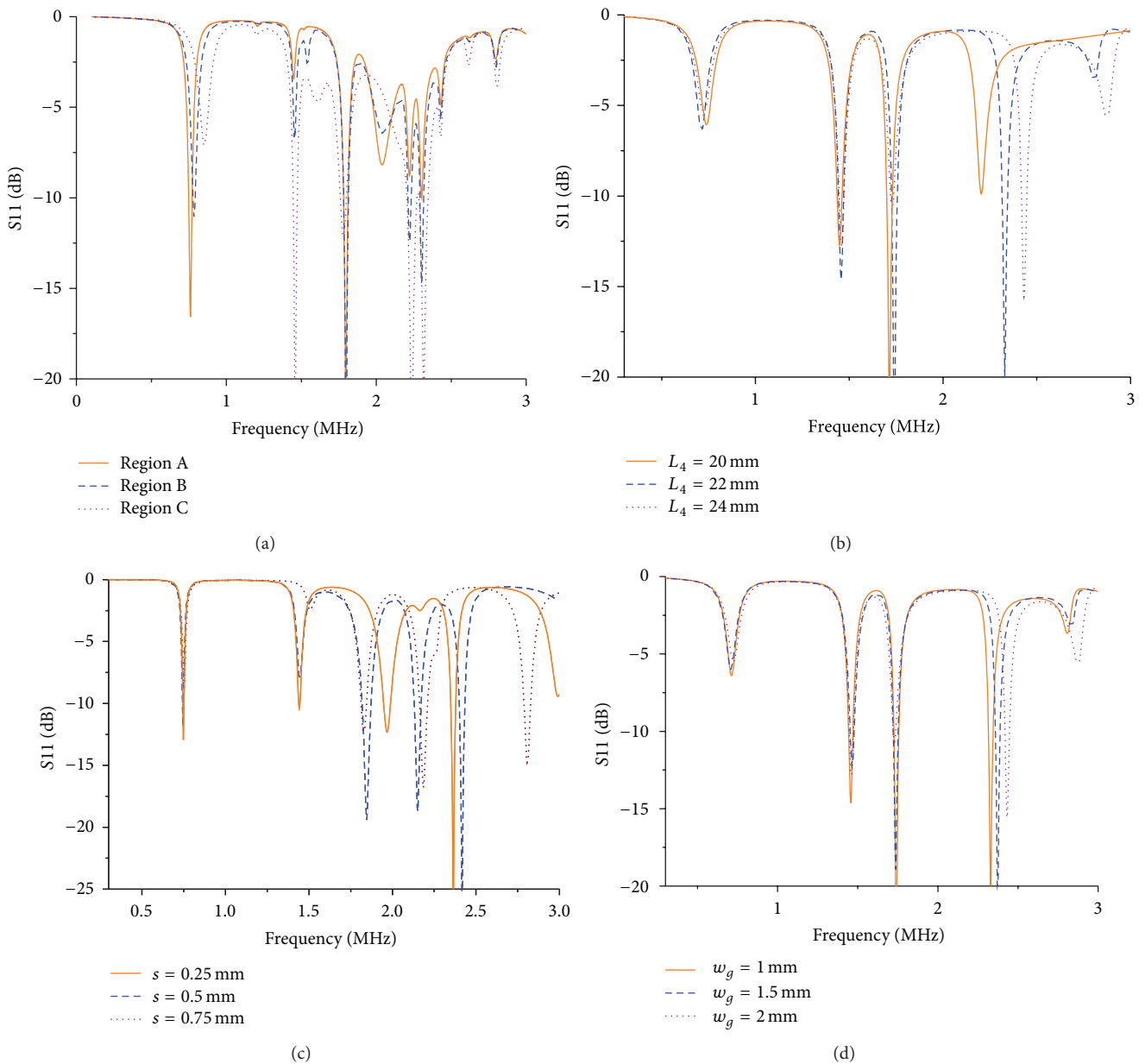


FIGURE 6: (a) Shorting pins position effect on S11. (b) Effect of slot length on S11. (c) Effect of slot width on S11. (d) Effect of varying the width of vacuum gaps inserted in FR-4 substrate on S11.

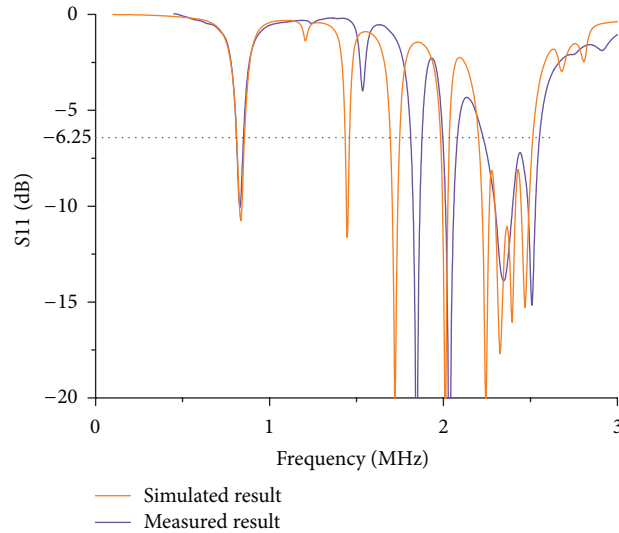


FIGURE 7: Comparison of simulated and measured S11 results for the proposed model.

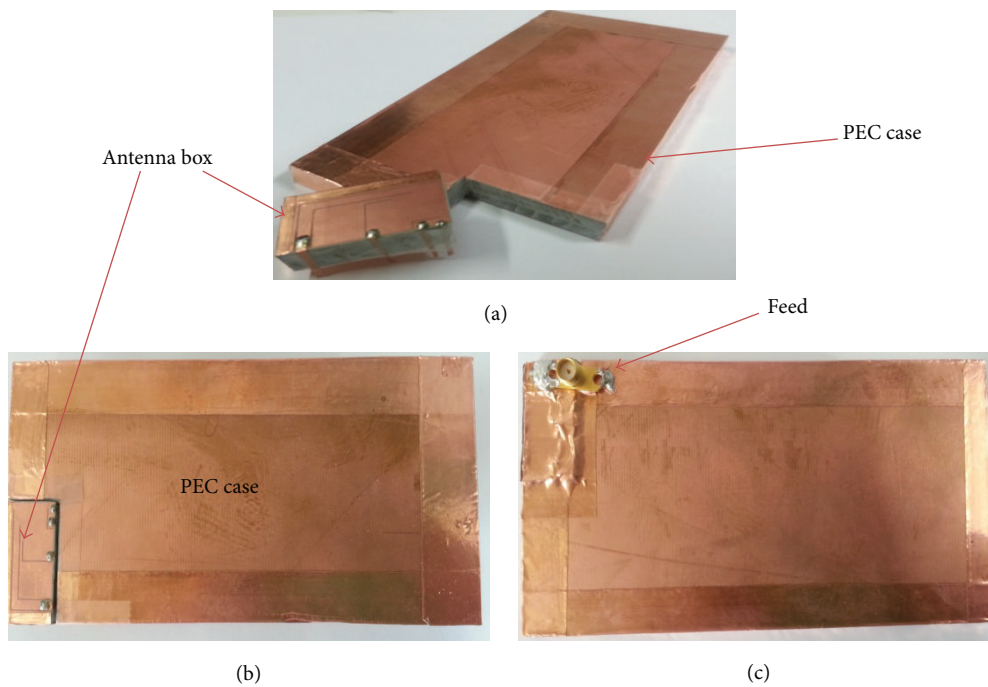


FIGURE 8: (a) Antenna box and *PEC case*. (b) Top view. (c) Bottom view.

may decrease or increase the resonant frequency of the cavity. Moreover, change in resonant frequency can also be related to the stored electric and magnetic energies inside the cavity as well. We choose the orientation and position for the vacuum gap using parametric sweep option in 3D simulation tool used for designing this model. Considering that the fields inside the cavity are approximately the same before and after the substrate tempering or perturbation, we may conclude that the resonant frequency of the cavity may increase or decrease after tempering the substrate depending upon the position of tempering or perturbation inside the cavity [26, 27].

3. Results and Discussion

The proposed model is simulated with the High Frequency Structural Simulator (HFSSv13.0) and a prototype for the proposed model is also designed. The comparison of the simulated and measured S11 results is shown in Figure 7. Section 3.1 deals with the benefits of the enhancements we applied to the model. In Section 3.2, S11 and the magnitude of the E-field at the corresponding resonant frequencies are elaborated. Section 3.3 covers the details of the bandwidths and the gains at corresponding resonant frequencies.

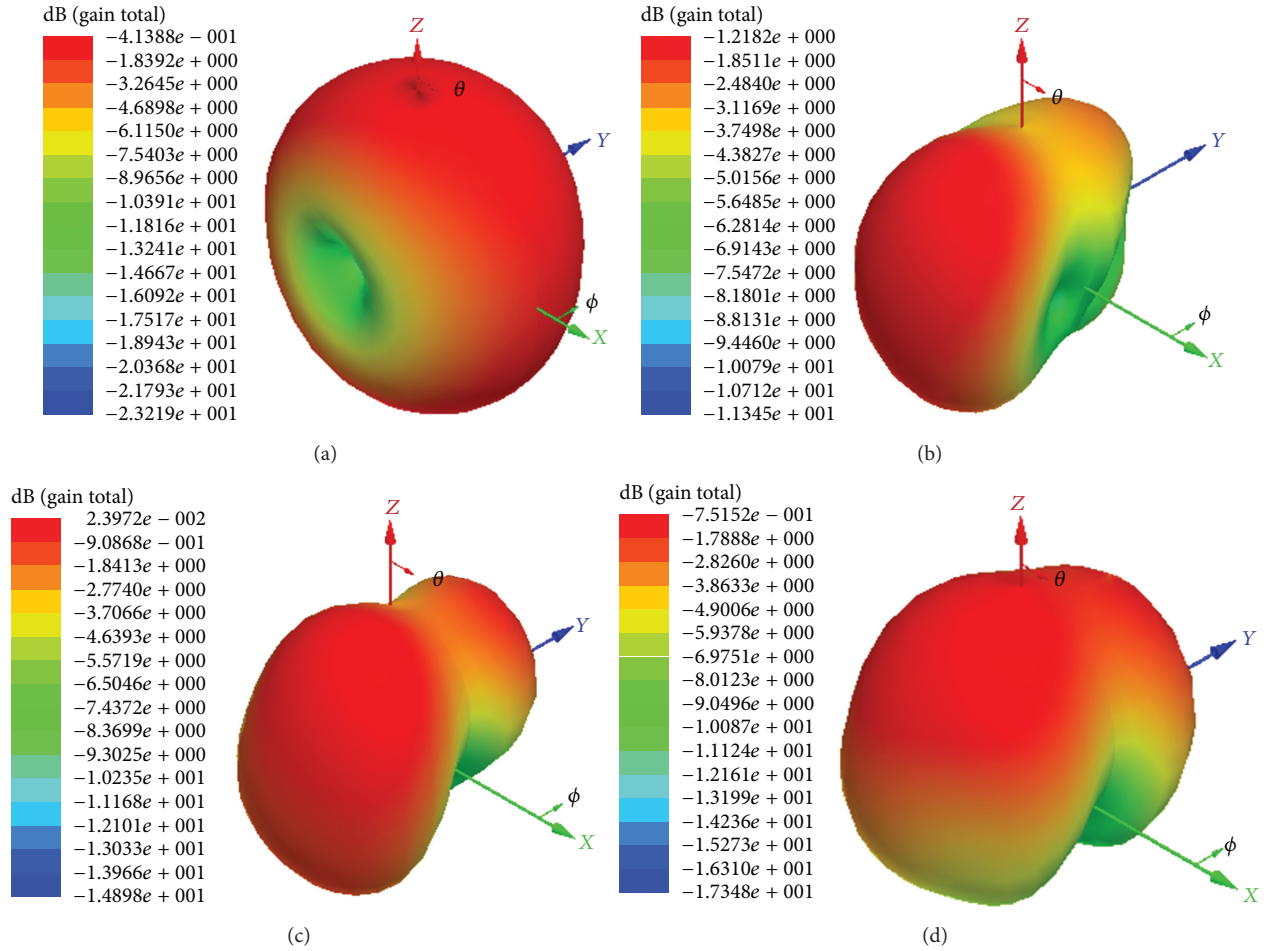


FIGURE 9: (a) Gain at the resonant frequency 875 MHz. (b) Gain at the resonant frequency 1.735 GHz. (c) Gain at the resonant frequency 2.035 GHz. (d) Gain at the resonant frequency 2.35 GHz.

3.1. Effects of the Enhancements. The enhancements that we have applied to the proposed model have resulted in allowing us to obtain the wide bandwidths at the resonant frequencies. The enhancements are inserting slots in the radiating patch, a parasitic patch with the PEC boundary, multiple shorting pins, and substrate tempering by inserting vacuum gaps inside the FR-4 substrate. The effects of these enhancements on the S11 curve are clear in Figure 6.

In Figure 6(a), the shift in the resonant frequency bands is shown when shorting pins are swept along region A, region B, and region C as mentioned in Figure 4. The S11 result in Figure 6(a) clearly shows that the PIFA model provides a narrow bandwidth when the shorting pins are close to the feeding pin. Because the electric length between region A and the feed point is the shortest compared to regions B and C, the bandwidth is narrow. When shorting pins are applied in region C, the bandwidth is wider. To increase the bandwidth of our proposed model, the shorting pins can be swept along regions A, B, and C, respectively.

In Figures 6(b) and 6(c), the effects of varying the slot length and slot width on the S11 curve are shown. Figure 6(b) shows the effect of changing the length of slot L_4 (shown in

Figure 4). The simulated S11 results for three different values of the slot length are evident that changing the length of slot L_4 ($L_4 = 20$ mm, $L_4 = 22$ mm, and $L_4 = 24$ mm) effects the extreme resonant bands by and large. The effect on the lower resonant band is minor but the higher resonant band is almost shifted completely, which is favorable in cases where higher resonant bands need a shift. On the other hand, the middle resonant band has remained fixed. In Figure 6(c), the S11 results show that changing the slot width also affects the S11 curve. It is clear that another way to shift the resonant bands could be just by varying the slot width. The S11 results are presented for three different values of slot width, that is, $s = 0.25$ mm, $s = 0.5$ mm, and $s = 0.75$ mm. The resonant bands at higher frequencies shift their positions in the simulated S11 curve and the lowest band remains unchanged.

Furthermore, to improve the efficiency and gain another enhancement we used was to insert the vacuum gaps inside the dielectric material which we denote as substrate tempering. The width and position of the vacuum gaps affect the S11 curve which is shown in Figure 6(d). For three different values of vacuum gap widths, that is, $w_g = 1$ mm, $w_g = 1.5$ mm, and $w_g = 2$ mm, the S11 results show that

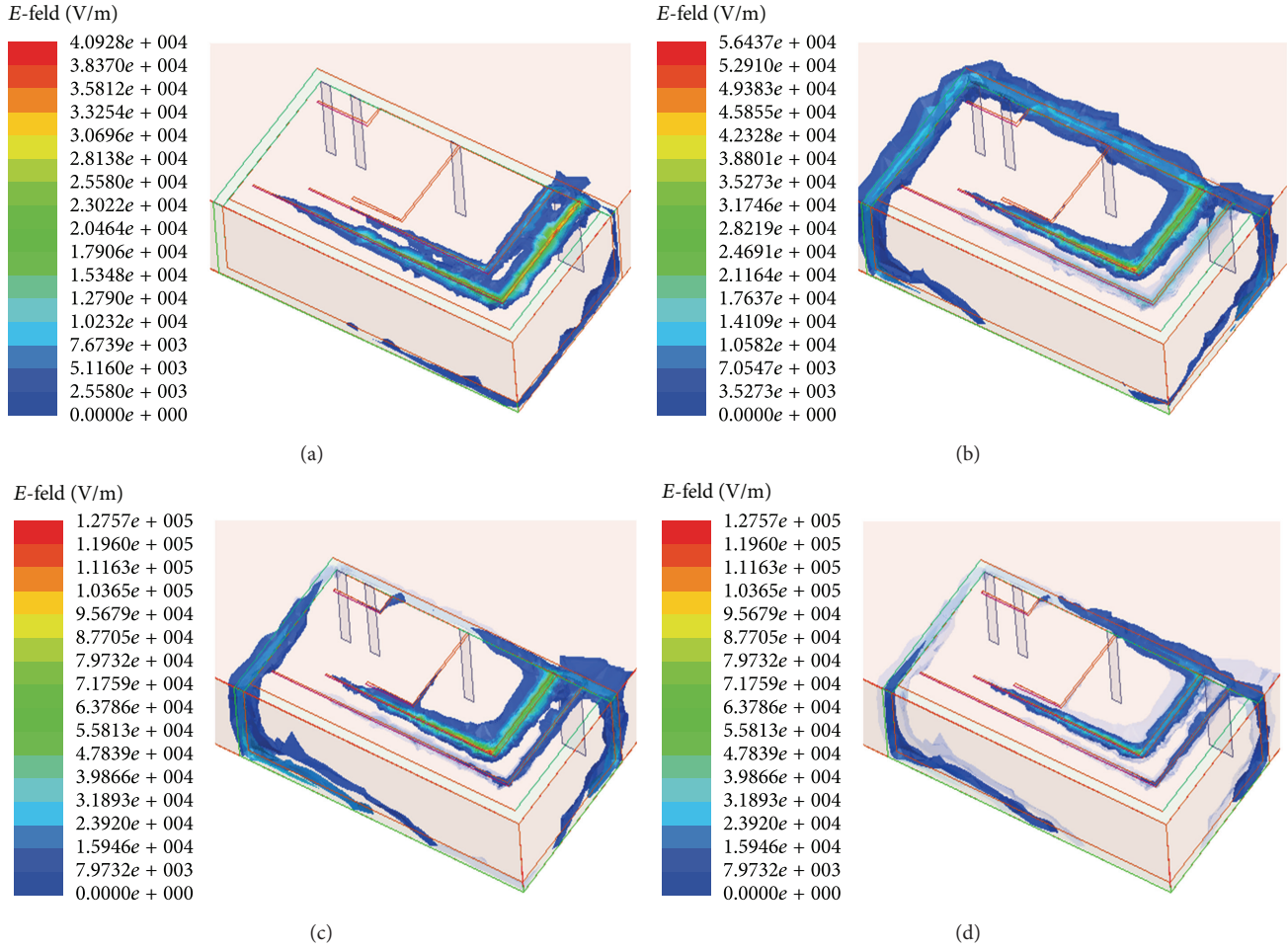


FIGURE 10: (a) Magnitude of the E-field at resonant frequency 875 MHz. (b) Magnitude of the E-field at resonant frequency 1.735 GHz. (c) Magnitude of the E-field at resonant frequency 2.035 GHz. (d) Magnitude of the E-field at resonant frequency 2.35 GHz.

changing the width of the vacuum gaps affect the higher resonant band of frequencies because it shifts them further towards the higher frequency regions which is in agreement with our previous discussion that dielectric materials help to miniaturize antenna models. Tempering the substrate can help in two ways; one way is to shift the resonant band and the other way is to increase the efficiency of the antenna design. In our proposed model, tempering helped in both ways. Shifting of the higher resonant band with substrate tempering is realized in Figure 6(d). In Section 3.2 along with the multiband resonant S11 curve, the magnitude of the E-field at corresponding resonant frequencies and improvement in gain due to substrate tempering are presented and discussed.

3.2. Characteristics of the Proposed Model. The properties of our proposed PIFA in terms of the S11 curve, the magnitude of the E-field at corresponding resonant frequencies, and the gain at the center of each resonant frequency bands are presented in this section. The optimized S11 result for the proposed model simulated with the HFSSv13.0 is shown in Figure 7, which has multiple resonant bands. The simulated S11 result is compared with the measured S11 and is close to

agreement with each other. All the resonant bands are shifted a little towards right. It might be because of the fabrication tolerance. The resonant frequency bands mentioned in Figure 7 (1st, 2nd, 3rd, and 4th) are used in most communication devices for GSM, UMTS, Bluetooth, and WLAN. The gain for the corresponding resonant frequencies is shown in Figure 9, and it is in agreement with the requirements.

The gain for the corresponding resonant frequencies is shown in Figure 9 and meets the requirements. The gains at resonant frequencies are greater than the minimum value required by the communication devices that work on these frequency ranges. At 875 MHz in Figure 9(a), the gain is approximately -0.414 dB and its shape is just like a dipole field. Dipole like shape of the radiating field at lower resonant frequency is because *PEC case* and radiating patch both act like a dipole connected to the feed. For all the other resonant bands the field is being radiated in all the directions. Therefore, radiation pattern is like a monopole because radiating patch radiates field. The radiation pattern at higher resonant frequencies is roughly omnidirectional. At 1.735 GHz in Figure 9(b), the gain is -1.22 dB, and its shape is amorphous, but the directivity is such that it

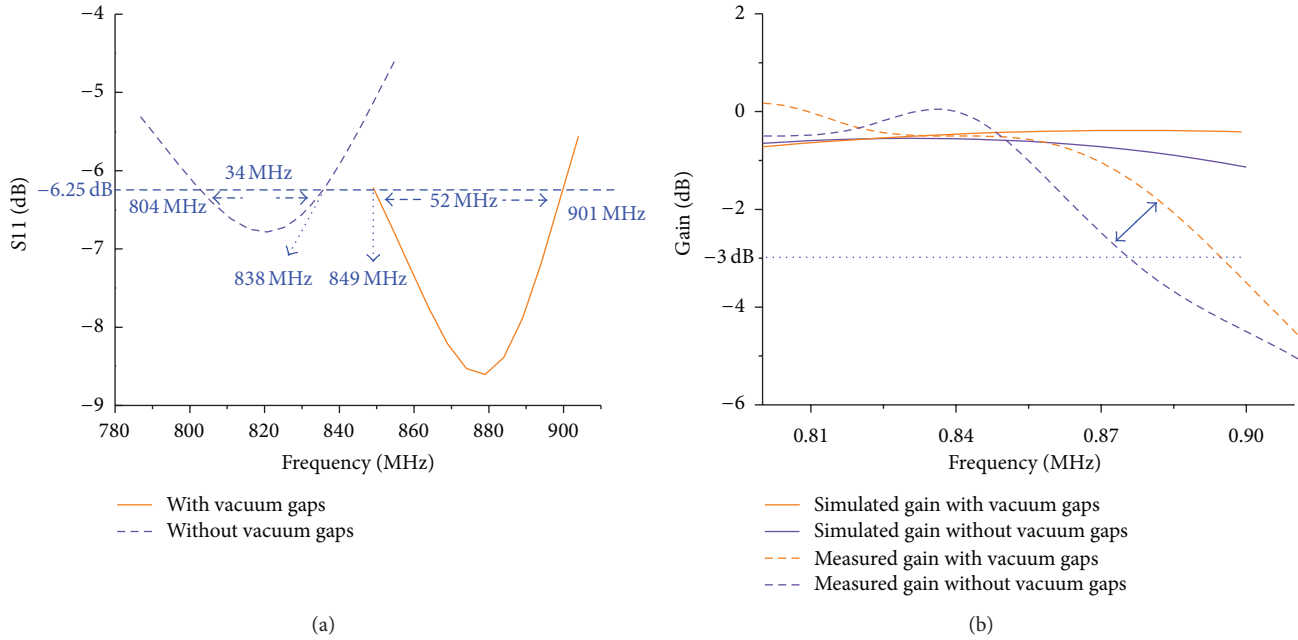


FIGURE 11: (a) Bandwidth comparison for the simulated substrate tempering at a resonant frequency band centered at 875 MHz. (b) Gain comparison with and without substrate tempering for the resonant frequency band centered at 875 MHz.

can offer a minimum SAR. In Figures 9(c) and 9(d), the gain at 2.035 GHz and 2.35 GHz is 0.024 dB and -0.75 dB, respectively. The directivity of the proposed model at higher frequencies has a roughly omnidirectional shape which is essential for many handheld communication devices working in this frequency range.

In Figure 10, the magnitude of the E-field at the corresponding resonant frequencies is shown. From these figures, we can determine the path followed by the current for every resonant frequency band. Different paths followed by the current on the radiating sheet are evident of the fact that inserting slots in the radiating patch provides multiple paths for the current to flow and therefore gives rise to multiple resonant frequencies. Furthermore, these resonant frequencies and corresponding bandwidths can be enhanced with shorting pins, parasitic patch, and other techniques.

3.3. Bandwidths and Corresponding Gains. In this section, the bandwidths, resonant frequencies, and gain for those corresponding bands of frequencies (1st, 2nd, 3rd, and 4th resonant bands) are discussed. The results show a wide bandwidth at the resonant frequencies. These are the optimized results of all the enhancements that we have applied to the proposed model which are discussed in Section 2 in detail.

In Figures 11(a) and 11(b), a comparison of the bandwidths and corresponding gains is presented. The optimized result for the proposed model at the 1st resonant band (lowest resonant band) shows a difference in the bandwidth and gain with and without tempering of the substrate. It is clear that inserting the vacuum gaps in the substrate, in order to exploit the impedance bandwidth Q , not only provides a wide bandwidth but also helps to improve the gain. In our

proposed model, the simulated results show an increment in the bandwidth from 34 MHz to 52 MHz and gain is increased and stabilized. One should choose the position and width for the vacuum gap wisely (as already mentioned in Section 2.4, position is important because it defines whether the resonant frequency of the cavity is increased or decreased).

The gain is nearly flat and stable for all these resonant band of frequencies shown in Figure 12 and is preferred by most communications devices that work in this range of frequencies.

4. Conclusion

In this paper, a new design for a low profile PIFA model is presented. In general, applications may include communication devices that work for GSM 850/900, UMTS 850/900/1700/1900/2100, LTE 2300/2500, and ISM 2400 bands used for Bluetooth and WLAN. The design is unique and simple. In contrast to a traditional PIFA model, this design is covered with PEC boundaries from all sides. By introducing a few slots in the radiating patch, applying a parasitic patch, tempering the substrate, and using multiple shorting pins in the model, four resonant bands centered at 875 MHz, 1735 MHz, 2035 MHz, and 2350 MHz have been achieved with bandwidths of 52 MHz, 60 MHz, 73 MHz, and 319 MHz, respectively. The gain for the corresponding resonant bands is relatively flat. Multiple aspects of this design were studied which we have presented in this paper, and it is evident that this model has the ability to maintain its performance even in adverse and unfriendly environments. The proposed design methodology can be useful in low profile multiband resonant communication devices, in particular, in the design of antennas for mobile handsets.

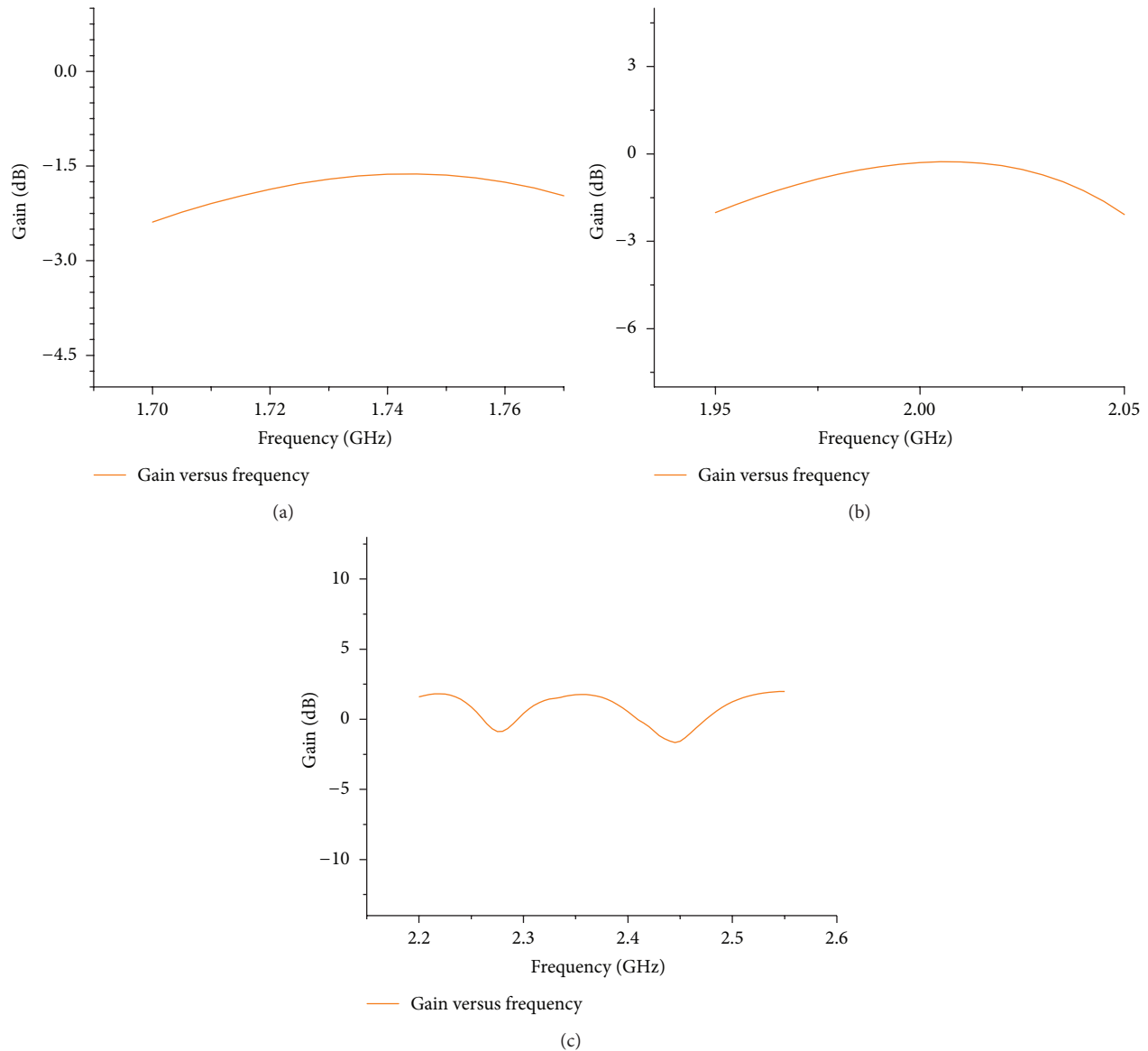


FIGURE 12: (a) Gain offered by the resonant band centered at 1.735 GHz. (b) Gain offered by the resonant band centered at 2.035 GHz. (c) Gain for the corresponding resonant band centered at 2.35 GHz.

Conflict of Interests

The authors declare that there is no conflict of interests regarding the publication of this paper.

Acknowledgment

This research was supported by the Research Fund BK21 plus of Kyungpook National University in 2013.

References

- [1] H. T. Chattha, Y. Huang, and Y. Lu, "PIFA bandwidth enhancement by changing the widths of feed and shorting plates," *IEEE Antennas and Wireless Propagation Letters*, vol. 8, pp. 637–640, 2009.
- [2] C. W. Chiu and F. L. Lin, "Compact dual-band PIFA with multi-resonators," *Electronics Letters*, vol. 38, no. 12, pp. 538–540, 2002.
- [3] C. See, H. Hraga, and R. A. Hameed, "A low-profile ultra-wideband modified planar inverted-F antenna," *IEEE Transactions on Antennas and Propagation*, vol. 61, no. 1, pp. 100–108, 2012.
- [4] N. Haider, D. Caratelli, and A. G. Yarovoy, "Recent developments in reconfigurable and multiband antenna technology," *International Journal of Antennas and Propagation*, vol. 2013, Article ID 869170, 14 pages, 2013.
- [5] A. Cabedo, J. Anguera, C. Picher, M. Ribó, and C. Puente, "Multiband handset antenna combining a PIFA, slots, and

- ground plane modes," *IEEE Transactions on Antennas and Propagation*, vol. 57, no. 9, pp. 2526–2533, 2009.
- [6] J. S. McLean, "A re-examination of the fundamental limits on the radiation Q of electrically small antennas," *IEEE Transactions on Antennas and Propagation*, vol. 44, no. 5, pp. 672–676, 1996.
- [7] D. F. Sievenpiper, D. C. Dawson, M. M. Jacob et al., "Experimental validation of performance limits and design guidelines for small antennas," *IEEE Transactions on Antennas and Propagation*, vol. 60, no. 1, pp. 8–19, 2012.
- [8] M. Koubeissi, M. Mouhamadou, C. Decroze, D. Carsenat, and T. Monédière, "Triband compact antenna for multistandard terminals and user's hand effect," *International Journal of Antennas and Propagation*, vol. 2009, Article ID 491262, 7 pages, 2009.
- [9] T. Tashi, M. S. Hasan, and H. Yu, "Design and simulation of UHF RFID tag antennas and performance evaluation in presence of a metallic surface," in *Proceedings of the 5th International Conference on Software, Knowledge Information, Industrial Management and Applications (SKIMA '11)*, vol. 1, pp. 1–5, Benevento, Italy, September 2011.
- [10] D. Qi, B. Li, and H. Liu, "Compact triple-band planar inverted-F antenna for mobile handsets," *Microwave and Optical Technology Letters*, vol. 41, no. 6, pp. 483–486, 2004.
- [11] M. S. Kim, "PIFA device for providing optimized frequency characteristics in a multi-frequency environment and method for controlling the same," US patent application US 7 385 557 B2, 2008.
- [12] W. K. W. Ali, "Broadband square microstrip patch antenna with suspended parasitic element," in *Proceedings of the 6th International Symposium on Antennas, Propagation and EM Theory*, pp. 50–53, Beijing, China, November 2003.
- [13] A. Moleiro, J. Rosa, R. Nunes, and C. Peixeiro, "Dual band microstrip patch antenna element with parasitic for GSM," in *IEEE Antennas and Propagation Society International Symposium*, vol. 4, pp. 2188–2191, Salt Lake City, Utah, USA, July 2000.
- [14] Y. Belhadeif and N. B. Hacene, "Design of new multiband slotted PIFA antennas," *International Journal of Computer Science Issues*, vol. 8, no. 4, pp. 325–330, 2011.
- [15] W. F. Richards, S. Davidson, and S. A. Long, "Dual-band reactively loaded microstrip antenna," *IEEE Transactions on Antennas and Propagation*, vol. 33, no. 5, pp. 556–561, 1985.
- [16] H. Wong, K. M. Luk, and C. H. Chan, "Small antennas in wireless communications," *Proceedings of the IEEE*, vol. 100, no. 7, pp. 2109–2121, 2012.
- [17] M. Sonkki, M. Cabedo-Fabrés, E. Antonino-Daviu, M. Ferrando-Bataller, and E. T. Salonen, "Creation of a magnetic boundary condition in a radiating ground plane to excite antenna modes," *IEEE Transactions on Antennas and Propagation*, vol. 59, no. 10, pp. 3579–3587, 2011.
- [18] A. D. Yaghjian and S. R. Best, "Impedance, bandwidth, and Q of antennas," *IEEE Transactions on Antennas and Propagation*, vol. 53, no. 4, pp. 1298–1324, 2005.
- [19] A. O. Karilainen, P. M. T. Ikonen, C. R. Simovski et al., "Experimental studies on antenna miniaturisation using magneto-dielectric and dielectric materials," *IET Microwaves, Antennas & Propagation*, vol. 5, no. 4, pp. 495–502, 2011.
- [20] Y.-T. Jean-Charles, V. Ungvichian, and J. A. Barbosa, "Effects of substrate permittivity on planar inverted-F antenna performances," *Journal of Computers*, vol. 4, no. 7, pp. 610–614, 2009.
- [21] G. A. E. Vandenbosch, "Reactive energies, impedance, and Q factor of radiating structures," *IEEE Transactions on Antennas*, vol. 58, no. 4, pp. 1112–1127, 2010.
- [22] S. A. Long, "A mathematical model for the impedance of the cavity-backed slot antenna," *IEEE Transactions on Antennas and Propagation*, vol. 25, no. 6, pp. 829–833, 1977.
- [23] H. K. Smith and P. E. Mayes, "Stacking resonator to increase the bandwidth of low profile antennas," *IEEE Transactions on Antennas and Propagation*, vol. 35, no. 12, pp. 1473–1476, 1987.
- [24] J. Eichler, P. Hazdra, M. Capek, and M. Mazanek, "Modal resonant frequencies and radiation quality factors of microstrip antennas," *International Journal of Antennas and Propagation*, vol. 2012, Article ID 490327, 9 pages, 2012.
- [25] M. Capek, P. Hazdra, and J. Eichler, "A method for the evaluation of radiation Q based on modal approach," *IEEE Transactions on Antennas and Propagation*, vol. 60, no. 10, pp. 4556–4567, 2012.
- [26] P. Vainikainen, J. Ollikainen, O. Kivekäs, and I. Kelder, "Resonator-based analysis of the combination of mobile handset antenna and chassis," *IEEE Transactions on Antennas and Propagation*, vol. 50, no. 10, pp. 1433–1444, 2002.
- [27] D. M. Pozar, *Microwave Engineering*, John Wiley & Sons, New York, NY, USA, 2nd edition, 1998.

Research Article

Multiband Printed Asymmetric Dipole Antenna for LTE/WLAN Applications

Chia-Mei Peng,^{1,2} I-Fong Chen,^{1,2} and Chin-Hao Liu³

¹ Department of Electronic Engineering, Jinwen University of Science and Technology, 23154 No. 99, An-Chung Road, Hsin-Tien, New Taipei City, Taiwan

² Wieson Corp. Tech., 221 No. 276, Section 1, Datong Road, Sijihih, New Taipei City, Taiwan

³ Department of Electronic Engineering, National Taiwan University of Science and Technology, 10608 No. 43, Section 4, Keelung Road, Daan, Taipei, Taiwan

Correspondence should be addressed to I-Fong Chen; ex0206@just.edu.tw

Received 16 September 2013; Accepted 7 December 2013

Academic Editor: Xiao Ping Chen

Copyright © 2013 Chia-Mei Peng et al. This is an open access article distributed under the Creative Commons Attribution License, which permits unrestricted use, distribution, and reproduction in any medium, provided the original work is properly cited.

The ability of a single layer strip fed printed asymmetric dipole antenna, which is composed of top-loading, asymmetric coplanar waveguide (ACPW) and stepped-feeding structure, to operate at three wide frequency bands (698~960 MHz, 1710~2620 MHz, and 5150~5850 MHz) to cover WLAN and LTE operation has been demonstrated. A prototype of the proposed antenna with 57.5 mm in length, 0.4 mm in thickness, and 5 mm in width is fabricated and experimentally investigated. The experimental results indicate that the VSWR 2.5:1 bandwidths achieved were 74.3%, 40.8%, and 18.2% at 700 MHz, 2450 MHz, and 5500 MHz, respectively. Experimental results are shown to verify the validity of theoretical work.

1. Introduction

Recently, the antennas desired features include multiband, broad bandwidth, simple impedance matching to the feed line, and low profile, to be used in various wireless communication applications, such as the IEEE 802.11 wireless local area network (WLAN) standards, and the pre-4G technologies such as long term evolution (LTE) standards. A variety of printed monopole antennas for covering multibands have been reported in the published articles [1–5], those types of printed monopole antenna designs occupy a relatively larger space and they are difficult to meet the size-limitation of the external antenna. In industrial applications involving external antennas with tapered streamline radome covers, the space limitations are an important issue. In this paper, we present a single layer multiband printed asymmetric dipole antenna for LTE/WLAN external antenna applications. The arm-lengths of dipole are designed to response two different resonant frequencies, respectively. It is beneficial to enhance antenna performance by letting the length of the ground-arm of dipole antenna be larger than the signal-arm [6]. In

other words, the signal-arm of dipole antenna is designed for upper-operating band, and the ground-arm is designed for lower-operating band. The proposed antenna is consisted of top loading, asymmetric coplanar waveguide (ACPW) and stepped-feeding structure, which was developed by modifying the structure of printed sleeve monopole antenna [7]. The feasibility of wide bandwidth operation has been proven by the design of ACPW feeding structure and ground-trace structure that operates in the WLAN and LTE bands. Details of the design considerations of the proposed antenna and the experimental results of constructed prototypes are presented and discussed.

2. Antenna Structure and Design

As for the specification requirement of wireless products, the multiband antenna is required to enable operations at the two WLAN and the LTE bands, whose bandwidths and list of the corresponding bands are detailed in Table 1. The operating frequency range is divided into three bands: 700 MHz

TABLE 1: Considered WLAN and LTE bands.

| Allocated bands | | Frequency range (MHz) |
|---|------|-----------------------|
| | LTE | |
| FDD | | |
| #5, #6, #8, #12, #13, #14, #17, #18, #19, #20 | | 698–960 |
| #1, #2, #3, #4, #9, #10 | | 1900–2620 |
| TDD | | |
| #33, #34, #35, #36, #37, #38, #39, #40, #41 | | 1850–2690 |
| | WLAN | |
| 2.4 GHz | | 2400–2500 |
| 5 GHz | | 5150–5850 |

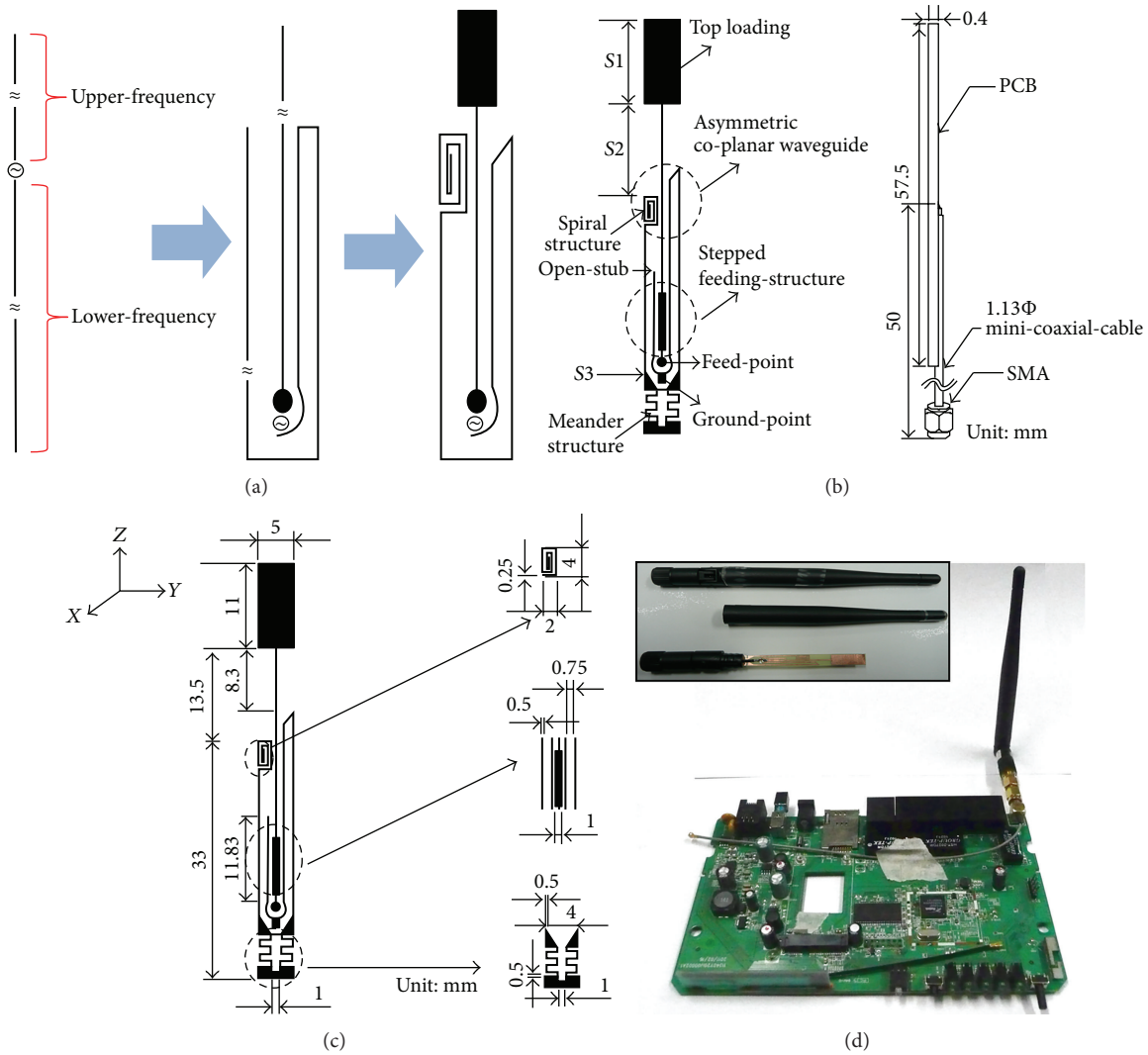


FIGURE 1: (a) The original geometry structure of the proposed antenna. (b) Profile and side view of the proposed antenna. (c) Configuration and dimensions of the proposed antenna. (d) The tapered streamline radome cover of antenna.

band (698 MHz–960 MHz), 2450 MHz band (1710 MHz–2620 MHz), and 5500 MHz band (5150 MHz–5850 MHz); in which the 700 MHz band was denoted as lower-operating band, and 2450 MHz and 550 MHz bands were denoted as upper-operating band.

Accordingly, a good impedance matching in those operating ranges is needed. Such a requirement has been conveniently expressed in terms of VSWR by imposing a suitable threshold on the magnitude values of the VSWR ≤ 2.5 . Figure 1(a) shows the original geometry asymmetric dipole

TABLE 2: Measured results of the antenna bandwidth as a function of varying antenna structure.

| Antenna structure | Lower band | Upper band (I) | Upper band (II) |
|-------------------|---------------------------------|---------------------------------|---------------------------------|
| | Bandwidth, $f_L \sim f_U$ (MHz) | Bandwidth, $f_L \sim f_U$ (MHz) | Bandwidth, $f_L \sim f_U$ (MHz) |
| Case I | 300, 950~1250 | 650, 2000~2650 | 400, 5100~5500 |
| Case II | 250, 880~1130 | 1000, 2000~3000 | 600, 4900~5500 |
| Case III | 300, 700~1000 | 600, 2000~2600 | 800, 4500~5300 |
| Proposed antenna | 520, 680~1200 | 1000, 1700~2700 | 1000, 4700~5700 |

TABLE 3: The measured antenna gains and efficiencies within the operating bandwidth of the proposed antenna.

| Frequency | Gain (dBi) | | | Efficiency (%) |
|-----------|--------------------------|--------------------------|--------------------------|----------------|
| | xy -plane Max. gain | yz -plane Max. gain | zx -plane Max. gain | |
| 700 MHz | 0.08 | 1.62 | 1.77 | 58.57 |
| 960 MHz | 0.81 | 1.41 | 1.81 | 63.47 |
| 1710 MHz | 0.65 | 0.57 | 0.8 | 54.91 |
| 2170 MHz | 0.44 | 0.83 | 0.71 | 55.6 |
| 2450 MHz | 0.98 | 1.09 | 1.17 | 62.3 |
| 2700 MHz | 1.18 | 1.44 | 1.21 | 60.7 |
| 5150 MHz | 1.01 | 1.22 | 1.31 | 62.1 |
| 5500 MHz | 0.54 | 0.88 | 1.15 | 56.8 |
| 5850 MHz | 0.35 | 0.48 | 0.77 | 51.6 |

“Max.: maximum.”

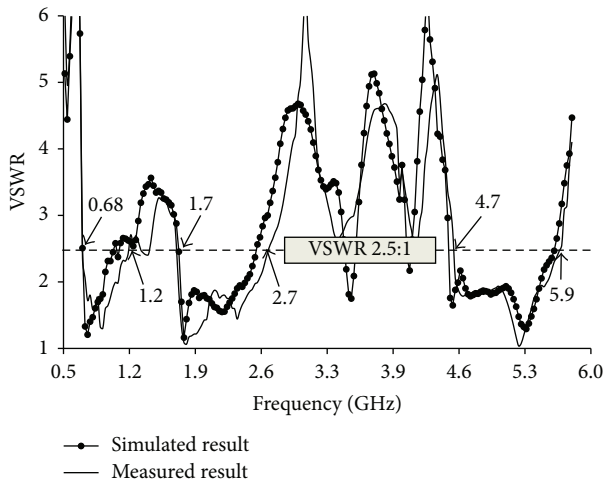


FIGURE 2: Measured and Simulated VSWR against frequency.

antenna for multiband applications. The lengths of signal arm and ground-arm are related to the upper- and lower-frequency, respectively. The presented antenna structure is composed of an upper-element section of length S_1 , and the lower-element section of length S_2 , and the ground-trace section of electrical length S_3 . These sections are all printed on a 1.6 mm-thick FR4 glass epoxy substrate (the relative permittivity is 4.3, and the loss tangent is 0.022) at the same layer and the profile and side view of the proposed antenna are shown in Figure 1(b). The resonant mode of total shape ($S_1 + S_2$) is designed to occur at 2450 MHz, the lower-element

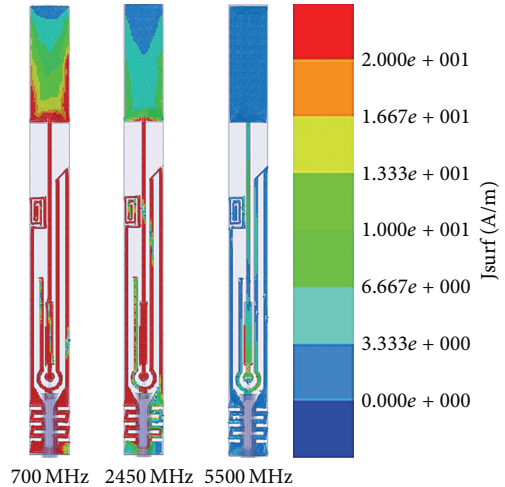


FIGURE 3: The simulated current distribution of the proposed antenna at 700 MHz, 2450 MHz, and 5500 MHz.

(S_2) is designed to resonate at 5500 MHz, and the ground-trace (S_3) is designed to resonate at 700 MHz. The length of radiating elements can be determined from about quarter-wave length at the resonant frequencies. Note that the widths of these sections are not identical. By selecting appropriate dimensions (S_1, S_2, S_3) of the antenna structure, good impedance matching of the printed asymmetric dipole can be obtained across an extended bandwidth. The corresponding characteristics of resonant frequency, input impedance and bandwidth are a function of the geometrical parameters of

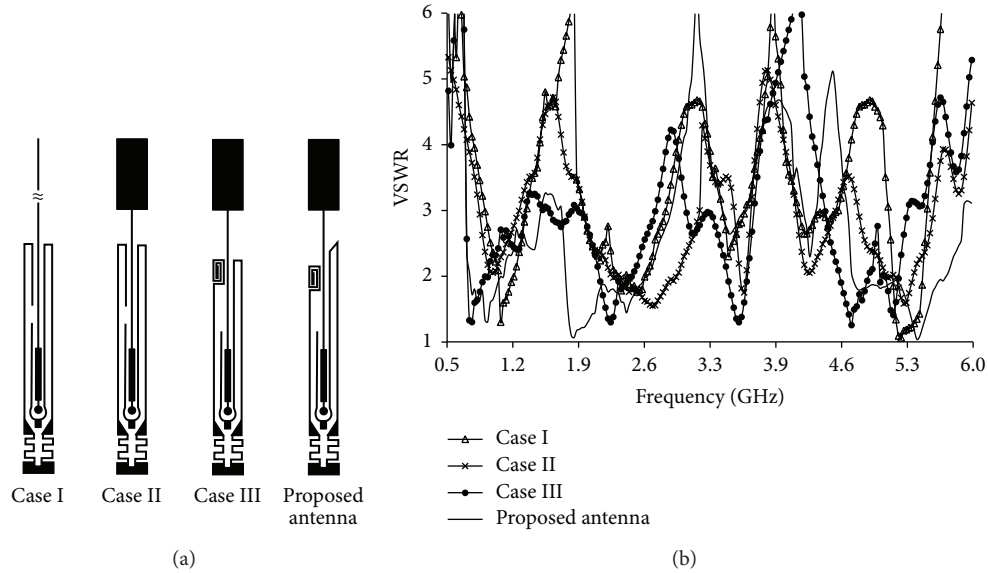


FIGURE 4: (a) The configuration of varying antenna structure. (b) Measured VSWR against frequency of the corresponding antenna structure.

the top-loading and ACPW structure, the configuration and dimensions of the proposed antenna are shown in Figure 1(c).

When the dimension of the top-loading is varied, the impedance bandwidth and resonant frequency will change in the 2450 MHz band. An ACPW feeding structure excites the end of S2-segment as shown in Figure 1(b). The impedance matching at 2450 MHz and 5500 MHz bands can be tuned by this structure, which was found to be effective in obtaining a wider impedance bandwidth in the antenna's upper-operating band. In addition, it should be noted that the ground-trace length (S3) and configuration could also affect the resonant frequency and operating bandwidth of 700 MHz band; when the printed ground-trace was curled a meander-structure and spiral-structure, the operating bandwidth will increase. The bended ground-trace is designed for the lower-operating band, which is also act as a sleeve balun for the upper-operating band, a complete radiation pattern-shape can be obtained. The bandwidth enhancement results are demonstrated in the following section. Furthermore, the impedance matching at 700 MHz, 2450 MHz, and 5500 MHz bands can be tuned by the stepped-feeding of signal-trace and the open-stub of the ground-trace, which was found to be effective in securing triple band. The access point (AP) is the intended platform of antenna integration. The proposed antenna's size is based on the size of tapered streamline radome cover, as shown in Figure 1(d).

3. Experimental Results and Discussion

In the experiment, the feeding-point and ground-point are connected to a 1.13 \varnothing 3 cm mini-coaxial cable with 50 Ω SMA connector. By utilizing the above-mentioned design procedure, a wide band antenna was constructed to operate at the ranges of WLAN and LTE system (698~960 MHz,

1710~2690 MHz and 5150~5850 MHz). Figure 2 shows the simulated (by Ansoft HFSS) and measured VSWR plot of the wideband antenna as a result of this geometry. The measured VSWR ≤ 2.5 bandwidths are 74.3% at 700 MHz, 40.8% at 2450 MHz and 18.2% at 5500 MHz. There is good agreement between the measured and simulated results. Figure 3 presents the simulated current distribution of the proposed antenna at 700 MHz, 2450 MHz, and 5500 MHz which are corresponding to the resonant lengths of the S3, S1 + S2 and S2, respectively; simulation results are shown to verify the validity of theoretical work.

The effect of varying the top-loading, feeding structure and the ground-trace structure on the antenna performance has been studied. The configuration of varied antenna structure is shown in Figure 4(a), and the measured VSWR plot of the corresponding structure is shown in Figure 4(b). From Figure 4(b), it is obviously that the tuning of the 2450 MHz band was acquired by adjusting the size of top-loading to produce the required frequency response characteristic. The top-loading width increase will lead to an increase of impedance bandwidth and a decrease resonant frequency in the 2450 MHz band, as shown in Figure 4(b). In addition, to let the co-planar waveguide feeding structure to be an asymmetric structure, it was observed that the resonant frequency and impedance bandwidth will increase in 2450 MHz and 5500 MHz bands and nevertheless, the effect in 700 MHz band is very small. Furthermore, when the printed ground-trace was curled a meander-structure and spiral-structure, the operating bandwidth will increase. The ground-trace length (S3) and configuration could also affect the resonant frequency and operating bandwidth of the 700 MHz band. The quantitative comparisons of the effects of varying antenna structure on the antenna's resonant frequency and impedance bandwidth were studied experimentally, as shown in Table 2 (the configuration of

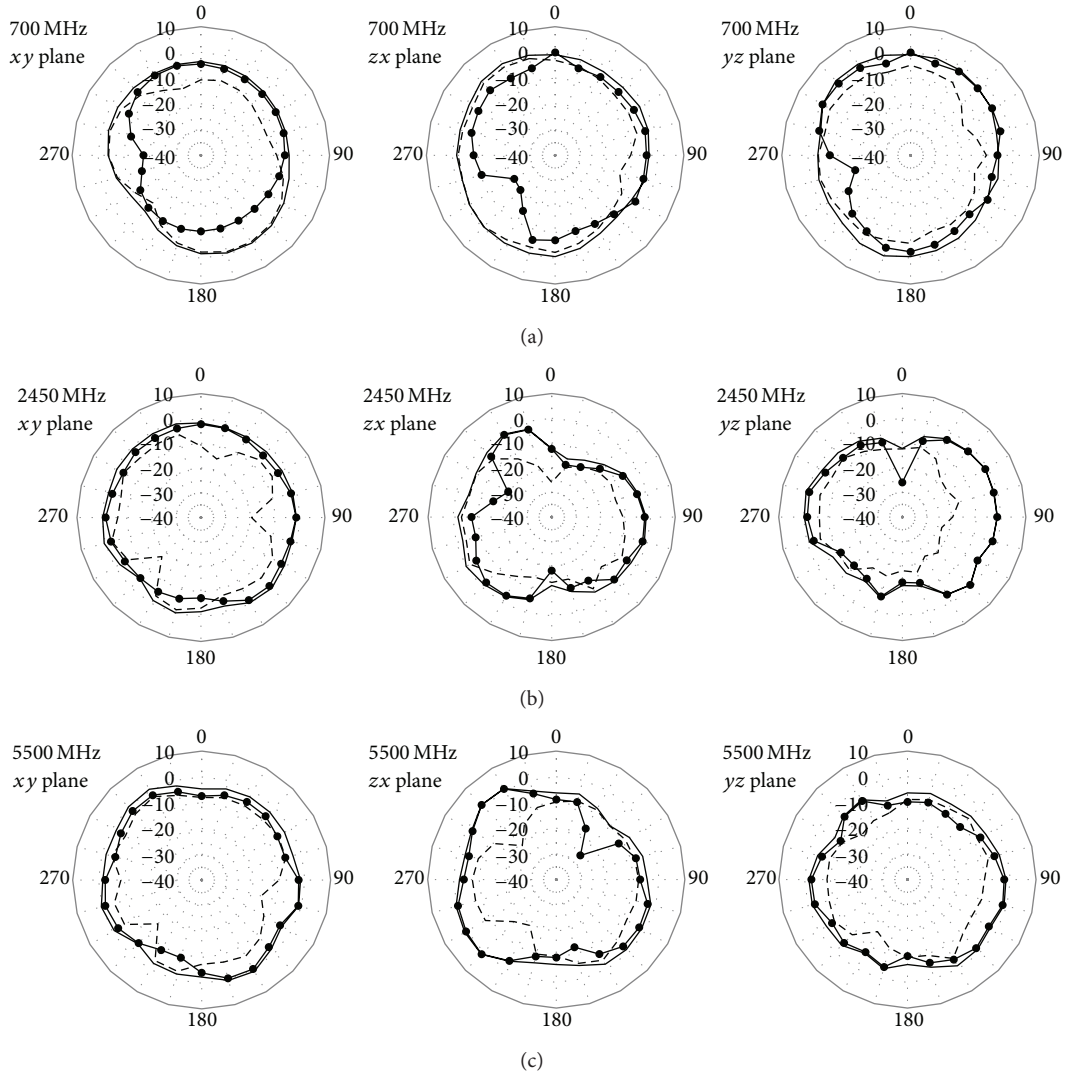


FIGURE 5: Measured radiation patterns for the proposed antenna. “— Total”, “•—• co-pol.”, “- - - cross-pol.” (a) 700 MHz. (b) 2450 MHz. (c) 5500 MHz.

varying antenna structure with 57.5 mm in length, 0.4 mm in thickness, and 5 mm in width, $VSWR \leq 2.5$). The impedance matching was also achieved by optimizing the stepped-feeding trace and open-stub. The measured radiation patterns for free space at 700 MHz, 2450 MHz, and 5500 MHz in the xy -plane, yz -plane, and zx -plane are shown in Figure 5, respectively. Table 3 shows the measured antenna gains and 3D pattern efficiency within the operating bands of the proposed antenna. Stable radiation patterns are observed. The total 3D pattern efficiency is defined as $(\text{gain}/\text{directivity}) \times 100\%$, which was done by using pattern integration employing the ETS-Lindgren anechoic chamber. Acceptable radiation characteristic for the practical applications is obtained for the proposed antenna. The omnidirectional feature of the proposed antenna can also be observed from the xy -plane, where the gain variation between maximum and minimum levels is less than 3 dB. The overall signal trace length is about one wavelength long and there are normally four lobes at the 5500 MHz band, but, due to the ground trace is also acts as a

sleeve balun, a close to complete radiation shape (there are a few variations in the radiation pattern-shapes) was obtained.

4. Conclusion

In this paper, a dual-band wideband printed asymmetric dipole antenna suitable for WLAN and LTE applications has been proposed. The antenna is characterized by reduced dimensions and suitable impedance matching over the presented operating band. The performances of the synthesized antenna have been numerically and experimentally verified. The proposed antenna can be easily fabricated and modified to various AP and router as a compact external antenna.

Acknowledgments

This work was sponsored by the National Science Council, under the Contract 101-2221-E-228-004-MY2 and Wieson Corp. Tech. (<http://www.wieson.com>), Taiwan, under the

Contract JW101-F-411-148. The authors also appreciate the reviewer's comments to improve the quality of this paper.

References

- [1] J. D. Kraus and R. J. Marhefka, *Antennas*, McGraw-Hill, New York, NY, USA, 2002.
- [2] L. Lizzi and A. Massa, "Dual-band printed fractal monopole antenna for LTE applications," *IEEE Antennas and Wireless Propagation Letters*, vol. 10, pp. 760–763, 2011.
- [3] J. Ma, Y. Z. Yin, J. L. Guo, and Y. H. Huang, "Miniature printed octaband monopole antenna for mobile phones," *IEEE Antennas and Wireless Propagation Letters*, vol. 9, pp. 1033–1036, 2010.
- [4] K. Chung, S. Hong, and J. Choi, "Ultrawide-band printed monopole antenna with band-notch filter," *IET Microwaves, Antennas and Propagation*, vol. 1, no. 2, pp. 518–522, 2007.
- [5] T.-G. Ma and S.-K. Jeng, "Planar miniature tapered-slot-fed annular slot antennas for ultrawide-band radios," *IEEE Transactions on Antennas and Propagation*, vol. 53, no. 3, pp. 1194–1202, 2005.
- [6] A. Cabedo, J. Anguera, C. Picher, M. Ribó, and C. Puente, "Multiband handset antenna combining a PIFA, slots, and ground plane modes," *IEEE Transactions on Antennas and Propagation*, vol. 57, no. 9, pp. 2526–2533, 2009.
- [7] I.-F. Chen and C.-M. Peng, "Printed broadband monopole antenna for WLAN/WiMAX applications," *IEEE Antennas and Wireless Propagation Letters*, vol. 8, pp. 472–474, 2009.

Research Article

Microstrip Folded Dipole Antenna for 35 GHz MMW Communication

Guang Hua, Chen Yang, Ping Lu, Hou-Xing Zhou, and Wei Hong

State Key Laboratory of Millimeter Waves, School of Information Science and Engineering, Southeast University, Nanjing 210096, China

Correspondence should be addressed to Guang Hua; huaguang@seu.edu.cn

Received 8 October 2013; Accepted 27 November 2013

Academic Editor: Guo Qing Luo

Copyright © 2013 Guang Hua et al. This is an open access article distributed under the Creative Commons Attribution License, which permits unrestricted use, distribution, and reproduction in any medium, provided the original work is properly cited.

A microstrip asymmetric folded dipole antenna on chip is proposed in this paper. The construction of balun feed line is adopted to provide wideband. A new design procedure based on the odd-even mode method to calculate the input impedance of an asymmetric strip folded dipole antenna is presented. The folded dipole antenna has the advantage of small size, low profile, low cost, and so forth. The measured results show that a miniaturized antenna has the bandwidth of more than 14.2% ($VSWR \leq 2$); gain of the antenna is 5.7 dB at 35 GHz.

1. Introduction

Recently, substantial knowledge about the 35 GHz millimeter-wave (MMW) channel has been accumulated and different architectures have been analyzed to develop new MMW communication systems for commercial applications. MMW technique has been used as a favorite data transmission means for wireless or mobile communications. MMW integrated antenna, as the most effective reconnaissance tool, is popularly applied in many fields and becomes more and more indispensable. As is used in various fields for a highly attractive solution, several rigorous requirements for antennas such as small size, wide bandwidth, and stable radiation pattern are under consideration when the antenna is applied [1–3].

In this paper, a strip asymmetric folded dipole antenna and a new design procedure based on the odd-even mode method to calculate the input impedance of the antenna have been proposed to realize wide bandwidth and high gain. The method is explicit and simple. The construction of balun fed by microstrip is used to provide 180 phase difference and wideband. In order to integrate the antenna on chip, the structure traditional analysis method, and high frequency characteristic of antenna have to be taken into account.

2. Antenna Design

The configuration of the proposed antenna is shown in Figure 1. The antenna is constructed by using microstrip folded dipoles connected with a balun feed line on a bottom substrate having a thickness of 0.635 mm and a relative permittivity of 10.2. The asymmetric strip folded dipole is designed on the top of the substrate, which has a thickness of 0.1 mm and a relative dielectric constant of 2.2. The values of design parameters are listed in Table 1.

The strip asymmetric folded dipole is shown in Figure 2. The geometries such as L , b , d , s , $W1$, and $W2$ are adjusted to tune the input impedance and to widen the bandwidth. The antenna is accompanied without ground plane, so its radiation pattern is similar to the dipole of the same length l , but it provides about four times larger input impedance than that of the conventional dipole when $l \leq \lambda/2$. The length of a single-wire dipole is usually $\lambda/4 \leq l \leq \lambda/2$ for best directivity with no side lobes. Usually, l is about half wavelength and $s < 0.002\lambda$. The separation distance b between the two strip transmission lines of the folded dipole should not exceed 0.05λ .

According to the traditional analysis method [4], the excitation of a folded dipole is decomposed into two fundamental

TABLE 1: Values of design parameters (all in millimetres).

| L | d | s | b | W_0 | W_1 | W_2 | W_3 | W_4 | l_1 | l_2 | l_3 | h_1 | h_2 | ϵ_1 | ϵ_2 |
|------|------|-----|------|-------|-------|-------|-------|-------|-------|-------|-------|-------|-------|--------------|--------------|
| 3.44 | 0.12 | 0.1 | 0.11 | 0.6 | 0.318 | 0.462 | 0.13 | 0.1 | 0.237 | 0.13 | 0.87 | 0.1 | 0.635 | 2.2 | 10.2 |

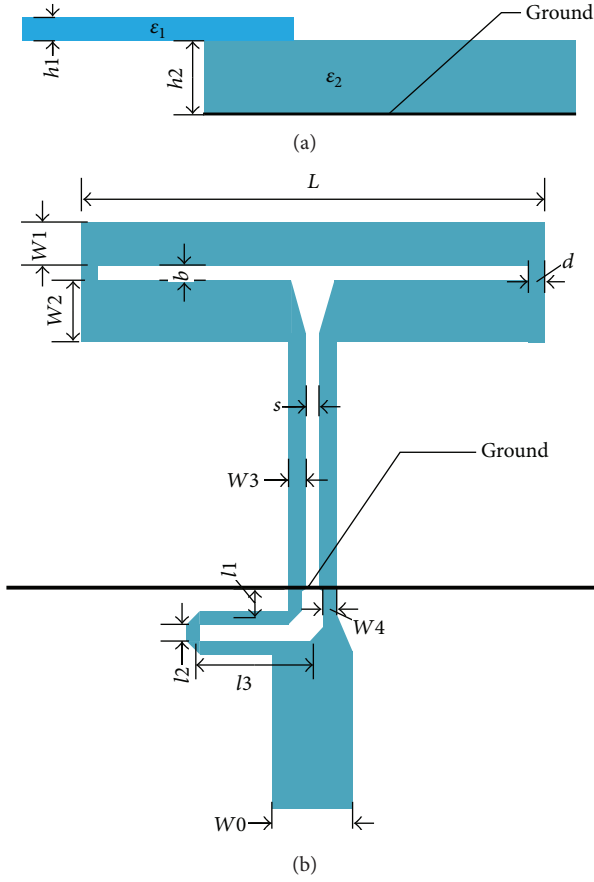


FIGURE 1: The construction of the antenna: (a) side view; (b) top view.

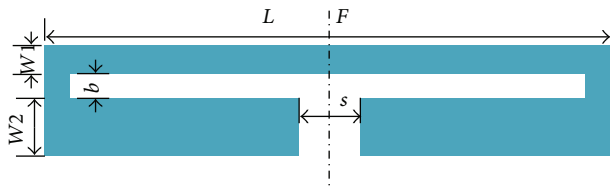


FIGURE 2: The schematic diagram of strip asymmetric folded dipole.

modes: the transmission line mode and unbalanced antenna radiation mode, as described in Figure 3, where I_a is the antenna current of the dipole and I_T is the transmission line current. The feed port input impedance of folded dipole is given by [5]:

$$Z_{in} = \frac{2(1 + \gamma)^2 Z_D Z_T}{(1 + \gamma)^2 Z_D + 2Z_T}, \quad (1)$$

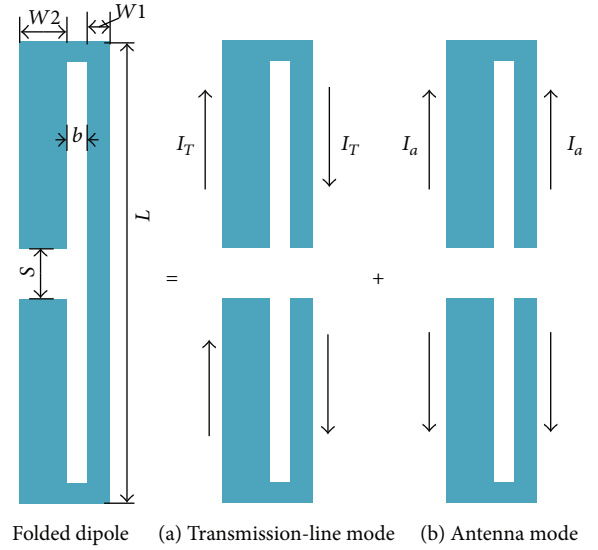


FIGURE 3: Current distribution on a folded dipole.

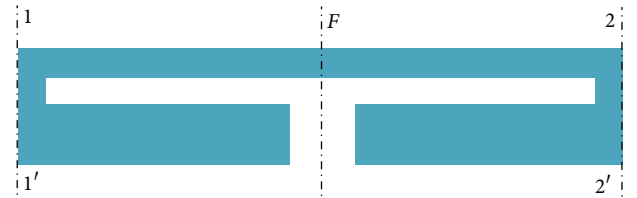


FIGURE 4: A strip asymmetric folded dipole in antenna mode.

where Z_D is the input impedance of strip dipole antenna with length of L and width of W_1 . Z_T is the input impedance of the asymmetric strip. Consider

$$Z_T = jZ_c \tan\left(\frac{\beta L}{2}\right), \quad (2)$$

where Z_c is characteristic impedance of transmission line and $K(k)$ is the elliptic function; $K'(k) = K(k')$, $k'^2 = 1 - k^2$,

$$Z_c = \frac{120\pi}{\sqrt{\epsilon_r}} \frac{K(k)}{K'(k)},$$

$$\gamma = \frac{\ln\left[4C + 2\sqrt{(2C)^2 - (W_1/2)^2}\right] - \ln W_1}{\ln\left[4C + 2\sqrt{(2C)^2 - (W_2/2)^2}\right] - \ln W_2}, \quad (3)$$

$$C = \frac{b}{2} + \frac{W_1}{4} + \frac{W_2}{4},$$

where $2C$ is the distance between middles of two strip dipole line and $(1 + \gamma)^2$ is the impedance ratio. Since Z_D and Z_T are

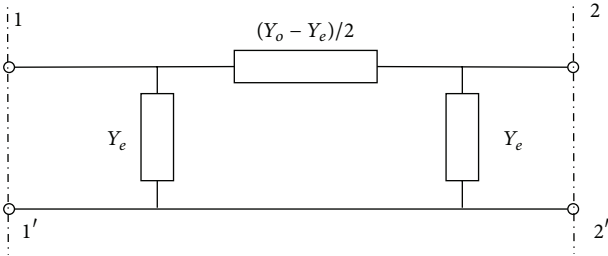


FIGURE 5: Equivalent two-port network for strip asymmetric folded dipole.

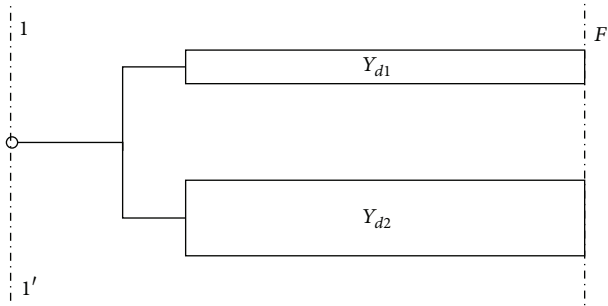


FIGURE 6: Equivalent network with electric and magnet wall.

too complicated to be calculated, so an explicit and simple method is presented.

The design procedure involves two steps. The first is to calculate the input impedance of asymmetric strip line in transmission mode. The second step is to calculate the input impedance of asymmetric folded dipole in antenna mode. Then according to the traditional method equivalent input impedance is obtained [4].

2.1. *Input Impedance of Transmission Line.* The input impedance in asymmetric transmission can be viewed as two-series transmission line. An input impedance can be obtained by

$$Z_t = \left[Z_0 \left(\frac{Z_L + jZ_0 \tan(\beta l/2)}{Z_0 + jZ_L \tan(\beta l/2)} \right) \right], \quad (4)$$

where Z_0 is the characteristic impedance of a strip transmission line. The characteristic impedance of W_1 and W_2 strip is calculated by Agilent ADS or Ansoft Designer, respectively.

2.2. *Input Impedance of Folded Dipole Antenna.* In case of symmetrical geometry of microstrip antennas or arrays with any voltage excitation, generalize odd-even mode expansion method can be used. An asymmetric folded dipole in antenna mode can be viewed as symmetric two-port microwave network, as shown in Figures 4 and 5. The characteristic impedance can be determined by odd-even method. The symmetric plane F is magnet wall in even mode situation and electric wall in odd mode situation, respectively. The input impedance (resistance and reactance) of a very thin dipole of length l and diameter d ($l \gg d$) can be computed using either

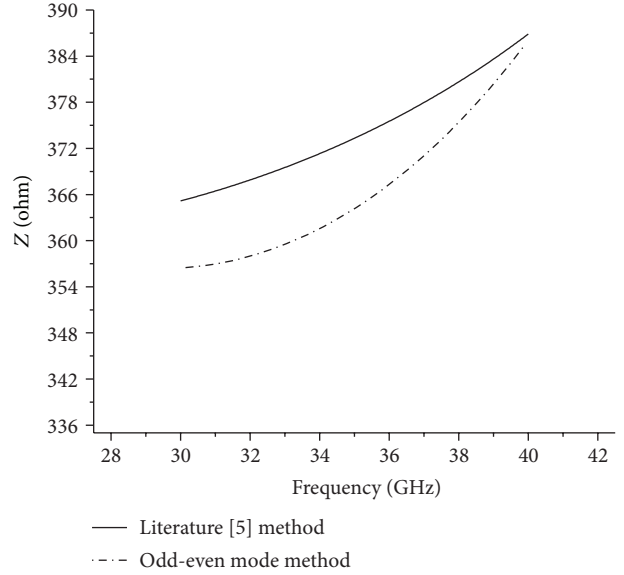


FIGURE 7: Comparison with odd-even mode and literature [5] method.

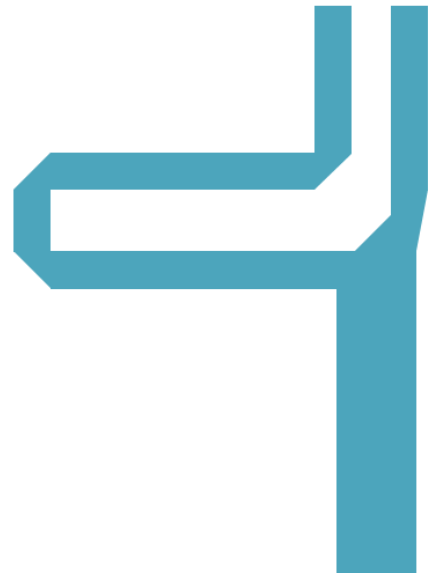


FIGURE 8: The schematic diagram of balun.

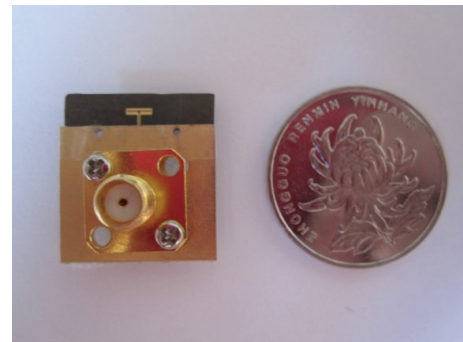


FIGURE 9: The front of the proposed antenna.



FIGURE 10: The back of the proposed antenna.

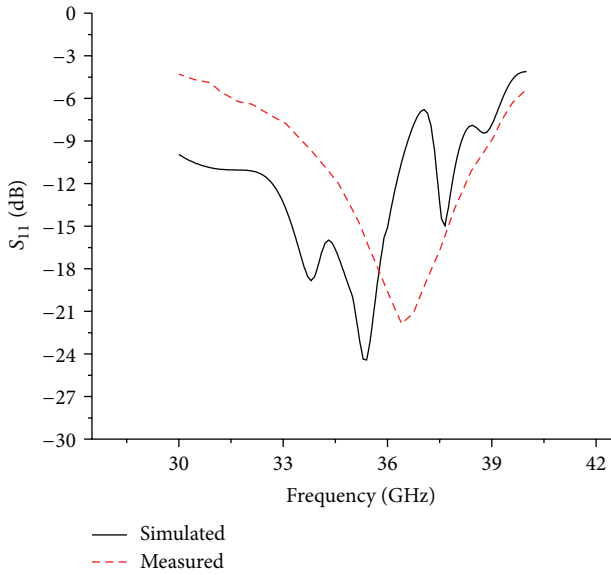


FIGURE 11: The measured and simulated return loss of the proposed antenna.

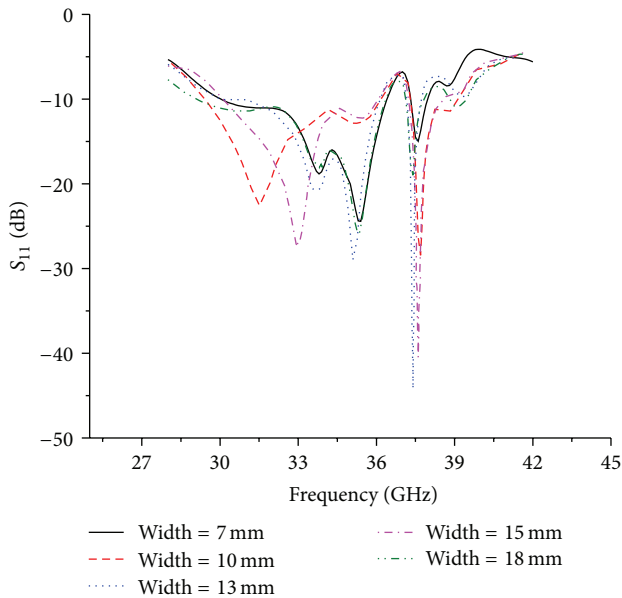


FIGURE 12: The simulated return loss with different width of the ground.

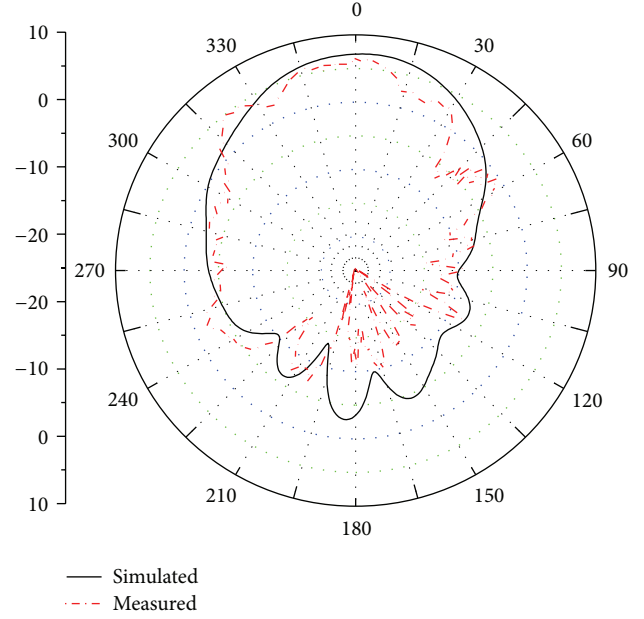


FIGURE 13: E-plane radiation pattern at 35 GHz.

Pocklington's integral equation or Hallen's integral equation [4]. The equivalent radius of strip dipole can determine that Hallen's theory of cylindrical antennas could be extended to antennas having noncircular cross section [4].

To derive an equation for the input impedance, let us refer to the model of Figure 6. When the electric and magnet wall were taken at the F plane, odd admittance Y_o and even admittance Y_e at the terminals 1-1' are obtained, respectively. Consider

$$Y_i \left(\frac{L}{2} \right) = Y_{di} \frac{Y_L + jY_{di} \tan(\beta L/2)}{Y_{di} + jY_L \tan(\beta L/2)} \quad i = 1, 2, \quad (5)$$

where Y_{d1} , Y_{d2} is radiation admittance in correspondence of W_1 and W_2 strip dipole.

The odd mode excitation ($Y_L \rightarrow 0$) is as follows:

$$Y_{o1} \left(\frac{l}{2} \right) = jY_{d1} \tan \frac{\beta l}{2}, \quad Y_{o2} \left(\frac{l}{2} \right) = jY_{d2} \tan \frac{\beta l}{2}. \quad (6)$$

The even mode excitation ($Y_L \rightarrow \infty$) is as follows:

$$Y_{e1} \left(\frac{l}{2} \right) = -jY_{d1} \cot \frac{\beta l}{2},$$

$$Y_{e2} \left(\frac{l}{2} \right) = -jY_{d2} \cot \frac{\beta l}{2},$$

$$[Y] = \frac{1}{2} \begin{pmatrix} Y_e + Y_o & Y_e - Y_o \\ Y_e - Y_o & Y_e + Y_o \end{pmatrix},$$

$$Y_o = Y_{o1} + Y_{o2} \quad Y_e = Y_{e1} + Y_{e2}. \quad (7)$$

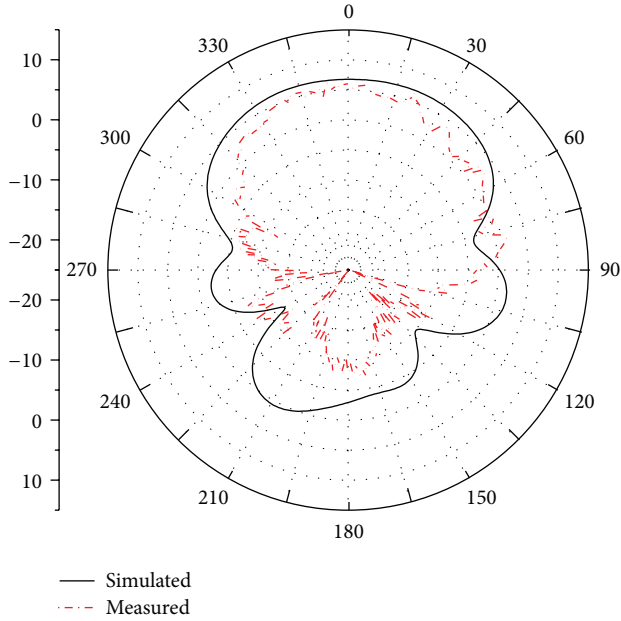


FIGURE 14: H-plane radiation pattern at 35 GHz.

The input admittance Y_d and input impedance Z_d are

$$Y_d = Y_o - Y_e, \quad Z_d = \frac{1}{Y_d}. \quad (8)$$

A solution of input impedance Z_{in} is similar to the traditional analysis method, when the input impedance Z_T in transmission line mode and the input impedance Z_d in antenna mode are obtained. The curves comparison with odd-even mode method and method of literature [5] is shown in Figure 7.

Balun is an electrical device that converts an unbalanced signal (two signals working against each other where ground is irrelevant) to a balanced signal (a single signal working against ground or pseudo-ground), and vice versa. It has many forms and may include devices that also transform impedance. Transformer baluns can also be used to match impedance of differing transmission lines.

A simple structure using the shown microstrip feeding in Figure 8 is designed for the proposed balun to extend the bandwidth. The length difference between two arms of transmission line is $\lambda/2$, where λ is the wavelength of microstrip [6–9].

3. Simulated and Experimental Results

The front and back view of the proposed antenna are shown in Figures 9 and 10, which has the similar size with the Chinese coin of one yuan.

The analysis of the proposed antenna is completed by using the Ansys HFSS. The simulated and measured S-parameter of the antenna from 30 GHz to 40 GHz are shown in Figure 11. It can be seen that the antenna has a simulation bandwidth of 5 GHz and a measured bandwidth of 3.5 GHz.

The central frequency has moved to 36.5 GHz. The simulated return loss with different width of the ground is shown in Figure 12. As width grew, the central frequency has moved to low frequency.

The measured E-plane and H-plane patterns at 35 GHz are shown in Figures 13 and 14, respectively. From the figures of radiation pattern, it is observed that gain of the antenna is 5.7 dB, lesser than the simulated result. It is considered that the measured results do not perfectly match the simulated results which are caused by the limits of manufacturing technology and the influence of measurement environment; all these deficiencies need to be considered seriously and improved in further research.

4. Conclusion

A microstrip folded dipole antenna on chip is proposed with 5 GHz bandwidth ($VSWR \leq 2$) and central frequency of 35 GHz. It has been demonstrated that the design takes the advantages of small size, wide impedance bandwidth, and stable radiation pattern. A new odd-even mode design procedure to calculate input impedance for asymmetric strip folded dipole is presented. It was verified that it is explicit and simple by another method [5] and another experiment.

Acknowledgments

This work was supported by the National Basic Research Program of China (no. 2009CB320203 and 2010CB327400) and in part by the National Science and Technology Major Project of China under Grant no. 2010ZX03007-001-01.

References

- [1] G. Hua, J. Zhang, J. Wu, and W. Hong, "Design and optimization of a millimetre wave compact folded magic-T," *International Journal of Antennas and Propagation*, vol. 2012, Article ID 838962, 6 pages, 2012.
- [2] S. Montusclat, F. Giancesello, and D. Gloria, "Silicon full integrated LNA, filter and antenna system beyond 40 GHz for MMW wireless communication links in advanced CMOS technologies," in *Proceedings of the IEEE Radio Frequency Integrated Circuits Symposium*, pp. 77–80, June 2006.
- [3] K. H. Park, "Generation of CW MMW using optical signal propagating nonlinear materials for wireless communications and ubiquitous communications systems," *Electronics Letters*, vol. 41, no. 10, pp. 599–601, 2005.
- [4] C. A. Balanis, *Antenna Theory: Analysis and Design*, John Wiley & Sons, Hoboken, NJ, USA, 3rd edition, 2012.
- [5] S. Keyrouz, H. J. Visser, R. J. M. Vullers, and A. G. Tjihuis, "Novel analytical procedures for folded strip dipole antennas," in *Proceedings of the 6th IEEE European Conference on Antennas and Propagation (EUCAP '12)*, pp. 2479–2482, 2012.
- [6] P.-C. Yeh, W.-C. Liu, and H.-K. Chiou, "Compact 28-GHz sub-harmonically pumped resistive mixer MMIC using a lumped-element high-pass/band-pass balun," *IEEE Microwave and Wireless Components Letters*, vol. 15, no. 2, pp. 62–64, 2005.
- [7] F. Hettstedt, W. Stellmach, T. von Hofe, R. Knächel, and E. Quandt, "3D thin film Guanella-balun," in *Proceedings of the 7th German Microwave Conference (GeMiC '12)*, pp. 1–4, 2012.

- [8] Y. Dai, H. Yin, Y. Feng, P. Li, Q. Han, and M. Han, "A LTCC miniaturized broadband modified Marchand balun," in *Proceedings of the International Symposium on Communications and Information Technologies (ISCIT '12)*, pp. 110–113, 2012.
- [9] C. Inui, M. Yasuo, and M. Fujishima, "On-chip S-shaped rat-race balun for millimeter-wave band using wafer-level chip-size package process," in *Proceedings of the European Microwave Integrated Circuit Conference (EuMIC '08)*, pp. 32–35, October 2008.

Research Article

BCB-Si Based Wide Band Millimeter Wave Antenna Fed by Substrate Integrated Waveguide

Hamsakutty Vettikalladi and Majeed A. S. Alkanhal

Department of Electrical Engineering, King Saud University, Riyadh 11421, Saudi Arabia

Correspondence should be addressed to Hamsakutty Vettikalladi; hvettikalladi@ksu.edu.sa

Received 10 September 2013; Revised 20 November 2013; Accepted 20 November 2013

Academic Editor: Guo Qing Luo

Copyright © 2013 H. Vettikalladi and M. A. S. Alkanhal. This is an open access article distributed under the Creative Commons Attribution License, which permits unrestricted use, distribution, and reproduction in any medium, provided the original work is properly cited.

A benzocyclobutene (BCB) silicon (Si) based wideband antenna for millimeter wave applications is presented. The antenna consists of multilayer with one layer of BCB and the remaining three layers of Si. A patch is etched on the Si substrate above the air gap, which is excited through a slot. This architecture of slot, air gap, and patch will produce wide bandwidth by merging each one of resonances. The simulated results show that the antenna provides an $S_{11} < -10$ dB bandwidth of 9.7 GHz (17%) starting from 51.5 GHz to 61.2 GHz around 57 GHz central frequency. The antenna provides a maximum gain of 8.9 dBi with an efficiency of 70%.

1. Introduction

The trend towards wireless communication and demand for large bandwidth in wireless local area networks (WLAN)/ wireless personal area networks (WPAN) environment is increasing rapidly, for example, wireless high definition multimedia interface (HDMI) devices, streaming and content download, peer-to-peer device communication, and high-speed internet access. For this purpose, 60 GHz is the natural candidate [1]. This continuous 7 GHz unlicensed band, around 60 GHz, has emerged as a worldwide opportunity for a range of short-range wireless applications. Oxygen absorption phenomenon is maximum at 60 GHz, which makes it the most suitable choice for WLAN, WPAN indoor secure communication [2]. Antenna is the fundamental element in all wireless communications. Currently, researchers all over the world are trying to produce some efficient small antennas/array system for deploying in 60 GHz applications. At this frequency band, different antenna designs have been proposed. Previously, many papers have been published in designing microstrip patch antennas/array. These antennas are lossy and have high level of back radiations pattern due to traditional planar feeding, such as microstrip lines [3], and coplanar waveguides [4]. The conduction and radiation losses problems are even more dominant at millimeter wave

V-band communication. Due to these problems, the antenna efficiency is degraded, especially in antenna array scenario, because of high level of back radiations. In microwave engineering, rectangular waveguides are widely used, because of their merits such as low losses, high power handling, and high isolation [4]. However, applications of these waveguides at millimeter wave frequencies are still very limited by high manufacturing cost, relatively large volumes, and difficulty of integration with other components.

The classical design techniques are not appropriate for millimeter wave frequency band as microstrip line designs exhibit large ohmic losses and spurious radiation. On the other hand, bulky waveguides designs are incompatible to deploy on such a compact circuitry. At this frequency band, we need to design a highly efficient antenna system, having optimum radiation characteristics (gain, radiation efficiency, and operating bandwidth), along with technology reliability, low cost, and compatibility with other RF modules. The current research challenges are not only to achieve large bandwidth around 60 GHz but also to design an efficient feeding network that does not affect the antenna array performance. Recently substrate integrated waveguide (SIW) technology is introduced for designs at millimeter wave frequency bands [5]. SIW technique is a transition between microstrip and dielectric filled waveguide (DFW) which

TABLE I: Design parameters.

| Parameter | W_{siw} | D_{via} | S_{via} | W_{trans} | L_{trans} | W_s | L_s | W_p | L_p | X_s | Y_s |
|----------------------|------------------|------------------|------------------|--------------------|--------------------|-------|-------|-------|-------|-------|-------|
| Numerical value (mm) | 2.35 | 0.156 | 0.50 | 1.98 | 2.61 | 0.34 | 2.20 | 1.5 | 3.80 | -0.10 | 3.12 |

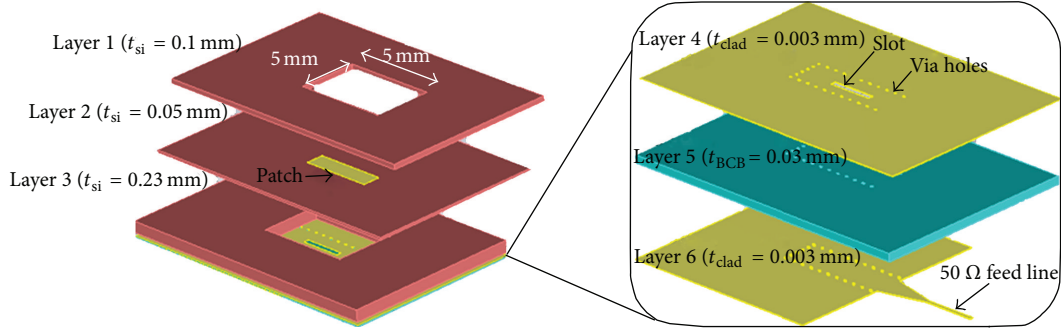


FIGURE 1: 3D exploded model view.

uses top and bottom metallization of the substrate and the metallized via-holes to create an artificial waveguide. It has been used and preferred in many millimeter wave circuits as a new type of transmission line for guiding the electromagnetic energy to excite the antenna structure [6, 7]. SIW has the qualities of low loss, high power handling capabilities, and being easy to integrate within millimeter wave circuits and components. On-chip antenna designs are preferred in terms of cost and compatibility with millimeter wave circuits. BCB based system-on-package (SOP) technology can be a good candidate for antenna packaging trends, because BCB has a low relative dielectric constant and a low tangent loss. Si layers with the rectangular cavities are created for bandwidth and gain enhancement of the antenna [8, 9].

The need for a low-volume and high-performance radiofrequency (RF) front-end module makes the RF packaging issues more important with increase in millimeter-wave applications. Here authors are presenting SIW based, multilayer antenna design technology using BCB-Si substrate. The fundamental design consists of an aperture antenna on the BCB layer excited by SIW, which acts as source antenna. Multiple layers of Si are used above the BCB layer. Our purpose is to design an efficient antenna with high gain and wide bandwidth.

2. Antenna Design

The 3D view of the antenna structure is shown in Figure 1. It consists of six layers. From top, the upper three silicon layers, layer 1, layer 2, and layer 3, have the thickness (t_{si}), 0.1 mm, 0.05 mm, and 0.23 mm, respectively with permittivity $\epsilon_r = 11.9$ and loss tangent $\tan \delta = 0.003$. A $5 \times 5 \text{ mm}^2$ cavity is created in layer 1 and layer 3, which helps to enhance the bandwidth. There is a patch etched at the upper face of the layer 2, with optimized dimensions of $1.5 \times 3.8 \text{ mm}^2$. SIW is designed at the last three layers (layer 4, layer 5, and layer 6). Layer 4 and layer 6 are copper metal with thickness (t_{clad}) of 0.003 mm having conductivity $\sigma = 58 \times$

10^6 s/m . Layer 5 is BCB with thickness (t_{BCB}) of 0.03 mm having permittivity $\epsilon_r = 2.3$ and loss tangent $\tan \delta = 0.003$. The SIW parameters, calculated from the guidelines given in [10], are shown in Figure 2. SIW width (W_{siw}) is the inner separation between the sidewalls created by via-holes, D_{via} is the diameter, and S_{via} is the center-to-center distance between two consecutive via-holes. The length and wall-to-wall width of SIW antenna element are 5.13 mm and 2.35 mm, respectively. A 50Ω microstrip line with a transition from microstrip to SIW having width W_{trans} and length L_{trans} [11] is designed on the bottom of the structure at layer 6, which excites the slot. A longitudinal slot is engraved at the ground layer (layer 4), having width W_s and length L_s and displacement from the symmetry axis is X_s . One end of the SIW is made short circuit to produce standing waves inside; Y_s is the distance from the short circuit end to the middle of the slot. A patch is etched on the upper face of the layer 2 and L_p and W_p are the length and width of the patch, which helps to enhance the gain. The standing waves will be radiated through the aperture created in the form of a longitudinal slot on the ground layer 4. The optimized numerical values of the design parameters are given in Table 1. The antenna is designed and simulated using both CST Microwave Studio and HFSS.

3. Results and Discussion

3.1. Return Loss, Gain, and Directivity. The simulated return losses (S_{11}) both in CST and HFSS are shown in Figure 3. We have taken into effect all the losses in simulations. The impedance bandwidth ($S_{11} < -10 \text{ dB}$) is 9.7 GHz, from 51.50 GHz to 61.20 GHz in CST and more in HFSS. The large bandwidth is due to the merging of three resonances as shown in CST results, which are due to the resonance from slot, air cavity, and the upper patch. There are three resonances in HFSS results too, but the third one comes after 62 GHz. The maximum gain and directivity are found to be 8.9 dBi and 10 dBi at 59 GHz with 70% radiation efficiency.

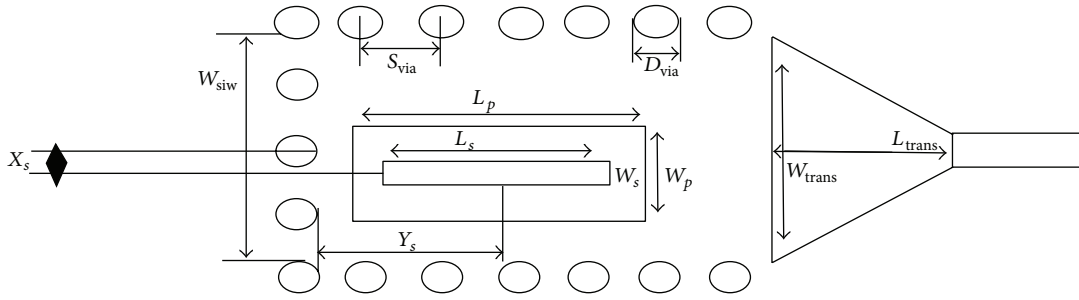


FIGURE 2: 2D top view, SIW parameters.

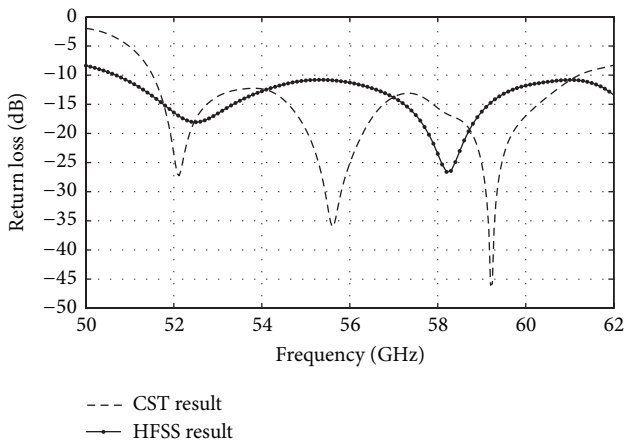


FIGURE 3: Simulated return loss.

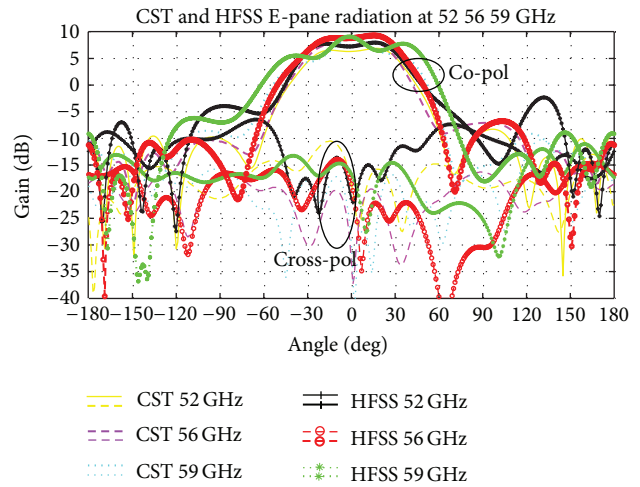


FIGURE 4: E-plane radiation patterns.

3.2. *Radiation Characteristics.* The E-plane and H-plane radiation characteristics using CST and HFSS simulations are shown in Figures 4 and 5, respectively. Both the simulation results are in good agreement. The simulated results for three frequencies (52 GHz, 56 GHz, and 59 GHz) are presented. The co-polar and cross-polar levels can be seen in each plane. Efficient radiation characteristics are achieved in terms of co-polar and cross-polar levels. The 3 dB beam width is 69 degree for the E-plane and 71 degree for the H-plane at 56 GHz. The bore sight to back radiation level difference is more than 17 dB in both the cases. The side lobe levels are almost 15 dB in both the planes. All the radiation patterns are good within the bandwidth in both the planes.

4. Conclusion

A BCB-Si based wide band millimeter wave antenna is designed. The antenna provides a wide bandwidth with good gain and efficiency. This antenna finds application in millimeter wave high speed communication systems.

Acknowledgment

The authors would like to thank King Abdulaziz City for Science and Technology (KACST) for providing fund through the Project no. ARP 34-137.

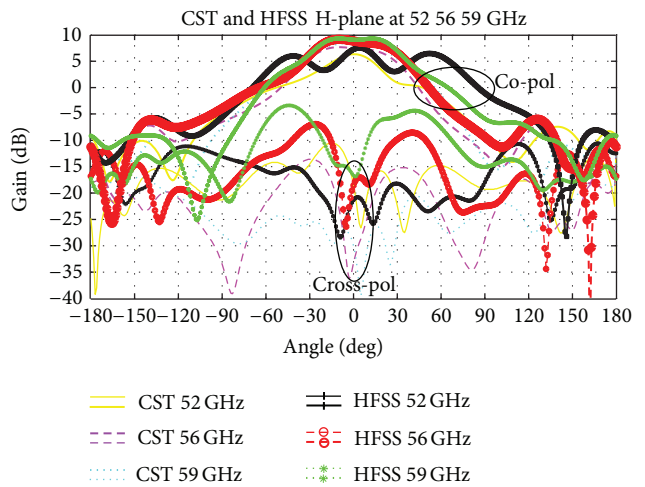


FIGURE 5: H-plane radiation patterns.

References

[1] S. Ohmori, Y. Yamao, and N. Nakajima, "Future generations of mobile communications based on broadband access technologies," *IEEE Communications Magazine*, vol. 38, no. 12, pp. 134-142, 2000.

- [2] R. C. Daniels and R. W. Heath Jr., "60 GHz wireless communications: emerging requirements and design recommendations," *IEEE Vehicular Technology Magazine*, vol. 2, no. 3, pp. 41–50, 2007.
- [3] H. Vettikalladi, O. Lafond, and M. Himdi, "High-efficient and high-gain superstrate antenna for 60-GHz indoor communication," *IEEE Antennas and Wireless Propagation Letters*, vol. 8, pp. 1422–1425, 2009.
- [4] J. W. Digby, C. E. McIntosh, G. M. Parkhurst et al., "Fabrication and characterization of micromachined rectangular waveguide components for use at millimeter-wave and terahertz frequencies," *IEEE Transactions on Microwave Theory and Techniques*, vol. 48, no. 8, pp. 1293–1302, 2000.
- [5] M. Bozzi, A. Georgiadis, and K. Wu, "Review of substrate-integrated waveguide circuits and antennas," *IET Microwaves, Antennas and Propagation*, vol. 5, no. 8, pp. 909–920, 2011.
- [6] T. Sarrazin, H. Vettikalladi, O. Lafond, M. Himdi, and N. Rolland, "Low cost 60 GHz new thin pyralux membrane antennas fed by substrate integrated waveguide," *Progress In Electromagnetics Research B*, vol. 42, pp. 207–224, 2012.
- [7] H. Vettikalladi, O. Lafond, and M. Himdi, "Membrane antenna arrays fed by substrate integrated waveguide for V-band communication," *Microwave and Optical Technology Letters*, vol. 55, no. 8, pp. 1746–1752.
- [8] N. Jeon, Y. Kim, I. Min, Y.-M. Ryoo, and K.-S. Seo, "System-on-package platform with thick benzocyclobutene layer for millimeter-wave antenna application," *Japanese Journal of Applied Physics*, vol. 51, no. 2, Article ID 02BB02, 5 pages, 2012.
- [9] D. Hou, Y.-Z. Xiong, W. Hong, W. L. Goh, and J. Chen, "Silicon-based on-chip antenna design for millimeter-wave/THz applications," in *Proceedings of the IEEE Electrical Design of Advanced Packaging and Systems Symposium (EDAPS '11)*, pp. 1–4, Hanzhou, China, December 2011.
- [10] W. M. Abdel-Wahab and S. Safavi-Naeini, "Wide-bandwidth 60-GHz aperture-coupled Microstrip Patch Antennas (MPAs) fed by Substrate Integrated Waveguide (SIW)," *IEEE Antennas and Wireless Propagation Letters*, vol. 10, pp. 1003–1005, 2011.
- [11] H. Kumar, R. Jadhav, and S. Ranade, "A review on substrate integrated waveguide and its microstrip interconnect," *Journal of Electronics and Communication Engineering*, vol. 3, no. 5, pp. 36–40, 2010.

Research Article

A Wireless and Real-Time Monitoring System Design for Car Networking Applications

Li Wenjun, Zhong Yiming, and Li Wenbin

Key Laboratory of RF Circuits and Systems of National MOE, Hangzhou Dianzi University, Hangzhou 310018, China

Correspondence should be addressed to Li Wenjun; liwenjun@hdu.edu.cn

Received 14 September 2013; Accepted 8 November 2013

Academic Editor: Guo Qing Luo

Copyright © 2013 Li Wenjun et al. This is an open access article distributed under the Creative Commons Attribution License, which permits unrestricted use, distribution, and reproduction in any medium, provided the original work is properly cited.

We described a wireless and monitoring system to obtain several classes of vehicle data and send them to the server via General Packet Radio Service (GPRS) in real-time. These data are consisted by on-board diagnostic (OBD) which get from the vehicle's OBD interface, Tire-Pressure Monitoring system (TPMS) and Global Positioning System (GPS). The main content of this paper is the hardware design of the system, especially RF modules and antennas.

1. Introduction

With the rapid development of automobiles, people need a more efficient way to manage cars. Sometimes we wish that not only drivers know the information about their cars, but also the administrator could do the same to all the cars which are the scope of his management in real-time. Even more we would like to store all the information data in the database so that we can analyze and check the history database, if needed. So the car networking has been put forward. Car networking means that we transform kinds of vehicle information into electronic singles, and we could exchange message with the outside communication systems, such as other cars, internet, and transport facilities [1]. In this way, we could manage the cars more effectively. However, car networking is just in its early stage since it could only communicate with internet. In this stage, car networking is mainly divided into three parts including data acquisition, data transmission, and data processing. Data acquisition and data transmission are implemented in in-vehicle terminal, as shown in Figure 1.

Many services which are based on Geographic Information System (GIS) are similar to this architecture, and supervisory system of school bus's track and the remote assistance system are examples of these services. They all need to upload the GPS data in real-time and store these data for check in the future [2]. However, if we could

upload more vehicle information like tire pressure, engine information, oil mass of fuel tank, and diagnostic trouble codes, the control of the cars would be more powerful. It will enormously push forward the development of car networking application. Generally, people add sensors or other measuring equipments to obtain more information. But it is noteworthy that a car itself is an electronic system. Automobile manufacturers integrate a lot of sensors into the car before it leaves factory. From a computer science perspective, one car is a complex distributed real-time system with up to 60 microcontroller based electronic control units (ECUs) that communicate via approximately 2500 different signals with each other [3]. And fortunately, we can have access to those data via a special interface called OBD. OBD stands for "on-board diagnostics," a computer-based system built into all model year (MY) 1996 and newer light-duty cars and trucks. OBD monitors the performance of some of the engines' major components, including individual emission controls. The system provides owners with an early warning of malfunctions by way of a dashboard "Check Engine" light (also known as a Malfunction Indicator Light or MIL, for short). By giving vehicle owners this early warning, OBD protects not only the environment but also consumers, identifying minor problems before they become major repair bills [4]. We can get the current operational status of the car or the diagnostic trouble codes by sending commands in accordance with a predetermined communication protocol

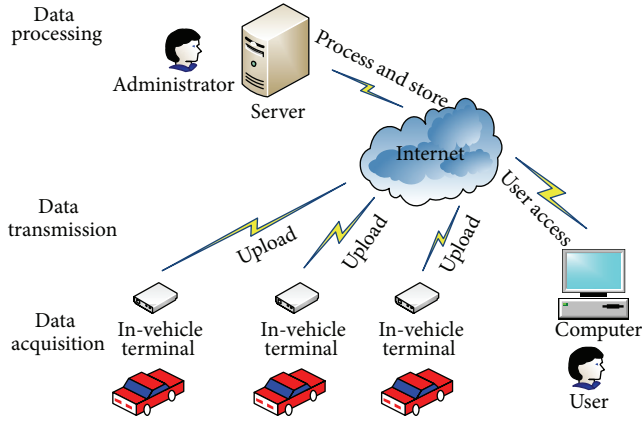


FIGURE 1: Car networking architecture in early stage.

standard [5]. The system introduced in this paper takes full advantages of the functionality provided by OBD. As referring to the international standards ISO15031-5 and ISO14230, the system could be compatible with most cars [6].

2. Design of In-Vehicle Terminal

The in-vehicle terminal is comprised of Microprogrammed Control Unit (MCU), Single chip OBD protocol converter, GPS module, GPRS module, and RF receiver chip. Its hardware design and the function modules are shown in Figure 2.

Even though OBD have the unified standard of application layer, there are different physical layers and network layers from different manufacturers. In order to be compatible with more manufacturers and increase the stability of the system, we choose single chip protocol converter TL718 as the protocol converter between MCU and the car's OBD interface. TL718 supports up to 16 kinds of OBD physical layers, so it could meet the requirement completely. TL718, GPS module and GPRS module are all connected with MCU via serial port, and the communication between RF module and MCU is based on a single data line. After receiving all data from TL718, GPS, and RF receiver chip, MCU will encapsulate those data as one data packet and sent it to GPRS module, then it uploaded it to server.

As we can see, the TPMS's communication, GPS data reception and GPRS data transmission all involve wireless communication, so we dig into the discussion on how to optimize the choice of those modules and which antennas which to match those modules to.

2.1. Wireless Tire Pressure Data Acquisition for Car. Some data show that there are more and more car accidents which are caused by tire burst, especially when a car is running at a high speed in summer. In most cases, the tire is very critical for the safety of the running automobile. Now, the most effective way to prevent tire burst is to monitor the temperature and pressure of the tires.

As we know, the sensor for tire pressure monitoring is installed in the tire, while the module for receiving tire pressure data should be placed within the carriage, considering

that the tire is a relatively independent unit which is located outside the carriage. Moreover, it is in the high-speed rotating state when the car is running. Thus the only way to realize the communication of real-time tire pressure monitoring system is to use the wireless communication technology.

Two of the commonest frequencies used in RF communication are 433 MHz and 2.4 GHz. Compared to 433 MHz, 2.4 GHz frequency band has a lot of advantages, such as fast communication rate, good safety and convenient protocol extension. However, our system does not need a high communication rate, because the kinds of data about tire are only temperature and pressure, and they all change at a relatively slow rate (checked once per half minute). Besides, there are a limited number of tires in one car, so we can set up a simple communication network by an easy protocol.

Moreover, the higher the frequency of the electromagnetic wave, the faster the attenuation. And the attenuation is more apparent, as the main material of car is metal. With comprehensive consideration, 433 MHz frequency is a better choice, which can be used easily, and the diffraction is better as its wavelength is longer [7].

Although there are many types of transceiver chip in 433 MHz frequency band, considering the actual application that the tire pressure sensor works in a single launching state and the car terminal works in a single receiving state, we choose independent single launching and receiving chip to save costs and bring down power consumption. From the application perspective, the low power consumption and stable performance are the most critical factors in the TPMS system then we find that launching chip MICRF112 and receiving chip MICRF211 of Micrel company can fulfill our requirement.

Next, we need to select the matching antenna for the RF chip. According to antenna theory, when the antenna length is proportional to the wavelength of the electromagnetic wave, sending and receiving efficiency will be the highest. This brings up the question if we chose the diffraction better and longer wavelength frequency band, it also means that we choose a longer antenna. At the same time, considering the rotation of the tire, omnidirectional antenna is more suitable antenna selection. As a result, we select helical antenna for the tire pressure sensor. According to the antenna theory, as the ratio of the wavelength and the diameter of the helical antenna D/λ meet $D/\lambda < 0.18$, the antenna radiation characteristics will be an omnidirectional radiation antenna. As the wavelength of 433 MHz band is 69 cm and the diameter of sensor is 1 cm, the ratio is given by $D/\lambda = 1/69 = 0.01 < 0.18$ which quite satisfies the inequality. This way, we can make an omnidirectional radiation antenna for RF module working in 433 MHz, and meanwhile the antenna is limited in a finite dimension [8].

2.2. GPS Data Acquisition Module. For all kinds of car networking applications, GPS information is almost essential information. Because the location for moving objects is one of the most critical attributes, so, we need to improve GPS signal quality as much as possible.

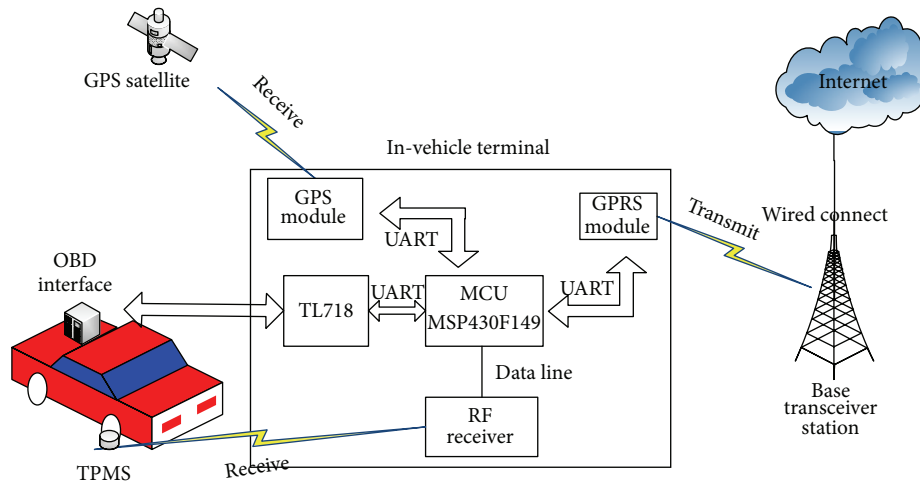


FIGURE 2: Hardware design structure and function of the terminal.

In the case of the original GPS design, two frequencies are utilized; one at 1575.42 MHz called L1; and a second at 1227.60 MHz called L2. And, in order to eliminate the Faraday rotation effect of the ionosphere to signal, GPS signal is a right-handed circularly polarized, so receiving antenna is also the right circular polarization mode [9].

Now, we consider two GPS antennas that are commonly used, patch antenna and helical antenna. Researches indicated that it is particularly difficult to achieve the crosspolarization rejection ratio and also to achieve adequate impedance matching at both the L1 and L2 frequencies using patch antenna. Patch antennas are narrow band, and a special feed is required to achieve the desired circular polarization. However, the study on the design based on an array of square helical antennas showed that the values of cross polarization rejection patterns slope satisfy the requirements to design a high-performance GPS receiving antenna [10]. Besides, the GPS client must receive the satellite signal directly, so the signal quality of a GPS receiver is generally weak.

Taking all above factors into account, we choose the helical antennas with a low noise amplifier. In order to reduce the signal attenuation, we extend the length of the antenna and place the receiver close to the window in the same time.

2.3. GPRS Module. The only way to send the car's information data to server is via wireless communication. Currently, there are multiple ways to construct wireless communication system, which are mainly divided into two classes, building their own private network and directly accessing to the public network. The first way, building their own private network, can significantly improve the communication efficiency and enrich vehicular networking functions. However, the biggest problem is the huge upfront cost to build communication infrastructure. Therefore, most of the prophase vehicular networking programs choose the second way, directly accessing to the public network. The greatest advantage of this way is that initial investment is lower and it can quickly come into use. Besides, another benefit of this way is that it has a large coverage area.

As we all know, there are two types of public communication technology, 2G like GSM and 3G like WCDMA. Compared with each other, the coverage area of GSM network is very wide because GSM technology has developed for so many years, but the disadvantage of GSM is that the bandwidth is small and the relative cost is high. 3G is the most advanced communication technology, which has been used. It greatly increases the communication bandwidth, so it is suitable for the transmission of large amounts of data, such as real-time video information. However, its main disadvantage is the limited network coverage area. Currently, 3G signal only covers the downtown with a lot of crowd. This limits the use scope of 3G communication systems.

The system described in this paper aims at vehicles which do not just move among densely populated urban. However, there are many areas without 3G signal, such as the lonely stretch of highway. At present, the information monitored by the system is only some character data, no images or video information. The bandwidth requirement is small but it requires a larger network coverage area. Therefore, the final selection of the system is GPRS. The system adopts SIM900A module of SIMcom company which uses SMT package and compact size of GSM/GPRS single-chip solution. This module has been maturely used in many fields. SIM900A connected with the MCU via the serial port receives the command and data packets sent by the MCU and then send them to the specified internet address.

GPRS operates at three frequency bands, 900 MHz, 1800 MHz, and 1900 MHz. The antennas of GPRS are called Flexible Printed Circuit Board (FPCB) Antennas which are frequently used in mobile phones and other mobile devices at present. FPCB antenna has wide bandwidth which is enough to support all three frequency bands of GPRS, as well as flexible and variable forms. It is easy to be integrated into a variety of terminal equipment [11].

As GPRS communications just need connecting with nearby base stations (much easier than GPS communications which have to connect directly with satellites), the quality of the communication signal is generally good.

TABLE 1: Frame Format of Frame's Header is "AM".

| | | | | | | | |
|------------|---------------------------|------------|------------|-------|---------------------------|-----|--|
| | | (a) | | | | | |
| 1 2 | 3 7 | 8 29 | 30 41 | 42 45 | 46 48 | | |
| AM | Vehicle ID | GPS data 1 | GPS data 2 | Time | Vehicle speed sensor data | | |
| | | (b) | | | | | |
| 49 52 | | 53 55 | | 56 59 | ... | 116 | |
| Engine RPM | Vehicle speed sensor data | Engine RPM | ... | END | | | |

TABLE 2: Frame Format of Frame's Header is "BM".

| | | | | | | | |
|-----------------|------------------------|---|------------|-------|----------------------------|--|--|
| | | (a) | | | | | |
| 1 2 | 3 7 | 8 29 | 30 41 | 42 45 | 46 48 | | |
| BM | Vehicle ID | GPS data 1 | GPS data 2 | Time | Engine coolant temperature | | |
| | | (b) | | | | | |
| 49 51 | | 52 54 | | 55 59 | 60 | | |
| Battery voltage | Intake air temperature | Distance travelled while MIT is activated | END | | | | |

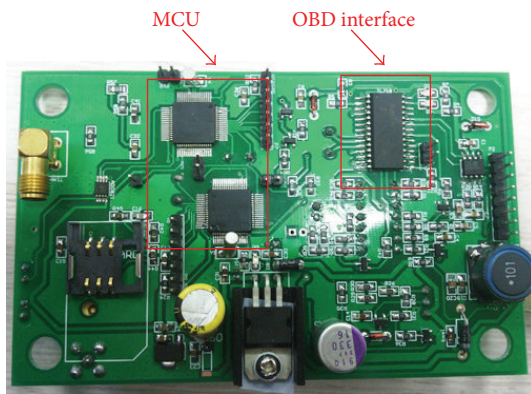


FIGURE 3: The top view of the terminal.



FIGURE 5: User interface via a browser of the system.



FIGURE 4: The reverse side view of the terminal.

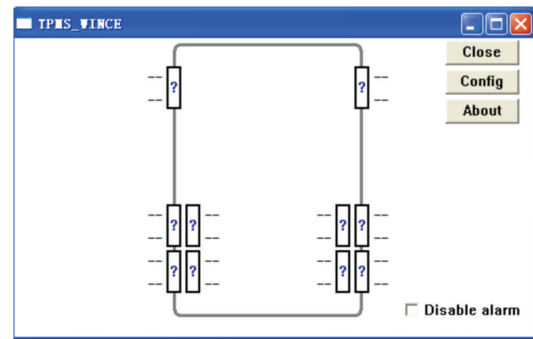


FIGURE 6: Software interface of TPMS data.

The server will receive three kinds of data packets, each of which has different frame formats.

In the end, the power of the in-vehicle terminal is supplied by OBD interface which outputs 12 V DC. Then the pictures of the in-vehicle terminal are shown in Figures 3 and 4.

3. Data Processing and Result

The frame header "AM," as shown in Table 1, means that this frame has Vehicle Speed Sensor data and Engine RPM data which read twice per second. But the frame is sent per five second so that we could make good use of GPRS's data traffic.

TABLE 3: Frame Format of Frame's Header is "CM".

| (a) | | | | | | | | | | | |
|---------------------|----|------------------|----|---------------------|----|------------|-----|------|----|------------------|----|
| 1 | 2 | 3 | 7 | 8 | 29 | 30 | 41 | 42 | 45 | 46 | 49 |
| CM | | Vehicle ID | | GPS data 1 | | GPS data 2 | | Time | | Tire A1 pressure | |
| (b) | | | | | | | | | | | |
| 50 | 52 | 53 | 57 | 58 | 61 | ... | 74 | | | | |
| Tire A1 temperature | | Tire A2 pressure | | Tire A2 temperature | | ... | END | | | | |

The frame header "BM," as shown in Table 2, means that this frame has some data which change slowly, so those data are read only once per five minute.

The frame header "CM," as shown in Table 3, means that this frame has the TPMS data.

Based on this data, user could check the car's information via a browser to access the server. People can review the history vehicle track and the running state of the car, as shown in Figure 5, or the car's tires pressure and temperature, as shown in Figure 6.

4. Conclusion

The results successfully show that the system can acquire and transmit a lot of imported data about vehicle. As making the most of those vehicle information, this system has broad prospects. This system can play the roles of Black Box for car. The running state data are very useful to analyze traffic incidents causation then it can be applied to insurance claims processing. And it could also be used in remote assistance system, by analyzing the diagnostic trouble codes.

Acknowledgment

The authors are thank for the help provided by the "The Key Technology And Application of Intelligent Identification" Priority Scientific and Technological Innovation Team from Zhejiang province (2010R50010).

References

- [1] G. Karagiannis, O. Altintas, E. Ekici et al., "Vehicular networking: a survey and tutorial on requirements, architectures, challenges, standards and solutions," *IEEE Communications Surveys and Tutorials*, vol. 13, no. 4, pp. 584–616, 2011.
- [2] Y.-H. Chou, "Automatic bus routing and passenger geocoding with a geographic information system," in *Proceedings of the 6th Vehicle Navigation and Information Systems Conference*, pp. 352–359, Seattle, Wash, USA, August 1995.
- [3] T. Steinbach, F. Korf, and T. C. Schmidt, "Real-time Ethernet for automotive applications: a solution for future in-car networks," in *Proceedings of the 1st IEEE International Conference on Consumer Electronics (ICCE '11)*, pp. 216–220, Berlin, Germany, September 2011.
- [4] H. J. Yun, S. K. Lee, and O. C. Kwon, "Vehicle-generated data exchange protocol for Remote OBD inspection and maintenance," in *Proceedings of the International Conference on*

Computer Sciences and Convergence Information Technology (ICCIT '11), pp. 81–84, Seogwipo, Republic of Korea, 2011.

- [5] L. E. Cordova-Lopez, A. Mason, J. D. Cullen, A. Shaw, and A. I. Al-Shamma'A, "Online vehicle and atmospheric pollution monitoring using GIS and wireless sensor networks," *Journal of Physics*, vol. 76, no. 1, Article ID 012019, 2007.
- [6] International Organization for Standardization, "Road vehicles—Communication between vehicle and external equipment for emissions-related diagnostics—part 5: emissions-related diagnostic services," ISO, ISO15031-5, 2006.
- [7] L. Shang and W. F. Li, "Choice of optimal frequency for radio orientation system in mine tunnel," *Safety in Coal Mines*, vol. 39, no. 3, pp. 22–25, 2008.
- [8] Y. Suo and J. H. Qiu, "Analysis and design of normal mode helical antenna," *Equipment Environmental Engineering*, vol. 5, no. 1, pp. 81–83, 2008.
- [9] K. Phaebua, C. Phongcharoenpanich, D. Torrungrueng, N. Surittikul, and W. Villarroel, "Dual-band antenna system for SDARS and GPS applications," in *Proceedings of the IEEE Antennas and Propagation Society International Symposium (APSURSI '10)*, pp. 1–4, Toronto, Canada, July 2010.
- [10] J. I. Ortigosa, N. Padros, and M. F. Iskander, "Comparative study of high-performance GPS receiving antenna designs," in *Proceedings of the Antennas and Propagation Society International Symposium*, vol. 3, pp. 1958–1961, Baltimore, Ma, USA, 1996.
- [11] X. Zhang and A. Zhao, "Flexible compact planar inverted-F antenna for GSM/DCS/PCS triple-band applications," in *Proceedings of the 8th International Symposium on Antennas, Propagation and EM Theory (ISAPE '08)*, pp. 15–18, November 2008.

Research Article

A Compact CPW-Fed UWB Antenna with Dual Band-Notched Characteristics

Aiting Wu¹ and Boran Guan²

¹ School of Electronic Engineering, Xidian University, Xi'an 710071, China

² Institute of Antenna and Microwave, Hangzhou Dianzi University, Hangzhou 310018, China

Correspondence should be addressed to Aiting Wu; wuaiting@hdu.edu.cn

Received 10 September 2013; Accepted 8 November 2013

Academic Editor: Guo Qing Luo

Copyright © 2013 A. Wu and B. Guan. This is an open access article distributed under the Creative Commons Attribution License, which permits unrestricted use, distribution, and reproduction in any medium, provided the original work is properly cited.

A compact CPW-fed planar UWB antenna with dual band-notched property is presented. The dual band rejection is achieved by etching a C-shaped slot on the radiation patch and two L-shaped parasitic strips in the ground plane. The experimental and measured results show that the proposed antenna exhibits an impedance bandwidth over an ultrawideband frequency range from 2.4 to 12.5 GHz with VSWR less than 2, except for two stopbands at 3.3 to 3.75 GHz and 5.07 to 5.83 GHz for filtering the WiMAX and WLAN signals, respectively. It also demonstrates a nearly omnidirectional radiation pattern. The fabricated antenna has a tiny size, only 32 mm × 32 mm × 0.508 mm. The simulated results are compared with the measured performance and show good agreement. The simple structure, compact size, and good characteristics make the proposed antenna an excellent candidate for UWB applications.

1. Introduction

Recently ultrawideband (UWB) communication systems have gained a great deal of attention due to their high data transmission rates, low consumption, good security, and immunity to multipath fading. Ever since 2002 when the US Federal Communication Commission (FCC) authorized the unlicensed use of UWB in the frequency band from 3.1 to 10.6 GHz [1], a lot of research efforts have been put into UWB communication systems which led to a great demand of UWB antennas. As one of the promising candidates, CPW-fed planar antennas have been investigated and reported in [2–6]. However, over the allocated frequency band, there are some existing narrow band services which may bring potential interferences to the UWB band, such as the IEEE 802.16 WiMAX system operating at 3.3–3.7 GHz and the IEEE 802.11a WLAN system operating at 5.15–5.825 GHz. To eliminate the interfaces antenna filtering technique has become an excellent candidate due to its simplicity, effectiveness, and low cost. Several methods have been proposed to design UWB antennas with band-notched functions, including etching C-shaped, L-shaped, T-shaped, H-shaped, U-shaped, E-shaped, and half-circle slots on the radiation patch or on the ground

plane [7–15], or by employing T-shaped, L-shaped, and spiral parasitic strips or open circuit stubs to the antennas [16–20].

In this paper, a compact novel CPW-fed planar ultrawideband antenna with dual band-notched characteristics is proposed and investigated in detail. Compared with the previous published antenna structures [7–20], the height of the proposed antenna is very small, only 0.508 mm, and its overall size is also quite compact, just 32 mm × 32 mm × 0.508 mm. By etching a C-shaped slot on the radiation patch, a single band-notched UWB antenna is first designed. Moreover, by adding another two L-shaped parasitic strips on the ground plane, the dual band-notched property is obtained. The simulated and measured VSWR results indicate that the proposed dual band-notched antenna could operate from 2.4 to 12.5 GHz with VSWR less than 2, except for two stopbands at 3.3 to 3.75 GHz and 5.07 to 5.83 GHz for filtering the WiMAX and WLAN signals. The simulated and measured radiation patterns of the proposed antenna are also presented. This paper is organized in the following 4 sections. In Section 2, the design and structure of the antenna are presented. Section 3 presents and analyses the simulated and measured results and further investigates the effect of the

TABLE 1: Optimized parameters of the single band-notched antenna.

| Parameters | L | W | L_1 | W_1 | d | g | s | d_w | L_{a_1} | L_{a_2} | m | t_a |
|-------------|-----|-----|-------|-------|-----|-----|-----|-------|-----------|-----------|-----|-------|
| Values (mm) | 32 | 32 | 26 | 16.8 | 7.2 | 0.3 | 1.4 | 0.3 | 7.1 | 4.2 | 7.8 | 1.05 |

TABLE 2: Optimized geometry parameters of the two L-shaped strips.

| Parameters | Lb_1 | Lb_2 | k | t_b |
|-------------|--------|--------|-----|-------|
| Values (mm) | 10 | 2.4 | 0.4 | 0.6 |

L is the total length of the C-shaped slot, ϵ_r is the relative dielectric constant, and c is the speed of light. Besides the slot length, its position and width also have great effects on the band rejection performance and should be tuned carefully. Note that when the C-shaped slot is etched on the radiation patch, there is no other tuning work needed for the primitive antenna structure. The optimized parameters of the antenna geometry are listed in Table 1.

2.2. Dual Band-Notched UWB Antenna Design. Besides WLAN systems, WiMAX applications operating from 3.3 to 3.7 GHz may bring interference to the UWB system as well. Based on the single band-notched antenna aforementioned, two L-shaped parasitic strips are added on the ground plane, and an extra 3.5 GHz band-notched function is achieved. The geometry of the dual band-notched antenna is shown in Figure 2. All the dimensions are the same as those shown in Figure 1, except for adding two extra L-shaped strips. The geometry parameters of the strips on the ground plane are given in Table 2. A common method to generate dual band-notched function is to etch two or more slots in the same patch [12–15], which may result in the complicated tuning process due to the mutual coupling effects of the slots. For the proposed antenna, the strips and the slot are totally independent for each other; thus the tuning process becomes much more simplified.

3. Experimental Results

3.1. Parameter Analysis. Both the single band-notched and the dual band-notched antenna prototypes are simulated and optimized using Ansoft HFSS software. Firstly the single band-notched antenna is simulated and investigated. The notched property is mainly determined by the length of the C-shaped slot $La = 2 * (La_1 + La_2)$. With the value of La_1 fixed, different values of La are got by varying the values of La_2 . Figure 3 shows the simulated VSWR result of the single band-notched antenna with different La_1 values. As shown in the figure, by increasing La_2 from 3.7 mm to 4.7 mm, the notched frequency is shifted from 5.75 to 5.25 GHz.

For the dual band-notched antenna, the length of the parasitic strip $Lb = Lb_1 + Lb_2$ determines the other notched band. With the value of Lb_1 fixed, different values of Lb are got by varying the values of Lb_2 . Figure 4 shows the simulated VSWR result of the dual band-notched antenna with different Lb_2 values. As shown in the figure, by increasing Lb_2 from



FIGURE 5: Photograph of the proposed dual band-notched antenna.

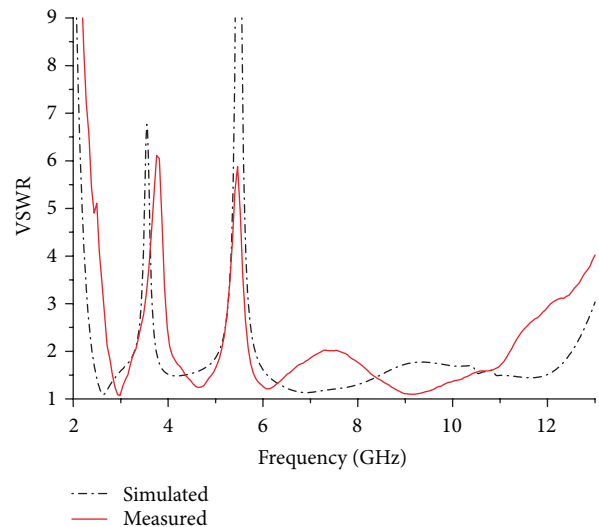


FIGURE 6: Simulated and measured VSWR of the proposed dual band-notched antenna.

1.4 mm to 3.4 mm, the second notched frequency is shifted from 4.05 to 3.4 GHz. It could be observed that the tuning of parameter Lb_2 has little affection on the 5.5 GHz notched band. Therefore the two notched bands could be tuned independently and no retuning work is needed for the antenna structure.

3.2. VSWR Results. To verify the design of the proposed antenna, a prototype of the dual band-notched antenna is fabricated and measured. Figure 5 shows the photograph of the fabricated antenna prototype. The antenna VSWR is measured by the Agilent 8719ES 50MHz—13.5 GHz Network Analyzer. The antenna is fed through a SMA connector. The simulated and measured results of the VSWR results are

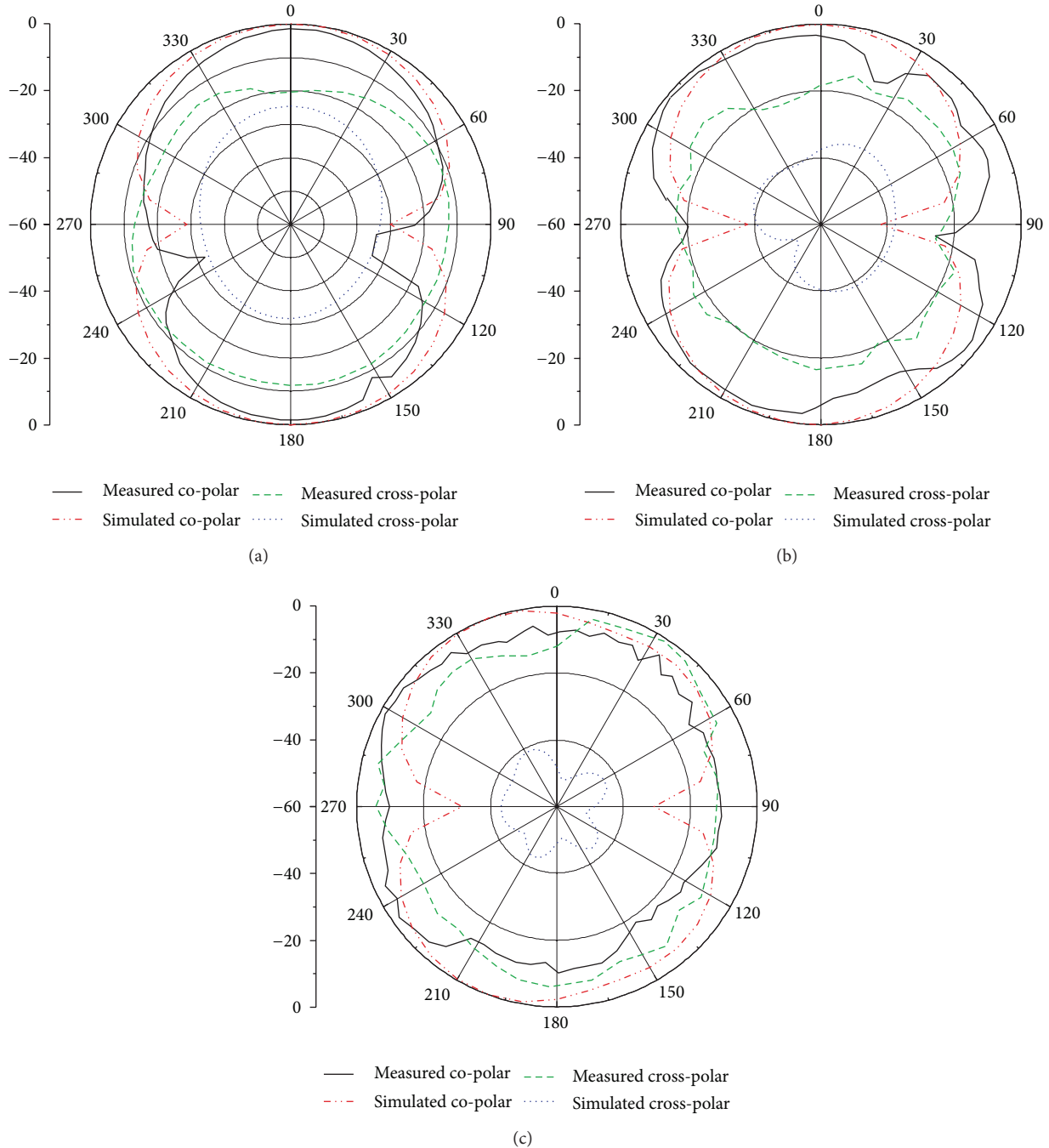


FIGURE 7: Simulated and measured E -plane radiation patterns at (a) 3 GHz, and (b) 6 GHz, (c) 9 GHz.

presented in Figure 6. As shown in Figure 6, the antenna impedance bandwidth extends from 2.4 to 12.5 GHz with VSWR less than 2, except for two stopbands at 3.3 to 3.75 GHz and 5.07 to 5.83 GHz. Thus it covers the whole UWB spectrum defined by FCC, which confirms the proposed antenna's good qualification for the UWB applications. It could be observed that there is a good agreement between the simulated and the measured results. The discrepancy between the simulated and the measured results might stem from SMA connector side effects and fabrication imperfections.

3.3. Radiation Pattern. Two planes are selected to show the radiation pattern of the proposed antenna, which are referred to as x - y plane or E -plane and y - z plane or H -plane, respectively. The simulated and the measured normalized radiation patterns of the antenna are shown in Figures 7 and 8, both co-polar and cross-polar results presented, at 3, 6, 9 GHz. We could clearly see that the simulated and measured results have a good agreement with each other. It is also observed that the radiation patterns in E -plane are almost bidirectional at lower frequencies, while at higher ranges

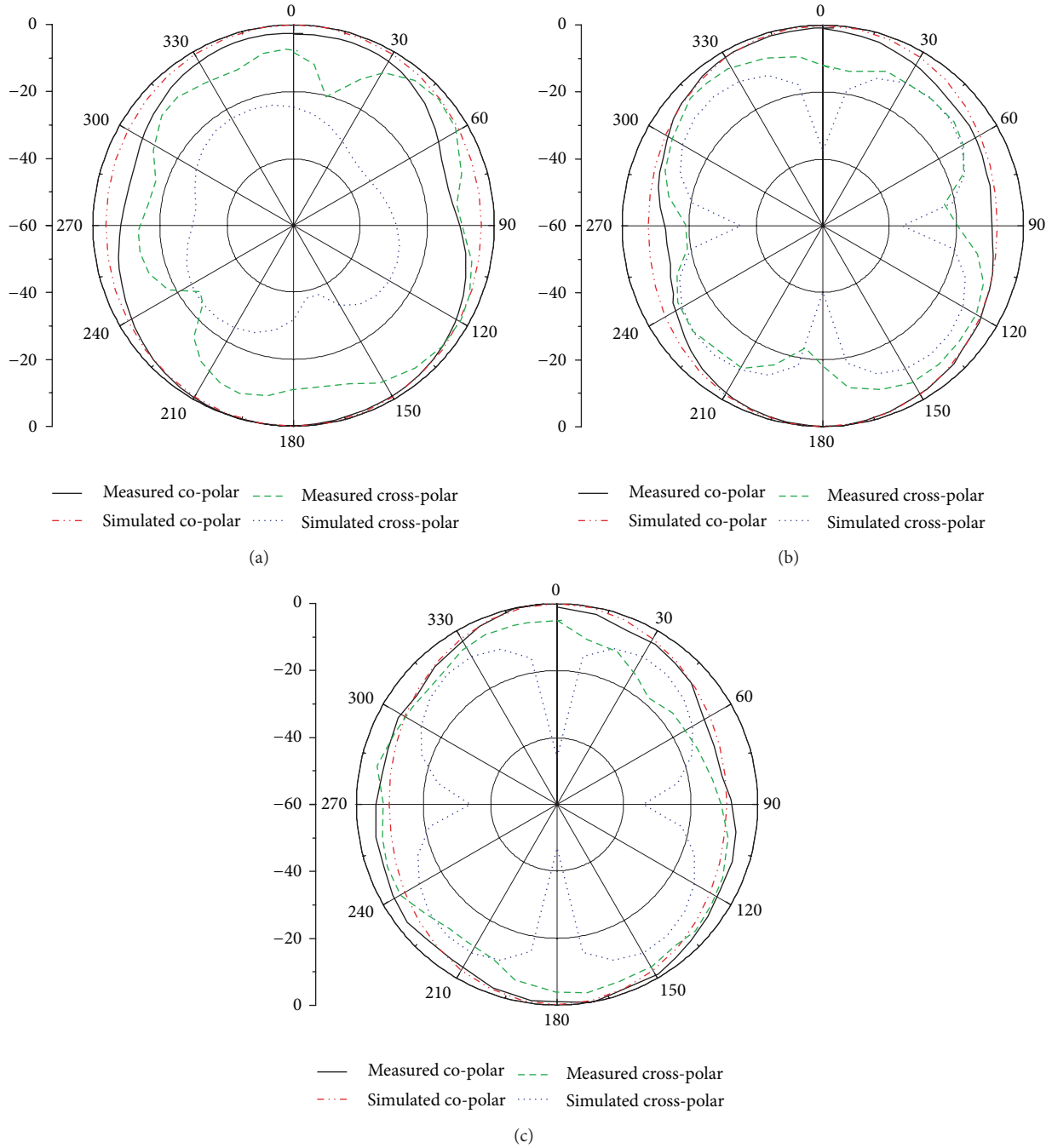


FIGURE 8: Simulated and measured H -plane radiation patterns at (a) 3 GHz, (b) 6 GHz, and (c) 9 GHz.

the radiation patterns are distorted. The H -plane radiation patterns conserve a clear omnidirectional characteristic at lower frequencies and vary a little at higher frequencies.

3.4. Current Distribution. Figure 9 shows the simulated surface current distributions at 3.5 GHz and 5.5 GHz. The larger current distribution is indicated in red, while the smaller one is in blue. It is observed that the surface current is highly concentrated at the C-shaped slot at 3.5 GHz and at the two L-shaped strips at 5.5 GHz, which means that a large portion

of electromagnetic energy has been stored around the slot or the strips rather than being radiated into the air, so that the radiation efficiency decreases at the rejected bands.

3.5. Radiation Gain. The simulated gain of the proposed antenna is illustrated in Figure 10. A stable gain with the average of about 4.0 dBi is obtained throughout the whole UWB operating band except at the two notched band frequencies. As desired, the antenna gain decreases sharply in the vicinity of 3.5 and 5.5 GHz, with the gain values about -1.5 dBi and

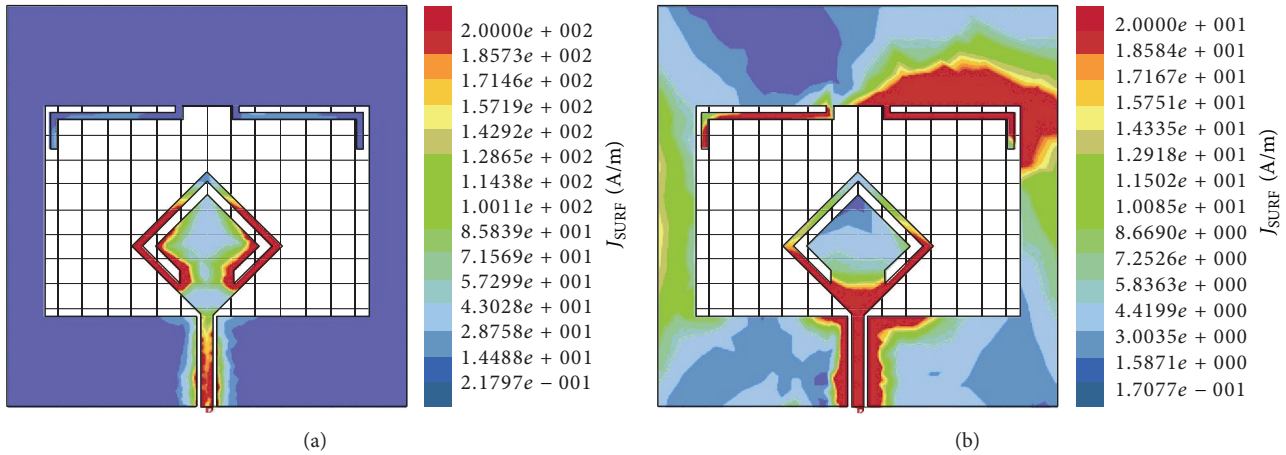


FIGURE 9: Simulated current distribution of the proposed antenna: (a) 3.5 GHz and (b) 5.5 GHz.

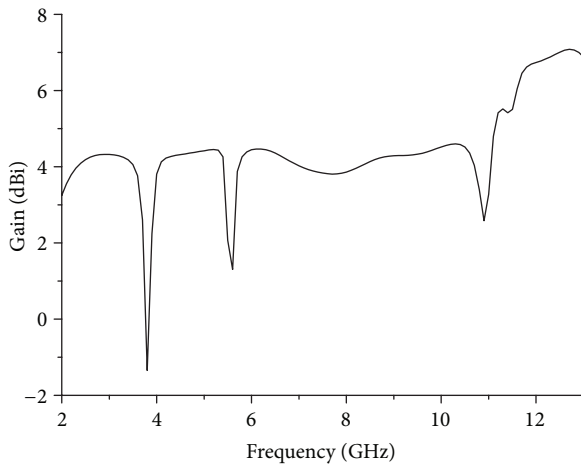


FIGURE 10: Simulated gain of the proposed antenna.

1 dBi, respectively. It just demonstrates and reinforces the good band-rejected function of the proposed antenna.

4. Conclusions

A novel compact CPW-fed planar UWB antenna with dual band-notched property is proposed and investigated. The primitive UWB antenna is fed by a simple diamond patch, with a compact size of $32 \text{ mm} \times 32 \text{ mm} \times 0.508 \text{ mm}$. The proposed antenna impedance bandwidth could cover the full UWB spectrum except for the two notched bands for WiMAX and WLAN applications, respectively. A C-shaped slot is etched on the patch and two parasitic strips are added to the ground plane to achieve 3.5 GHz and 5.5 GHz dual band-notched functions. The ultrawide bandwidth with dual band-notched characteristics, the compact size, and the simple structure of the proposed antenna make it an excellent candidate for UWB applications.

Acknowledgment

This work has been supported by the Zhejiang Provincial Department of Education Project under Grant no. Y201327468.

References

- [1] Federal Communications Commission, "Revision of part 15 of the commission's rules regarding ultra-wideband transmission systems," First Report and Order, FCC 2 V48, 2002.
- [2] R. Azim, M. T. Islam, and N. Misran, "Compact tapered-shape slot antenna for UWB applications," *IEEE Antennas and Wireless Propagation Letters*, vol. 10, pp. 1190–1193, 2011.
- [3] H.-D. Chen, "Broadband CPW-fed square slot antennas with a widened tuning stub," *IEEE Transactions on Antennas and Propagation*, vol. 51, no. 8, pp. 1982–1986, 2003.
- [4] S. T. Choi, K. Hamaguchi, and R. Kohno, "Small printed CPW-fed triangular monopole antenna for ultra-wideband applications," *Microwave and Optical Technology Letters*, vol. 51, no. 5, pp. 1180–1182, 2009.
- [5] M. Koohestani and M. Golpour, "Compact rectangular slot antenna with a novel coplanar waveguide fed diamond patch for ultra wideband applications," *Microwave and Optical Technology Letters*, vol. 52, no. 2, pp. 331–334, 2010.
- [6] T. A. Denidni and M. A. Habib, "Broadband printed CPW-fed circular slot antenna," *Electronics Letters*, vol. 42, no. 3, pp. 135–136, 2006.
- [7] X.-F. Zhu and D.-L. Su, "Symmetric E-shaped slot for UWB antenna with band-notched characteristic," *Microwave and Optical Technology Letters*, vol. 52, no. 7, pp. 1594–1597, 2010.
- [8] M. A. Habib, A. Bostani, A. Djaiz, M. Nedi, M. C. E. Yagoub, and T. A. Denidni, "Ultra wideband cpw-fed aperture antenna with wlan band rejection," *Progress in Electromagnetics Research*, vol. 106, pp. 17–31, 2010.
- [9] S. Barbarino and F. Consoli, "UWB circular slot antenna provided with an inverted-L notch filter for the 5 GHz WLAN band," *Progress in Electromagnetics Research*, vol. 104, pp. 1–13, 2010.

- [10] Y.-C. Lin and K.-J. Hung, "Compact ultrawideband rectangular aperture antenna and band-notched designs," *IEEE Transactions on Antennas and Propagation*, vol. 54, no. 11, pp. 3075–3081, 2006.
- [11] N. Pouyanfar, "CPW-FED UWB antenna with band-stop properties," *Microwave and Optical Technology Letters*, vol. 55, no. 7, pp. 1533–1537, 2013.
- [12] J. Xu, D. -Y. Shen, G. -T. Wang, X. -H. Zhang, X. -P. Zhang, and K. Wu, "A small UWB antenna with dual band-notched characteristics," *International Journal of Antennas and Propagation*, vol. 2012, Article ID 656858, 7 pages, 2012.
- [13] J. Liu, S. Gong, Y. Xu, X. Zhang, C. Feng, and N. Qi, "Compact printed ultra-wideband monopole antenna with dual band-notched characteristics," *Electronics Letters*, vol. 44, no. 12, pp. 710–711, 2008.
- [14] Q.-X. Chu and Y.-Y. Yang, "A compact ultrawideband antenna with 3.4/5.5 GHz dual band-notched characteristics," *IEEE Transactions on Antennas and Propagation*, vol. 56, no. 12, pp. 3637–3644, 2008.
- [15] H. Zhai, J. Ou, T. Li, G. Li, L. Li, and C. Liang, "A compact ultrawideband antenna with two band-notches," *Microwave and Optical Technology Letters*, vol. 55, no. 3, pp. 583–586, 2013.
- [16] W. X. Liu and Y. Z. Yin, "Dual band-notched antenna with the parasitic strip for UWB," *Progress in Electromagnetics Research Letters*, vol. 25, pp. 21–30, 2011.
- [17] M. Ojaroudi and N. Ojaroudi, "Low profile slot antenna with dual band-notched function for UWB systems," *Microwave and Optical Technology Letters*, vol. 55, no. 5, pp. 951–954, 2013.
- [18] C. -W. Zhang, Y. -Z. Yin, P. -A. Liu, and J. -Xie, "Compact dual band-notched UWB antenna with hexagonal slotted ground plane," *Journal of Electromagnetic Waves and Applications*, vol. 27, no. 2, pp. 215–223, 2013.
- [19] M.-F. Wang, J.-X. Xiao, and S.-W. Wang, "Study of a dual-band notched wideband circular slot antenna," *Journal of Electromagnetic Waves and Applications*, vol. 24, no. 17-18, pp. 2445–2452, 2010.
- [20] G.-M. Zhang, J.-S. Hong, and B.-Z. Wang, "Two novel band-notched UWB slot antennas fed by microstrip line," *Progress in Electromagnetics Research*, vol. 78, pp. 209–218, 2008.

Research Article

Implementation of Low-Cost UHF RFID Reader Front-Ends with Carrier Leakage Suppression Circuit

Bin You,¹ Bo Yang,¹ Xuan Wen,² and Liangyu Qu³

¹The Key Laboratory of RF Circuits and System of Ministry of Education, Hangzhou Dianzi University, Hangzhou 310018, China

²Nokia Siemens Networks Technology (Beijing) Co., Ltd., Hangzhou 310053, China

³Shanghai TYD Electronic Technology Co., Ltd., Shanghai 200233, China

Correspondence should be addressed to Bo Yang; jasonyoung327@gmail.com

Received 29 August 2013; Accepted 9 October 2013

Academic Editor: Bing Liu

Copyright © 2013 Bin You et al. This is an open access article distributed under the Creative Commons Attribution License, which permits unrestricted use, distribution, and reproduction in any medium, provided the original work is properly cited.

A new ultrahigh frequency radio frequency identification (UHF RFID) reader's front-end circuit which is based on zero-IF, single antenna structure and composed of discrete components has been designed. The proposed design brings a significant improvement of the reading performance by adopting a carrier leakage suppression (CLS) circuit instead of a circulator which is utilized by most of the conventional RF front-end circuit. Experimental results show that the proposed design improves both the sensitivity and detection range compared to the conventional designs.

1. Introduction

Although the theoretical basis of RFID technology has been established in 1948 [1], it took a long time before the technology advanced to current level. Unlike other wireless identification technology (such as bar codes and infrared technology), the UHF RFID uses backscattering communication which brings the noncontact, non-line-of-sight characteristics, and the long identified distance, high-speed reading, and other advantages make the UHF RFID becoming the most promising automatic identification technology around the world.

Nowadays, the development of UHF RFID front-end design has two trends: one is to use specific RFID ICs, such as Indy R2000 produced by Intel and AS3992 produced by austriamicrosystems; the other is to use discrete components. Using the specific ICs can shorten the development circle, while using the discrete components overcomes the limitation of protocols integrated in the specific ICs, makes the design more flexible and easier to optimize, and brings an enhancement of the performance and reduction of the cost. Thus, in today's market, most of the commercial UHF RFID reader's front-ends with high performances are designed by using discrete components.

In order to simplify the circuit structure, most of the RF front-ends are based on zero-IF and single-antenna structure.

Generally, the conventional RF front-end consists of four parts: the local oscillator (LO), transmitting circuit (Tx), receiving circuit (Rx), and the circulator. Figure 1 shows the block diagram of a conventional RF front-end built by discrete components. As it is known that one distinctive characteristic of the UHF RFID reader is that it transmits the strong carrier wave and receives the faint backscattered signals of tags at the same frequency simultaneously [2]. Because of the imperfect Tx to Rx isolation of the circulator (usually 22 dB), either a LNA or the receiver will be saturated by the strong Tx carrier wave leaks into the Rx, and the LNA is abnegated before the receiver in the conventional front-end; thus, the sensitivity and the performance of the reader is degraded drastically.

In this paper, a redesigned RF front-end circuit of UHF RFID reader based on zero-IF and single-antenna structure and built by discrete components is proposed. The circuit of the proposed front-end is more simplified than the conventional one, due to the integration of the LO and the modulator by choosing a proper chip. Besides, the performance of the reader is also improved by using a newly designed carrier leakage suppression (CLS) circuit instead of the circulator, and adding a LNA before the receiver.

The structure of this paper is as follows. Section 2 gives the design of the proposed UHF RF front-end. Section 3

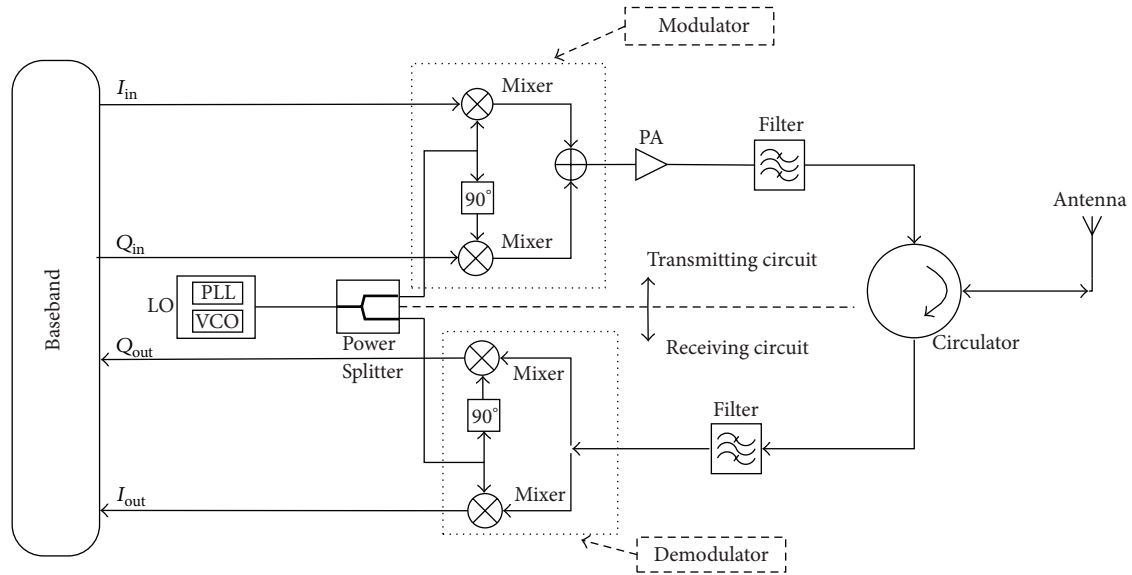


FIGURE 1: Block diagram of conventional RF front-end.

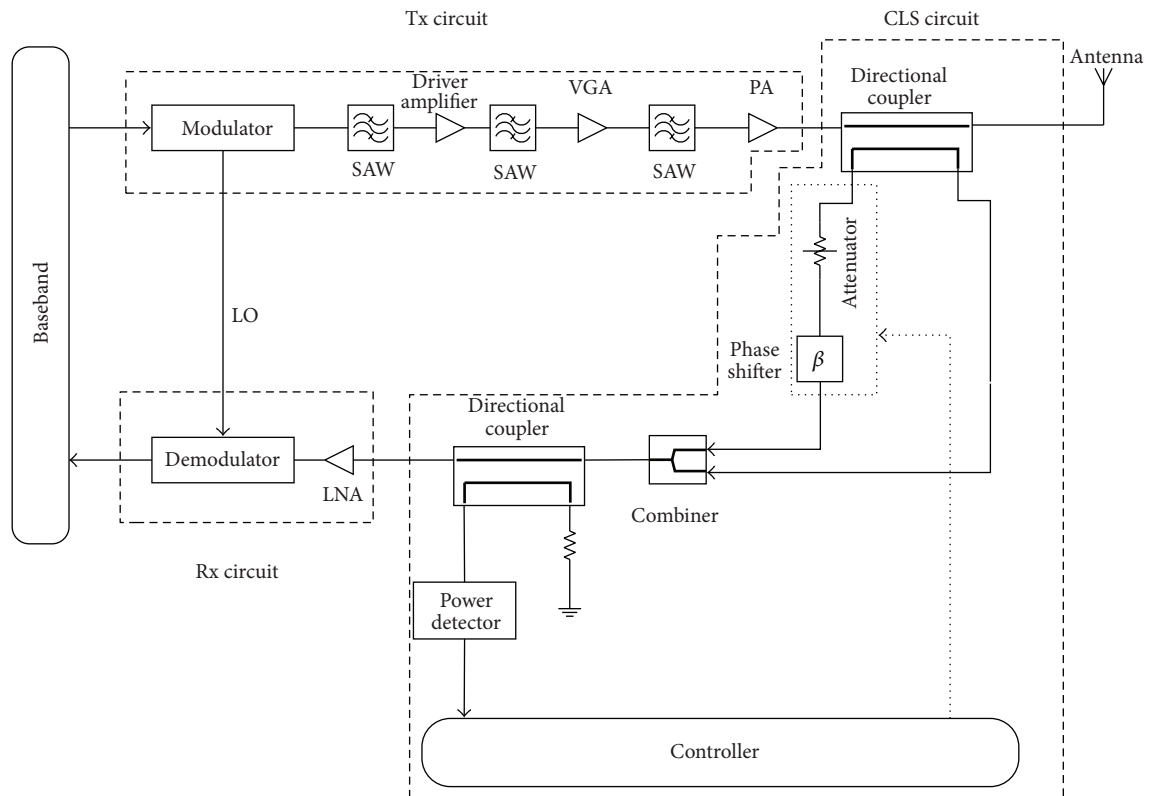


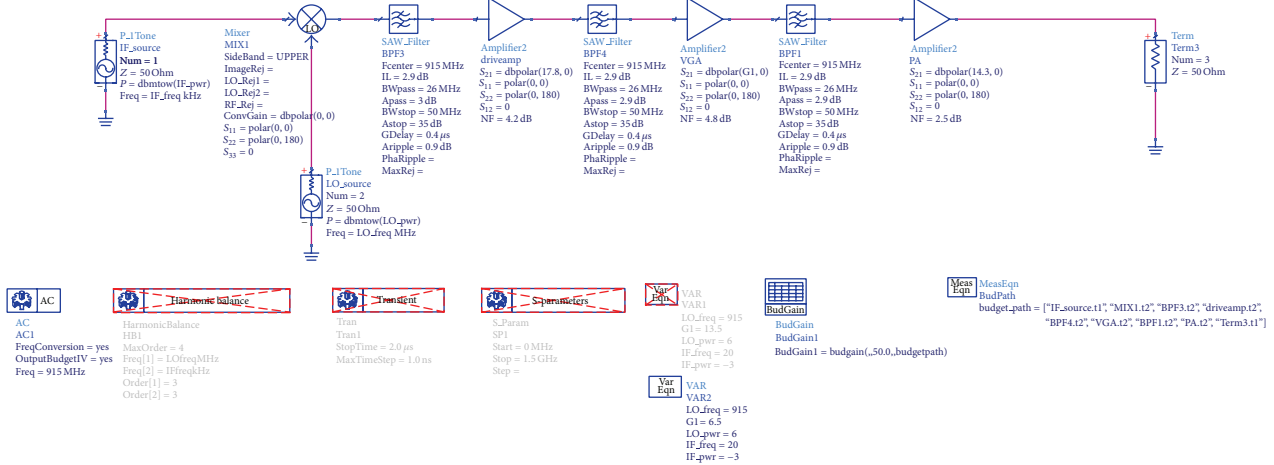
FIGURE 2: Block diagram of the proposed RF front-end.

demonstrates the implementation and the experimental results. The conclusion is drawn in Section 4.

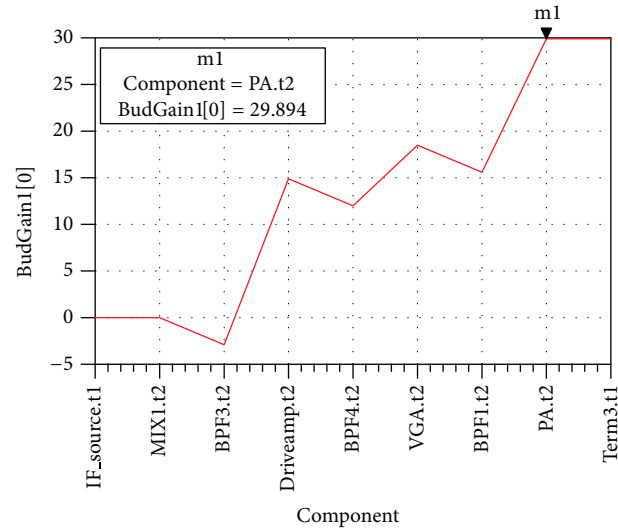
2. Design of the Proposed UHF RFID RF Front-End

The proposed RF front-end is composed of three parts: Tx circuit, Rx circuit, and CLS circuit, as is shown in Figure 2.

2.1. Tx Circuit. The main function of the Tx circuit is to modulate baseband signal and amplify the modulated signal. In order to simplify the RF front-end circuit, the ADF9010 is chosen as the modulator. It is not only because of its high output power (-3 dBm to 3 dBm) which can fulfill the input requirement of the later amplifier block, but also because of its integrated LO generation which is available at the output to drive an external RF demodulator. Moreover, the ADF9010



(a)



(b)

FIGURE 3: Link budget simulation of the proposed Tx circuit: (a) behavior model of the Tx circuit; (b) simulation result when VGA sets a 6.5 dB gain.

integrates a receive baseband PGA (Rx PGA) offering up to 24 dB voltage gain. The AVT54689 (Driver Amplifier), HMC-80110 (VGA), and ALM-32120 (PA), along with the SAW filters, compose the amplifier block. Figure 3 gives the link budget simulation of the Tx circuit by using the Advanced Design System (ADS). Figure 3(a) is the behavior model of the Tx circuit, and Figure 3(b) is the simulation result. It shows that when the VGA with a gain control range of -40 dB to 13.5 dB sets a 6.5 dB gain, the total gain of the Tx circuit can achieve nearly 30 dB, which means if the ADF9010 sets a 0 dBm output power, then the output power of the Tx can achieve 30 dBm easily.

2.2. Rx Circuit. The ADL5382 is chosen as the demodulator. With NF = 14 dB, IP1 dB = 14.7 dBm, and IIP3 = 33.5 dBm at 900 MHz, the ADL5382 offers an outstanding dynamic range which is suitable for the demanding infrastructure

direct-conversion requirements. In order to lower the Rx circuit's noise figure, the ADL5523, a low noise amplifier (LNA) is added before the demodulator. Figure 4 gives the Link budget simulation of the Rx circuit. According to the read-range analysis of the UHF RFID reader provided by the material [3], the input power of the receiver is set to -70 dBm in the simulation, assuming that the distance between the passive tag and the reader's antenna is 10 m. And the maximum gain of the Rx PGA in the ADF9010 is set.

The simulation result shows that the maximum gain of the Rx circuit can achieve nearly 74 dB, which means when a passive tag is 10 m far from the reader's antenna, the output power of the baseband signal can be 4 dBm, which fulfills the input requirement of the analog to digital converter (ADC).

2.3. CLS Circuit. One distinctive characteristic of the UHF RFID reader is that it transmits the carrier wave signal

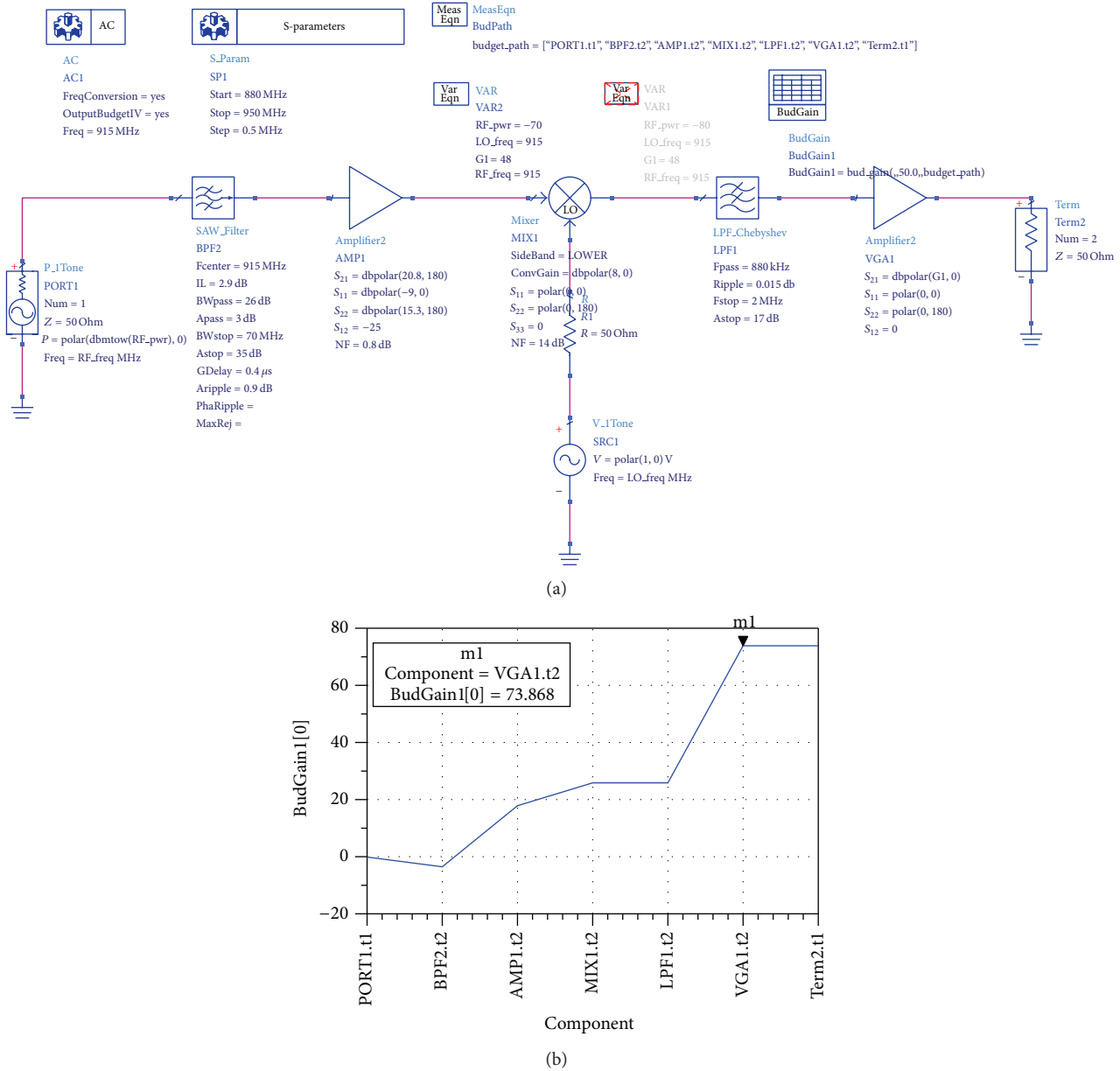


FIGURE 4: Link budget simulation of the proposed Rx circuit: (a) behavior model of the Rx circuit; (b) simulation result when the input power of the receiver is -70 dBm, and the voltage gain of the Rx PGA of the ADF9010 is 24 dB.

and receives the backscattered signal from tag in the same frequency band simultaneously. This characteristic results in that the reader's front-end circuit requires high isolation to prevent the transmitter's carrier signal from leaking into the receiver [4]. Thus in conventional RF front-end based on one antenna structure, a circulator or a directional coupler is used to isolate the Tx to Rx; however the isolation characteristic in well matched condition of these devices can hardly exceed 25 dB; moreover if the front-end is mismatched by an antenna, the isolation worsens [5]. In order to improve the isolation between Tx and Rx, a newly designed CLS circuit is proposed. Figure 5 gives out the block diagram of the proposed CLS circuit.

As is shown in Figure 5, the carrier signal received by the receiver (LNA input) is consisted of signal A and signal B. The signal A is the carrier leakage signal, which is a vector sum of three signals: the first one is the carrier leaks to the isolation port (Port4) due to the imperfect isolation of the directional coupler; the second one is the reflected signal from the antenna because of the input impedance mismatch of the antenna; the third one is the reflected signal from the coupling port (Port3) of the directional coupler due to the imperfect matching between the attenuator and the coupling port. The signal B is the coupled carrier signal. The principle of the proposed front-end is to properly adjust the magnitude and phase position of the coupled carrier signal

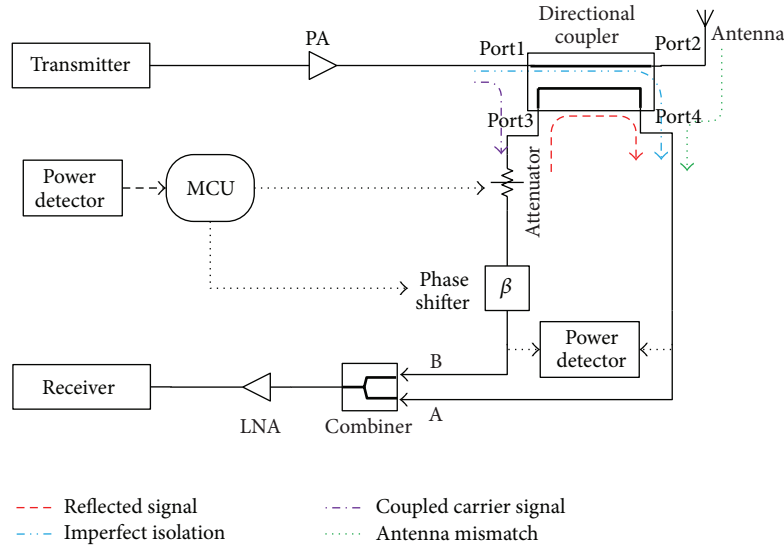


FIGURE 5: Block diagram of the proposed CLS circuit.

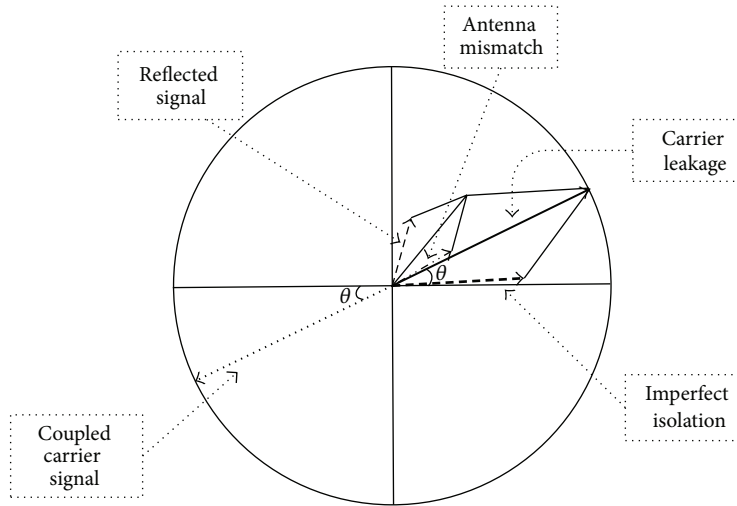


FIGURE 6: Vector representation of the carrier leakage signals and their cancellation using the coupled carrier signal.

by using the attenuator and the phase-shifter, to complete the carrier leakage suppression. Figure 6 shows the vector of the carrier leakage signals and their cancellation using the coupled carrier signal. Hence, as long as the operating frequency range of the attenuator and the phase-shifter can cover the UHF RFID frequency band, the proper cancellation can be achieved without worrying about the influence of the impedance matching of both the antenna and the attenuator.

3. Implementation and Experimental Results

In order to validate the performance of the proposed carrier leakage suppression (CLS) circuit, the CLS circuit has been fabricated. A 5 dB directional coupler of RN2's RCP890A05, an attenuator of Skyworks' AV101-12, which has a typical attenuation of 30 dB, a phase-shifter of Skyworks' PS094-315

with a 80–110 degree phase shift range, and a combiner of M/A-COM's MAPDCC0001 are used. The antenna of Laird's A9028L30NF has a gain of 8 dBi and an operating frequency range between 902 and 928 MHz, which is for one of the UHF RFID frequency bands. A photograph of the fabricated circuit is shown in Figure 7, including the schematic diagram of the experimental setup.

Figure 8 shows the isolation characteristics (S_{21}), tested by using the Agilent-8719ES (S-Parameter Network Analyzer), of the fabricated CLS circuit and conventional circulator at the center frequency of 915 MHz, respectively. The test environment is set in the open area of the laboratory. Experimental result shows that the isolation between the transmitter (Tx) and receiver (Rx) is improved by more than 45 dB at the center and by at least 30 dB within 20 MHz band from the center. Hence the leakage signal to the receiver can be removed almost totally.

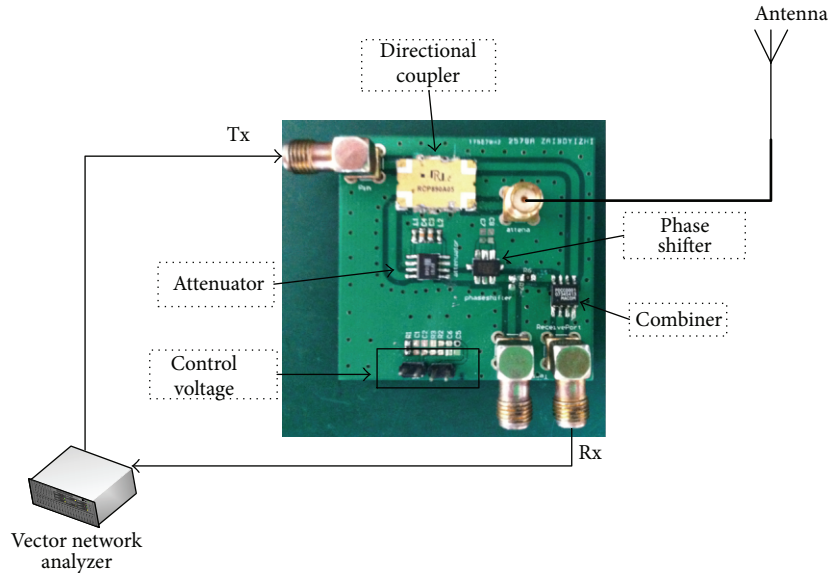


FIGURE 7: Photograph of the fabricated CLS circuit, including the schematic diagram of the experimental setup.

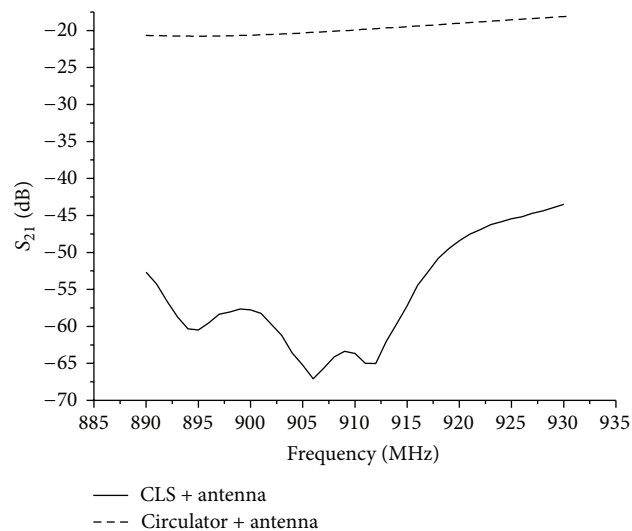


FIGURE 8: Isolation characteristics (S_{21}) of the fabricated CLS circuit and circulator.

The fabricated board of the proposed UHF RFID reader's front-end is shown in Figure 9. The main components and their specifications are listed in Table 1.

Figure 10 gives out both the test result and the measurement setup of testing the received signal by using circulator and CLS circuit, respectively. The output power at the Tx Test Point (PA output) is 20 dBm, and the distance between the tag and the antenna is 10 cm. In Figure 10(a) the CLS circuit in the fabricated frontend board shown in Figure 9 is disabled, and a circulator (MAFRIN0461) is added instead of the CLS circuit, the circulator's Port1 is connected to the Tx Test Point (PA output), the Port2 is connected to the antenna, and the spectrum analyzer (Agilent-E4440A) connected to the Port3 is used to measure the received signal. In Figure 10(b) the CLS circuit is enabled and the antenna

is connected to the Antenna Port of the board, while the spectrum analyzer is connected to the Rx test point1 (LNA input). Figure 10(c) is the testing results of (a) and (b). As it is shown in Figure 10(c), if the circulator is used instead of the CLS circuit, there is a very high carrier leakage signal (approximately 7 dBm) leaking into the Rx test point1 (LNA input), which can result in degrading the reader's sensitivity or even saturating the LNA. However when the CLS circuit is used and the control voltages of both the attenuator and phase-shifter are tuned manually to achieve the maximum cancellation, the carrier leakage reduces, about 50 dB. In addition, reading range measurement is setup in an open environment in the laboratory to see the reading distance by using the circulator and the CLS circuit, respectively. An Impinj's Monza 3 tag chip is used in the test. The tag, including

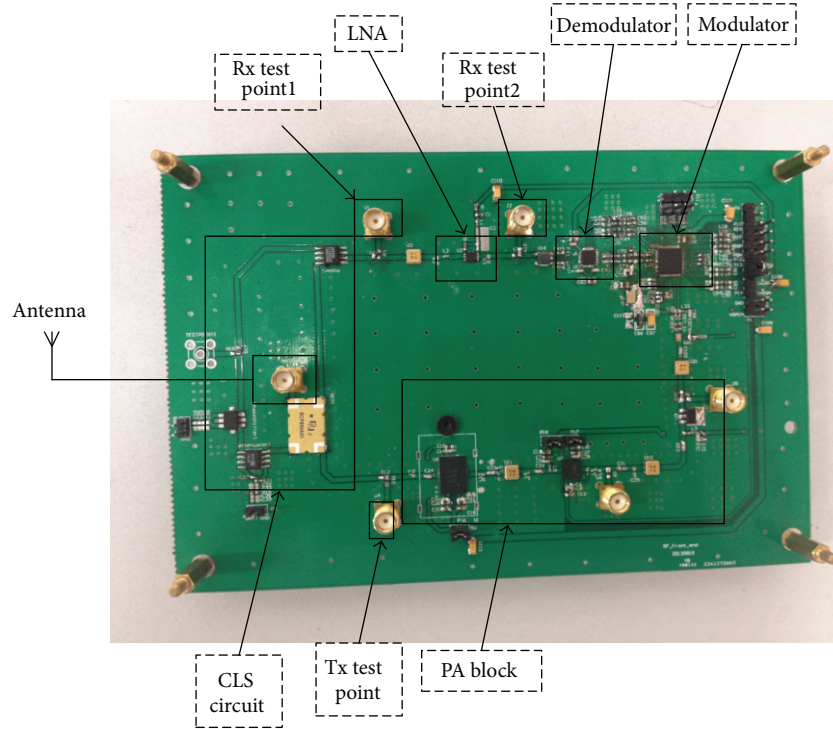


FIGURE 9: Photograph of the fabricated board.

TABLE 1: Summary of the components' specification.

| Part | Model | Specification |
|---------------------|------------|---|
| Modulator | ADF9010 | 3 dBm output power |
| Demodulator | ADL5382 | 14.7 input P1dB |
| Driver amplifier | AVT54689 | 17.8 dB gain and 17.2 dBm P1dB |
| VGA | HMC80110 | 13.5 dB gain with a control range of 53.5 dB, and 23.2 dBm P1dB |
| PA | ALM32120 | 14.3 dB gain and 34.4 dBm P1dB |
| LNA | ADL5521 | 20.8 dB gain with a NF of 0.8 dB, and 21.8 dBm P1dB |
| Directional coupler | RCP890A05 | 5 dB coupling and 23 dB isolation |
| Attenuator | AV101-12 | 30 dB attention |
| Phase shifter | PS094-315 | 80–110-degree phase shift range |
| Combiner | MAPDCC0001 | 0.5-degree phase balance |
| SAW | B3588U410 | 2.9 dB insertion loss |

the antenna, is attached on a plastic board, and is moved away from the reader's antenna by 5 cm steps. Table 2 gives out the summary of the reading distance. As can be seen from the measure result, with the help of the CLS circuit, the distance of the reading range has been improved by about 27%.

TABLE 2: Summary of the reading distance.

| Pout (dBm) | Reading distance (cm) | |
|------------|-----------------------|-----|
| | Circulator | CLS |
| 17 | 295 | 360 |
| 19 | 325 | 420 |
| 21 | 360 | 450 |
| 23 | 390 | 495 |

4. Conclusion

An UHF RFID reader's front-end with a new designed CLS circuit has been proposed. The front-end is based on zero-IF scheme and composed of discrete components in order to simplify the structure of the circuit and reduce cost. The CLS circuit consisted of a directional coupler and a magnitude and phase tuning circuit is used to improve the isolation between the transmitter and the receiver of the proposed UHF RFID reader's front-end.

The isolation between the Tx and Rx in the proposed CLS circuit used in the proposed UHF RFID reader's front-end has been improved more than 45 dB at the frequency point of 915 MHz and by at least 30 dB within 20 MHz band from the center by using the CLS circuit. Although the experimental result of the isolation performance in the proposed front-end is not so excellent as that of the CLS circuit itself, the improvement of the reader's sensitivity can be clearly seen from the reading distance increasing.

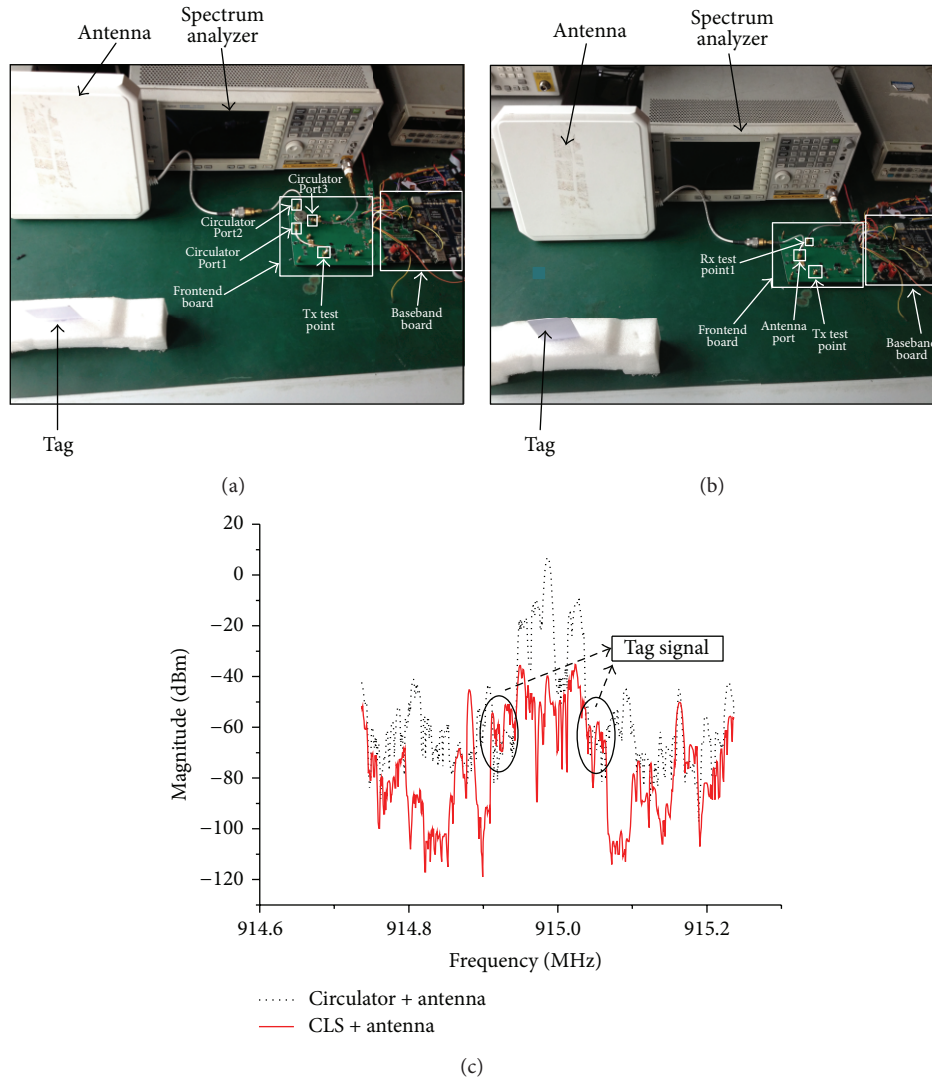


FIGURE 10: Measurement setup and testing result of the received signal of circulator and CLS circuit, respectively, at a Tx output power of 20 dBm; (a) measurement setup when testing the received signal by using circulator instead of CLS circuit; (b) measurement setup when testing the received signal by using CLS circuit; (c) testing result of (a) and (b).

Conflict of Interests

The authors declare that there is no conflict of interests regarding the publication of this paper.

Acknowledgment

This work was supported in part by Zhejiang Province Key Science and Technology Innovation Team (no. 2010R50010) and the Real-Time Anti-Theft System based on RFID technology (no. ZX130702307001).

References

- [1] H. Stockman, "Communication by means of reflected power," in *Proceedings of the IRE*, pp. 1196–1204, October 1948.
- [2] P. Bai, Y. Yin, and X. Yang, "A novel RX-TX front-ends for passive RFID reader with high isolation," in *Proceedings of the*

IEEE International Symposium on Microwave, Antenna, Propagation, and EMC Technologies for Wireless Communications (MAPE '07), pp. 332–335, August 2007.

- [3] J.-Y. Jung, C.-W. Park, and K.-W. Yeom, "A novel carrier leakage suppression front-end for UHF RFID reader," *IEEE Transactions on Microwave Theory and Techniques*, vol. 60, no. 5, pp. 1468–1477, 2012.
- [4] A. Safarian, A. Shamedi, A. Rofougaran, M. Rofougaran, and F. De Flaviis, "RF identification (RFID) reader front ends with active blocker rejection," *IEEE Transactions on Microwave Theory and Techniques*, vol. 57, no. 5, pp. 1320–1329, 2009.
- [5] W.-G. Lim, S.-Y. Park, W.-I. Son, M.-Q. Lee, and J.-W. Yu, "RFID reader front-end having robust Tx leakage canceller for load variation," *IEEE Transactions on Microwave Theory and Techniques*, vol. 57, no. 5, pp. 1348–1355, 2009.

Research Article

Cavity-Backed Dipole Antenna for Intelligent Lock Communication

Bo Yuan, Wen Wang, Xiao Hong Zhang, and Guo Qing Luo

The Key Laboratory of RF Circuits and System of Ministry of Education, Hangzhou Dianzi University, Hangzhou 310018, China

Correspondence should be addressed to Guo Qing Luo; luoguoqing@hdu.edu.cn

Received 13 September 2013; Accepted 23 October 2013

Academic Editor: Bing Liu

Copyright © 2013 Bo Yuan et al. This is an open access article distributed under the Creative Commons Attribution License, which permits unrestricted use, distribution, and reproduction in any medium, provided the original work is properly cited.

This paper introduces a $20 \times 40 \text{ mm}^2$ planar folded L-shaped dipole antenna operated under surroundings of an iron cavity for intelligent lock communication. The height of the slot antenna is shortened and the bandwidth for 2.4 GHz band has been widened. This antenna provides a solution for antenna surrounded by metal background. Good performances on return loss, radiation pattern are obtained over 2.4 GHz operating bands. The operation distance in front and back sides for the antenna has been calculated by Friis transmission equation.

1. Introduction

With the recent developments of wireless communication systems, the radiation antennas with unidirectional radiation pattern for cavity-backed applications are in great demand, such as substrate integrated waveguide (SIW) cavity-backed antenna or just metallic-backed surfaces or cavity in [1]. Cavity-backed slot antenna shows good characteristic. Luo et al. [2]. proposed a SIW cavity-backed slot antenna for 10 GHz. A lot of applications of cavity-backed slot antennas had been given in [3–5]. However, in practice, the shape of cavity behind the antenna is complex and even not complete. So, how to deal with this situation is really a challenge. On the other hand, the front-to-back ratio needs to be above 20 dB. So how to properly design the antenna and position the antenna is the second problem we need to solve. From Friis transmission equation, how to calculate the relationship between distances the antenna radiates and the input power is the third issue.

In this paper, we proposed a cavity-backed dipole antenna for intelligent lock application. The slot antenna for cavity-backed case cannot be used in our design; this is because the slot is too wide to be excited compared with [3–5]. Other kinds of independent antenna should be taken into account. When a metal is placed too near to the antenna, it will introduce a significant capacitance to its input impedance; thus, it will sharply reduce the bandwidth of the antenna, and

the resonant frequency of it will change [6]. So for balanced antenna, it does not excite the basic (ground) mode; we have to place it to the proper position and orientation and preserve enough distances from the metal (the iron cavity) to the antenna. Calculating the distances the antenna can radiate is practical for real life. By adopting Friis transmission equation, we calculated the front-to-back distance ratio; the antenna would work under the requirement of distance of 3 m and 20 cm in the front and back. The resonant frequency of the antenna is chosen to be 2.4 GHz band and the bandwidth of the antenna needs to be cooperated with CC2500 RF transceiver, so the bandwidth of the frequency needs to cover 2400.0 MHz~2483.5 MHz. As the remote sensor only has to transport password to the intelligent lock, the data volume is small, so the bandwidth and efficiency are not a key characteristic for this antenna. The size of the iron lock is $290 \times 70 \times 25 \text{ mm}^3$ and the thickness of the iron lock is 6 mm, so it has been hollowed with a space of $278 \times 58 \times 13 \text{ mm}^3$. The whole cavity has been considered as a reflector for the dipole antenna, while the cavity-backed slot antenna and SIW cavity-backed antenna have considered the whole cavity as a part of the antenna in [2–5]. For the properly designed target of unidirectional radiation pattern, we do not have to consider the iron cavity as a part of the antenna. However, for the strong coupling effect, a part of the energy has been coupled into the iron cavity, so the bandwidth has been narrowed; the efficiency would be reduced. We have

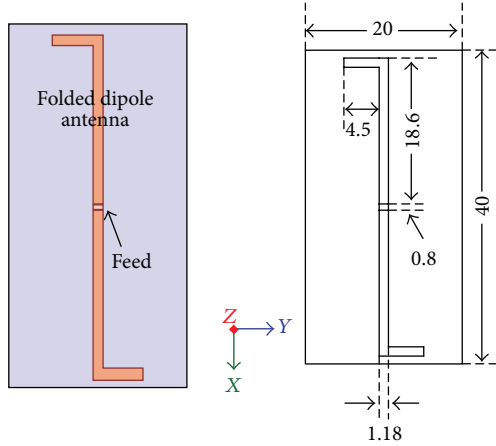


FIGURE 1: Configuration and dimensions of the proposed printed dipole antenna (unit: mm).

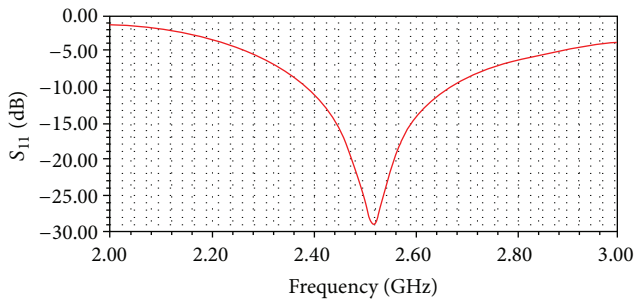


FIGURE 2: Simulated return loss for the proposed printed dipole antenna.

compared the results of the antenna with and without the iron cavity. This is also the drawback of the antenna. The antenna has been folded to two L-shapes to reduce the length of it.

2. Antenna Design and Analysis

For a simple planar dipole antenna working at 2.5 GHz band, the size of the antenna, the return loss, and its radiation pattern of xz and yz planes simulated by HFSS13 have been given in Figures 1, 2, and 3, respectively. From Figure 1, we can see that the size of the dipole antenna has been reduced to $40 \times 20 \text{ mm}^2$; the branch of the dipole has been folded to L-shape to reduce the length of the branch. The antenna is fabricated on a 1 mm thick FR4 substrate of relative permittivity 4.4 and loss tangent 0.02. From Figure 2, one can see that the central resonant frequency of the antenna is 2.5 GHz. The bandwidth is large enough to cover 2.4–2.65 GHz under 10 dB return loss. From Figure 3, one can get that the radiation pattern of the dipole antenna is omnidirectional. According to the geometry theory of diffraction (GTD), the corrugated ups and downs in Figure 3(b) are caused by the interference between the radiation field and the diffraction field [6].

When an iron cavity is placed at the back of the dipole antenna, the strong coupling effect would introduce a significant capacitance (reactance component) to the antenna input

impedance, which can cause the energy to be reflected at the antenna feeding terminals due to impedance mismatching to real impedance. On the other hand, the iron cavity would act as a reflector for the printed dipole antenna; the radiation pattern of the antenna would be unidirectional. The size of the iron cavity, the return loss of the printed dipole antenna, and the radiation pattern at 2.4 GHz have been given in Figures 4, 5, and 6, respectively.

In Figure 4, the size of the iron cavity is $290 \times 70 \times 25 \text{ mm}^3$, the thickness of the cavity is 6 mm, and the inner part of the cavity is hollowed. A $97 \times 58 \times 6 \text{ mm}^3$ window has been opened on the iron cavity. The printed dipole antenna is at the right side of the window. From Figure 5, one can see that the bandwidth of the dipole antenna has been narrowed compared with Figure 2; this is because that the energy has been coupled into the iron cavity, and the iron cavity introduces a capacitance (reactance component) to the antenna input impedance. On the Smith Chart the resonant frequency would be deviated from the central point. Although the distance between the antenna and the iron cavity is beyond the Fraunhofer region, the strong coupling effect cannot be ignored. The bandwidth of the antenna under the surrounding of an iron cavity is 2.4 GHz–2.48 GHz of 10 dB return loss. In Figure 6, the radiation pattern of the antenna becomes unidirectional, and the front-to-back ratio for the gain is nearly 28 dB.

3. Calculation

The Friis transmission equation can be expressed as follows in its simplest form [7]:

$$\frac{P_r}{P_t} = G_t G_r \left(\frac{\lambda}{4\pi R} \right)^2. \quad (1)$$

Given two antennas; P_r is the power available at the input of the receiving antenna, P_t is the output power of the transmitting antenna, where G_t and G_r are the antenna gains (with respect to an isotropic radiator) of the transmitting and receiving antennas, respectively, λ is the wavelength, and R is the distance between the antennas. To use the equation as written, the antenna gain may not be in units of decibels, and the wavelength and distance units must be the same. If the gain has units of dB, the equation is slightly modified to

$$P_r = P_t + G_t + G_r + 20 \log_{10} \left(\frac{\lambda}{4\pi R} \right). \quad (2)$$

Gain has units of dB, and power has units of dBm or dBW.

For front side and back side of our dipole antenna, we add f and b to the subscripts in (2). Equation (2) for front and back sides of the antenna becomes

$$P_{rf} = P_{tf} + G_{tf} + G_{rf} + 20 \log_{10} \left(\frac{\lambda}{4\pi R_f} \right), \quad (3)$$

$$P_{rb} = P_{tb} + G_{tb} + G_{rb} + 20 \log_{10} \left(\frac{\lambda}{4\pi R_b} \right), \quad (4)$$

where P_{rf} and P_{rb} are the receiving power in the front and back sides. P_{tf} and P_{tb} are the transmitting power in the front

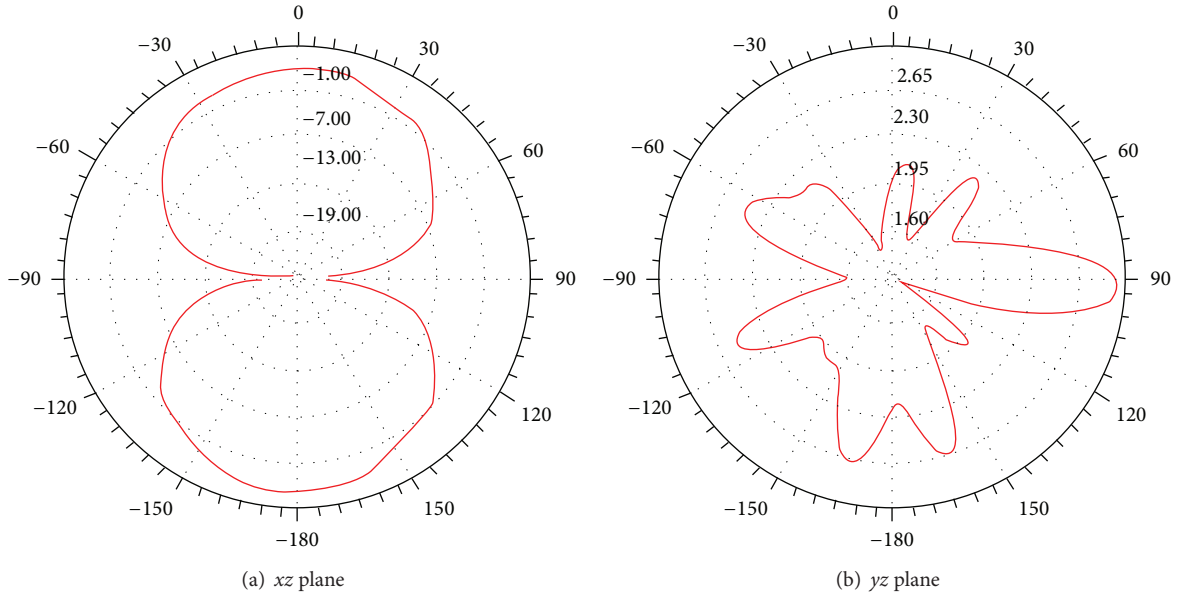


FIGURE 3: Simulated radiation patterns at 2.4 GHz.

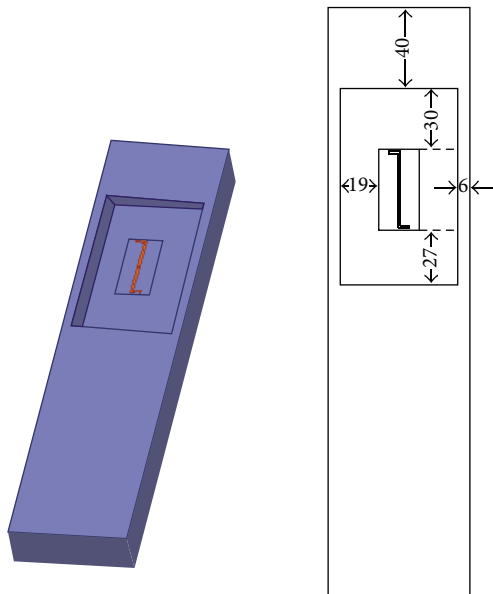


FIGURE 4: Configuration and dimensions of the proposed printed dipole antenna backed by an iron cavity (unit: mm).

and back sides. G_{tf} and G_{tb} are the transmitting antenna's gain in the front and back sides. G_{rf} and G_{rb} are the receiving antenna's gain in the front and back sides. R_f and R_b are the distances between the antennas in the front and back sides. Well, in our design, the antenna in remote sensor has fixed receiving power and gain in front and back sides, so $P_{rf} = P_{rb}$, $G_{rf} = G_{rb}$. The antenna in our design is the transmitting antenna for (2), the transmitting power for the front and back sides is equal, so $P_{tf} = P_{tb}$. However, from Figure 6, one can see that gain of the designed antenna in the front and back

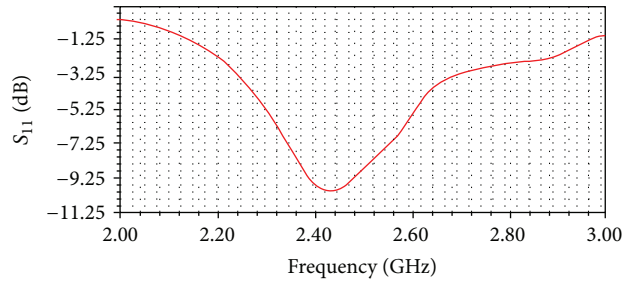


FIGURE 5: Simulated return loss for the proposed cavity-backed printed dipole antenna.

sides has 28 dB differences, so $G_{tf} - G_{tb} = 28$ dB. Subtract (4) from (3), one can get

$$G_{tf} - G_{tb} = 20 \log_{10} \left(\frac{R_f}{R_b} \right). \quad (5)$$

So, $R_f/R_b = 25$. The distances in front side between the antenna of remote sensor and antenna of our design are 25 times that in the back side. That means when one properly adjusts the transmitting power and receiving power of the antennas in the remote sensor and the intelligent lock, the distance for the front side can be tuned to 3 m, and then the distance for the back side is only 12 cm. It would be useful for the intelligent lock communication. The lock could be opened by the remote sensor in 3 m in the front side and could not be opened larger than 12 cm in the back side. This function is much useful and safer for the customers.

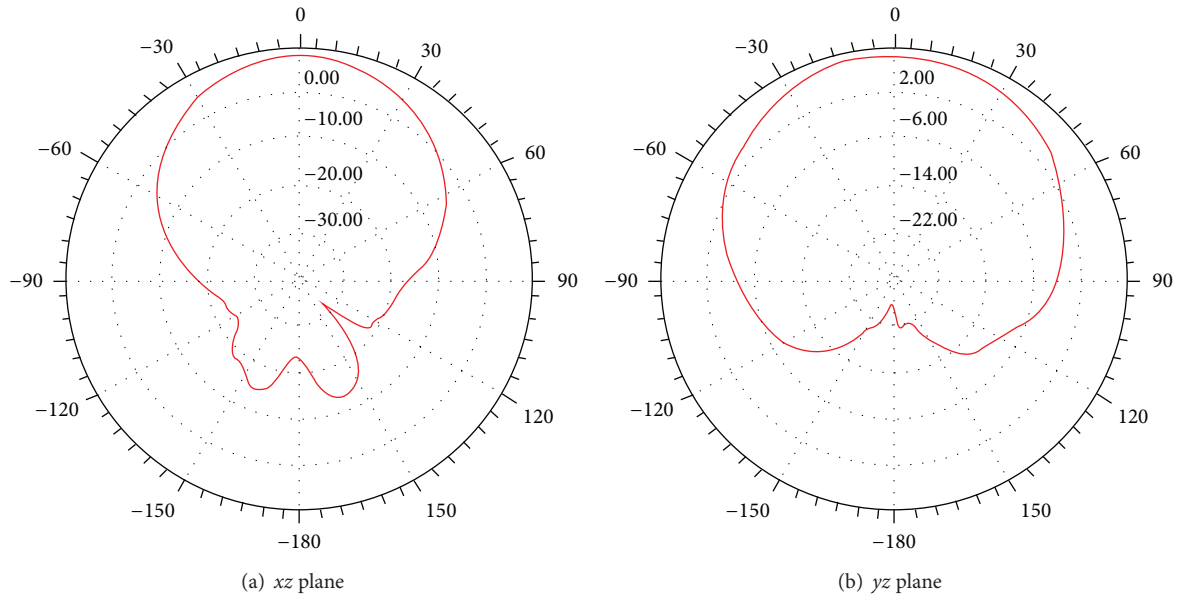


FIGURE 6: Simulated radiation patterns at 2.4 GHz.

4. Conclusion

In this paper, we introduced a printed dipole antenna backed by a special-shaped cavity for the intelligent lock communication. The difference between the traditional printed dipole antenna and the metal nearby dipole antenna has been discussed and explained. The distance for the front-to-back ratio has been calculated. This antenna shows good characteristic for wireless communication for the intelligent lock of unidirectional radiation pattern and enough bandwidth.

Acknowledgments

This work was supported in part by the National Basic Research Program of China under Contract 2010CB327403, the National Natural Science Foundation of China under Contract 61372020, and the Zhejiang Provincial Natural Science Foundation of China under Contract R1110003.

References

- [1] J. L. Wong and H. E. King, "A cavity-backed dipole antenna with wide-bandwidth characteristics," *IEEE Transactions on Antennas and Propagation*, vol. 21, no. 5, pp. 725–727, 1973.
- [2] G. Q. Luo, Z. F. Hu, L. X. Dong, and L. L. Sun, "Planar slot antenna backed by substrate integrated waveguide cavity," *IEEE Antennas and Wireless Propagation Letters*, vol. 7, pp. 236–239, 2008.
- [3] Y. Liu, Z. Shen, and C. L. Law, "A compact dual-band cavity-backed slot antenna," *IEEE Antennas and Wireless Propagation Letters*, vol. 5, no. 1, pp. 4–6, 2006.
- [4] B. Zheng and Z. Shen, "Effect of a finite ground plane on microstrip-fed cavity-backed slot antennas," *IEEE Transactions on Antennas and Propagation*, vol. 53, no. 2, pp. 862–865, 2005.
- [5] Q. Li and Z. Shen, "Inverted microstrip-fed cavity-backed slot antennas," *IEEE Antennas and Wireless Propagation Letters*, vol. 1, pp. 98–101, 2002.
- [6] B. Yuan, Y. Cao, G. Wang, and B. Cui, "Slot antenna for metal-rimmed mobile handsets," *IEEE Antennas and Wireless Propagation Letters*, vol. 11, pp. 1334–1337, 2012.
- [7] J. D. Kraus, *Antennas*, McGraw-Hill, New York, NY, USA, 2nd edition, 1988.

Research Article

Millimeter Wave on Chip Antenna Using Dogbone Shape Artificial Magnetic Conductor

Guo Qing Luo, Zheng Zheng Song, Xiao Hong Zhang, and Xiao Ping Hu

The Key Laboratory of RF Circuits and System of Ministry of Education, Hangzhou Dianzi University, Hangzhou 310018, China

Correspondence should be addressed to Guo Qing Luo; gqluo@emfield.org

Received 6 September 2013; Accepted 28 September 2013

Academic Editor: Yu Jian Cheng

Copyright © 2013 Guo Qing Luo et al. This is an open access article distributed under the Creative Commons Attribution License, which permits unrestricted use, distribution, and reproduction in any medium, provided the original work is properly cited.

An artificial magnetic conductor (AMC) applied in millimeter wave on chip antenna design based on a standard $0.18\ \mu\text{m}$ CMOS technology is studied. The AMC consisting of two-dimensional periodic dogbone shape elements is constructed at one metal layer of the CMOS structure. After its performance has been completely investigated, it has been used in an on chip dipole antenna design as an artificial background to enhance efficiency of the dipole antenna. The result shows that 0.72 dB gain has been achieved at 75 GHz when the AMC is constructed by a 4×6 dogbone array.

1. Introduction

In recent years, applications of millimeter-wave systems have great significance in communications, radar, guidance system, remote sensing technology, radio astronomy, and so on. Millimeter-wave band is defined as a spectrum from 30 GHz to 300 GHz, whose corresponding wavelength is from 10 mm to 1 mm. Millimeter-wave system researches were firstly started in the United States, Japan, Europe, and other advanced countries. In the past, millimeter-wave systems were used in the military and the scientific community. Now, they are widely used in commercial applications, such as automotive collision avoidance radar, local multipoint distribution services (LMDS), and local area networks (WLANs) [1–4]. Because of the short wave length in millimeter-wave band, millimeter-wave devices have small size, strong anti-interference, and other advantages.

Reflector antennas, horn antennas and lens antennas, are typically used for millimeter-wave antenna of the radio system [5–7]. Reflector antenna and horn antenna are mechanical structures and occupy large volumes. With the development of wireless communication and semiconductor technology, antenna on chip (AoC) was presented to meet the requirement of high integration and compact size. In this paper, a standard $0.18\ \mu\text{m}$ CMOS technology with six metal layers is used in AoC design. In order to avoid the

low radiation efficiency, the bottom metal layer cannot be used as the shield between the silicon dioxide layer and the silicon substrate. But most of the power will be dissipated in the silicon substrate as heat for its low resistivity and high permittivity. For instance, a 140 GHz on chip antenna implemented in 65 nm CMOS process by [8] has a gain of only -25 dB. Therefore, gain enhanced methods of AoC should be investigated.

Artificial magnetic conductor (AMC) inserted between antenna and the silicon substrate is presented in [9–12]. AMC can be adopted to redirect one-half of the radiation back to the opposite direction so that antenna gain can be enhanced to some extent. In this paper, an AMC composed of periodic dogbone shape conductors above a ground plane is placed underneath a dipole to improve the proposed on chip antenna performance.

2. Dogbone Shape AMC

The dogbone shape AMC, as a sort of the texture presented in [13], provides a good shielding and reflecting capability. Its shape and dimension are shown in Figure 1. Its equivalent circuit model provides an approximate method to calculate the magnetic resonant frequency of a ground-backed dogbone element. According to the equations, we can easily

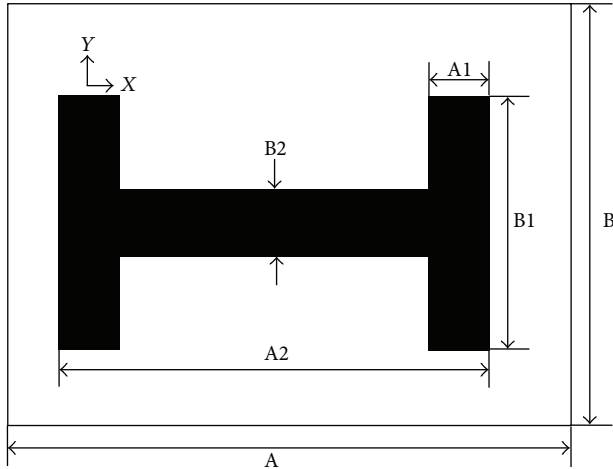


FIGURE 1: Geometrical configuration of a dogbone shape element.

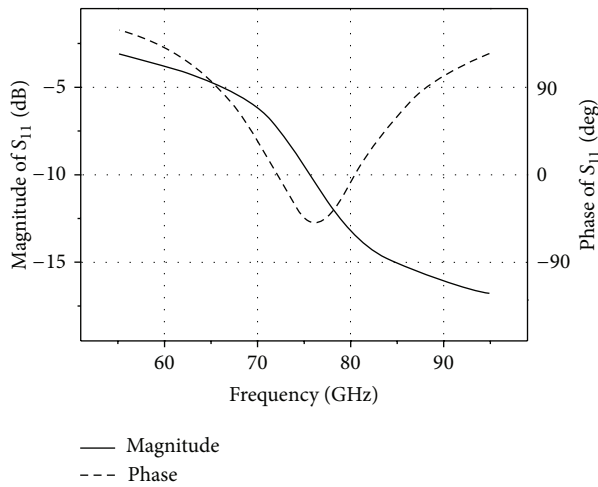


FIGURE 2: Magnitude and phase of reflection coefficient of the dogbone shape AMC.

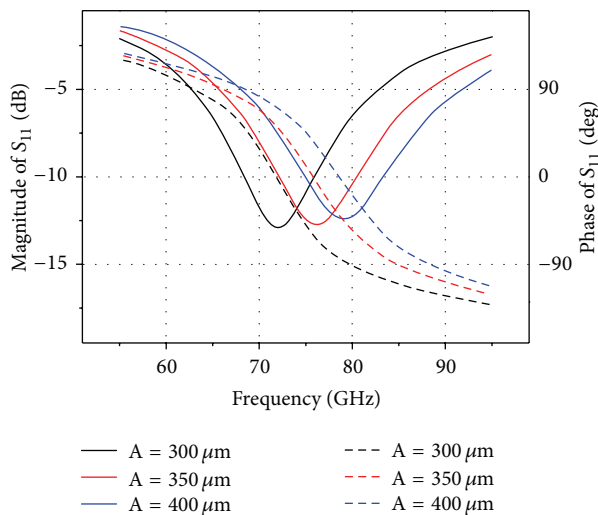


FIGURE 3: Magnitude and phase of reflection coefficient versus geometrical parameter A of the proposed AMC.

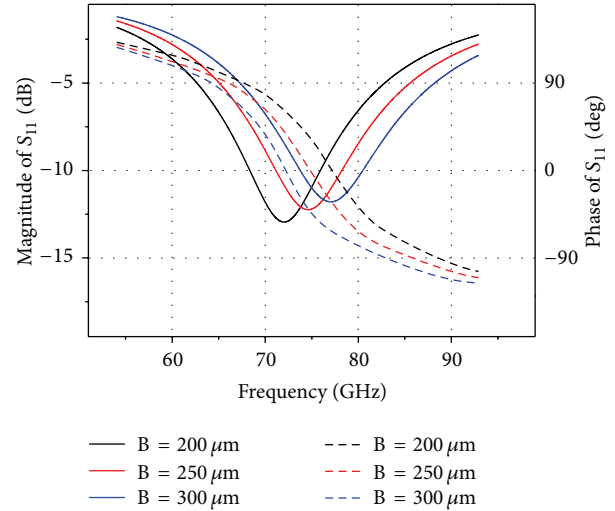


FIGURE 4: Magnitude and phase of reflection coefficient versus geometrical parameter B.

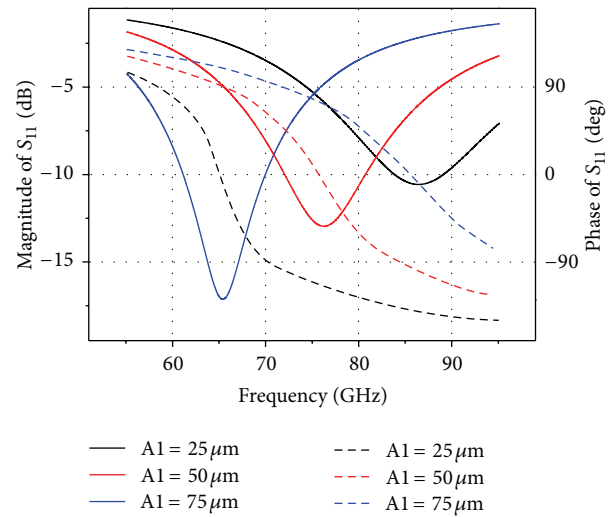


FIGURE 5: Magnitude and phase of reflection coefficient versus geometrical parameter A1.

get geometrical parameters of a dogbone element whose resonant frequency is 75 GHz.

A simulation setup of plane wave incidence on an AMC made by a periodic array of ground-backed dogbone unit cell with geometrical parameters of $A = 350$, $B = A2 = 250$, $C = B1 = 150$, $B2 = 20$, and $A1 = 50$ (unit: μm) has been done. Periodic boundary conditions are applied in the simulation. The magnitude and phase of the plane wave reflection coefficient are shown in Figure 2. From the figure, it can be found that the proposed structure acts as AMC within a frequency range ($-90^\circ < \text{phase} < 90^\circ$) from 67 to 83 GHz. Frequency responses of the proposed AMC varied with different geometrical parameters are shown in Figures 3, 4, 5, 6, 7, and 8. The proposed AMC operating frequency is mainly determined by the geometrical parameters of A1, A2,

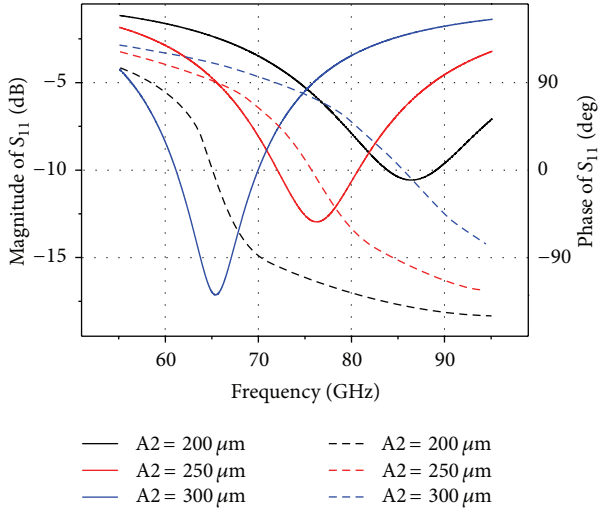


FIGURE 6: Magnitude and phase of reflection coefficient versus geometrical parameter A2.

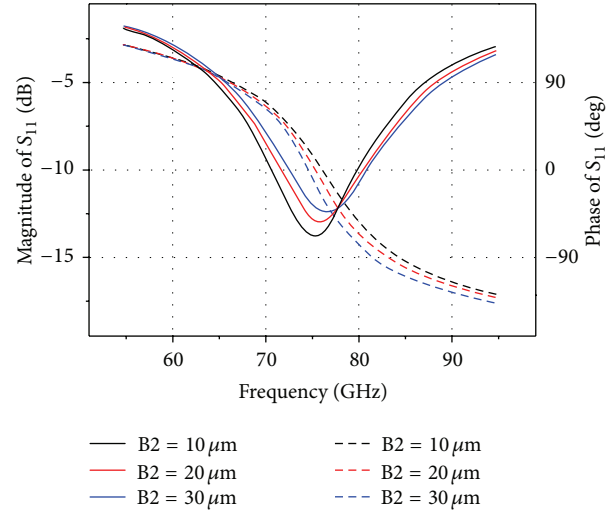


FIGURE 8: Magnitude and phase of reflection coefficient versus geometrical parameter B2.

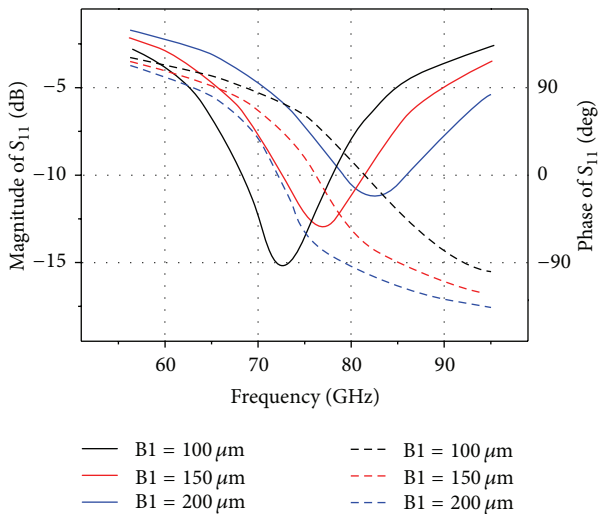


FIGURE 7: Magnitude and phase of reflection coefficient versus geometrical parameter B1.

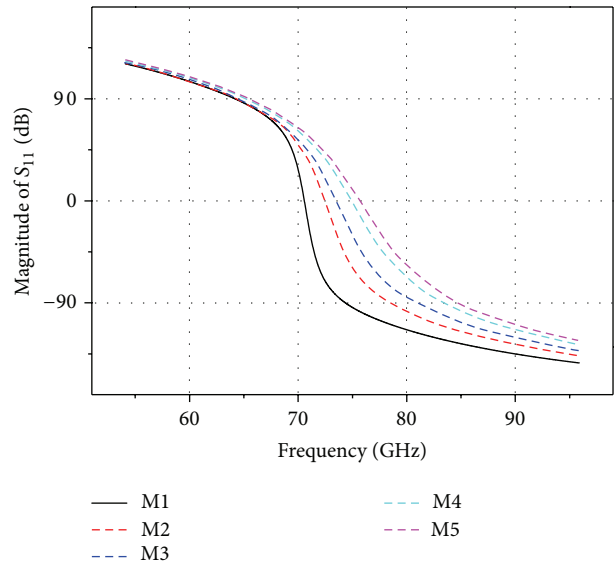


FIGURE 9: Variations of S_{11} phase when the AMC is constructed in CMOS different metal layers (from M1 to M5).

and B1, less determined by geometrical parameters of A, B, and B2.

As we can see, the influence of the structure parameters on S_{11} can be divided into three cases. For the magnitude of S_{11} , the cell size A and size B have similar influence. With increment of size A or B, the AMC operation frequency increases. Conversely, with increment of length A1, A2, or B1, the AMC operation frequency decreases. For the phase of S_{11} , with increment of size A, A1, or A2, the center operating frequency of the AMC increases. Conversely, with increment of length B or B1, the center operating frequency of the AMC decreases. However, the variation of width B2 has little influence on S_{11} , both its magnitude and phase.

3. On Chip Dipole Antenna

Figure 9 shows the phases of the reflection coefficient by implanting AMC into CMOS when its location is differed from M1 to M5. From the figure, it can be found that the AMC has the largest bandwidth when it is constructed in the M5 metal layer.

Figure 10 shows the configuration of a dipole antenna backed by the proposed AMC. The geometrical dimensions of the proposed AMC are shown in Figure 2. The dipole antenna is located on the top metal layer M6, while the AMC layer is located on M5. A metal ground plane is located on the bottom surface of the silicon substrate. The dipole length is $696 \mu\text{m}$.

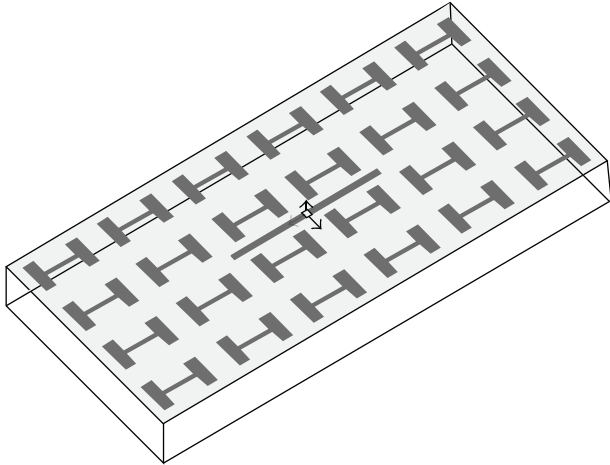


FIGURE 10: Dogbone shape AMC-backed dipole antenna.

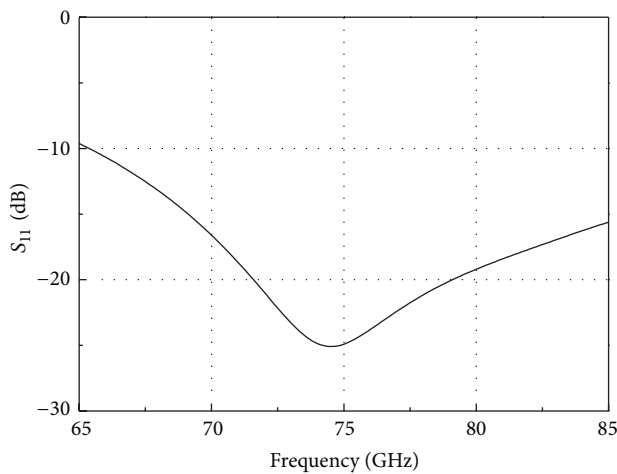
FIGURE 11: S_{11} of the proposed antenna.

TABLE 1: Realized gains of the proposed antenna backed by AMC with different element numbers.

| | 4 * 6 | 4 * 8 | 6 * 6 |
|---------------|----------|-----------|----------|
| Gain (75 GHz) | 0.72 dBi | -1.18 dBi | 0.24 dBi |

The antenna input reflection coefficient is plotted in Figure 11. Its matched input impedance bandwidth ($S_{11} < -10$ dB) is more than 20 GHz. Radiation patterns of the proposed antenna at 75 GHz are shown in Figure 12. Due to the perfect symmetry of the proposed antenna, its radiation patterns are symmetrical in both the E and H planes.

The proposed antennas whose AMC is constructed by different numbers of the dogbone shape element have been investigated. Their realized gains are listed in Table 1 when the dogbone shape array varies between 4*6, 4*8, and 6*6.

4. Conclusion

Artificial magnetic conductor (AMC) constructed by two-dimensional periodic dogbone shape element is applied in

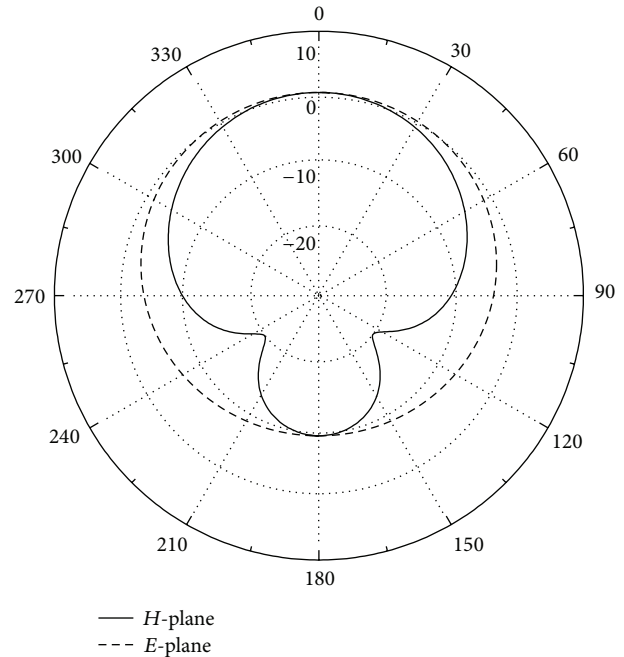


FIGURE 12: Radiation patterns of the proposed antenna.

millimeter-wave CMOS on chip dipole antenna design. The detailed frequency response of the proposed AMC has been completely studied. A gain of 0.72 dBi is realized at 75 GHz when the dipole antenna is backed by the proposed AMC with a 4*6 dogbone shape array.

Acknowledgments

This work was supported in part by the National Basic Research Program of China under Contract 2010CB327403, the NSFC under Contract 61372020, the FANEDD under Contract 201045, the NCET under Contract 09-0910, and the ZJNSF under Contracts R1110003 and Y1110992.

References

- [1] D. D. Falconer and J.-P. DeCruyenaere, "Coverage enhancement methods for LMDS," *IEEE Communications Magazine*, vol. 41, no. 7, pp. 86–92, 2003.
- [2] G. D. Wang and S. Halajian, "Processing methods enhance collision-warning systems," *Microwaves & RF*, vol. 36, no. 3, pp. 72–82, 1997.
- [3] H. H. Meinel, "Applications of microwaves and millimeterwaves for vehicle communications and control in Europe," in *Proceedings of the IEEE MTT-S International Microwave Symposium Digest*, vol. 2, pp. 609–612, June 1992.
- [4] C. O. McCaw, *Remarks at G-7 Information Society Conference*, Brussels, Belgium, 1995.
- [5] M. Cotp, "Crash avoidance FLR sensors," *Microwave Journal*, pp. 122–126, 1994.
- [6] E. O. Rausch, A. F. Peterson, and W. Wiebach, "Electronically scanned millimeter wave antenna using a Rotman lens," in *Proceedings of the Radar Edinburgh International Conference*, pp. 374–378, October 1997.

- [7] P. L. Lowbridge, "Low cost millimeter-wave radar systems for intelligent vehicle cruise control applications," *Microwave Journal*, vol. 38, no. 10, p. 7, 1995.
- [8] S. T. Nicolson, A. Tomkins, K. W. Tang, A. Cathelin, D. Belot, and S. P. Voinigesco, "A 1.2 V, 140 GHz receiver with on-die antenna in 65 nm CMOS," in *Proceedings of the IEEE Radio Frequency Integrated Circuits Symposium (RFIC '08)*, pp. 229–232, June 2008.
- [9] H. Chu, Y. X. Guo, F. Lin, and X. Q. Shi, "Wideband 60 GHz on-chip antenna with an artificial magnetic conductor," in *Proceedings of the IEEE International Symposium on Radio-Frequency Integration Technology (RFIT '09)*, pp. 307–310, Singapore, January 2009.
- [10] F. Lin and B. L. Ooi, "Integrated millimeter-wave on-chip antenna design employing artificial magnetic conductor," in *Proceedings of the IEEE International Symposium on Radio-Frequency Integration Technology (RFIT '09)*, pp. 174–177, Singapore, January 2009.
- [11] S. Pan, D. Wang, C. Guclu, and F. Capolino, "High impedance layer for CMOS on-chip antenna at millimeter waves," in *Proceedings of the IEEE International Symposium on Antennas and Propagation (APSURSI '11)*, pp. 903–906, Spokane, Wash, USA, July 2011.
- [12] P. Ying, M. A. Abdallah, and H. Zhirun, "A 60 GHz on-chip antenna with meta-material structure," in *Proceedings of the 28th National Radio Science Conference (NRSC '11)*, Cairo, Egypt, April 2011.
- [13] G. Donzelli, A. Vallecchi, F. Capolino, and A. Schuchinsky, "Metamaterial made of paired planar conductors: particle resonances, phenomena and properties," *Metamaterials*, vol. 3, no. 1, pp. 10–27, 2009.

Research Article

An AMC Backed Folded Dipole Slot Antenna Based on CMOS Process

Guo Qing Luo, Lin Qi Wu, and Xiao Hong Zhang

The Key Laboratory of RF Circuits and System of Ministry of Education, Hangzhou Dianzi University, Hangzhou 310018, China

Correspondence should be addressed to Guo Qing Luo; gqluo@emfield.org

Received 2 September 2013; Accepted 10 October 2013

Academic Editor: Bing Liu

Copyright © 2013 Guo Qing Luo et al. This is an open access article distributed under the Creative Commons Attribution License, which permits unrestricted use, distribution, and reproduction in any medium, provided the original work is properly cited.

A fold dipole slot antenna backed by artificial magnetic conductor (AMC) structure based on a standard 0.18 μm CMOS process on chip application is firstly proposed in this paper. Conventional silicon antenna on chip (AoC) suffers from low radiation performance because the most electromagnetic energy is restricted in silicon substrate as surface wave for its high dielectric permittivity. The energy is dissipated as thermal for low resistivity of silicon substrate. AMC constructed by a periodic 6×6 square patch array is adopted as background to improve radiation performance of the proposed folded dipole slot AoC. Gain of the proposed AMC backed AoC is improved about 3.5 dB compared with that of the same AoC without AMC background.

1. Introduction

Millimeter wave is a kind of electromagnetic wave whose frequency spectrum is from 30 GHz to 300 GHz and its corresponding wavelength varies from 10 to 1 mm. People pay more attention to the millimeter wave band according to the lack of available spectrum in radio frequency and microwave band. Different kinds of millimeter wave devices and systems have been exploited. Antenna, as an indispensable device of transmitting and/or receiving energy in wireless system, will directly affect performance of the whole wireless terminal system. With the development of wireless technology, people put forward higher requirements for the performance of antenna, which are specifically in the following areas: size reduction, broad bandwidth, multiband operation, and so forth. 140 GHz band is at the overlap of millimeter wave and terahertz wave (its frequency is 0.1~10 THz, wavelength is 3 mm~30 μm), whose development mainly depends on the technology of electronics. Terahertz is a band which is not completely recognized and explored by human beings. However, with the continuous development of stable terahertz sources during the past decade, recognition of terahertz communication increases gradually. Compared with microwave communication, the capacity of terahertz communication has a great promotion, which can support a high communication rate up to 10 GB/s. Terahertz wave

has better directivity, higher resolution and security, greater anti-interference ability, and smaller wavelength. Compared with optical communication, terahertz communication has a higher energy efficiency and a better penetrability.

For millimeter wave integrated circuit, CMOS technology is an excellent technical platform because it has the virtues of low cost, light weight, and so on. Recently antenna integration with RF front end circuit in a single wafer has been extensively investigated. Once the antenna integration realized successfully, the whole size of RF front end system will be very compact. Meanwhile, the interconnection loss between antenna and RF front end circuit will be greatly reduced. Therefore, the conception of antenna on chip (AoC) has been proposed. From the published literature it can be found that the forms of presented AoC are various [1–4]. A common problem of AoC is that its radiation efficiency is very low for the high dielectric constant and low resistivity of silicon substrate. Many ways can be used to improve AoC performance [5–10], such as removing silicon substrate under radiating element by micromachining, using ion implanting technology to increase silicon substrate resistivity. However, these improved methods need postprocessing, which will improve the cost. Therefore, high radiation efficiency antennas manufactured by the standard silicon process are the most required.

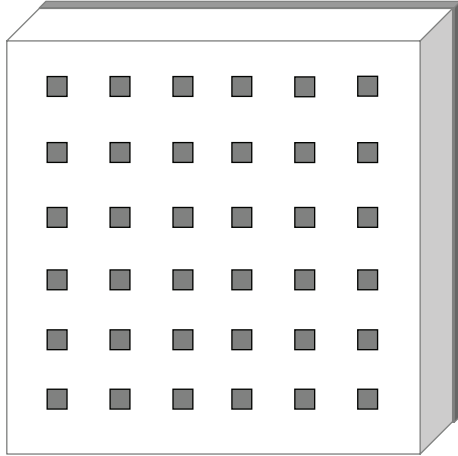


FIGURE 1: The proposed AMC structure.

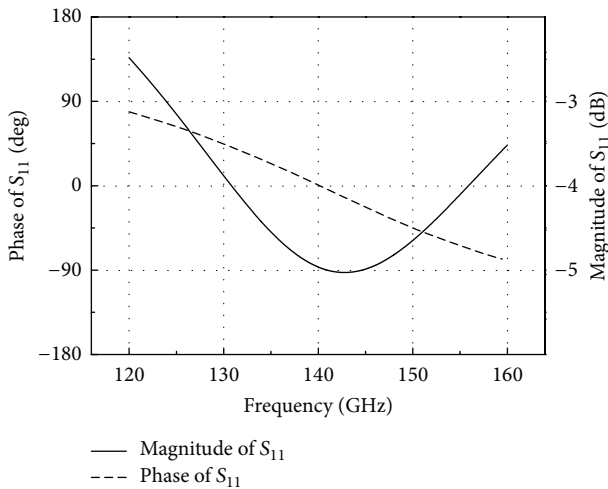
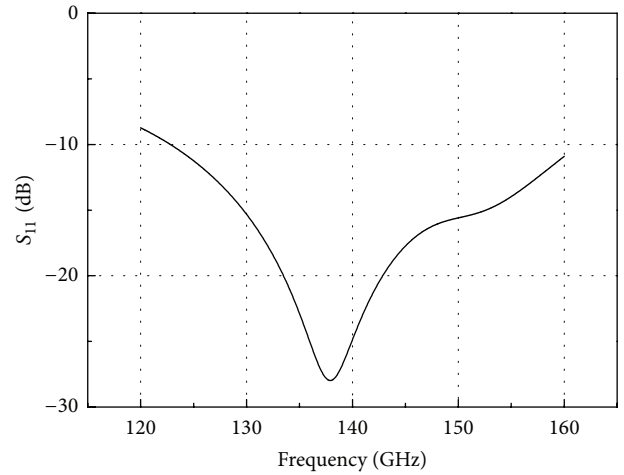


FIGURE 2: Phase and magnitude of reflection coefficient of the proposed AMC.

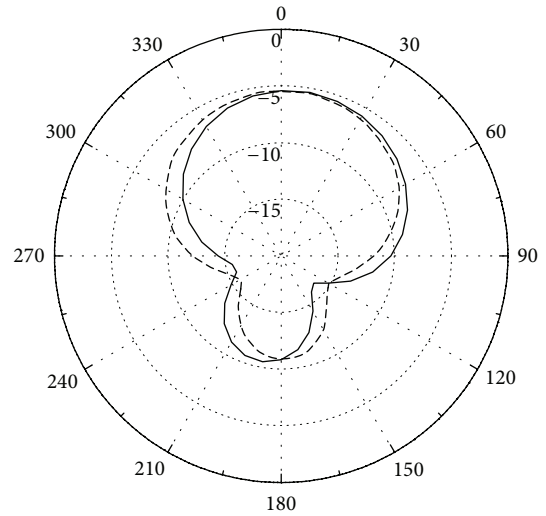
2. AMC

Artificial magnetic conductor (AMC), as a kind of periodic structure, has the same total reflection characteristic as that of perfect electric conductor (PEC) when they are excited by incident waves. A fundamental difference between these two materials is that AMC introduces a zero degree reflection phase shift to an incident wave but PEC introduces a 180-degree reflection phase shift to an incident wave. This special characteristic makes AMC suitable for application in low profile antenna design, in which efficiency of antenna will be improved if its radiating element is set more close to the AMC background.

Recently AMCs have been extensively used in low profile antennas and integrated antennas designs. In this paper, an AMC backed folded dipole slot antenna is proposed and investigated. The proposed AMC structure is plotted in Figure 1. It consists of three layers. The bottom layer is a full



(a)



— E-plane
 --- H-plane

(b)

FIGURE 3: (a) S_{11} of a folded dipole slot antenna without AMC. (b) Radiation pattern of a folded dipole slot antenna without AMC.

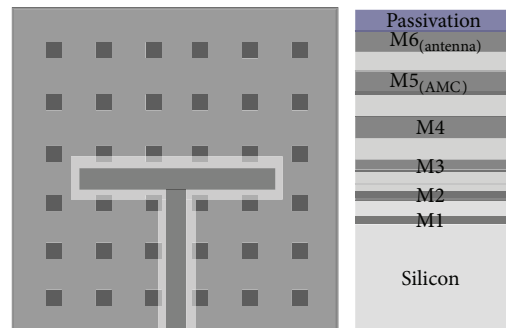


FIGURE 4: A folded dipole slot antenna backed by AMC.

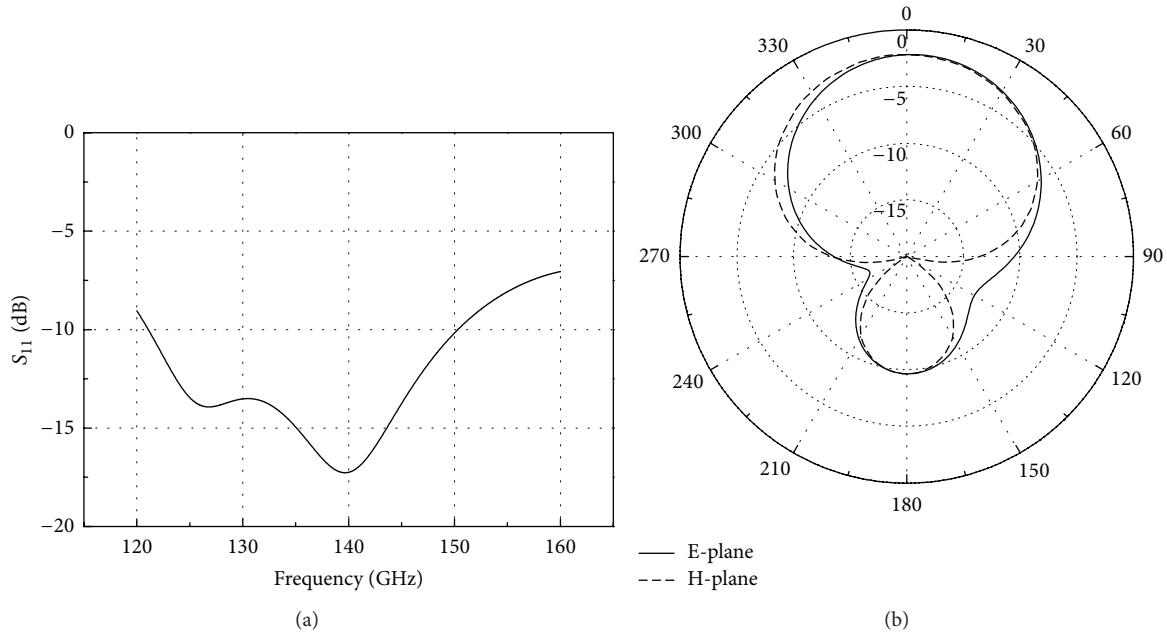


FIGURE 5: (a) S_{11} of a folded dipole slot antenna backed by AMC. (b) Radiation pattern of a folded dipole slot antenna backed by AMC.

metallic plane. The intermediate layer is a dielectric substrate layer. The top layer is a periodic square metallic patch array.

Frequency response of the proposed AMC is shown in Figure 2, in which it is calculated from that the AMC excited by a normally incident plane wave. From the phase and magnitude curves of the AMC reflection coefficient it can be found that the proposed AMC is operating at 140 GHz and its fractional operating bandwidth is about 25% (from 125 GHz to 160 GHz when phase varied from 90° to -90°). These results indicate that the proposed AMC can be used in low profile AoC designs.

3. AoC

A standard 0.18 μm CMOS process is employed in AoC design. The standard 0.18 μm CMOS structure consisted of six metal layers (copper or aluminum) and one polysilicon layer. There is silicon dioxide or its derivatives in metal layers with a relative dielectric constant of 4. There are two passivation layers above the top metal layer M6, which are silicon dioxide derivatives and silicon nitride. These two passivation layers are applied to prevent the whole circuit from oxidation and thus its performance deterioration. There is a doping silicon substrate about 290 nm thick below the polysilicon layer, whose relative dielectric constant is 11.9 and resistivity is about $10 \Omega\text{-cm}$. In particular, the conductivity of metal layers from M6 to M1 will gradually fade out. In order to maintain antenna performance the top metal layer M6 is usually used to fabricate the antenna.

In this paper AoC is a folded dipole slot, which is realized on the top metal layer (M6). The folded dipole slot antenna is fed by a 50 ohm coplanar waveguide. The proposed AoC without AMC background is firstly studied. Its frequency response and radiation performance are shown in Figure 3.

From these figures it can be found that the proposed AoC operates at 140 GHz with a matched impedance bandwidth more than 35 GHz. A peak gain of -5.5 dB and a back lobe level of -11 dB have been achieved. Radiation efficiency of the proposed AoC is very low because of the high loss characteristic of the silicon substrate. Most electromagnetic energy is restricted in the silicon substrate as surface wave and it is dissipated as thermal for the low resistivity of the silicon substrate.

In order to improve radiation efficiency of the proposed AoC, AMC is adopted as background inserted between the folded dipole slot antenna and the silicon substrate. Electromagnetic wave radiating from the antenna will be prevented propagating into the silicon substrate by the AMC background plane. Furthermore, this electromagnetic wave will be fully reflected by the AMC background without phase shift. It will be superposed with the positive radiating wave in phase and then a gain enhanced radiation is achieved.

Figure 4 shows a folded dipole slot antenna with an AMC background. The proposed AMC is constructed by a periodic 6×6 square patch array at the middle metallic layer M5. Its frequency response and radiation performance are shown in Figure 5. From these figures it can be found that the proposed AoC backed by AMC has a matched impedance bandwidth more than 29 GHz. A peak gain of -2 dB and a back lobe level of -10 dB have been achieved. Compared with AoC without AMC presented in Section 3, the peak gain of AoC with AMC has been improved about 3.5 dB. Its radiation efficiency has been enhanced more than 100%.

4. Conclusions

In this paper, an AMC backed AoC constructed by a standard 0.18 μm CMOS process is presented. The AoC is a folded

dipole slot antenna located at the top metal layer M6 and the AMC is constructed of a periodic 6*6 square patch array at the middle metal layer M5. By using AMC as background plane between the folded dipole slot antenna and the silicon substrate, peak gain of the proposed AoC has been improved about 3.5 dB and its radiation efficiency has been enhanced more than 100%.

Acknowledgments

This work was supported in part by the National Basic Research Program of China under Contract 2010CB327403, the National Science and Technology Major Project of China under Contract 2010ZX03007-001-01, the NSFC under Contract 61372020, the ZJNSF under Contract R1110003, and the FANEDD under Contract 201045.

References

- [1] K. T. Chan, A. Chin, Y. D. Lin et al., "Integrated antennas on Si with over 100 GHz performance, fabricated using an optimized proton implantation process," *IEEE Microwave and Wireless Components Letters*, vol. 13, no. 11, pp. 487–489, 2003.
- [2] C.-C. Lin, S.-S. Hsu, C.-Y. Hsu, and H.-R. Chuang, "A 60-GHz millimeter-wave CMOS RFIC-on-chip triangular monopole antenna for WPAN applications," in *Proceedings of the IEEE Antennas and Propagation Society International Symposium*, pp. 2522–2525, June 2007.
- [3] A. Babakhani, X. Guan, A. Komijani, A. Natarajan, and A. Hajimiri, "A 77-GHz phased-array transceiver with on-chip antennas in silicon: receiver and antennas," *IEEE Journal of Solid-State Circuits*, vol. 41, no. 12, pp. 2795–2805, 2006.
- [4] C.-S. Wang, J.-W. Huang, S.-H. Wen, S.-H. Yeh, and C.-K. Wang, "A CMOS RF front-end with on-chip antenna for V-band broadband wireless communications," in *Proceedings of the 33rd European Solid State Circuits Conference*, pp. 143–146, September 2007.
- [5] S. Pan and F. Capolino, "Design of a CMOS on-chip slot antenna with extremely flat cavity at 140 GHz," *IEEE Antennas and Wireless Propagation Letters*, vol. 10, pp. 827–830, 2011.
- [6] S. Pan, D. Wang, and F. Capolino, "Novel high efficiency CMOS on-chip antenna structures at millimeter waves," in *Proceedings of the IEEE International Symposium on Antennas and Propagation (APSURSI '11)*, pp. 907–910, July 2011.
- [7] E. Öjefors, H. Kratz, K. Grenier, R. Plana, and A. Rydberg, "Micromachined loop antennas on low resistivity silicon substrates," *IEEE Transactions on Antennas and Propagation*, vol. 54, no. 12, pp. 3593–3601, 2006.
- [8] B. Biglarbegan, M. R. Nezhad-Ahmadi, C. Hoggat, S. Hose, M. Fakhrazadeh, and S. Safavi-Naeini, "A 60 GHz on-chip slot antenna in silicon integrated passive device technology," in *Proceedings of the IEEE Antennas and Propagation Society International Symposium (APSURSI '10)*, pp. 1–4, July 2010.
- [9] A. Fonte, S. Saponara, G. Pinto, and B. Neri, "Feasibility study and on-chip antenna for fully integrated μ RFID tag at 60 GHz in 65 nm CMOS SOI," in *Proceedings of the IEEE International Conference on RFID-Technologies and Applications (RFID-TA '11)*, pp. 457–462, September 2011.
- [10] S. Pan, D. Wang, C. Guclu, and F. Capolino, "High impedance layer for CMOS on-chip antenna at millimeter waves," in *Proceedings of the IEEE International Symposium on Antennas and Propagation (APSURSI '11)*, pp. 903–906, July 2011.

Review Article

Review of Low Profile Substrate Integrated Waveguide Cavity Backed Antennas

Guo Qing Luo, Tian Yang Wang, and Xiao Hong Zhang

Microelectronic CAD Center, Hangzhou Dianzi University, Hangzhou 310018, China

Correspondence should be addressed to Guo Qing Luo; gqluo@emfield.org

Received 12 September 2013; Accepted 12 October 2013

Academic Editor: Bing Liu

Copyright © 2013 Guo Qing Luo et al. This is an open access article distributed under the Creative Commons Attribution License, which permits unrestricted use, distribution, and reproduction in any medium, provided the original work is properly cited.

Low profile cavity backed antennas (CBA) based on substrate integrated waveguide (SIW) technology presented in published papers have been reviewed in this paper. Their operating mechanisms have been discussed and methods for improving the performance, such as bandwidth enhancement, size reduction, and gain improvement, have been presented. These novel antennas retain the advantage of conventional metallic cavity backed antenna, including high gain, high front-to-back ratio, and low cross polarization level, and also keep the advantages of planar antenna including low profile, light weight, low fabrication cost, and easy integration with planar circuit.

1. Introduction

Conventional metallic cavity backed antennas (CBA) have been extensively presented for their satisfactory radiation performances [1, 2]. Figure 1 shows the classical conventional CBA, and the depths of their metallic backed cavities are roughly one-quarter wavelength. Their bulky volumes make the conventional metallic CBA not suitable for some practical applications.

Substrate integrated waveguide (SIW) technique has been developed to design microwave and millimeter wave components and subsystems. SIW structure keeps the advantages of conventional metallic waveguides, such as high Q-factor, high selectivity, cutoff frequency characteristic, and high power capacity. It also has the advantages of low profile, light weight, conformability to planar or curved surfaces, and easy integration with planar circuits. In order to achieve low profile CBA, SIW is firstly adopted into CBA designs [3–5]. The backed cavity can be realized by using metallized via arrays through a single or multilayer substrate (referred to as SIW). In order to make the SIW cavity equivalent to the conventional metallic cavity, the conditions of $d/d_p \geq 0.5$ and $d/\lambda_0 \leq 0.1$ must be satisfied, where d , d_p , and λ_0 are the metallized vias diameter, the spacing between two neighboring vias, and the free space wavelength, respectively.

SIW cavity backed antennas are generally comprised of two types: SIW cavity backed patch antenna (shown in Figure 2(a)) and SIW cavity backed slot antenna (shown in Figure 2(b)). Both of these low profile SIW cavity backed antennas cannot only be fed by planar transmission lines such as microstrip line, coplanar waveguide (CPW), and grounded coplanar waveguide (GCPW) but also be fed by non-planar transmission lines such as probe and waveguide. In this paper, SIW cavity backed antennas, with different configurations, different feeding structures, and different performances, presented by international researchers are reviewed and their performance improvement methods are also discussed.

2. SIW Cavity Backed Antenna

SIW used in antenna design was firstly introduced in [6], in which SIW slot array antennas were designed similar to classical slotted waveguides antennas by etching longitudinal slots on the top metal surface of their substrates. SIW cavity backed antennas were also firstly presented in [3] with the form of cavity backed slot antenna.

SIW cavity backed slot antenna with linearly polarized performance was proposed in [4], in which a $50\ \Omega$ GCPW line is adopted as a feeding element to stimulate a square SIW

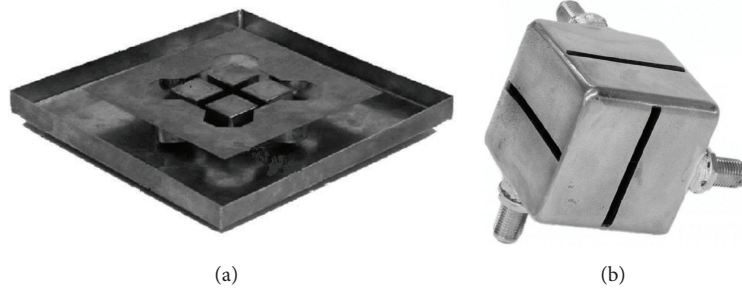


FIGURE 1: Conventional metallic cavity backed antennas.

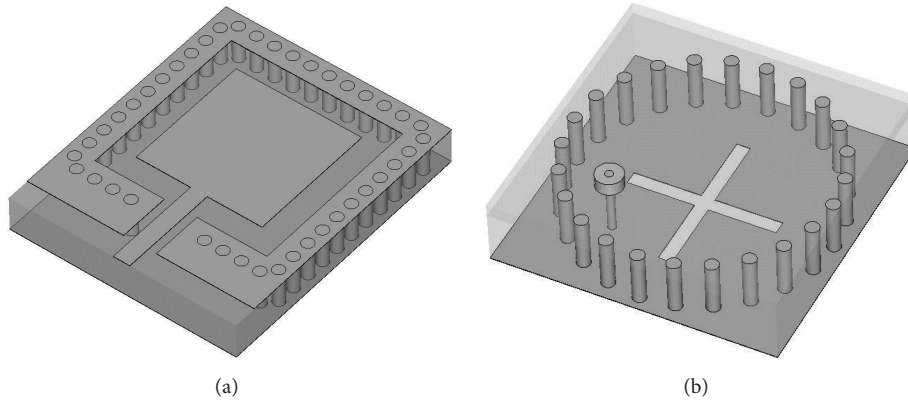


FIGURE 2: Low profile SIW cavity backed antennas: (a) patch antenna; (b) slot antenna.

backed cavity and a resonating slot etched at the center of the SIW backed cavity metal surface is used as the radiating element. When the square SIW cavity was in TE_{120} resonating mode, the dominant electric field at the two sides of the slot has opposite phase. Then, there is transverse electric field across the slot and thus energy can radiate into space by the slot. Another linearly polarized SIW cavity backed slot antenna was proposed in [7]. Its radiation was generated from a rectangular one point shorted slot when the antenna was fed by a coax-to-SIW transition. The concept of SIW cavity backed slot antenna applied in on-chip antenna design was investigated in [8], in which a fully on-chip antenna operating at 140 GHz was fabricated with a standard CMOS technology. Its radiating slot was backed with an extremely thin cavity formed by two CMOS inner metal layers and the through metal via arrays. The SIW backed cavity prevents radiation from going into the lossy silicon substrate. Its radiation efficiency of 18% and gain of -2 dB were achieved, which has an evident enhancement compared with those of conventional silicon on chip antennas. A dual frequency dual linearly polarized SIW cavity backed slot antenna was studied in [9]. A crossed slot, whose arms are parallel to the rectangular SIW cavity edges, is etched at the center of one SIW backed cavity metal surfaces. A single GCPW located at one diagonal line of the SIW cavity is employed as the feeding element to stimulate the cavity. When two cavity modes TE_{120} and TE_{210} were successfully excited, radiation from each arm was generated at a different frequency and each one has a different linear

polarization. As one of the most important parameters of a dual frequency antenna, the frequency ratio r_f of the proposed antenna is less than 2.

SIW cavity backed slot antennas with circularly polarized radiation were firstly discussed in [3, 5, 9], whose SIW backed cavity with two dimensions rotational symmetries was requisite. Crossed slot at the center of one metal surface of the SIW backed cavity was adopted as a radiating element. A single GCPW or probe located at one diagonal line of the crossed slot was used to excite the cavity. In order to simultaneously excite the two degenerate modes in the cavity by a single feed, a small perturbation of lengths of the crossed slot two arms must be introduced. When two orthogonal degenerate cavity modes (TM_{110} or TE_{120} and TE_{210}) were successfully excited, circularly polarized radiation was produced by tuning the two arms' length difference to achieve a 90° phase difference between the radiations from the two arms. A SIW fed SIW cavity backed ring slot antenna for circularly polarized application was presented in [10]. Its circularly polarized radiation was generated by shorting the top patch and bottom ground plane using via. A broadband impedance matching was accomplished by inserting inductive via arrays at the input port. An X-band circularly polarized SIW cavity backed square ring slot antenna was proposed in [11], whose circularly polarized wave was generated by a combination of a shortened square ring slot etched in the SIW top wall and a shorting via placed between the area bounded by the ring and the SIW bottom wall.

Another type of SIW cavity backed antenna was developed in [12]. The proposed SIW cavity backed patch antenna was comprised of a stack of two substrates, a microstrip substrate, and a cavity substrate. A square patch was printed on the microstrip substrate and fed by a microstrip line. The ground of the microstrip substrate and the top layer of the cavity substrate had a circular opening underneath the patch. Circular SIW backed cavity was constituted by metallized via array spaced along the circular opening. The proposed antenna exhibits a high-efficiency performance with an aperture radiation efficiency of better than 70% over a wide frequency range. A simple SIW cavity backed patch antenna presented by the same authors is shown in [13], which was fully constructed on a single substrate. A probe fed square patch was printed on the top conductor layer of the microstrip substrate and the top conductor layer also had a square opening around the patch. Metallized via arrays spaced along the square opening constituted the SIW cavity to back the radiating patch. The proposed antenna had a higher aperture radiation efficiency of 80% and a higher gain had been achieved.

SIW cavity backed patch antenna with circularly polarized radiation was proposed in [14]. Its circular polarization was generated by a conventional perturbed circular patch with a shorted-end via. The SIW cavity is used as a background to get a higher gain and a lower back lobe radiation. The proposed antenna was fed by SIW with an impedance matching network integrated with an asymmetric inductive diaphragm using via arrays and a broadband-matched impedance bandwidth of 17.32% had been achieved. A broad circularly polarized SIW fed patch antenna with 3 dB axial bandwidth of 7.1% was investigated in [15]. The proposed antenna comprised of two layers, the top patch layer and the bottom SIW layer. The metal sheet between these two layers is a ground plane for the patch. The patch is fed from the waveguide through two apertures at the ground plane by two probes. Circular polarization was produced with a proper choice of the locations of the two probes.

3. Bandwidth Enhancement of SIW CBA

Low profile SIW cavity backed antennas have a drawback of narrow bandwidth for their compact sizes. Bandwidth-enhanced method should be studied in order to make them suitable for practical applications. A bandwidth-enhanced linearly polarized SIW cavity backed slot antenna was presented in [16], which was a single GCPW fed rectangular SIW cavity backed long slot antenna. The long slot was a completely matching slot other than the previously used resonating slot and its length is far more than a half resonant wavelength. After properly setting, two hybrid modes can be excited in the SIW cavity, which were two different combinations of the TE_{110} and TE_{120} resonances. One is a combination of a strong TE_{110} resonance and a weak TE_{120} resonance and the other is a combination of a strong TE_{120} resonance and a weak TE_{110} resonance. Although the fields distributing at the two sides of the slot are in phase, their huge magnitude difference also can make the slot radiate electromagnetic wave. Radiations generated from the two hybrid modes

are consistent because their equivalent currents distributed in the slot are nearly the same. Compared with those of the previously presented SIW cavity backed slot antenna, fractional impedance bandwidth of the proposed antenna was improved about 4 times. Its gain and radiation efficiency are also slightly improved about 0.6 dB and 8%, respectively. Its SIW cavity size is reduced about 30%. A probe fed SIW cavity backed slot antenna using a via hole above the slot was studied in [17]. Two parallel cavity edges of the rectangular SIW backed cavity had a same quarter-wavelength length in the direction of perpendicular to the slot. A dog-bone shape half wavelength slot was used for an inductive loading of the slot to decrease the slot length. A via hole was placed above the slot for the dual resonance and then a 60% bandwidth had been achieved. Instead of using a via hole above the slot, the removal of the substrate underneath the slot also can be used to broaden the matched impedance bandwidth of an SIW cavity backed slot antenna [18]. When the substrate underneath the dog-bone shape slot was removed, the quality factor of the antenna resonator decreased and then a bandwidth enhancement of 24% and a radiation efficiency improvement of 6.2% had been achieved. A wideband SIW backed wide slot antenna was proposed in [19], which consisted of an aperture for radiating on the top surface of the top substrate and two rectangular SIW cavities with different sizes for mode generating and coupling that is embedded in the multilayer substrate. It exhibited a measured matching impedance bandwidth of 12.1%.

A broadband SIW cavity backed patch antenna was developed in [20], which was a coplanar stripline (CPS) fed SIW cavity backed folded dipole antenna. By observing the magnetic field distribution figures, it can be found that an additional half open cavity resonance was introduced besides the folded dipole inherent resonance. The proposed antenna had a broadband fractional matching impedance bandwidth of more than 30% by tuning the two different resonances. Radiations generated by these two resonances were also consistent. A bandwidth enhanced SIW cavity backed patch array was presented in [21]. The proposed array consisted of two stacked substrates. Patch elements were printed on the top microstrip substrate and the SIW backed cavities were constructed by many via holes spaced along circular openings at the bottom cavity substrate. The bottom metal surface of the microstrip substrate and the top metal surface of the cavity substrate had common circular openings underneath the patch. The top microstrip substrate was kept thin in order to minimize the surface wave and the associated feeding network losses. The bottom cavity substrate was relatively thick for bandwidth enhancement. Since the required fractional matching impedance bandwidth of the proposed antenna was inversely proportional to the square root of the dielectric constant, increment of the bottom cavity substrate thickness was used to improve bandwidth. As SIW cavity backed E-shape patch antenna was introduced in [22], which comprised of two substrates with three metal layers. The SIW cavity was formed by metallized via arrays through two substrates and two metal layers at the top and bottom surfaces of the stack structure. The E-shape radiating patch was on the top metal layer. The feeding structure, which is located on the middle metal layer,

consisted of a feeding via, a feeding stripline, and tunable loaded stubs. The bottom metal layer is a conductor ground plane. Measured results showed that the proposed antenna element had a wide impedance bandwidth of 10.9%.

The fractional 3 dB axial ratio (AR) bandwidth of a low profile single fed circularly polarized SIW cavity backed antenna is far less than its fractional matching impedance bandwidth. Three dB AR bandwidth becomes the major factor which limits the operating bandwidth of a single fed circularly polarized SIW cavity backed antenna. In order to increase the operating bandwidth, it is preferable to employ multifeed configurations such as a series feed and a parallel feed as feeding networks. A T-junction power divider with equal magnitude and 90° phase difference outputs was adopted as the two-point parallel feed to excite a single SIW cavity backed cross slot antenna [23]. Its measured 3 dB AR bandwidth was about two times that of a single point fed SIW cavity backed cross slot antenna. A dual circularly polarized SIW cavity backed cross slot antenna was proposed in [24], in which the single SIW cavity was stimulated by a branch line coupler. The hybrid coupler generated two signals with equal magnitude and quadrature phase. So, it was not only used to improve the AR bandwidth, but also used to obtain the dual circularly polarized radiation. Right-hand circularly polarized or left-hand circularly polarized radiation can be easily achieved by selecting one port as the feed port while terminating the other port with a matched load. Sequential rotated feeding scheme is another widely used feeding network to improve 3 dB AR bandwidth of circularly polarized antenna array. Four linearly polarized SIW cavity backed slot antennas fed by a microstrip sequential rotated feeding network were presented in [25] and four circularly polarized SIW cavity backed ring slot antennas fed by a SIW sequential rotated feeding network were presented in [26]. By using these multipoint parallel feeding schemes, great enhancement of 3 dB AR bandwidths and evidently improvement of circular polarization purity were achieved.

4. Size Reduction of SIW CBA

The cavity size of a normal SIW cavity backed antenna is about $0.5\lambda_0 * 0.5\lambda_0$, which is not suitable for array application. Miniaturization of a radiating slot, as one of the popular size reduction methods of SIW cavity backed antennas, had been investigated by many researchers. A size-reduced SIW cavity backed slot antenna had been proposed in [27], whose slot consisted of a pair of meandered slots. Its size reduction of 50% was accomplished by inserting a capacitive element into the SIW cavity, which leads the increment of the stored electric energy and nearly unaffected the stored magnetic energy. A cylindrical metal post, through the thickness of the cavity and aligned parallel to the electric field, was implemented as the capacitive element. The post was isolated from the top metal surface of the SIW cavity by using a ring slot. A miniaturized SIW cavity backed slot antenna with dual polarized radiation was discussed in [28]. Two orthogonal feeding lines, which were directly connected to the antenna slot, were used to excite the SIW cavity and to provide the impedance conversion. The two ports are perpendicularly placed to

generate two orthogonal polarizations. The size reduction was achieved by meandering the slot line. Another miniaturized SIW cavity backed meandered slot antenna array was shown in [29]. The meandered slot acted as a left-handed (LH) capacitor and vias constructing SIW acted as LH inductors. Their cooperation led to a negative resonance existence in the SIW cavity. Electromagnetic waves propagate below the cutoff frequency of the fundamental mode, which leads to the reduction of the antenna size. Mutual coupling between two adjacent elements of the proposed miniaturized SIW backed meandered slot antenna array was significantly small.

Another popular size-reducing method of SIW cavity backed antennas is achieved by cavity size reduction. A super compact SIW cavity backed slot antenna was introduced in [30]. The backed cavity was miniaturized by folding the cavity using multilayer substrate and meandering the passage from the bottom of the cavity to the radiating slot. A size-reduced cavity backed antenna was proposed in [31] by using half mode substrate integrated waveguide (HMSIW) technique. The backed cavity of the antenna is triangular in shape, which was realized by metallized vias array through the substrate, the bottom ground plane, and the top triangular patch. This triangular cavity was a half mode cavity in which the field distribution was almost half of that in the original SIW cavity. The resonating frequency of the proposed triangular HMSIW cavity is equal to that of its corresponding square SIW one. Radiating field was generated by dominant TE_{110} cavity mode through a dielectric aperture created by HMSIW. The proposed antenna was reduced to half of its corresponding SIW cavity backed antenna. A quarter-mode substrate integrated waveguide (QMSIW) cavity backed antenna also had been reported in [32]. The QMSIW cavity was the quadrant sector of a square SIW cavity, which is realized by bisecting the HMSIW cavity into two parts along the fictitious quasi-magnetic wall. The QMSIW cavity preserved the field distribution of an SIW cavity and leaky wave was achieved from the dielectric aperture. The size of the proposed antenna was about 25% of that of counterpart SIW cavity backed antenna.

A wearable SIW cavity backed slot antenna was presented in [33], which was implemented with textile materials. The cavity substrate was closed-cell expanded rubber protective foam typically used in firefighter suits. Its top and bottom metal layers were implemented using a conductive fabric. The proposed textile antenna exhibited high robustness against bending and low influence on the human body, and suited for on-body use. Another wearable textile antenna was proposed in [34] based on an HMSIW cavity. Its top and bottom metal surfaces were formed of silver-coated fabric and HMSIW cavity was implemented through via-walls made of a conductive yarn. The antenna radiated through a thin aperture. The ground plane provided a good isolation for the human body in wearable application.

5. Gain Improvement of SIW CBA

In many practical applications, high gain radiation is required. Single gain improved antenna element and antenna array designs are the most common methods to meet this

requirement. A gain enhanced SIW cavity backed dual slot antenna was presented in [35]. The two parallel slots close to the cavity edges and perpendicular to the GCPW feeding line were used as radiating elements. When TE_{120} resonance was successfully excited in the SIW cavity, the field drastic transition domains were located at the cavity center and the cavity edges. Effective electromagnetic waves were radiated from the two parallel slots and then a high gain radiation was generated when the radiated waves were superposed in phase in the farfield. A gain enhanced cavity backed slot antenna using high order cavity resonance was proposed in [36]. A GCPW line located at one diagonal line of the SIW cavity was used as the feeding element to excite the TE_{220} resonance in the cavity. Triple parallel slots, parallel to the two cavity edges, were used as the radiating elements. One of the triple parallel slots was etched at one center line of the SIW cavity. The other two slots were symmetrically distributed about the SIW cavity center line and they were close to the SIW cavity walls. Three groups of tuning posts located at the two center lines of the SIW cavity were used as the auxiliary tuning elements to excite the required TE_{220} resonance. This design method can be extended to be used at the higher order cavity resonances, such as TE_{230} , TE_{330} , and TE_{440} , to get a much higher gain radiation. An SIW cavity backed slot array antenna was introduced in [37]. The proposed antenna had two substrate layers (microstrip line substrate and cavity substrate) and three metal surfaces. SIW cavity backed slot array was etched on the top metal surface and the microstrip feeding line was located at the bottom metal surface. Energy coupling to the SIW cavity was achieved by means of a coupling slot etched on the middle metal surface. The middle metal surface also served as the ground plane of the microstrip feeding line. The SIW cavity was designed to excite TE_{508} resonance to the required frequency. Some tuning posts were introduced to suppress the mode TE_{706} , the closest unwanted mode. The tuning posts should be placed in the points, where the electric field associated with the desired mode is null and that of the closest unwanted mode is as high as possible. The number of array elements was determined by the desired gain, which corresponds to a specified cavity mode.

An SIW cavity backed slot antenna array was reported in [38], which was fed by a T-type microstrip power divider network. Comparing to that of a single antenna element, the antenna array gain had been improved of 5.8 dB by using a 2×2 array. An SIW cavity backed wide slot antenna array operating at 60 GHz was studied in [39]. The proposed antenna behaved the dual-resonance operating mechanism. Its backed cavities were not only reflectors for the radiating slots but also radiating elements. Measured results showed that the proposed 2×4 antenna array had a gain of 12 dBi and a cross polarization level lower than 25 dB over its whole operating bandwidth of about 11.6%.

6. Active SIW CBA

An active SIW cavity backed antenna is defined as an antenna with active device integrated in the SIW cavity backed antenna. It includes reconfigurable antenna, oscillator antenna, and so forth. An SIW cavity backed slot antenna

with a reconfigurable circular polarization was investigated in [40]. A crossed slot etched on the top metal plane was used as a radiator. Its two arms were orthogonal and identical. Two pairs of shorting posts were located at the extended center lines of the cross slot with the same distance. Two pairs of diodes with opposite biased states were used to switch the shorting posts. When one pair of diodes was switched on and the other one was switched off, a perturbation caused by shorting diodes pair was more than that caused by opening diodes pair. Then the two near degenerate cavity modes, TM_{110} resonances, were excited. Radiating waves from each arms of the cross slot can be set to have equal magnitude and 90° phase difference. Then a circularly polarized radiation was produced. By controlling the biased states of the two pairs of diodes, a reconfigurable circular polarization of the left hand or the right hand can be easily achieved. A novel varactor-tuned SIW cavity backed slot antenna was presented in [41]. It used four varactors mounted on a dumbbell-shaped slot, which was etched on one metal surface of the SIW cavity. The operating frequency of the proposed antenna was tuned from 5.5 GHz to 7.6 GHz, preserving the radiation pattern over the entire tuning range. Its frequency reconfigurability was easily achieved without additional bias network. A novel tunable SIW cavity backed slot antenna was proposed in [42]. Two parallel ferrite slabs with the same height of the SIW cavity were inserted into the cavity, which were also parallel to the cavity edges. The magnets were used to supply the bias magnetic field. The field strength is changed by tuning the distance between the two magnets along the cavity height direction. The operating frequency of the proposed antenna was tuned by means of a magnetic biasing field.

A tunable SIW cavity backed active slot antenna oscillator was investigated in [43]. A more compact radiating slot, with the shape of dog bone, was etched at the bottom metal layer of the SIW cavity. One via of the SIW cavity wall was removed and a varactor diode was connected between the SIW cavity top metal layer and a radial stub in order to obtain a tunable capability. Tuning of the varactor bias voltage produces a change in the loading of the cavity and consequently modifies its resonance frequency. Another tunable SIW cavity backed active patch antenna oscillator was studied in [44]. A rectangular ring slot was etched on the bottom metal surface of the SIW cavity to form a patch antenna. A GCPW feeding line on the top metal surface of the SIW cavity was extended inside the cavity, and a slot was etched perpendicular to the GCPW feeding line on the same metal surface. The gate of the active device was connected to the cavity's feeding line. The oscillator was self-biased by placing two resistors from the source terminals to ground. Stubs were used in the feeding line to eliminate the unwanted parasitic oscillations and additionally fine-tune the oscillation frequency.

7. Conclusions

A review of low profile cavity backed antennas based on SIW technique has been presented in this paper. Recent advances of SIW cavity backed antennas have been described. Performance improvements of SIW cavity backed antenna have been investigated, including bandwidth enhancement, size

reduction, and gain improvement. Active antennas comprised of SIW cavity backed antennas also have been studied.

Acknowledgments

This work was supported in part by the National Basic Research Program of China under Contract 2010CB327403, the National Science and Technology Major Project of China under Contract 2010ZX03007-001-01, the NSFC under Contract 61372020, the ZJNSF under Contract R1110003, and the FANEDD under Contract 201045.

References

- [1] J. Sarrazin, Y. Mahé, S. Avrillon, and S. Toutain, "Investigation on cavity/slot antennas for diversity and MIMO systems: the example of a three-port antenna," *IEEE Antennas and Wireless Propagation Letters*, vol. 7, pp. 414–417, 2008.
- [2] M. Manteghi and Y. Rahmat-Samii, "Multiport characteristics of a wide-band cavity backed annular patch antenna for multipolarization operations," *IEEE Transactions on Antennas and Propagation*, vol. 53, no. 1, pp. 466–474, 2005.
- [3] Q. L. Guo and L. S. Ling, "Circularly polarized antenna based on dual-mode circular SIW cavity," in *Proceedings of the International Conference on Microwave and Millimeter Wave Technology (ICMMT '08)*, vol. 13, pp. 1077–1079, Nanjing, China, April 2008.
- [4] G. Q. Luo, Z. F. Hu, L. X. Dong, and L. L. Sun, "Planar slot antenna backed by substrate integrated waveguide cavity," *IEEE Antennas and Wireless Propagation Letters*, vol. 7, pp. 236–239, 2008.
- [5] G. Q. Luo, L. L. Sun, and L. X. Dong, "Single probe fed cavity backed circularly polarized antenna," *Microwave and Optical Technology Letters*, vol. 50, no. 11, pp. 2996–2998, 2008.
- [6] L. Yan, W. Hong, G. Hua, J. Chen, K. Wu, and T. J. Cui, "Simulation and experiment on SIW slot array antennas," *IEEE Microwave and Wireless Components Letters*, vol. 14, no. 9, pp. 446–448, 2004.
- [7] J. Lacik and T. Mikulasek, "Substrate integrated waveguide rectangular ring slot antenna," in *Proceedings of the 13th International Conference on Electromagnetics in Advanced Applications (ICEAA '11)*, pp. 1164–1167, September 2011.
- [8] S. Pan and F. Capolino, "Design of a CMOS on-chip slot antenna with extremely flat cavity at 140 GHz," *IEEE Antennas and Wireless Propagation Letters*, vol. 10, pp. 827–830, 2011.
- [9] G. Q. Luo, Z. F. Hu, Y. Liang, L. Y. Yu, and L. L. Sun, "Development of low profile cavity backed crossed slot antennas for planar integration," *IEEE Transactions on Antennas and Propagation*, vol. 57, no. 10, pp. 2972–2979, 2009.
- [10] D. Kim, J. W. Lee, C. S. Cho, and T. K. Lee, "X-band circular ring-slot antenna embedded in single-layered SIW for circular polarisation," *Electronics Letters*, vol. 45, no. 13, pp. 668–669, 2009.
- [11] J. Lacik, "Circularly polarized SIW square ring-slot antenna for X-band applications," *Microwave and Optical Technology Letters*, vol. 54, no. 11, pp. 2590–2594, 2012.
- [12] M. H. Awida and A. E. Fathy, "Substrate-integrated waveguide Ku-band cavity-backed 2×2 microstrip patch array antenna," *IEEE Antennas and Wireless Propagation Letters*, vol. 8, pp. 1054–1056, 2009.
- [13] M. H. Awida, E. Elkhoully, and A. E. Fathy, "Low-cost high-efficiency substrate-integrated cavity-backed single element antenna," in *Proceedings of the IEEE International Symposium on Antennas and Propagation (AP-S/URSI '10)*, pp. 1–4, Toronto, Canada, July 2010.
- [14] D.-Y. Kim, J. W. Lee, T. K. Lee, and C. S. Cho, "Design of SIW cavity-backed circular-polarized antennas using two different feeding transitions," *IEEE Transactions on Antennas and Propagation*, vol. 59, no. 4, pp. 1398–1403, 2011.
- [15] T. Mikulasek and J. Lacik, "Circularly polarized microstrip patch antenna fed by substrate integrated waveguide," in *Proceedings of the 6th European Conference on Antennas and Propagation*, pp. 2380–2383, March 2012.
- [16] G. Q. Luo, Z. F. Hu, W. J. Li, X. H. Zhang, L. L. Sun, and J. F. Zheng, "Bandwidth-enhanced low-profile cavity-backed slot antenna by using hybrid SIW cavity modes," *IEEE Transactions on Antennas and Propagation*, vol. 60, no. 4, pp. 1698–1704, 2012.
- [17] S. Yun, D. Kim, and S. Nam, "Bandwidth enhancement of cavity-backed slot antenna using a via-hole above the slot," *IEEE Antennas and Wireless Propagation Letters*, vol. 11, pp. 1092–1095, 2012.
- [18] S. Yun, D. Kim, and S. Nam, "Bandwidth and efficiency enhancement of cavity-backed slot antenna using a substrate removal," *IEEE Antennas and Wireless Propagation Letters*, vol. 11, pp. 1458–1461, 2012.
- [19] K. J. Lee, J. A. Lee, and M. Kim, "Multilayer dielectric cavity antenna design for wide bandwidth," *Microwave and Optical Technology Letters*, vol. 54, no. 9, pp. 2046–2049, 2012.
- [20] G. Q. Luo, "Low profile cavity backed antennas based on substrate integrated waveguide technology," in *Proceedings of the IEEE Asia-Pacific Conference on Antennas and Propagation*, pp. 275–276, Singapore, August 2012.
- [21] M. H. Awida, S. H. Suleiman, and A. E. Fathy, "Substrate-integrated cavity-backed patch arrays: a low-cost approach for bandwidth enhancement," *IEEE Transactions on Antennas and Propagation*, vol. 59, no. 4, pp. 1155–1163, 2011.
- [22] W. Yang and J. Zhou, "Wideband low profile substrate integrated waveguide cavity backed E-shaped patch antenna," *IEEE Antennas and Wireless Propagation Letters*, vol. 12, pp. 143–146, 2013.
- [23] G. Q. Luo, Z. F. Hu, X. H. Zhang, L. X. Dong, and L. L. Sun, "A T-junction power divider FED circularly polarized cavity backed slot antenna," *Microwave and Optical Technology Letters*, vol. 54, no. 1, pp. 107–109, 2012.
- [24] G. Q. Luo, P. Li, Z. C. Zheng, and L. L. Sun, "A dual circularly polarized antenna with improved axial ratio bandwidth," in *Proceedings of the China-Japan Joint Microwave Conference (CJMW '11)*, pp. 179–182, Hangzhou, China, April 2011.
- [25] G. Huang and G. Q. Luo, "Circularly polarized cavity backed slot antenna with sequential-rotated feeding," *Chinese Journal of Electron Devices*, vol. 34, no. 2, pp. 146–149, 2011.
- [26] E. Jung, J. W. Lee, T. K. Lee, and W. K. Lee, "SIW-based array antennas with sequential feeding for X-band satellite communication," *IEEE Transactions on Antennas and Propagation*, vol. 60, no. 8, pp. 3632–3639, 2012.
- [27] C. A. T. Martinez, J. C. B. Reyes, O. A. N. Manosalva, and N. M. P. Traslavina, "Volume reduction of planar substrate integrated waveguide cavity-backed antennas," in *Proceedings of the 6th European Conference on Antennas and Propagation*, pp. 2919–2923, March 2012.
- [28] Y. Dong and T. Itoh, "Miniaturized cavity-backed dual-polarized slot antenna," in *Proceedings of the IEEE Antennas and Propagation Society International Symposium*, pp. 1–2, July 2012.

- [29] P. Loghmannia, M. Kamyab, M. Ranjbar Nikkhah, and R. Rezaiesarlak, "Miniaturized low-cost phased-array antenna using SIW slot elements," *IEEE Antennas and Wireless Propagation Letters*, vol. 11, pp. 1434–1437, 2012.
- [30] W. Hong and K. Sarabandi, "Platform embedded slot antenna backed by shielded parallel plate resonator," *IEEE Transactions on Antennas and Propagation*, vol. 58, no. 9, pp. 2850–2857, 2010.
- [31] S. A. Razavi and M. H. Neshati, "Development of a low profile circularly polarized cavity backed antenna using HMSIW technique," *IEEE Transactions on Antennas and Propagation*, vol. 61, no. 3, pp. 1041–1047, 2013.
- [32] C. Jin, R. Li, A. Alphones, and X. Bao, "Quarter-mode substrate integrated waveguide and its application to antennas design," *IEEE Transactions on Antennas and Propagation*, vol. 61, no. 6, pp. 2921–2928, 2013.
- [33] R. Moro, S. Agneessens, H. Rogier, and M. Bozzi, "Wearable textile antenna in substrate integrated waveguide technology," *Electronics Letters*, vol. 48, no. 16, pp. 985–987, 2012.
- [34] T. Kaufmann and C. Fumeaux, "Wearable textile half-mode substrate integrated cavity antenna using embroidered vias," *IEEE Antennas and Wireless Propagation Letters*, vol. 12, pp. 805–808, 2013.
- [35] J. X. Li, G. Q. Luo, Y. Liang, W. J. Li, L. X. Dong, and L. L. Sun, "Cavity backed dual slot antenna for gain improvement," *Microwave and Optical Technology Letters*, vol. 52, no. 12, pp. 2767–2769, 2010.
- [36] G. Q. Luo, X. H. Zhang, L. X. Dong, W. J. Li, and L. L. Sun, "A gain enhanced cavity backed slot antenna using high order cavity resonance," *Journal of Electromagnetic Waves and Applications*, vol. 25, no. 8-9, pp. 1273–1279, 2011.
- [37] M. J. Jiménez-Fernández, R. Torres-Sánchez, and P. Otero, "Cavity-backed slot array antenna in substrate-integrated waveguide technology," *Microwave and Optical Technology Letters*, vol. 53, no. 9, pp. 2105–2108, 2011.
- [38] K. Jiang, G. Q. Luo, W. J. Li, G. Huang, P. Li, and L. L. Sun, "A 2*2 antenna array consisting of low profile cavity backed slot antennas," in *Proceedings of the China-Japan Joint Microwave Conference (CJMW'11)*, pp. 74–76, Hangzhou, China, April 2011.
- [39] K. Gong, Z. N. Chen, X. Qing, P. Chen, and W. Hong, "Substrate integrated waveguide cavity-backed wide slot antenna for 60 GHz bands," *IEEE Transactions on Antennas and Propagation*, vol. 60, no. 12, pp. 6023–6026, 2012.
- [40] G. Q. Luo and L. L. Sun, "A reconfigurable cavity backed antenna for circular polarization diversity," *Microwave and Optical Technology Letters*, vol. 51, no. 6, pp. 1491–1493, 2009.
- [41] A. H. Mohammadi and K. Fororaghi, "A varactor-tuned substrate-integrated cavity-backed dumbbell slot antenna," in *Proceedings of the 15th International Symposium on Antenna Technology and Applied Electromagnetics*, pp. 1–3, June 2012.
- [42] L. Tan, R. Wu, C. Wang, and Y. Poo, "Magnetically tunable ferrite loaded SIW antenna," *IEEE Antennas and Wireless Propagation Letters*, vol. 12, pp. 273–275, 2013.
- [43] F. Giuppi, A. Georgiadis, A. Collado, M. Bozzi, and L. Perregrini, "Tunable SIW cavity backed active antenna oscillator," *Electronics Letters*, vol. 46, no. 15, pp. 1053–1055, 2010.
- [44] F. Giuppi, A. Georgiadis, A. Collado, M. Bozzi, S. Via, and L. Perregrini, "An X band, compact active cavity backed patch oscillator antenna using a substrate integrated waveguide (SIW) resonator," in *Proceedings of the IEEE International Symposium on Antennas and Propagation*, pp. 1–4, Toronto, Canada, July 2010.

Research Article

Uniplanar Millimeter-Wave Log-Periodic Dipole Array Antenna Fed by Coplanar Waveguide

Guohua Zhai,¹ Yong Cheng,² Qiuyan Yin,¹ Shouzheng Zhu,¹ and Jianjun Gao¹

¹ School of Information and Science Technology, East China Normal University, Shanghai 200241, China

² Tianhua College, Shanghai Normal University, Shanghai 201815, China

Correspondence should be addressed to Guohua Zhai; ghuzhai@gmail.com

Received 29 August 2013; Revised 9 September 2013; Accepted 11 September 2013

Academic Editor: Guo Qing Luo

Copyright © 2013 Guohua Zhai et al. This is an open access article distributed under the Creative Commons Attribution License, which permits unrestricted use, distribution, and reproduction in any medium, provided the original work is properly cited.

A uniplanar millimeter-wave broadband printed log-periodic dipole array (PLPDA) antenna fed by coplanar waveguide (CPW) is introduced. This proposed structure consists of several active dipole elements, feeding lines, parallel coupled line, and the CPW, which are etched on a single metallic layer of the substrate. The parallel coupled line can be optimized to act as a transformer between the CPW and the PLPDA antenna. Meanwhile, this transform performs the task of a balun to achieve a wideband, low cost, low loss, simple directional antenna. The uniplanar nature makes the antenna suitable to be integrated into modern printed communication circuits, especially the monolithic millimeter-wave integrated circuits (MMIC). The antenna has been carefully examined and measured to present the return loss, far-field patterns, and antenna gain.

1. Introduction

With the development of the modern wireless communication systems with low transmitted power and high data rate demand, the wideband and high-directivity antenna becomes an essential component in the front-end system. The traditional log-periodic dipole array (LPDA) antenna in a free space environment is first introduced by Isbell [1]. Because of its end-fire characteristics, such as the fixed peak radiation and the stable radiation pattern, and broad bandwidth, the LPDA antenna has been widely studied and applied in many communication systems, such as TV, radar, satellite, and indoor communications [2–7]. However, the traditional LPDA antenna is a dimensional structure, so it is difficult to design, debug, and achieve mass productivity at high frequency band, especially at millimeter-wave band. More seriously, it cannot be integrated with modern planar communication system.

In order to overcome the drawbacks of the LPDA antenna, the dipole elements and the feeding lines can be achieved by using the modern printed circuit board (PCB) technology; this antenna can be called printed log-periodic dipole arrays (PLPDA) antenna [8–13]. Therefore, the PLPDA antenna takes the advantages of low profile,

low cost, high stability, and ease to be massively produced and deeply integrated into modern planar integrated wireless communication systems.

Similar to the printed quasi-Yagi [14], the performances and design complexity are mainly challenged by the selection of an appropriate feeding network. The PLPDA antenna was initially introduced by Camblen et al. [8]. The antenna is designed on a double-layer substrate, and its dipole elements, fed by the stripline in the middle metallic layer, are cross-symmetrically distributed on the top and the bottom metallic layer, respectively. But double-layer substrate configuration increases the cost of the antenna [8–11]. In order to reduce the fabrication cost, the single layer PLPDA antennas fed by coaxial cables have been proposed [12, 13]. Unfortunately, the coaxial cables should be welded with the top and bottom feeding lines of the PLPDA antenna, which will bring significant fabrication error at high frequency band. Substrate integrated waveguide (SIW) [15–18], also named laminated waveguide [19] or postwall waveguide [20], has been deeply studied on the operation principle and widely applied in the design of the microwave and millimeter-wave antenna, filter, coupler, and systems [21–26]. Because of the intrinsic balun characteristics between the top and bottom metallic layer,

the SIW can be applied to the feeding network design of the PLPDA antenna [27]. However, the size of the SIW is larger than that of the traditional printed transmission lines, such as the slot line, microstrip, and CPW. More seriously, the dipole elements of the PLPDA antenna mentioned above are totally cross-symmetrically spaced along the parallel feeding line on respective sides of the dielectric substrate, which increases the PCB fabrication cost compared to the single metallic layer design.

It is well known that, for millimeter-wave integrated circuits, CPW has several distinct advantages over microstrip, which includes the surface-mount integration, lower phase velocity variation, and good characteristic impedance control [28]. Specifically, the CPW features a wideband, low loss and fabrication cost, and simple uniplanar structure without the need for the vias and bottom metallic ground compared to the conductor-backed CPW structure [14, 29–32]. The slot PLPDA antenna can be fed by CPW [33], but the slot antenna suffers from high insertion loss and lower power handling capability.

In this paper, a new broadband CPW feed for the uniplanar PLPDA antenna is proposed. The advantage of the novel proposed antenna is that it avoids bond wires or air-bridge lines, and all the printed dipoles and the feeding lines as well as the CPW are printed on only one side of the substrate without the vias. Therefore, this novel uniplanar millimeter-wave PLPDA antenna alleviates the design complexity, reduce the cost, and can be easy to integrate with MMIC.

2. Antenna Design Principle

2.1. Geometrical Layout. The proposed PLPDA antenna with four dipole elements fed by CPW is shown in Figure 1. In the antenna design, the dipole elements are symmetrically distributed along the two feeding lines on the top metallic layer of the substrate. A gap W_g is to lead the opposite current direction between the two feeding lines. L_n , W_n , and S_n are the length, width, and spacing of the dipole elements for the PLPDA antenna. W_{sef} is the width of both the feed line and the central line of the CPW. The 50 Ω CPW is transited to the two feed lines by the two parallel uniplanar couple lines. One parallel line is connected to the central line of the CPW, and the other one is connected to one side of the ground of the CPW. The array is fed from the longest element. The proposed antenna is printed on a single layer dielectric substrate, and h depresses its height. The dipole elements, the feeding lines, the parallel uniplanar couple lines; and the CPW are totally etched on the top side of the substrate.

2.2. Current Distribution. The magnetic distribution of the CPW at dominant mode, including the side view and the top view, is shown in Figure 2. It can be seen that a 180° phase difference is presented between the central line and the ground of the CPW. The CPW can perform a good balun line to feed the PLPDA antenna over wide operating frequency band because of the wide bandwidth of its dominant mode.

Sometimes the CPW should be balanced between the left and the right ground with air-bridge line, which greatly

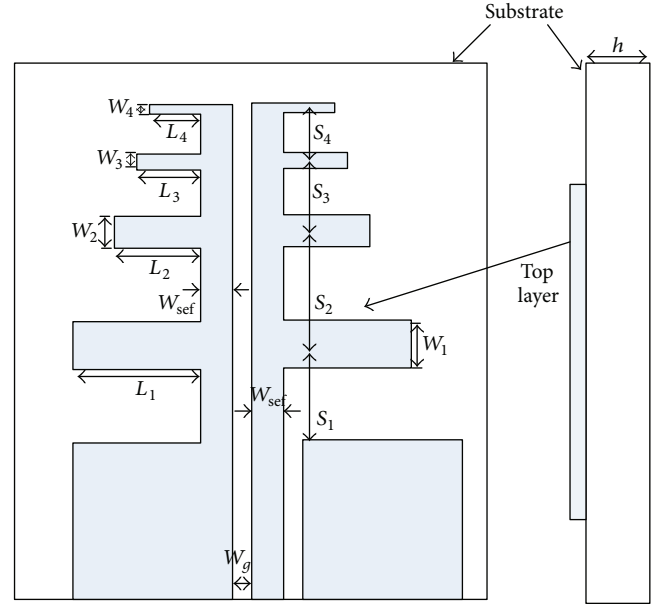


FIGURE 1: Geometry of the proposed CPW PLPDA antenna.

complexes the circuits design and increases the fabrication cost. In this design, the CPW is connected to the PLPDA antenna by the parallel uniplanar couple lines, which can be carefully designed to take the task of a balun to avoid the air-bridge line. Therefore, the length of the parallel uniplanar couple lines is the key factor for the proposed CPW PLPDA antenna.

Figure 3 shows the simulated current distribution of the dipole element at 35 GHz. The current is mainly concentrated in the region between the second and third dipole elements at 35 GHz. It can be seen that the currents of the second and third dipole elements on the left side are in phase with that printed in the opposite direction on the right side of the substrate, and the currents of other dipole elements on the left side are out of phase with that printed in the opposite direction on the right side of the substrate. Therefore, it is demonstrated that the proposed CPW PLPDA antenna can be radiated in the monodirection towards the shorter elements.

2.3. Parameters Determination. The proposed CPW PLPDA antenna is composed of three parts: dipole elements spaced with the feeding lines, parallel couple lines, and the CPW. At first, the parameters of the dipole elements spaced with the feeding lines can be primarily determined by the modified Carrel's method [2], including the consideration of the effective relative dielectric permittivity in computations to dipole lengths and spacing.

The length of each half wavelength dipole is depressed by L_{en} , which can be given by

$$L_{en} = 2 * (L_{(n+1)} + W_{\text{sef}}) + W_g, \quad (1)$$

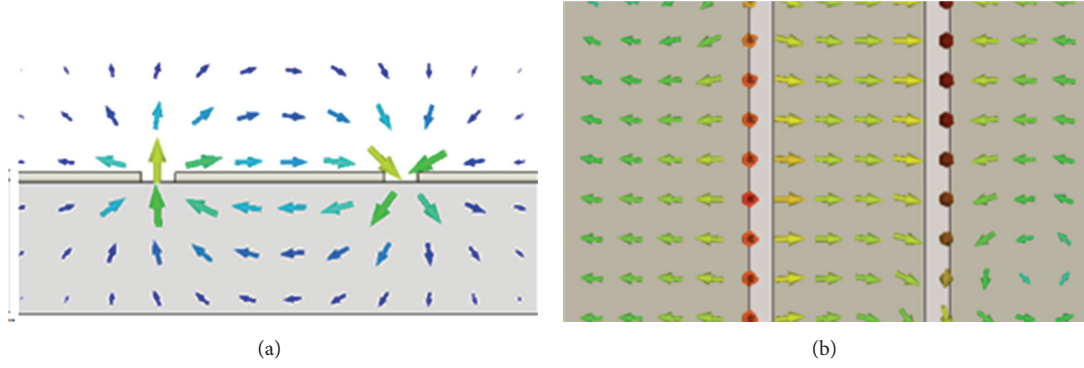


FIGURE 2: Simulated magnetic field distribution of the dominant mode in the cross view (a) and the top view (b) of the CPW.

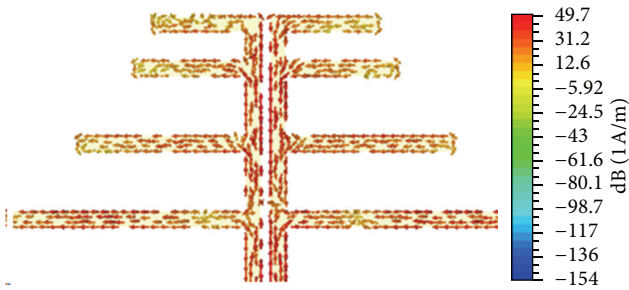


FIGURE 3: Simulated current distribution of the CPW PLPDA antenna at 35 GHz.

and according to the PLPDA antenna design principle, the parameters L_n , S_n , and W_n can be determined by the scale factor τ and spacing factor σ as given by [7]

$$\tau = \frac{L_{e(n+1)}}{L_{en}} = \frac{W_{n+1}}{W_n}, \quad (2)$$

$$\sigma = \frac{1 - \tau}{4 * \tan \alpha} = \frac{S_n}{2 * L_{en}}, \quad (3)$$

where L_1 can be calculated by

$$L_1 + W_{\text{sef}} + \frac{W_g}{2} = \frac{\lambda_{\text{eff min}}}{4} = \frac{c}{4 f_{\text{max}} \sqrt{\epsilon_{\text{eff}}}}, \quad (4)$$

$$\epsilon_{\text{eff}} = \frac{\epsilon_r + 1}{2} + \frac{\epsilon_r - 1}{2} \frac{1}{\sqrt{1 + 12h/W_1}},$$

where $\lambda_{\text{eff min}}$ is the shortest effective working wavelength, ϵ_{eff} is the effective dielectric permittivity, ϵ_r is the dielectric constant, h is the substrate thickness, and W_1 is the width of the first dipole element.

The proposed CPW PLPDA antenna is fabricated on Fr-4 with a thickness of 0.5 mm, $\epsilon_r = 4.3$, $\tan \delta = 0.025$, and then the parameters of the 5Ω CPW W_g and W_{sef} can be determined according to the transmission line theory.

The parallel couple line can take the tasks of the balun. It performs as a transformer between the CPW and PLPDA antenna. So the determination of S_1 is one of the key factors

for the antenna design, which can be primarily chosen as quarter operating wavelength.

The length of the longest dipole L_1 can be calculated from (4) according to the lowest operating frequency. Then the length of the other elements can be calculated from (2); meanwhile, the parameters W_1 and W_{sef} can be optimized by the full-wave simulation software HFSS. The width of the other elements W_n and the spacing between the elements S_n can be obtained from (2) and (3). After optimization, the detailed dimensions of the proposed antenna are $W_1 = 0.9$ mm, $W_2 = 0.7$ mm, $W_3 = 0.5$ mm, $W_4 = 0.4$ mm, $L_1 = 2.63$ mm, $L_2 = 1.63$ mm, $L_3 = 0.88$ mm, $L_4 = 0.63$ mm, $S_1 = 1.7$ m, $S_2 = 1$ mm, $S_3 = 1$ mm, $S_4 = 0.6$ mm, $W_{\text{sef}} = 0.8$ mm, and $W_g = 0.13$ mm.

3. Experimental Results

The CPW PLPDA antenna at 25 GHz–40 GHz is designed, fabricated, and tested. The measured and simulated input return losses of the proposed antenna are presented by Figure 4. The $|S_{11}|$ is better than 10 dB from 28 GHz to 38.5 GHz. Note that over a narrow band (around 35 GHz), return loss values in excess of 15 dB can be obtained. However, compared with the simulated result, the measured center frequency of the proposed antenna is shifted toward the lower frequency about 1.5 GHz, which is mainly introduced by the relationship between the frequency and the dielectric permittivity without consideration in the simulation.

The radiation patterns and gain are examined in the microwave chamber. The measured and simulated antenna gain of the proposed antenna is shown in Figure 5. It can be seen that the CPW PLPDA antenna can achieve the maximum gain of 4 dBi at 39 GHz. The low gain, varying from 1.5 dBi to 4 dBi over the entire operating frequency band, is resulted from the large substrate losses of the Fr-4. The measured antenna gain of the CPW PLPDA antenna is less than that of the simulated results, which is mainly provided by the losses of the connectors and the increasing substrate loss of the antenna at millimeter-waves.

The radiation patterns of the 28 GHz–40 GHz CPW PLPDA antenna are measured over the entire band, which present the similar characteristics. So for brevity, only

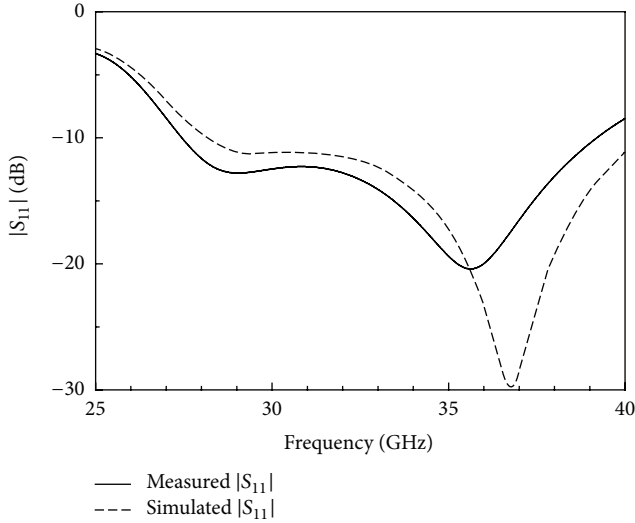


FIGURE 4: Simulated and measured return loss of the proposed antenna.

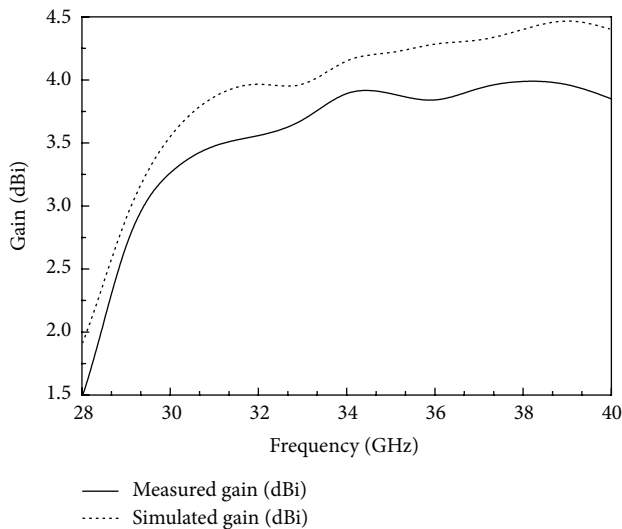


FIGURE 5: Simulated and measured gain of the proposed antenna.

the 35 GHz radiation patterns are shown in Figure 6, which shows that the front-to-back ratio is larger than 15 dB. However, the main beam is shifted from the bore sight, which is caused by the nature asymmetrical feature between the central line and the ground of the CPW.

4. Conclusion

The proposed PLPDA antenna fed by CPW provides a viable choice for millimeter-wave broadband printed antennas in modern wireless communication system. The new CPW feed is more appropriate than that introduced before at millimeter-wave frequency, as it avoids the requirement for air-bridge line, vias, and any additional balun design in direct CPW-to-PLPDA connections. Therefore, the proposed antenna can be achieved on only one metallic layer of a single

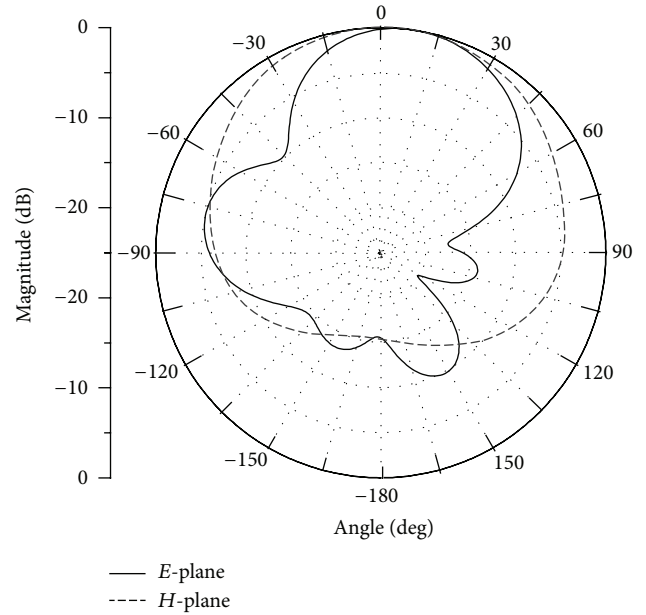


FIGURE 6: Measured far-field of the proposed PLPDA antenna at 30 GHz.

layer substrate, which can reduce the loss, cost, and complexity for the fabrication. The prototype for the proposed uniplanar CPW PLPDA antenna has been fabricated and measured. Radiation pattern and gain of the CPW PLPDA antenna are studied and presented. The advantages such as low cost, broadband, compactness, and simplicity are verified by the experiment. The design concept can easily be scaled for applications with different bandwidth and directivity requirements by adjusting the parameters of τ , σ , W_1 , S_1 , and W_{sep} , which can also improve the VSWR. So the proposed antenna can be used for wideband integrated multimode radio communication such as a digital cordless system (DCS), personal communication system (PCS), WLAN, UWB systems, and some systems required to work at Ka band.

Acknowledgments

This work was supported in part by NSFC under Grant 61201069, in part by Research Fund for the Doctoral Program of Higher Education of China under Grant 20120076120035, and in part by Open Foundation of State Key Laboratory of Millimeter-Waves under Grant 201308.

References

- [1] D. Isbell, "Log periodic dipole arrays," *IRE Transactions on Antennas and Propagation*, vol. 8, no. 3, pp. 260–267, 1960.
- [2] R. Carrel, "The design of the log-periodic dipole antenna," in *Proceedings of the IRE International Conventional Record*, vol. 9, pp. 61–75, March 1961.
- [3] J. Carr, "Some variations in log-periodic antenna structures," *IRE Transactions on Antennas and Propagation*, vol. 9, no. 2, pp. 229–230, 1961.

- [4] R. Mittra and K. E. Jones, "Theoretical Brillouin (k - β) diagrams for monopole and dipole arrays and their applications to log-periodic antennas," *IEEE Transactions on Antennas and Propagation*, vol. 51, no. 3, pp. 533–540, 1964.
- [5] N. Barbano, "Waveguide-fed log periodic antennas," *IRE Transactions on Antennas and Propagation*, vol. 16, no. 3, pp. 357–358, 1968.
- [6] J. Wolter, "Solution of Maxwell's equations for log-periodic dipole antennas," *IEEE Transactions on Antennas and Propagation*, vol. 18, no. 6, pp. 734–741, 1970.
- [7] A. B. Constantine, *Antenna Theory: Analysis and Design*, Wiley-Interscience, New York, NY, USA, 2005.
- [8] C. K. Campbell, I. Traboulay, M. S. Suuthers, and H. Kneve, "Design of a stripline log-periodic dipole antenna," *IEEE Transactions on Antennas and Propagation*, vol. 25, no. 5, pp. 718–721, 1977.
- [9] P. Alakananda and G. Inderjeet, "An analysis of log periodic antenna with printed dipoles," *IEEE Transactions on Antennas and Propagation*, vol. 29, no. 2, pp. 114–119, 1981.
- [10] R. R. Pantoja, A. R. Sapienza, and F. M. Filho, "A microwave printed planar log-periodic dipole array antenna," *IEEE Transactions on Antennas and Propagation*, vol. 35, no. 10, pp. 1176–1178, 1987.
- [11] F. Merli, J.-F. Zurcher, A. Freni, and A. K. Skrivervik, "Analysis, design and realization of a novel directive ultrawideband antenna," *IEEE Transactions on Antennas and Propagation*, vol. 57, no. 11, pp. 3458–3466, 2009.
- [12] X. Liang and Y. W. M. Chia, "New precision wideband direction finding antenna," *IEE Proceedings: Microwaves, Antennas and Propagation*, vol. 148, no. 6, pp. 363–364, 2001.
- [13] D. E. Anagnostou, J. Papapolymerou, M. M. Tentzeris, and C. G. Christodoulou, "A Printed Log-Periodic Koch-Dipole Array (LPKDA)," *IEEE Antennas and Wireless Propagation Letters*, vol. 7, pp. 456–460, 2008.
- [14] H. K. Kan, R. B. Waterhouse, A. M. Abbosh, and M. E. Bialkowski, "Simple broadband planar CPW-fed quasi-Yagi antenna," *IEEE Antennas and Wireless Propagation Letters*, vol. 6, pp. 18–20, 2007.
- [15] D. Deslandes and K. Wu, "Integrated microstrip and rectangular waveguide in planar form," *IEEE Microwave and Wireless Components Letters*, vol. 11, no. 2, pp. 68–70, 2001.
- [16] D. Deslandes and K. Wu, "Design consideration and performance analysis of substrate integrated waveguide components," in *Proceedings of the 32nd European Microwave Conference*, pp. 1–4, Milan, Italy, September 2002.
- [17] F. Xu, Y. Zhang, W. Hong, K. Wu, and T. J. Cui, "Finite-difference frequency-domain algorithm for modeling guided-wave properties of substrate integrated waveguide," *IEEE Transactions on Microwave Theory and Techniques*, vol. 51, no. 11, pp. 2221–2227, 2003.
- [18] L. Yan, W. Hong, K. Wu, and T. J. Cui, "Investigations on the propagation characteristics of the substrate integrated waveguide based on the method of lines," *IEE Proceedings: Microwaves, Antennas and Propagation*, vol. 152, no. 1, pp. 35–42, 2005.
- [19] H. Uchimura, T. Takenoshita, and M. Fujii, "Development of a 'laminated waveguide,'" *IEEE Transactions on Microwave Theory and Techniques*, vol. 46, no. 12, pp. 2438–2443, 1998.
- [20] J. Hirokawa and M. Ando, "45° linearly polarized post-wall waveguide-fed parallel-plate slot arrays," *IEE Proceedings on Microwave, Antennas and Propagation*, vol. 147, no. 6, pp. 515–519, 2000.
- [21] G. Q. Luo, Z. F. Hu, W. J. Li, X. H. Zhang, L. L. Sun, and J. F. Zheng, "Bandwidth-enhanced low-profile cavity-backed slot antenna by using hybrid SIW cavity modes," *IEEE Transactions on Antennas and Propagation*, vol. 60, no. 4, pp. 1698–1704, 2012.
- [22] G. Q. Luo, Z. F. Hu, Y. Liang, L. Y. Yu, and L. L. Sun, "Development of low profile cavity backed crossed slot antennas for planar integration," *IEEE Transactions on Antennas and Propagation*, vol. 57, no. 10, pp. 2972–2979, 2009.
- [23] G. Q. Luo, Z. F. Hu, L. X. Dong, and L. L. Sun, "Planar slot antenna backed by substrate integrated waveguide cavity," *IEEE Antennas and Wireless Propagation Letters*, vol. 7, pp. 236–239, 2008.
- [24] G. Q. Luo, L. L. Sun, and L. X. Dong, "Single probe fed cavity backed circularly polarized antenna," *Microwave and Optical Technology Letters*, vol. 50, no. 11, pp. 2996–2998, 2008.
- [25] X.-P. Chen and K. Wu, "Substrate integrated waveguide cross-coupled filter with negative coupling structure," *IEEE Transactions on Microwave Theory and Techniques*, vol. 56, no. 1, pp. 142–149, 2008.
- [26] G. H. Zhai, W. Hong, K. Wu et al., "Folded half mode substrate integrated waveguide 3 dB coupler," *IEEE Microwave and Wireless Components Letters*, vol. 18, no. 8, pp. 512–514, 2008.
- [27] G. H. Zhai, W. Hong, K. Wu, and Z. Q. Kuai, "Wideband substrate integrated printed log-periodic dipole array antenna," *IET Microwaves, Antennas and Propagation*, vol. 4, no. 7, pp. 899–905, 2010.
- [28] I. Wolff, "Design rules and realization of coplanar circuits for communication applications," in *Proceedings of the 23rd European Microwave Conference*, pp. 36–41, Madrid, Spain, September 1993.
- [29] F. Taringou, D. Dousset, J. Bornemann, and K. Wu, "Broadband CPW feed for millimetre-wave SIW-based antipodal linearly slot antenna," *IEEE Transactions on Antennas and Propagation*, vol. 61, no. 4, pp. 1756–1762, 2013.
- [30] A. Grbic and G. V. Eleftheriades, "Leaky CPW-based slot antenna arrays for millimeter-wave applications," *IEEE Transactions on Antennas and Propagation*, vol. 50, no. 11, pp. 1494–1504, 2002.
- [31] M. A. P. Lazaro and R. Judaschke, "A 150-GHz CPW-Fed Tapered-Slot Antenna," *IEEE Microwave and Wireless Components Letters*, vol. 14, no. 2, pp. 62–64, 2004.
- [32] S. Mestdagh, W. de Raedt, and G. A. E. Vandenbosch, "CPW-fed stacked microstrip antennas," *IEEE Transactions on Antennas and Propagation*, vol. 52, no. 1, pp. 74–83, 2004.
- [33] S. H. Kim, J. H. Choi, J. W. Baik, and Y. S. Kim, "CPW-fed log-periodic dumb-bell slot antenna array," *Electronics Letters*, vol. 42, no. 8, pp. 436–438, 2006.

Research Article

Design and Implementation of Double-Transmitter-Coil Antenna Used for the Tag Test System

Bin You,¹ Haoling Yue,¹ Xuan Wen,² and Liangyu Qu³

¹The Key Laboratory of RF Circuits and System of Ministry of Education, Hangzhou Dianzi University, Hangzhou 310018, China

²Nokia Siemens Networks Technology (Beijing) Co., Ltd., Hangzhou 310053, China

³Shanghai TYD Electronic Technology Co., Ltd., Shanghai 200233, China

Correspondence should be addressed to Haoling Yue; yuehaoling@gmail.com

Received 30 August 2013; Accepted 22 September 2013

Academic Editor: Yu Jian Cheng

Copyright © 2013 Bin You et al. This is an open access article distributed under the Creative Commons Attribution License, which permits unrestricted use, distribution, and reproduction in any medium, provided the original work is properly cited.

At present, more and more electronic tags are used in Antitheft system; it is important to examine the performance of electronic tags. The traditional single-transmitter-coil antenna (STC antenna) of the electronic tags tester has some serious drawbacks. So a novel double-transmitter-coil antenna (DTC antenna) is presented in this paper. Compared to the traditional STC antenna, this new antenna has a more excellent performance in the tag test systems, especially when it is used for testing the quality factor of tags.

1. Introduction

As the promotion of RFID and the widespread use of Antitheft system, the quality of electronic tags has gained more and more attentions [1]. But most of the tag detection systems cannot get the tag parameters accurately, especially the quality factor. Meanwhile, the detecting antenna plays an important role in the tag detection systems. So the research of detecting antenna has a great significance [2]. This paper designs a new DTC antenna which can perfectly solve the problems existed in traditional STC antenna and can be better applied to the tag detection systems. Besides, the DTC antenna can be also used for estimating Q_{eff} of tags [3].

2. The Design of Antennas

The frequency characteristic of tags cannot be measured directly. A test method based on the electromagnetic induction is often adopted. According to electromagnetic induction, two different coils are usually used as the antenna in the tag test systems [4, 5]. One of these two coils is used as the transmitter-coil which sends the swept-frequency signal needed; the other one is used as the receiver-coil which tests the change of electromagnetic field around in

real time. In this paper, this antenna is named as STC antenna. The electromagnetic field will change when there exists the electromagnetic induction between tags and the transmitter-coil. And then the change of electromagnetic field will be measured by the receiver-coil. Though simple, the STC antenna has some serious drawbacks. So this paper proposes a novel DTC antenna. This DTC antenna comprises two transmitter-coils and one receiver-coil and can perfectly solve the problems existed in STC antenna.

2.1. The STC Antenna. STC antenna has been widely used in tag test systems for a long time. The equivalent circuit of the STC antenna and the tag is shown in Figure 1. In Figure 1, $L1$ represents the transmitter-coil of the STC antenna, LC resonance circuit represents the tag, and $L3$ represents the receiver-coil of the STC antenna.

In order to simplify analysis, we assume that the current in receiver-coil is zero. According to electromagnetic induction, there is no electromagnetic field induced by the receiver-coil. In other words, the receiver coil only can test the change of electromagnetic field around, but it will not interfere with the tag and transmitter-coil. Now, the current in transmitter-coil is I_1 , and the current in the tag is I . So according to *KVL*, there are two equations (1) and (2) below

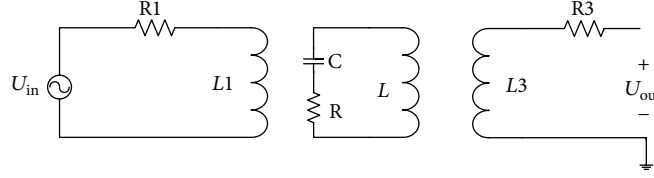


FIGURE 1: The equivalent circuit of the STC antenna and the tag.

where Z_1 , Z , and M_1 represent the equivalent resistance of transmitter-coil, the equivalent resistance of tag, and the mutual inductance between transmitter-coil and the tag, respectively as follows:

$$U_{in} = I_1 Z_1 + j\omega M_1 I, \quad (1)$$

$$0 = IZ + j\omega M_1 I_1. \quad (2)$$

From the analysis of the equivalent circuit shown in Figure 1, the receiver-coil will be affected by both the tag and transmitter-coil simultaneously. Under the effect of the tag, the induced voltage output U_{01} can be shown as follows:

$$U_{01} = j\omega M_3 I = \frac{\omega^2 M_1 M_3}{Z_1 Z + \omega^2 M_1^2} U_{in}. \quad (3)$$

Similarly, the induced voltage output U_{02} can be shown under the effect of the transmitter coil as follows:

$$U_{02} = j\omega M_{13} I_1 = \frac{j\omega M_{13} Z}{Z_1 Z + \omega^2 M_1^2} U_{in}. \quad (4)$$

Finally, the total induced voltage output U_0 can be shown as follows:

$$U_0 = U_{01} + U_{02} = \frac{j\omega M_{13} Z + \omega^2 M_1 M_3}{Z_1 Z + \omega^2 M_1^2} U_{in}. \quad (5)$$

The induced voltage measured by the receiver-coil is the sum of U_{01} and U_{02} . Though the effect of transmitter-coil is relatively weak, it will finally affect the test result.

2.2. The DTC Antenna. From the analysis in Section 2.1, the STC antenna has two disadvantages. The first one is that the interference of tags with transmitter-coil may change the electromagnetic field distribution of transmitter-coil. The other one is that the interference of transmitter-coil with receiver-coil may finally change the test result. The design and implementation of DTC antenna are introduced in this paper. The most significant feature of the DTC antenna is that it can perfectly solve the mentioned problems existed in the STC antenna above.

The schematic diagram of DTC antenna is depicted in Figure 2. There is an operational amplifier in Figure 2. But the operational amplifier is not the essential part of the novel antenna. The effect of the operational amplifier is that it can make sure that the current in the receiver-coil is nearly zero because of its high input impedance. So According to

electromagnetic induction, there is no electromagnetic field induced by receiver-coil. In other words, the electromagnetic field induced by tags will impact on receiver-coil, but not vice versa. Besides, the receiver-coil will not impact on the transmitter-coil. It is the premise of all next analysis. Moreover, the output voltage signal can be amplified by the operational amplifier so that it can be easily met the requirements of signal processing next.

The structure diagram of DTC antenna is shown in Figure 3. In Figure 3, the coil 1-1 and the coil 1-2 together make up the first transmitter-coil. Similarly, the coil 2-1 and the coil 2-2 constitute the second transmitter-coil. The two transmitter-coils must be placed symmetrically. In addition, the coil 3-1 and the coil 3-2 together make up a receiver-coil. Finally, two transmitter-coils and one receiver-coil make up the novel DTC antenna.

When the signal is sent to the two transmitter-coils, the directions of magnetic field induced by the coil 1-1 and coil 1-2 are opposite. Thus, the magnetic flux of first transmitter-coil is zero; in the same way the magnetic flux of the second transmitter-coil is zero. Meanwhile, the magnetic field induced by the coil 1-1 and coil 2-1 superimpose in one direction. In a word, the symmetrical structure of the two transmitter-coils insures that the receiver-coil will not interfere with the transmitter-coil.

So the induced voltage of receiver-coil U_{out} entirely depends on the tag. At last, there is an equation of U_{out} shown below where the M_3 represents the mutual inductance between the receiver-coil and the tag and I represents the current in the tag as follows:

$$U_{out} = j\omega M_3 I. \quad (6)$$

When tags are placed at the middle region of the coil 3-1, the magnetic flux of the closed region shaped by the coil 1-1 and coil 2-1 or the closed region shaped by the coil 1-2 and 2-2 are all zero, no matter what the direction of magnetic field induced by tags is. In other words, the magnetic field induced by transmitter-coil can impact on tags, but not vice versa. Unlike the double layer structure of transmitter-coils, the receiver-coil has only one layer. Meanwhile, the magnetic field induced by tags almost exists in the middle area of the coil 3-1. As a result, the coil 3-2 has been less affected by the magnetic field induced by tags than the coil 3-1. So the change of magnetic flux of the receiver-coil is only dependent on the tag. The DTC antenna makes sure that there is no interference of the tag with transmitter-coils.

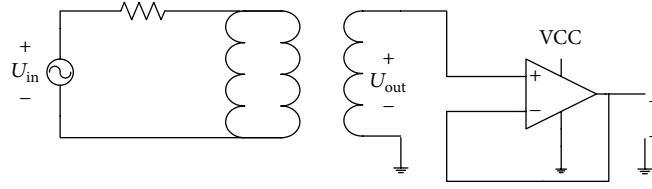


FIGURE 2: The schematic diagram of DTC antenna.

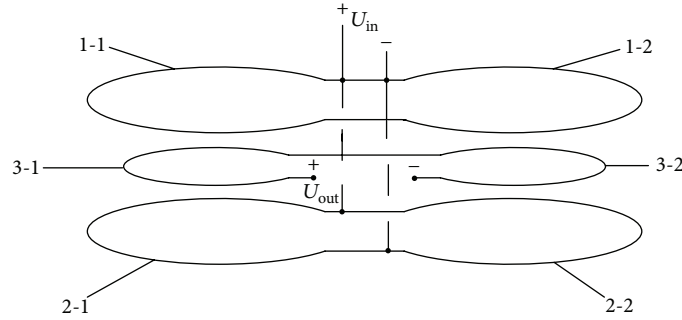


FIGURE 3: The structure diagram of DTC antenna.

So there are two equations as follows:

$$U_{in} = I_1 Z_1, \quad (7)$$

$$0 = IZ + j\omega M_1 I_1. \quad (8)$$

By synthesizing (6), (7), and (8), we can get

$$U_{out} = \left(\frac{\omega^2 M_1 M_3}{Z_1 Z} \right) U_{in}. \quad (9)$$

From (9), the relationship between U_{out} and frequency can be clearly found. The amplitudes of U_{in} , M_1 , M_3 , Z_1 , and Z in (9) are all constants for a given antenna. So the output voltage U_{out} only changes with frequency and can reflect the impedance characteristic of the tag.

3. The Hardware Implementation and Test of the DTC Antenna

3.1. The Hardware Design of the DTC Antenna. According to the theoretical analysis above, the DTC antenna comprises two transmitter-coils which should overlap each other closely and a receiver-coil which should be placed between the two transmitter-coils. So the double-layers PCB as shown in Figure 4 is designed.

The two transmitter-coils are placed on the top layer and the bottom layer, respectively. The receiver-coil is placed on the top layer. Moreover, both the two transmitter-coils and the receiver-coil have the dumbbell-shaped structure. There are four via holes on the PCB; two of them on the middle of the dumbbell-shaped structure of the two transmitter-coils are used to import signals, and the rest two on the middle of the dumbbell-shaped structure of the receiver-coil are used to export signals. Furthermore, no matter which side of

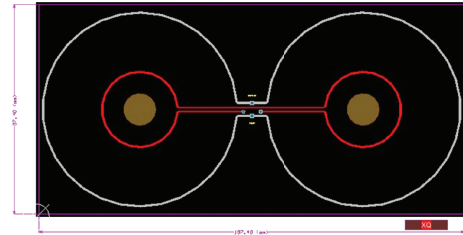


FIGURE 4: The PCB layout design of DTC antenna.

the dumbbell-shaped of the receiver-coil the tag are placed on, the test result will be the same.

In order to compare the performance of the two antennas, STC antenna is also designed on a single layer PCB shown in Figure 5. The concentric circle structure is adopted in the design. The bigger circle with two via holes stands for the transmitter-coil, and the smaller one represents the receiver-coil.

3.2. The Performance Test of Two Antennas. A vector network analyzer E5071C, two antennas above, and some tags with known parameters such as the quality factor and center frequency are used in the test. The operational amplifier is not the essential part of the novel antenna. But in the practical application, in order to make sure the current in receiver-coil is zero, the output signal must be inputted into a signal amplification circuit. In the test, we use AD8067 as our operational amplifier. The complete testing circuit of the STC antenna is presented in Figure 6, and the testing circuit of the DTC antenna is presented in Figure 7. In the complete test, Port1 of E5071C supplies the swept-frequency signal needed to the transmitter-coil of the antenna. When the tags are placed on the antenna, the signal tested by the receiver-coil

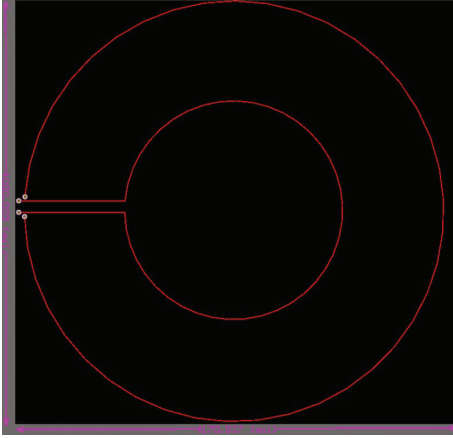


FIGURE 5: The PCB layout design of STC antenna.

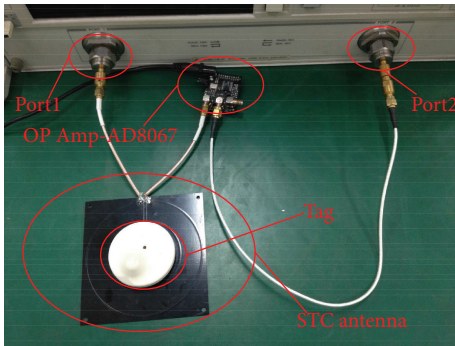


FIGURE 6: The complete testing circuit of the STC antenna.

TABLE 1: The test result of resonant frequency.

| | f | f_1 | f_2 |
|-------|-----------|-----------|-----------|
| Tag 1 | 8.179 MHz | 8.162 MHz | 8.175 MHz |
| Tag 2 | 8.053 MHz | 8.000 MHz | 8.033 MHz |
| Tag 3 | 4.590 MHz | 4.680 MHz | 4.610 MHz |
| Tag 4 | 4.759 MHz | 4.880 MHz | 4.809 MHz |
| Tag 5 | 8.037 MHz | 7.990 MHz | 8.020 MHz |

is outputted to the input end of AD8067. The signal amplified by AD8067 is finally outputted to Port2 of E5071C so that we can clearly see the curves below.

When the tag with the center frequency 8.179 MHz and the quality factor 151.1 is tested, there are test results as shown in Figures 8 and 9.

The test result of the STC antenna is shown in Figure 8.

It can be seen from Figure 8 that the test center frequency is 8.162 MHz and the test quality factor is 125.5.

From Figure 9, it can be seen that the test center frequency is 8.175 MHz and the test quality factor is 151.3.

Compared to two test results, the amplitude-versus-frequency curve measured by DTC antenna is more similar to the frequency characteristic curve of LC resonance circuit. At the same time, the center frequency and the quality factor of tags measured by DTC antenna are more close to the real

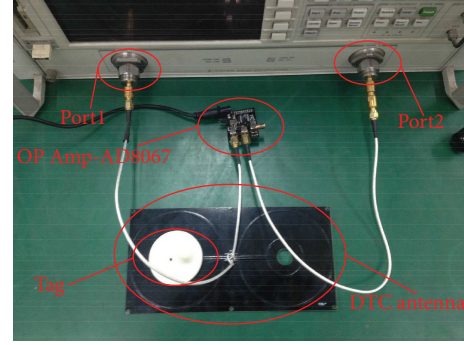


FIGURE 7: The complete testing circuit of the DTC antenna.

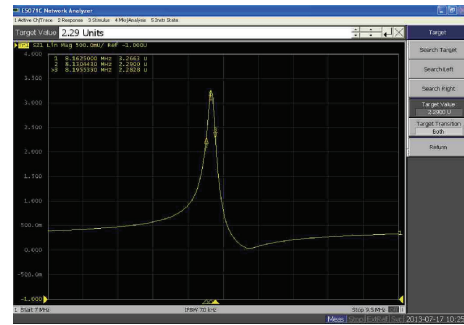


FIGURE 8: The test result of STC antenna.

TABLE 2: The test result of quality factor.

| | Q | Q_1 | Q_2 |
|-------|-------|-------|-------|
| Tag 1 | 151.1 | 125.5 | 151.3 |
| Tag 2 | 45 | 36.5 | 47.8 |
| Tag 3 | 96.9 | 55.1 | 102.4 |
| Tag 4 | 109 | 54.2 | 106.9 |
| Tag 5 | 49.1 | 36.3 | 48.3 |

values. Compared to the two curves in Figures 8 and 9, there exists an unavoidable interference in STC antenna. The unavoidable interference of transmitter-coil with receiver-coil finally leads to the difference between the two measured curves.

To proof the advantage of DTC antenna adequately, some kinds of tags are tested, and the test results are shown in Tables 1 and 2.

As shown in Table 1, the f is the real center frequency of tags. The f_1 , f_2 present the center frequency of tags measured by STC antenna and DTC antenna, respectively. The Q in Table 2 is the real quality factor of tags, while Q_1 , Q_2 present the quality factor of tags measured by STC antenna and DTC antenna, respectively.

According to Table 1, the two measured center frequency are both close to the real values. But the measured curve of DTC antenna is more similar to the frequency characteristic curve of LC resonance circuit. From Table 2, it can be clearly known that the quality factor measured by DTC antenna is

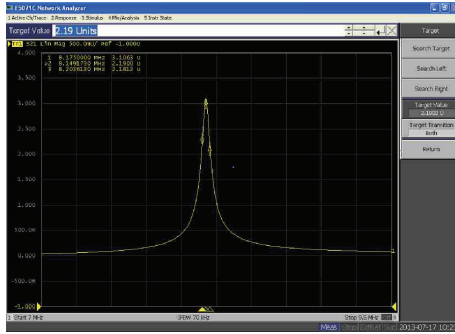


FIGURE 9: The test result of DTC antenna.

more close to the real value. To sum up, the performance of DTC antenna is better than STC antenna.

4. Conclusions

In this paper, a novel DTC antenna is proposed and completed. Experiments by DTC antenna have shown good capability in testing the quality factor and the center frequency of tags. So such an antenna model is more suitable for the tag detection systems than the STC antenna, especially the systems for obtaining the quality factor of tags.

Conflict of Interests

The authors declare that there is no conflict of interests regarding the publication of this paper.

Acknowledgments

This work was supported in part by the Zhejiang Province Key Science and Technology Innovation Team (no. 2010R50010) and the Real-time Antitheft system based on RFID technology (no. ZX130702307001).

References

- [1] R. Want, "An introduction to RFID technology," *IEEE Pervasive Computing*, vol. 5, no. 1, pp. 25–33, 2006.
- [2] Z. Ya-Ping, Z. Wei-Hong, X. Wei-Hua, and Y. Cheng-Zhong, "Development of EAS RF tag quality online detection sensor," *Journal of Zhejiang University (Engineering Science)*, vol. 46, no. 4, pp. 719–724, 2012.
- [3] W. B. Zou, Y. Wu, and Y. Zhao, "Automatic testing system for UHF passive RFID tag performance," in *Proceedings of the 2009 International Conference on Networking and Digital Society, ICNDS 2009*, pp. 79–82, Guiyang, China, May 2009.
- [4] L. Jia-Jun, Y. Cheng-Zhong, Y. Zhi-Kai, and H. Lin, "The value of Q stability analysis by electronic anti-theft labels detection system," *Journal of Hangzhou Dianzi University*, vol. 32, no. 4, pp. 148–150, 2012.
- [5] Z. Yanbin and L. Qin, "Design and realization of pulsed electronic article surveillance system," *IEEE Intelligent Computation Technology and Automation*, vol. 31, no. 2, pp. 28–29, 2011.

Research Article

Simplified Printed Log-Periodic Dipole Array Antenna Fed by CBCPW

Guohua Zhai,¹ Yong Cheng,² Qiuyan Yin,¹ Shouzheng Zhu,¹ and Jianjun Gao¹

¹ School of Information and Science Technology, East China Normal University, Shanghai 200241, China

² Shanghai Normal University, Tianhua College, Shanghai 201815, China

Correspondence should be addressed to Guohua Zhai; ghuzhai@gmail.com

Received 29 August 2013; Accepted 3 September 2013

Academic Editor: Xiao Ping Chen

Copyright © 2013 Guohua Zhai et al. This is an open access article distributed under the Creative Commons Attribution License, which permits unrestricted use, distribution, and reproduction in any medium, provided the original work is properly cited.

A novel simple approach for designing single-layer printed log-periodic dipole array (PLPDA) antenna fed by conductor-backed coplanar waveguide (CBCPW) is presented. The PLPDA antenna has the merits of wide bandwidth, low profile, and stable radiation pattern, which should be fed by the balanced line. The balanced line, created by the geometric features of the CBCPW, provides a balun with a considerably wide bandwidth with low profile, broad bandwidth, low insertion loss, and so forth. The prototype of the proposed CBCPW-fed printed log-periodic array at Ka band is designed and fabricated; the measured data are in good agreement with the simulated results.

1. Introduction

As an end-fire type antenna, the log-periodic dipole array (LPDA) antenna has the merits of fixed peak radiation and stable radiation pattern within the operating frequency, so it is one of the candidates for the modern wireless communications system. Numerous studies have been documented on the design method and the performance of the conventional LPDA antenna since the 1960s [1–7].

In order to achieve low profile, printed log-periodic dipole arrays (PLPDA) antenna was proposed based on the printed integrated board (PCB) technology [8–14]. Practically, the performance of the PLPDA antenna is determined by the feeding network. At an early stage, the PLPDA antenna was designed on a piece of the double-layer printed circuit board [8–11], but it increases the fabrication cost and limits the productivity. Then, the fabrication cost is reduced by using single-layer printed circuit, so the single-layer PLPDA antennas with two coaxial cables as the feeding network were proposed [12, 13]. However, soldering coaxial cables bring significant fabrication error and misalignment, especially at millimeter-wave frequencies. A single-layer slot PLPDA antenna fed by coplanar waveguide (CPW) was proposed [14], the CPW transmission line has been widely used in

the monolithic millimeter-wave integrated circuits (MMIC), but this transmission line suffers from high insertion loss in the transition, radiation loss, serious crosstalk, and lower power handling capability because of its open structure.

Recently, the substrate integrated circuits (SIC) concept, in particular substrate integrated waveguide (SIW) technique, has been demonstrated as a promising scheme for low-cost, small size, relatively high power, low radiation loss, and high-density integrated microwave and millimeter-wave components and systems, which has been widely used in the low profile antenna design [15–18]. And the substrate integrated PLPDA antenna is proposed [19]. However, this new feeding network is larger, especially at lower frequency. And the printed dipoles of the PLPDA antenna mentioned above are all cross-symmetrically spaced along the parallel feed lines on both sides of the dielectric substrate. So, it necessitates two sides of the substrate to be etched.

In this paper, a simplified PLPDA antenna fed by CBCPW is presented, which can be called CBCPW PLPDA antenna. The geometry of the proposed antenna is shown in Figure 1. It has advantages of low profile, broadband, light weight, and ease of integration to the planar circuits. The entire structure is fabricated on a piece of PCB. And all the printed dipoles and

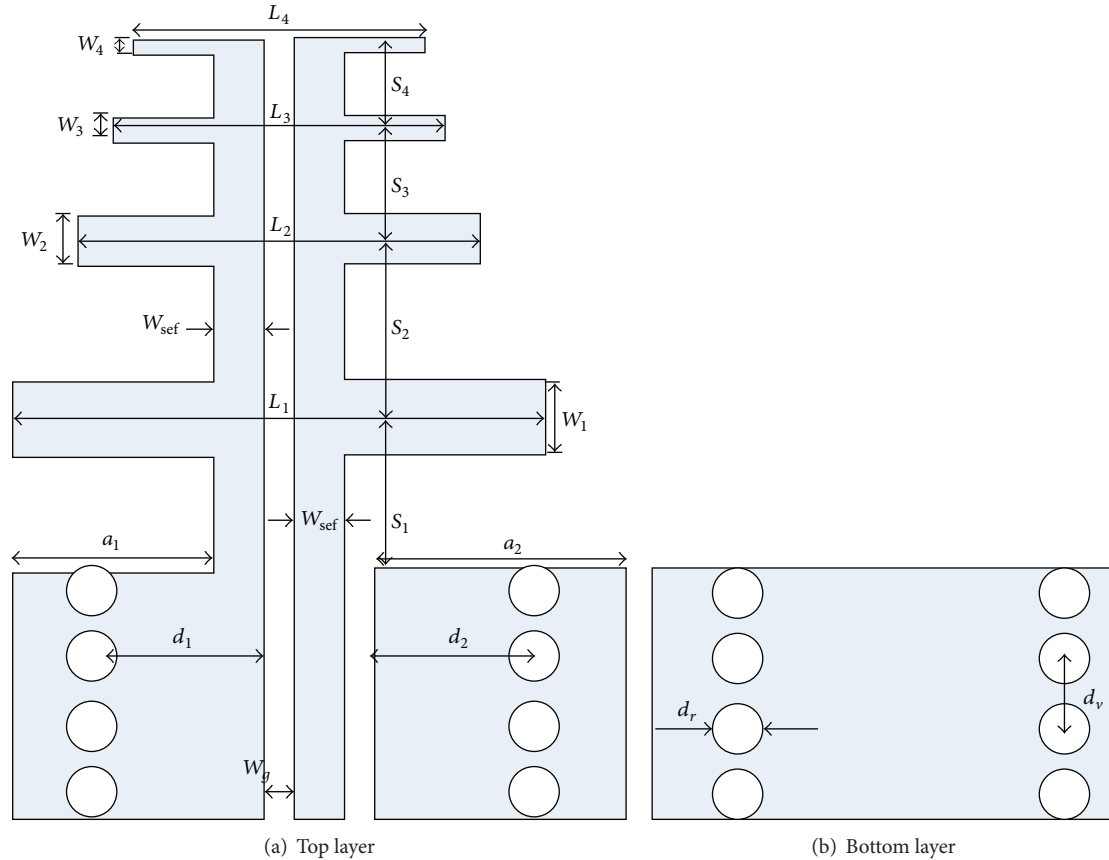


FIGURE 1: Geometry of the proposed CBCPW PLPDA antenna.

the feed lines of the PLPDA antenna are printed on only one side of the dielectric substrate. Therefore, this novel antenna alleviates the design complexity, reduces the cost, and can be easily integrated with MMIC.

2. CBCPW PLPDA Antenna Design

For the proposed antenna design, the $50\ \Omega$ CBCPW is directly transitioned to the two parallel transmission strip lines, along which the dipole elements are symmetrically distributed on the top metallic layer of the substrate. One parallel line is connected to the central line of the CBCPW, and the other one is connected to one side of the ground on the top side of the CBCPW. The bottom ground of the CBCPW is etched on the bottom layer of the substrate; the top and the bottom metallic layers of the CBCPW are connected by the metallic vias to balance the transmission line.

Figure 2 depicts the dominant mode in the cross-section of the CBCPW, which clearly shows the 180° phase difference between the central line and the ground of the CBCPW. Therefore, the structure of CBCPW can provide a good performance over a fairly wide bandwidth and perform a good balun line for the feeding network of the single-layer PLPDA antenna.

The electromagnetic power excited by the feeder is transmitted from CBCPW to the dipole elements along the

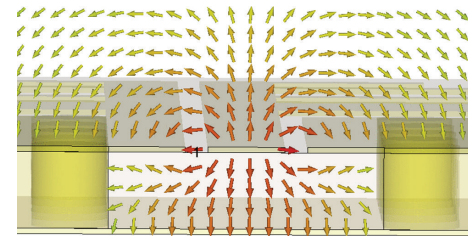


FIGURE 2: Simulated electric field distribution of the dominant mode in the cross-section of the CBCPW.

two parallel transmission strips line, which is shown in Figure 3. And the parallel transmission strip lines acts as a transformer between the CBCPW and the PLPDA antenna; it also performs as the balun. Therefore, the currents of the dipole elements on the left side are in phase with those printed in the opposite direction on the right side of the substrate, which results in mono-directional radiation towards the shorter elements.

The parameters of the proposed antenna are determined by the modified Carrel method [2], including an effective relative dielectric permittivity in computations to dipole lengths and spacing. According to the principle of the PLPDA antenna, the optimum values of the parameters L_n , S_n , and W_n

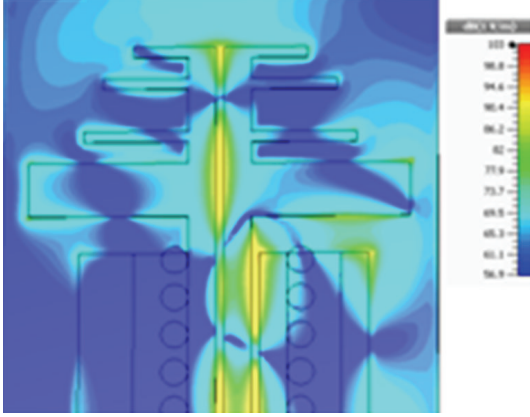


FIGURE 3: Simulated electric field density distributions of the proposed antenna (35 GHz).

can be determined by the scale factor τ and spacing factor σ as given by [7, 8]

$$\tau = \frac{L_{(n+1)}}{L_n} = \frac{W_{n+1}}{W_n}, \quad (1)$$

$$\sigma = \frac{1 - \tau}{4 * \tan \alpha} = \frac{S_n}{4 * L_n}. \quad (2)$$

The value of the structure bandwidth $B_s = B \times B_{ar}$, where B is the desired bandwidth ratio and B_{ar} is the bandwidth for the active region given by [7, 8]

$$B_{ar} = 1.1 + 7.7(1 - \tau)^2 \cot \alpha. \quad (3)$$

The number of the dipole elements N is obtained from [7, 8]

$$N = 1 + \frac{\log B_s}{\log (1/\tau)}. \quad (4)$$

The actual half-length of the largest dipole element adjacent to the feed point is given by [7, 8]

$$L_1 = \frac{\lambda_{\text{eff min}}}{2} = \frac{c}{2f_{\text{max}} \sqrt{\epsilon_{\text{eff}}}}, \quad (5)$$

$$\epsilon_{\text{eff}} = \frac{\epsilon_r + 1}{2} + \frac{\epsilon_r - 1}{2} \frac{1}{\sqrt{1 + 12h/W_1}},$$

where $\lambda_{\text{eff min}}$ is the shortest effective working wavelength, ϵ_{eff} is the effective dielectric permittivity, ϵ_r is the dielectric constant, h is the substrate thickness, and W_1 is the width of the first dipole element.

Hence, the parameters of this structure to be tuned are τ , σ , W_1 , S_1 , and W_{sef} , which can be optimized to further enhance the performance. In this paper, the proposed CBCPW PLPDA antenna is designed at 25–40 GHz, which is printed on one side of a 0.5 mm thick FR-4 substrate with the permittivity of 4.3. The size parameters of the 50 Ω CBCPW can be first decided, and then the length of the longest dipole L_1 can be calculated from (5). Then, the length of the other elements can be calculated from (1); meanwhile, the width of

TABLE 1: Dimensions of CBCPW PLPDA antenna.

| Symbol | Quantity |
|------------------|----------|
| W_1 | 1 |
| W_4 | 0.2 |
| L_3 | 4.3 |
| S_2 | 1 |
| W_{sef} | 0.5 |
| d_1 | 1 |
| a_2 | 2 |
| W_2 | 0.2 |
| L_1 | 7 |
| L_4 | 3.2 |
| S_3 | 1 |
| W_g | 0.15 |
| d_2 | 1 |
| d_r | 0.25 |
| W_3 | 0.2 |
| L_2 | 5 |
| S_1 | 1.2 |
| S_4 | 0.6 |
| h | 0.5 |
| a_1 | 2 |
| d_v | 0.8 |

Unit: mm.

the longest dipole W_1 , the feed line W_{sef} , and the distance from the feed point to the first dipole S_1 can be optimized by the full-wave simulation software HFSS. The width of the other elements W_n and the spacing between the elements S_n can be obtained from (1) and (2). After optimization with the full-wave simulation software HFSS, the dipole element N is 4, and the other geometry parameters of the proposed antenna are shown in Table 1.

3. Experimental Results

The proposed PLPDA antenna at 25 GHz–40 GHz is designed, fabricated, and measured. The measured and simulated return losses of the proposed PLPDA antenna are shown in Figure 4. All of the measured results shown below include the losses of 50 Ω CBCPW insertion loss, the 2.4 mm to 3.5 mm adapters, and the SMA connectors. It can be seen that the $|S_{11}|$ is below -10 dB from 28 GHz to 40 GHz. There is a little difference in the center frequency between measurement and simulation, which may be brought by the fabrication errors and frequency dependent dielectric permittivity without consideration in the simulation.

Figure 5 shows the measured antenna gain of the proposed antennas. The peak antenna gain of the CBCPW PLPDA antenna is 4.3 dBi at 34 GHz. The measured antenna gain of the CBCPW PLPDA antenna is less than that of the simulated results, which maybe brought by the losses of the SMA connector and the increasing substrate loss of the antenna at millimeter-waves.

The far-field radiation pattern of the proposed antenna is measured which shows the similar characteristics across

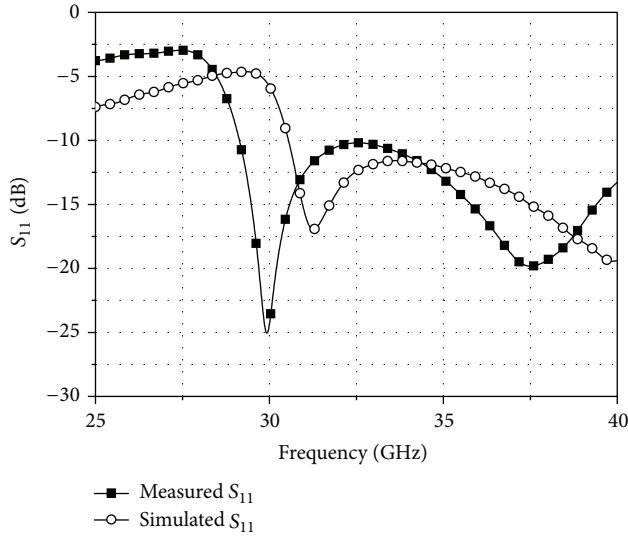


FIGURE 4: Simulated and measured return loss of the proposed antenna.

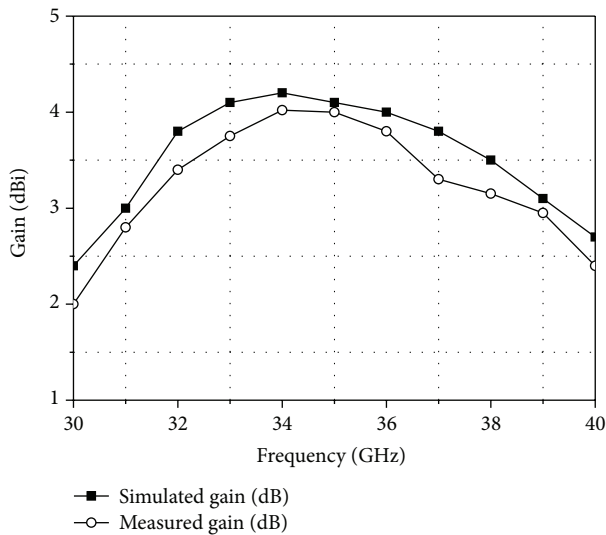


FIGURE 5: Simulated and measured gain of the proposed antenna.

the operating bandwidth. And for brevity, only the 35 GHz radiation patterns are shown in Figure 6, which shows that the front-to-back ratio is larger than 15 dB, and the 3D far-field pattern of the proposed antenna at 35 GHz is given in Figure 7, which shows that the proposed CBCPW PLPDA antenna has a good end-fire radiation characteristic.

4. Conclusion

In this paper, a low profile, low-cost, and simple design PLPDA antenna fed by CBCPW has been proposed. The prototype for the proposed CPW PLPDA antenna has been designed, fabricated, and measured. It is simple to make a prototype by using standard PCB fabrication technique. Because the feeding network does not require additional devices, such as a T-junction, power divider, or microstrip-to-coplanar strip line (CPS) balun, this antenna is simple

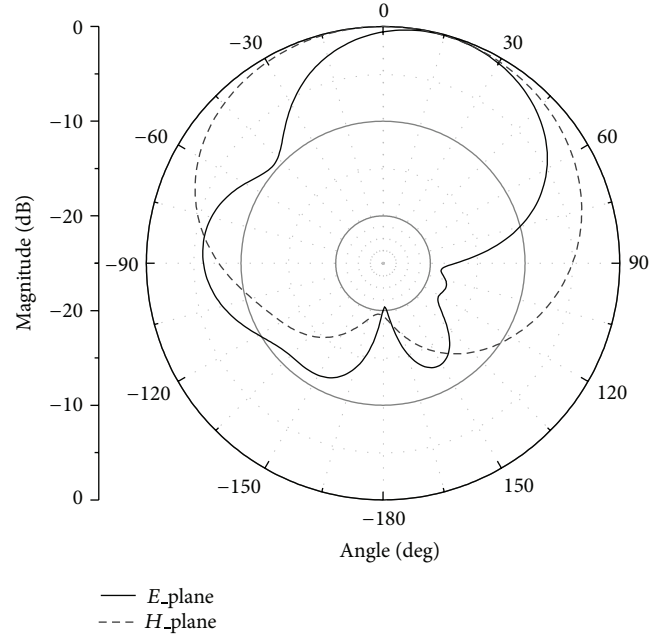


FIGURE 6: Measured far-field of the proposed PLPDA antenna at 35 GHz.

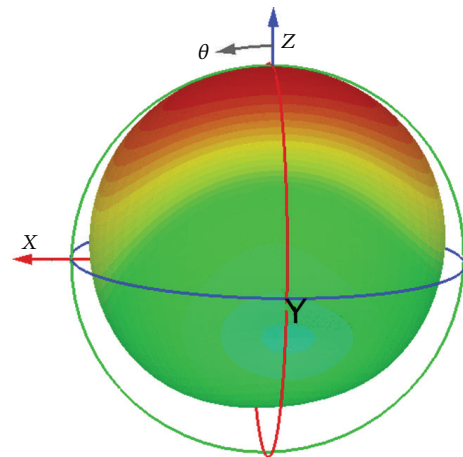


FIGURE 7: Simulated 3D far-field of the proposed PLPDA antenna at 35 GHz.

to design. The low profile antenna structure results in ease of integration into planar microwave and millimeter-wave wireless communications systems. The proposed concept reduces the size and design complexity of the antenna. Radiation pattern and antenna gain of the CBCPW PLPDA antenna are presented and studied. The advantages such as low cost, broadband, compact, and simplicity are verified by the experiment.

Acknowledgments

This work was supported in part by NSFC under Grant 61201069, in part by Research Fund for the Doctoral Program of Higher Education of China under Grant 20120076120035,

and in part by Open-Foundation of State Key Laboratory of Millimeter-Waves under Grate 201308.

References

- [1] D. Isbell, "Log periodic dipole arrays," *IRE Transactions on Antennas and Propagation*, vol. 8, no. 3, pp. 260–267, 1960.
- [2] R. Carrel, "The design of the log-periodic dipole antenna," *IRE International Conventional Record*, vol. 9, part 1, pp. 61–75, 1961.
- [3] J. Carr, "Some variations in log-periodic antenna structures," *IRE Transactions on Antennas and Propagation*, vol. 9, no. 2, pp. 229–230, 1961.
- [4] R. Mittra and K. E. Jones, "Theoretical brillouin (k - β) diagrams for monopole and dipole arrays and their applications to log-periodic antennas," *IEEE Transactions on Antennas and Propagation*, vol. 51, no. 3, pp. 533–540, 1964.
- [5] N. Barbano, "Waveguide-fed log periodic antennas," *IRE Transactions on Antennas and Propagation*, vol. 16, no. 3, pp. 357–358, 1968.
- [6] J. Wolter, "Solution of Maxwell's equations for log-periodic dipole antennas," *IEEE Transactions on Antennas and Propagation*, vol. 18, no. 6, pp. 734–741, 1970.
- [7] A. B. Constantine, *Antenna Theory: Analysis and Design*, Wiley-Interscience, New York, NY, USA, 2005.
- [8] C. K. Campbell, I. Traboulay, M. S. Suuthers, and H. Kneve, "Design of a stripline log-periodic dipole antenna," *IEEE Transactions on Antennas and Propagation*, vol. 25, no. 5, pp. 718–721, 1977.
- [9] P. Alakananda and G. Inderjeet, "An analysis of log periodic antenna with printed dipoles," *IEEE Transactions on Antennas and Propagation*, vol. 29, no. 2, pp. 114–119, 1981.
- [10] R. R. Pantoja, A. R. Sapienza, and F. C. Medeiros Filho, "A microwave printed planar log-periodic dipole array antenna," *IEEE Transactions on Antennas and Propagation*, vol. 35, no. 10, pp. 1176–1178, 1987.
- [11] F. Merli, J.-F. Zurcher, A. Freni, and A. K. Skrivervik, "Analysis, design and realization of a novel directive ultrawideband antenna," *IEEE Transactions on Antennas and Propagation*, vol. 57, no. 11, pp. 3458–3466, 2009.
- [12] X. Liang and Y. W. M. Chia, "New precision wideband direction finding antenna," *IEE Proceedings: Microwaves, Antennas and Propagation*, vol. 148, no. 6, pp. 363–364, 2001.
- [13] D. E. Anagnostou, J. Papapolymerou, M. M. Tentzeris, and C. G. Christodoulou, "A printed Log-Periodic Koch-Dipole Array (LPKDA)," *IEEE Antennas and Wireless Propagation Letters*, vol. 7, pp. 456–460, 2008.
- [14] S. H. Kim, J. H. Choi, J. W. Baik, and Y. S. Kim, "CPW-fed log-periodic dumb-bell slot antenna array," *Electronics Letters*, vol. 42, no. 8, pp. 436–438, 2006.
- [15] G. Q. Luo, Z. F. Hu, W. J. Li, X. H. Zhang, L. L. Sun, and J. F. Zheng, "Bandwidth-enhanced low-profile cavity-backed slot antenna by using hybrid SIW cavity modes," *IEEE Transactions on Antennas and Propagation*, vol. 60, no. 4, pp. 1698–1704, 2012.
- [16] G. Q. Luo, Z. F. Hu, Y. Liang, L. Y. Yu, and L. L. Sun, "Development of low profile cavity backed crossed slot antennas for planar integration," *IEEE Transactions on Antennas and Propagation*, vol. 57, no. 10, pp. 2972–2979, 2009.
- [17] G. Q. Luo, Z. F. Hu, L. X. Dong, and L. L. Sun, "Planar slot antenna backed by substrate integrated waveguide cavity," *IEEE Antennas and Wireless Propagation Letters*, vol. 7, pp. 236–239, 2008.
- [18] G. Q. Luo, L. L. Sun, and L. X. Dong, "Single probe fed cavity backed circularly polarized antenna," *Microwave and Optical Technology Letters*, vol. 50, no. 11, pp. 2996–2998, 2008.
- [19] G. H. Zhai, W. Hong, K. Wu, and Z. Q. Kuai, "Wideband substrate integrated printed log-periodic dipole array antenna," *IET Microwaves, Antennas and Propagation*, vol. 4, no. 7, pp. 899–905, 2010.

Application Article

Broadband Multilayered Array Antenna with EBG Reflector

P. Chen,^{1,2} X. D. Yang,² C. Y. Chen,¹ and Z. H. Ma¹

¹ College of Information Engineering, Jimei University, Xiamen 361021, China

² College of Information and Communication Engineering, Harbin Engineering University, Harbin 150001, China

Correspondence should be addressed to P. Chen; symoux@gmail.com

Received 11 June 2013; Accepted 29 August 2013

Academic Editor: Zhang Cheng Hao

Copyright © 2013 P. Chen et al. This is an open access article distributed under the Creative Commons Attribution License, which permits unrestricted use, distribution, and reproduction in any medium, provided the original work is properly cited.

Most broadband microstrip antennae are implemented in the form of slot structure or laminate structure. The impedance bandwidth is broadened, but meanwhile, the sidelobe of the directivity pattern and backlobe level are enlarged. A broadband stacked slot coupling microstrip antenna array with EBG structure reflector is proposed. Test results indicate that the proposed reflector structure can effectively improve the directivity pattern of stacked antenna and aperture coupled antenna, promote the front-to-back ratio, and reduce the thickness of the antenna. Therefore, it is more suitable to be applied as an airborne antenna.

1. Introduction

As the wideband communication system and high-resolution radar popularization, microstrip antenna claims more demands for bandwidth. In order to expand bandwidth, increasing the number of resonate frequencies is an effective solution. The above purpose can be achieved by clipping patch or using the coupled patch. However, this method will break the completeness of original microstrip antenna, for antenna pattern the sidelobe will increase, the gain and front-to-back ratio will decrease. Meanwhile, the asymmetry of slot and coupling patch makes antenna radiation patterns lack symmetry which will be more inconvenient in use [1, 2].

Electromagnetic band-gap (EBG) structure, which is a periodic structure composed of metal and medium can show band rejection characteristics when propagating electromagnetic wave. Many research results demonstrate that antenna with EBG structure will improve pattern performance effectively [3, 4]. This paper applied metal EBG structure to miniaturize antenna and fractal principle to increase the effective cycle length. The structure adjusts the antenna impedance characteristics, restrains backward radiation, increases the antenna front-to-back ratio, improves the symmetry of antenna patterns, and optimizes the antenna pattern characteristics without increasing the size of antenna.

2. Antenna Design

The period of the metal EBG can be calculated by Bragg reflection condition [5]

$$k_{\text{Bragg}} = 2k = \frac{2\pi}{e}, \quad (1)$$

where k is the wave number of guided wave modes, and a is the period of EBG structure. Consider the following:

$$e = \frac{\lambda_g}{2}. \quad (2)$$

Theory width of the traditional microstrip patch antenna is $\lambda_g/2$. With the miniaturization technology of microstrip antenna developing, the size of the microstrip antenna has been greatly reduced. The EBG antenna with the $\lambda_g/2$ period should greatly increase the size for miniaturization.

The fractal principle can solve the problem well. According to Cantor set, the equivalent length of the fractal structure can tend to infinity in the same area. Therefore, the fractal structure can be greatly reduced cycle length of EBG structure.

The generating elements of Minkowski fractal curve replace each side of the rectangle. The rectangular aperture takes fractal iteration to generate a curved fractal structure, shown in Figure 1. Different structures of the generated

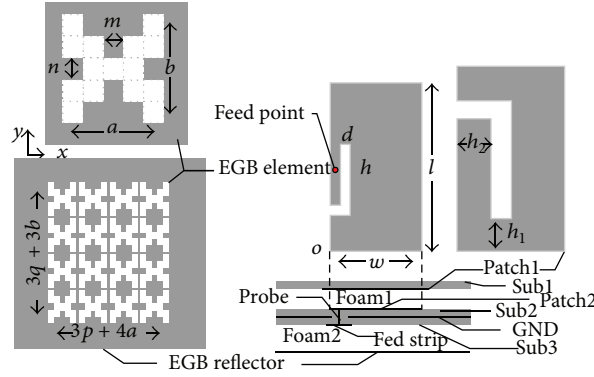


FIGURE 1: Element antenna structure.

elements cause different period lengths of the EBG elements in the direction of x and y , which are $5m + 4n + p$ and $2m + 5n + q$, respectively, where p and q are the element interval of EBG structure on the directions of x and y , respectively. While the period lengths of EBG structure are $a + p$ and $b + p$, where $a = 5m$, $b = 5n$, and p is the space between the EBG structures, m and n are the length and width of the rectangular aperture. Obviously, the EBG structure periods are shorter than the EBG element periods in both x and y directions. In this way, miniaturization is achieved. The EBG period length $5m + 4n + p$ is close to e , which provides a structure characteristic of EBG.

Metal EBG structure is etched on the metal floor to inhibit the motivation of the higher modes. The miniaturization metal EBG structure mentioned in this paper has high impedance surface characteristics in the experiment. In the effective bandwidth, the structure makes vertical incident wave total reflection with the reflection characteristics and enhancement at the same phase in less than spacing $\lambda_g/4$. Using miniaturization metal EBG structure, this paper puts forward an aperture coupling multilayer broadband microstrip array antenna with EBG reflector, which can effectively inhibit backside and side radiation of multilayer gap microstrip antenna, promote front-to-back ratio of the antenna, reduce the mutual coupling effect between element antennas, and improve antenna pattern performance. The element antenna structure is shown in Figure 1.

The antenna uses double patches with multilayer coupling radiation structure, which etches L-shape on the double patches. Patch 1 adhered to dielectric substrate 1 is the radiation patch, and patch 2 adhered to dielectric substrate 2 is the coupling patch. Foam 1 is inserted between two-layer metal patches to improve resonance bandwidth. According to the slot antenna principle, slot can change current path of patch surface to form the resonance frequency points. According to the principle of laminated antenna, it can make multiple layer antenna form many resonance frequency points that have different sizes of radiation and coupling patches and different dielectric constants of the substrates. Adjusting the structure parameters of foam 1 thickness, w , l , h , d , h_1 , h_2 , and so on, can make more resonant frequency points distribution in working band to reduce the reflection coefficient and effectively extend antenna impedance bandwidth.

TABLE 1: The sizes of array antenna (unit: mm).

| | w | l | d | h | h_1 | h_2 |
|---------|-----|-----|-----|------|-------|-------|
| Patch 1 | 11 | 19 | 2 | 12.5 | 3.3 | 3.6 |
| Patch 2 | 8.5 | 16 | 1 | 6.6 | 3.4 | 1 |

EBG reflector uses metal EBG structure shown in Figure 1. The shadow region is copper clad area. Compared with the traditional reflector, the distance from EBG reflector to radiation source is less than $\lambda_g/4$ and the thickness of foam 2 and the antenna is reduced. At the same time, the maximum level of sidelobe and backlobe radiation pattern of the antenna is also reduced.

In Figure 1, three-layer substrate is FR4 with relative permittivity $\epsilon_1 = \epsilon_3 = 2.2$ and $\epsilon_2 = 2.9$, loss tangent of 0.002, and thickness of 1.6 mm. The material of foam is Rohacell 71 HF with relative permittivity of 2.65; the thickness of foam 1 is 5.3 mm and thickness of foam 2 is 6.4 mm. The diameter of probe interconnected with coupling patch is 0.5 mm.

Equal-amplitude and Phase Multiport Feeding Network is employed. Array configuration is equally spaced arrays, with element spacing $0.75\lambda_0$. According to the array size, EBG periodic expansion can be performed. In design, the array antenna adopts 6×6 element EBG reflector ($m = 2.2$ mm, $n = 2.4$ mm, $p = 1.1$ mm, and $q = 1.3$ mm).

After the simulation optimization, the sizes of array antenna are listed in Table 1, and the designed antenna is shown in Figure 2.

3. Experiment Results and Discussion

In order to avoid the impact of the array factors, this paper simulated the same element antenna with different reflector structure.

It can be seen in Figure 3 that, compared with antennae with common reflector and nonreflector structures, the backlobe level of antenna with EBG reflector is the minimum with a value of only -13.18 dBi. The front-to-back ratio is up to 22.41 dB, 4.15 dB higher than nonreflector structure and 1.07 dB higher than common reflector structure. The maximum side lobe level of E-plane is -10.05 dBi, 7.75 dB lower than nonreflector structure and 3.58 dB lower than

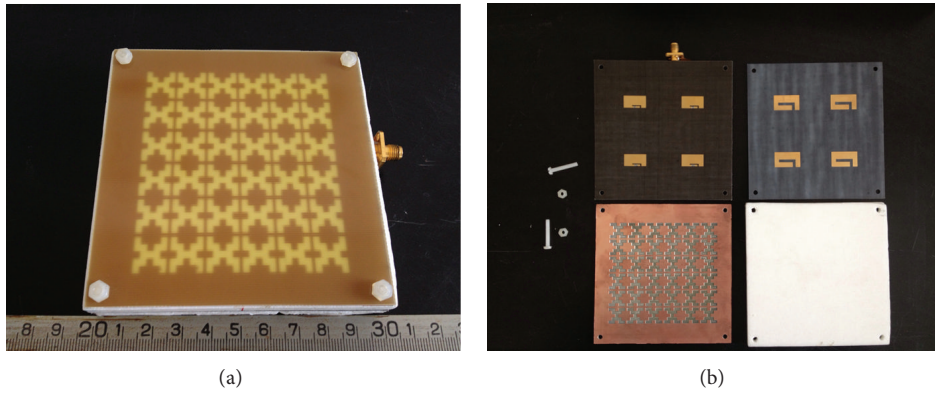


FIGURE 2: The designed array antenna. (a) Whole profile. (b) Each layer show.

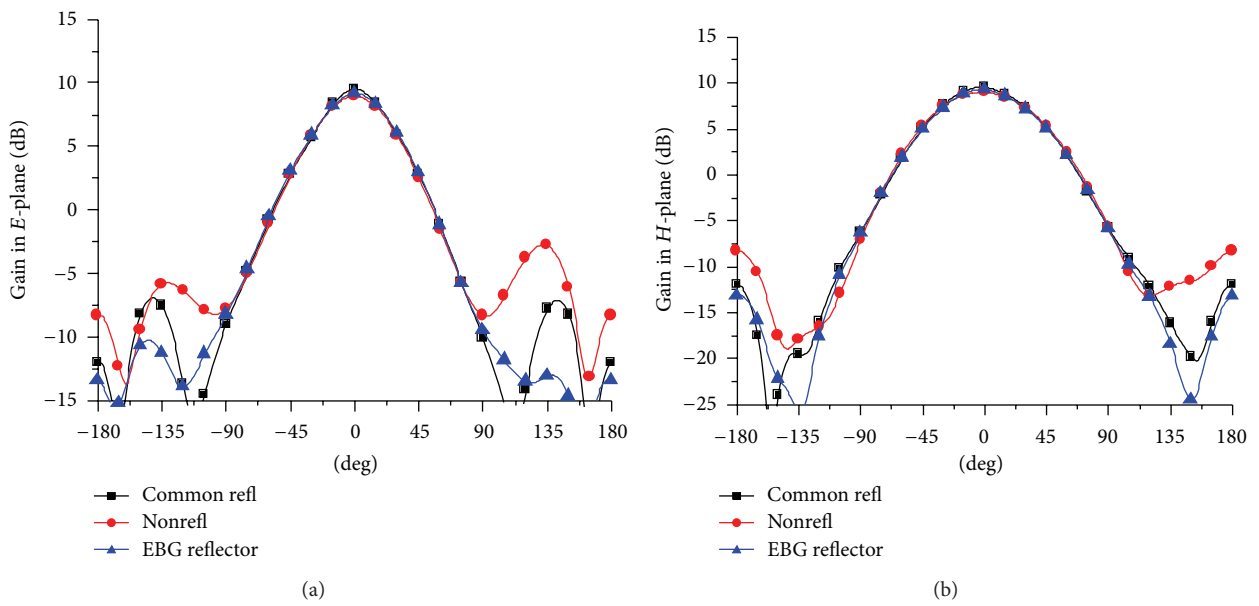


FIGURE 3: Element antenna radiation pattern with different reflector structures at 5.35 GHz.

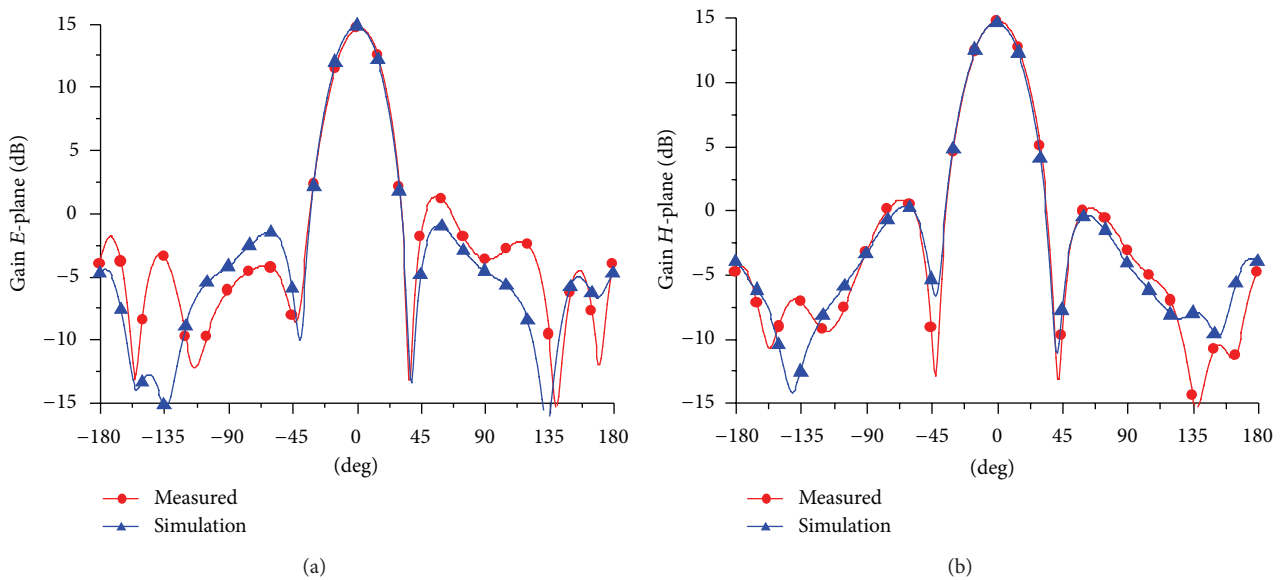


FIGURE 4: The radiation pattern of experimental array antenna at 5.35 GHz.

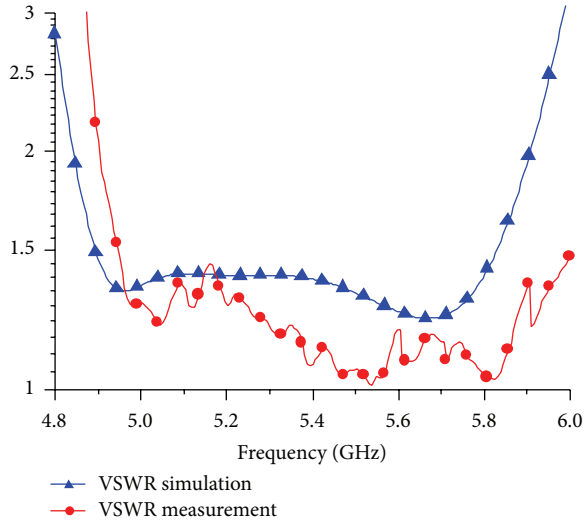


FIGURE 5: The VSWR of experimental array antenna.

common reflector structure. Common reflector or traditional reflector is constituted by a metal plane.

The proposed antenna is simulated based on the FEM method, using the Ansoft high frequency structure simulator (HFSS). The optimised antenna was also fabricated and tested. The measured curves are shown in Figure 4. Compared with simulation data, the maximum gain of E -plane and H -plane, the first zero degree and back lobe data are consistent with simulation results basically.

Agilent E8362B vector network analyzer is used to measure the antenna impedance characteristics, and the measured results are shown in Figure 5. The impedance bandwidth of $VSWR < 1.5$ is 1.1 GHz (4.9–6 GHz). The relative bandwidth reaches 20.2%. The VSWR coefficient is all less than 1.5. In contrast to four element array antenna, simulation results are close to the measured results. The VSWR curve integrally moves to high frequency direction. The designed center frequency 5.35 GHz excurses to 5.45 GHz, away from 0.1 GHz and relative offset of 1.9%.

4. Conclusion

Above all, microstrip array antenna with aperture coupling stacked structure and EBG reflector has the advantages of small size, wide bandwidth, high gain, suitable front-to-back ratio, symmetrical pattern, and good performance. The processing and assembling of antenna is simple. The stability of structure and electric fitting is high. This array antenna can be used in broadband radar or wireless communication field with better antenna direction and balance of wireless resource allocation.

Acknowledgments

This work was supported by Fujian Provincial Department of Science and Technology (no. 2013H0035), Natural Science Foundation of Heilongjiang Province (no. ZD201115),

and Science and Technology Projects in Xiamen (no. 3502Z20123028).

References

- [1] O. P. Falade and M. U. Rehman, "Single feed stacked patch circular polarized antenna for triple band GPS receivers," *IEEE Transactions on Antennas and Propagation*, vol. 60, no. 10, pp. 4479–4484, 2012.
- [2] D. Zhou, "Compact wideband balanced antenna for mobile handsets," *IET Microwaves, Antennas and Propagation*, vol. 4, no. 5, pp. 600–608, 2010.
- [3] L. Qiu, F. Zhao, K. Xiao, S.-L. Chai, and J.-J. Mao, "Transmit-Receive isolation improvement of antenna arrays by using EBG structures," *IEEE Antennas and Wireless Propagation Letters*, vol. 11, pp. 93–96, 2012.
- [4] A. Pirhadi, H. Bahrami, and J. Nasri, "Wideband high directive aperture coupled microstrip antenna design by using a FSS superstrate layer," *IEEE Transactions on Antennas and Propagation*, vol. 60, no. 4, pp. 2101–2106, 2012.
- [5] S. G. Johnson and J. D. Joannopoulos, *Photonic Crystals: The Road From theory To Practice*, Springer, New York, NY, USA, 2002.

Research Article

A Novel Dual-Shorting Point PIFA (GSM850 to IMT-A) for Mobile Handsets

Pengcheng Li, Jin Pan, Deqiang Yang, and Pingzai Nie

Department of Microwave Engineering, School of Electronic Engineering, University of Electronic Science and Technology of China (UESTC), Chengdu 610054, China

Correspondence should be addressed to Pengcheng Li; lipengcheng1986@yeah.net

Received 28 June 2013; Accepted 1 August 2013

Academic Editor: Xiao Ping Chen

Copyright © 2013 Pengcheng Li et al. This is an open access article distributed under the Creative Commons Attribution License, which permits unrestricted use, distribution, and reproduction in any medium, provided the original work is properly cited.

A novel planar inverted-F antenna (PIFA) with dual-shortening points is proposed for multiband mobile handsets. The antenna comprises a meandered strip, a feeding point, two shortening points, and a slotted ground plane. For bandwidth enhancement of DCS/PCS/UMTS/WLAN 11.b/LTE2300/2500 and IMT-Advanced (International Mobile Telecommunications-Advanced), the antenna applies a dual-shortening points design, which generates a multimode between 1707 and 2815 MHz. The proposed antenna has good impedance matching characteristics for GSM (824–960 MHz)/DCS (1710–1880 MHz)/PCS (1850–1990 MHz)/UMTS (1920–2170 MHz)/LTE (2300–2400 MHz, 2500–2690 MHz)/WLAN 11.b (2400–2480 MHz) and IMT-A (4200–4800 MHz). The measured radiation efficiencies of the proposed antenna were all higher than 60% in GSM850/900, DCS/PCS, UMTS, LTE2300/2500, and WLAN 802.11 b, and it is up to 86% in IMT-A.

1. Introduction

With the rapid development of wireless communications, the multistandard mobile communication systems (MSMCS) are required with low cost and compact size. Recently, the long-term evolution (LTE) system is introduced to afford better mobile services to the wireless wide area network (WWAN) and 4G (IMT-Advanced) [1–3]. Owing to the overall size limited for the placing of mobile terminal antenna, it becomes more difficult to achieve wide bandwidths. Conventional planar inverted-F antennas (PIFAs) are no longer a suitable option because of narrow bandwidth.

In order to obtain a wide frequency band, the coupled-fed structure is usually applied [4–7]. However, the performance, especially the high-frequency band, is susceptible to the width of the coupling gap. It is difficult to manufacture, and the cost will be increased significantly. Also, it is not suitable for IMT-A (4200–4800 MHz) operation. In order to obtain a compact-size antenna with large and multiple-frequency band, many other constructions for PIFA are applied with probe feeding [1–3, 8]. However, in these designs, it is difficult to realize multiband and wideband operations at the same time. Besides, with microelectromechanical systems (MEMS) element [4–7, 9], the cost is increased inevitably.

In this paper, a compact and low-profile antenna is presented. The proposed design has a wide bandwidth, a reduced size, and a high efficiency [10–13]. The presented PIFA occupies a small volume of $46 \times 19 \times 5.5 \text{ mm}^3$. In particular, low-frequency band operation is achieved by two parallel open-end slots on the ground plane. Based on the joint disposition of the PIFA and a meandered monopole in the structure, the multiband operation is realized. Reflection coefficient less than -6 dB is obtained in 704–970 MHz (31.8% relative bandwidth, GSM850/900), 1575–2820 MHz (56.7% relative bandwidth, DCS/PCS/UMTS/LTE2300/25000), and 3850–5490 MHz (35.1% relative bandwidth, IMT-A), respectively.

Another issue of mobile terminal antenna is the radiation efficiency. In our design, the efficiency is up to 69% at low-frequency band, it and is more than 52% in the high-frequency band. The structure of the rest of the paper is given as follows. In Section 2, geometric structure and prototype of the PIFA is first presented. With dual-shortening point structure, the effect of antenna geometric parameters on performance is discussed in details. To validate our design, simulation and measurement results are demonstrated in Section 3 for comparison. Finally, conclusions are summarized in Section 4.

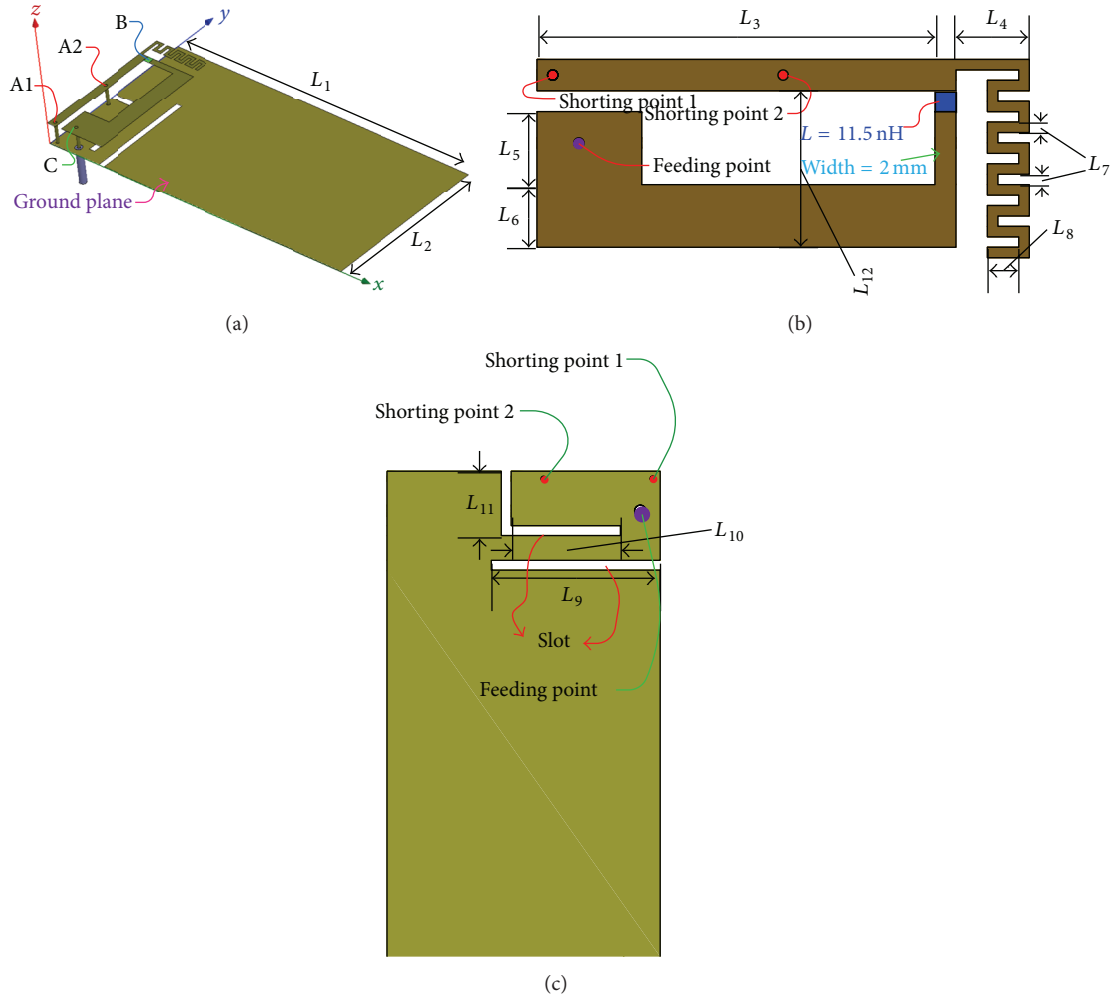


FIGURE 1: Proposed antenna configuration: (a) geometry of the proposed antenna, (b) detailed dimensions of the patch (top view), and (c) detailed dimensions of the ground plane (back view).

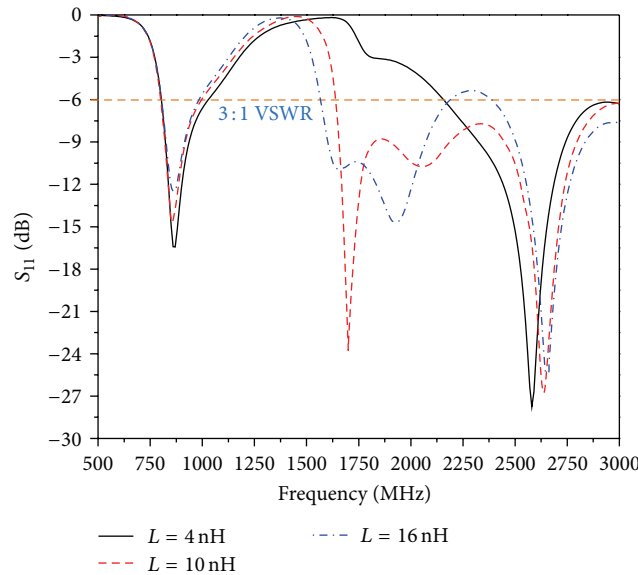


FIGURE 2: Simulated S parameter as a function of L.

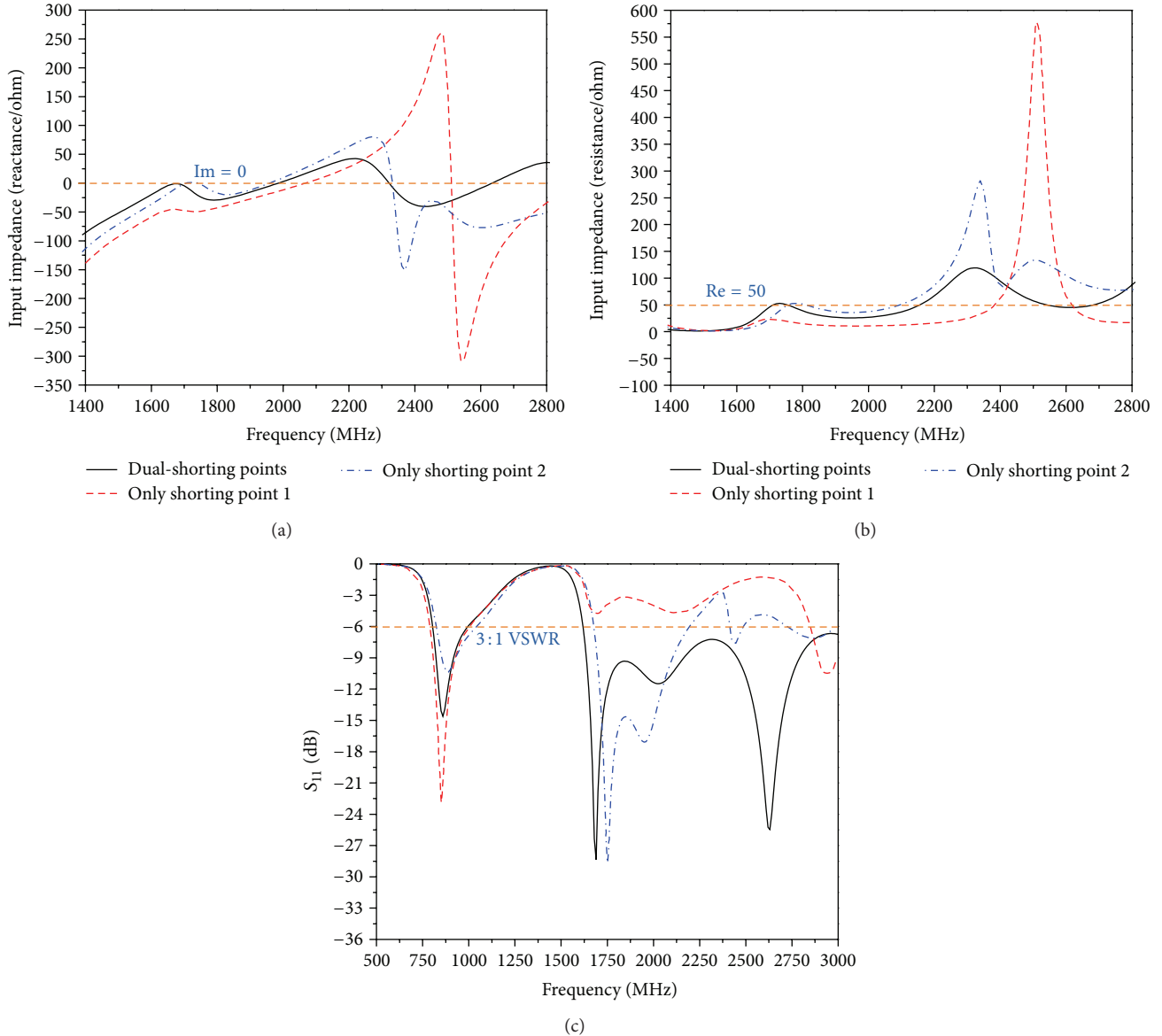


FIGURE 3: Simulated results with shorting points 1 and 2: (a) input impedance (reactance), (b) input impedance (resistance), and (c) S_{11} parameter.

2. Antenna Design and Parametric Study

The proposed antenna structure is shown in Figure 1. Length of handset boxes model used in the simulation and measurement is as those used today.

Its dimensions are given as follows: $L_1 = 110$ mm, $L_2 = 55$ mm, $L_3 = 38$ mm, $L_4 = 6$ mm, $L_5 = 8$ mm, $L_6 = 6$ mm, $L_7 = 1$ mm, $L_8 = 3$ mm, $L_9 = 32$ mm, $L_{10} = 24$ mm, $L_{11} = 10$ mm, $L_{12} = 10$ mm, and $L_{13} = 40$ mm. The little inductor is only 2×2 mm². But the presented PIFA totally occupies 46×19 mm².

Figure 1(a) shows the 3D mode of the proposed antenna. Points A (A1 and A2) and point C are the shorting points and the feeding point, respectively. For practical mobile

handset application, the PIFA is fed using a 50 ohm mini-coaxial line at point C. At point B, there is a chip-inductor-loaded strip which contributes to a wideband covering the DCS/PCS/UMTS/LTE2300/2500 and WLAN 11.b operation [9–12, 14–16]. The chip inductor used in the PIFA has an inductance of 11.5 nH. With the shorting points A1 and A2 in Figures 1(a) and 1(b), the meandered strip is proposed as a PIFA with two shorting points. In Figure 1(c), the two slots of the ground plane are applied for the low-frequency resonant band and for enhancing the antenna return loss in the lower part of the band [7, 9, 14–16].

Based on the bandwidth specification of 3:1 VSWR (6 dB return loss), which is widely approved as the fundamental design requirement of the internal handset antenna, the

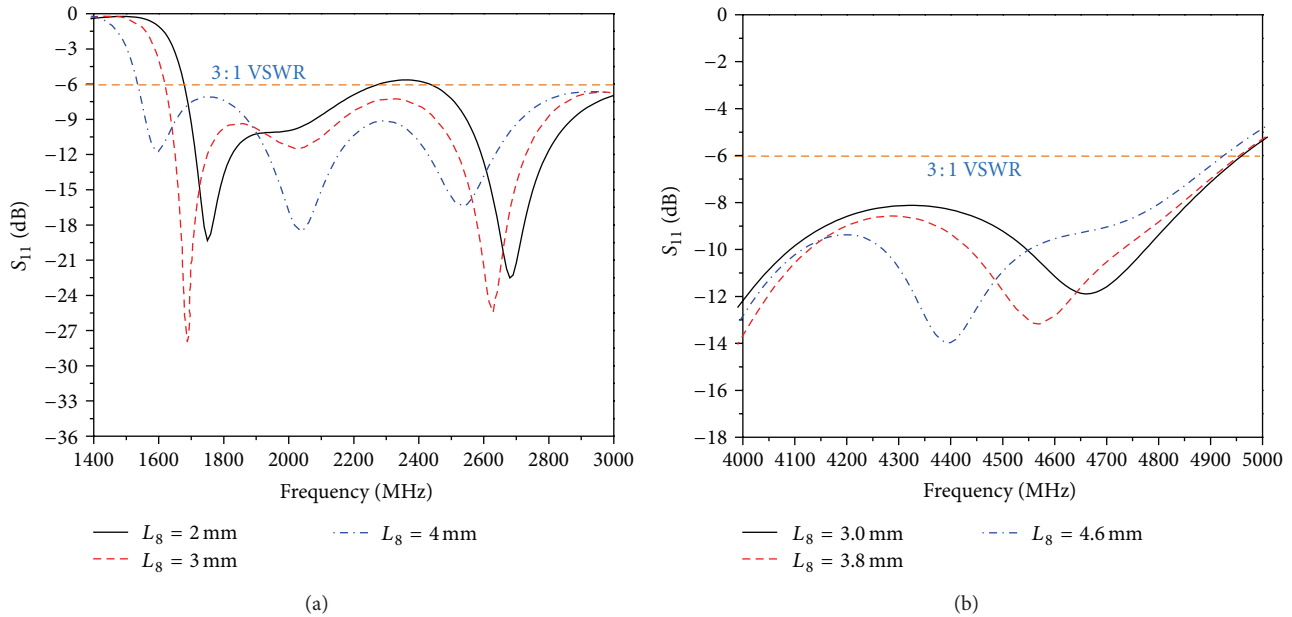


FIGURE 4: S parameter as a function of (a) L_8 (1400–3000 MHz) and (b) L_8 (4000–5000 MHz).

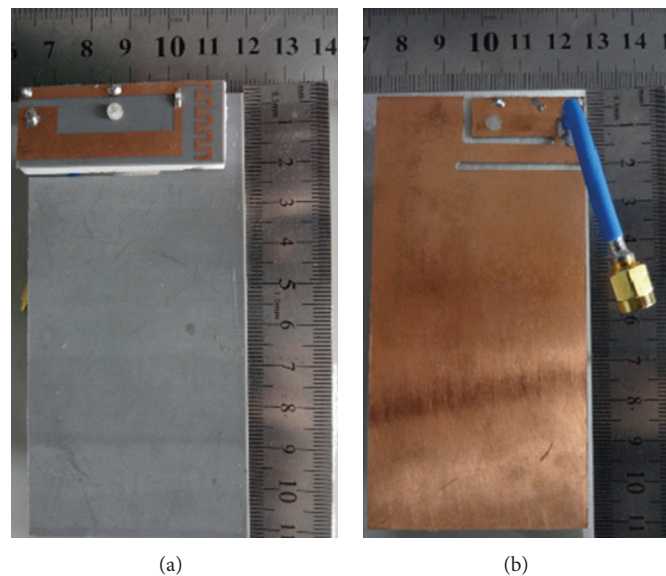


FIGURE 5: Photos of the manufactured antenna: (a) top side and (b) back side.

simulated S parameter of the proposed PIFA covers 745–1175 MHz, 1707–2815 MHz, and 3600–4900 MHz [11–13, 17–21]. The chip inductor with an inductance of 11.5 nH (L) is applied to the proposed PIFA. This chip inductor is used to improve the bandwidth required for DCS/PCS.

Figure 2 shows the influence of the chip inductor L for S parameter. Stronger influence on the impedance matching of DCS/PCS/UMTS can be observed, while the inductor L is changed from 4 to 16 nH. When a smaller inductance is used, the obtained bandwidth is decreased due to the decreasing of its resonant mode. After the optimizing, the impedance matching is improved when L is 11.5 nH. A comparison of the simulation reflection coefficient and the

input impedance (including the real and imaginary parts) is presented in Figure 3. Quite different from the obtained two resonant modes at about 1800 and 2600 MHz of the proposed PIFA, there is only one resonant mode excited at about 1900 for the single-shortened point antenna. The structure is helpful in achieving better impedance matching for UMTS/WLAN 11.b/LTE2300/2500 operation. In addition, as seen in Figure 3(c), the excited resonant mode for the higher-frequency band (2300–3000 MHz) is contributed by dual-shortening points.

The resonant mode at 1700 MHz and 2600 MHz also shifts down with the increasing of the length of the meandered strip (the function L_8). In Figure 4(a), the simulated S_{11}

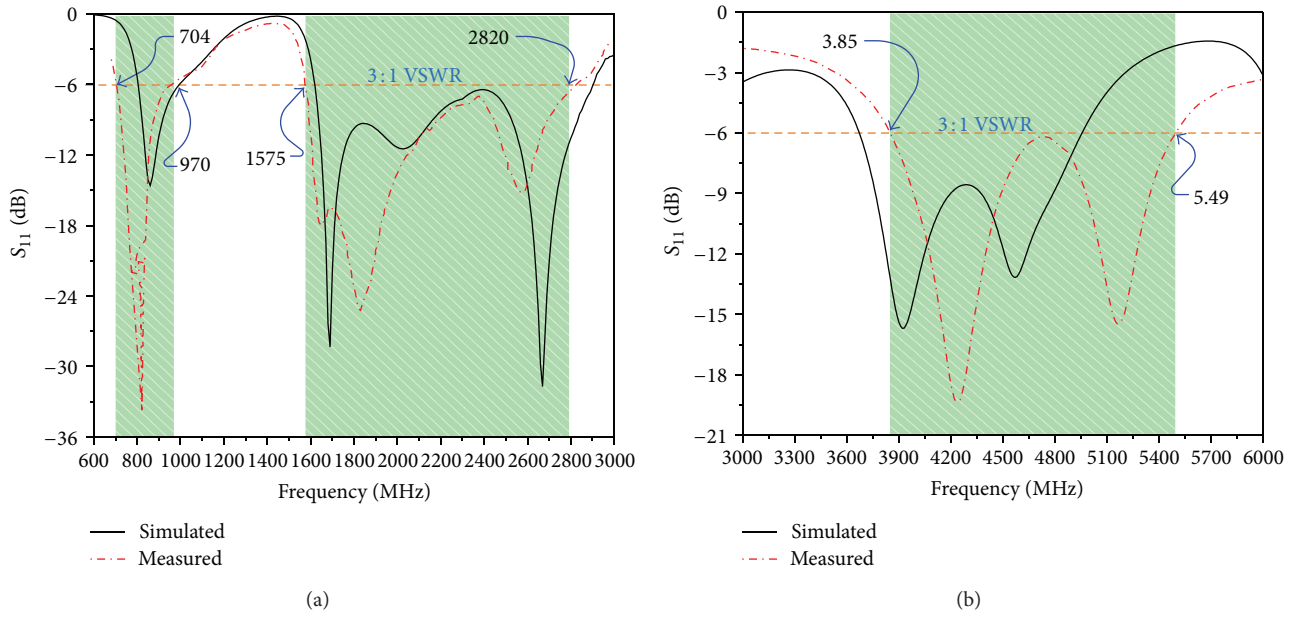


FIGURE 6: Measured S parameter and simulated S parameter: (a) 600–3000 MHz and (b) 3000–6000 MHz.

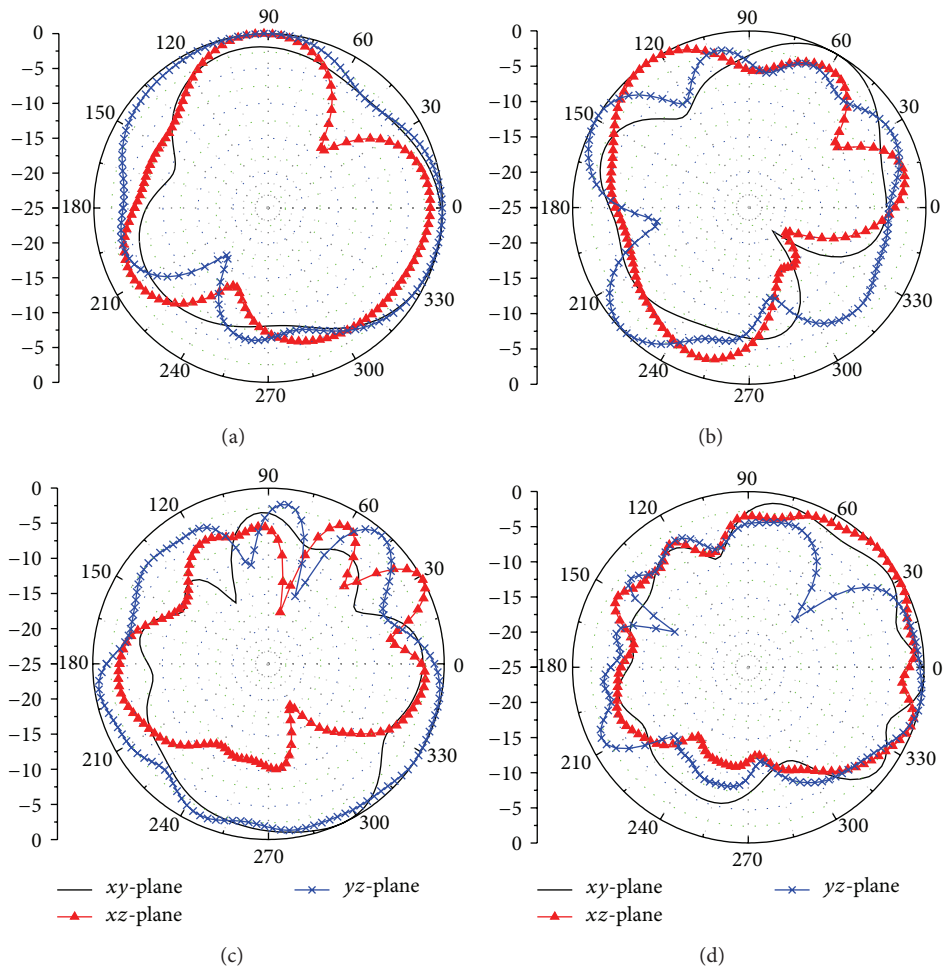


FIGURE 7: Measured 2D radiation patterns: (a) 900 MHz, (b) 1900 MHz, (c) 2500 MHz, and (d) 4500 MHz.

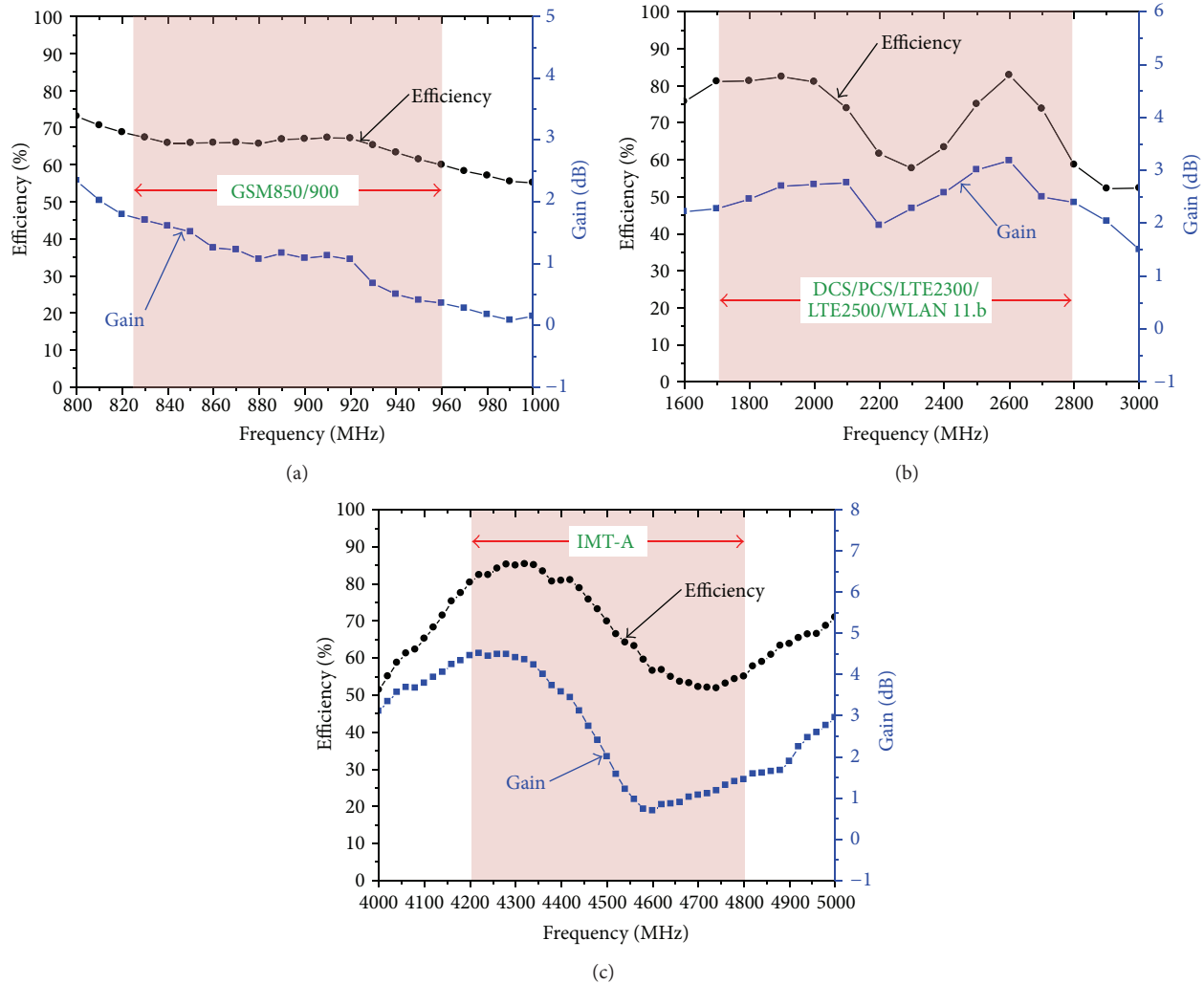


FIGURE 8: Measured antenna peak gain and radiation efficiency: (a) GSM850/900, (b) DCS1800/PCS1900/UMTS/WLAN 11.b/LTE2300/2500, and (c) IMT-A.

(1400–3000 MHz) is presented when the length L_8 varied from 2 mm to 4 mm. Besides, other parameters of the antenna are the same as given in Figure 1. Strong effects on the excited resonant modes indicate that proper selection of the L_8 is important in the proposed PIFA. The impedance matching over the DCS/PCS band is also strengthened. The simulated results of three different lengths $L_8 = 3, 3.8,$ and 4.6 mm are presented in Figure 4(b). Similar results can be observed compared with the results shown in Figure 4(a). The length L_8 of the meandered strip has a significant effect on the band of 4200–4800 MHz (IMT-A).

3. Measured Results

Based on the parameters study in Section 2, the PIFA prototype is manufactured as shown in Figure 5. Figure 6 presents the measured S parameter and the simulated S parameter. Because the value of L is not accurate to 11.5 nH, the measured data result is even better than that of the simulation. Three wide operating bands have been obtained for the antenna.

The radiation patterns, the total efficiency, and the peak gain are measured by the SATIMO measurement system. Figure 7 shows the normalized pattern in three principal planes. The measured total efficiency including the mismatching loss for the proposed antenna is presented in Figure 8. Over the lower band (800–1000 MHz and 1600–3000 MHz, Figures 8(a) and 8(b)), the total efficiency and the peak gain of the operation frequency band are 52%–55% and 0.3–2.8 dBi, respectively. For the upper band shown in Figure 8(c), the antenna gain varies from 0.7 to 4.1 dBi, while the total efficiency is better than 52%. From the obtained results, the proposed design for PIFA is a good option for practical internal mobile applications.

4. Conclusions

This paper presents a new design for PIFA. Using two open-end parallel slots in the ground plane, a significant improvement in the antenna operational bandwidth at the lower-frequency band can be achieved. The higher-frequency operating band is achieved by comprising two meandered

monopoles. Thus, triple-band impedance (704–970 MHz, 1575–2820 MHz, and 3850–5490 MHz) for $VSWR \leq 3$ is obtained. The main design dimensions of the meandered strip are studied and discussed. Measured results show that the proposed antenna has good radiation characteristics, including total efficiency and peak gain. With the presence of the multiband and the wideband features, the proposed design of PIFA is attractive for the practical mobile phones.

References

- [1] R. Sánchez-Montero, S. Salcedo-Sanz, J. A. Portilla-Figueras et al., "Hybrid PIFA-patch antenna optimized by evolutionary programming," *Progress in Electromagnetics Research*, vol. 108, pp. 221–234, 2010.
- [2] M. A. Ebrahimi-Ganjeh and A. R. Attari, "Interaction of dual band helical and PIFA handset antennas with human head and hand," *Progress in Electromagnetics Research*, vol. 77, pp. 225–242, 2007.
- [3] P. J. Soh, S. J. Boyes, G. A. E. Vandenbosch, Y. Huang, and S. L. Ooi, "On-body characterization of dual-band all-textile PIFAs," *Progress in Electromagnetics Research*, vol. 129, pp. 517–539, 2012.
- [4] R. Caso, A. D'Alessandro, A. A. Serra, P. Nepa, and G. Manara, "A compact dual-band PIFA for DVB-T and WLAN applications," *IEEE Transactions on Antennas and Propagation*, vol. 60, no. 4, pp. 2084–2087, 2012.
- [5] H. Wang and M. Zheng, "An internal triple-band WLAN antenna," *IEEE Antennas and Wireless Propagation Letters*, vol. 10, pp. 569–572, 2011.
- [6] Y. Sung, "Compact Quad-band reconfigurable antenna for mobile phone application," *Electronics Letters*, vol. 48, no. 16, pp. 977–979, 2012.
- [7] P. Jack Soh, G. A. E. Vandenbosch, S. Liam Ooi, and N. Husna Mohd Rais, "Design of a broadband all-textile slotted PIFA," *IEEE Transactions on Antennas and Propagation*, vol. 60, no. 1, pp. 379–384, 2012.
- [8] Y. Zhu, F. Gao, X. Yang et al., "The effect of microwave emission from mobile phones on neuron survival in rat central nervous system," *Progress in Electromagnetics Research*, vol. 82, pp. 287–298, 2008.
- [9] R. Hossa, A. Byndas, and M. E. Bialkowski, "Improvement of compact terminal antenna performance by incorporating open-end slots in ground plane," *IEEE Microwave and Wireless Components Letters*, vol. 14, no. 6, pp. 283–285, 2004.
- [10] M. Y. Man, R. Yang, Z. Y. Lei, Y. J. Xie, and J. Fan, "Ultra-wideband planer inverted-F antennas with cut-etched ground plane," *Electronics Letters*, vol. 48, no. 14, pp. 817–818, 2012.
- [11] K.-J. Kim, S.-H. Lee, B.-N. Kim et al., "Small antenna with a coupling feed and parasitic elements for multiband mobile applications," *IEEE Antennas and Wireless Propagation Letters*, vol. 10, pp. 290–293, 2011.
- [12] J. Kim, C. Yang, T. Yun, and C. Jung, "Multimode multi-band (VHF/UHF/L/802.11a/b) antennas for broadcasting and telecommunication services," *IEEE Antennas and Wireless Propagation Letters*, vol. 10, pp. 41–44, 2011.
- [13] C.-H. Chang and K.-L. Wong, "Printed $\lambda/8$ -PIFA for penta-band WWAN operation in the mobile phone," *IEEE Transactions on Antennas and Propagation*, vol. 57, no. 5, pp. 1373–1381, 2009.
- [14] K.-L. Wong, W.-Y. Chen, and T.-W. Kang, "On-board printed coupled-fed loop antenna in close proximity to the surrounding ground plane for penta-band WWAN mobile phone," *IEEE Transactions on Antennas and Propagation*, vol. 59, no. 3, pp. 751–757, 2011.
- [15] K.-L. Wong, W.-J. Chen, and T.-W. Kang, "Small-size loop antenna with a parasitic shorted strip monopole for internal WWAN notebook computer antenna," *IEEE Transactions on Antennas and Propagation*, vol. 59, no. 5, pp. 1733–1738, 2011.
- [16] K.-L. Wong, Y.-W. Chang, and S.-C. Chen, "Bandwidth enhancement of small-size planar tablet computer antenna using a parallel-resonant spiral slit," *IEEE Transactions on Antennas and Propagation*, vol. 60, no. 4, pp. 1705–1711, 2012.
- [17] A. P. Feresidis and Q. Li, "Miniaturised slits for decoupling PIFA array elements on handheld devices," *Electronics Letters*, vol. 48, no. 6, pp. 310–312, 2012.
- [18] Y. K. Park and Y. Sung, "A reconfigurable antenna for Quad-band mobile handset applications," *IEEE Transactions on Antennas and Propagation*, vol. 60, no. 6, pp. 3003–3006, 2012.
- [19] Z.-N. Ying, "Antennas in cellular phones for mobile communications," *Proceedings of the IEEE*, vol. 100, no. 7, pp. 2286–2296, 2012.
- [20] S. M. Mazinani and H. R. Hassani, "A wideband internal plate loaded planar monopole antenna for mobile handset," *Journal of Electromagnetic Waves and Applications*, vol. 23, no. 10, pp. 1273–1282, 2009.
- [21] B. H. Sun, J. F. Li, and Q. Z. Liu, "Compact broadband printed antenna for multi-functional mobile terminals," *Journal of Electromagnetic Waves and Applications*, vol. 22, no. 8-9, pp. 1292–1298, 2008.

Research Article

A UWB Band-Pass Antenna with Triple-Notched Band Using Common Direction Rectangular Complementary Split-Ring Resonators

Bo Yan, Di Jiang, Ruimin Xu, and Yuehang Xu

School of Electronic Engineering, University of Electronic Science and Technology of China, Chengdu 611731, China

Correspondence should be addressed to Di Jiang; merryjiangdi@163.com

Received 3 June 2013; Accepted 10 July 2013

Academic Editor: Guo Qing Luo

Copyright © 2013 Bo Yan et al. This is an open access article distributed under the Creative Commons Attribution License, which permits unrestricted use, distribution, and reproduction in any medium, provided the original work is properly cited.

A novel ultrawideband (UWB) antenna which has a triple-band notch function is presented. The proposed antenna can block interfering signals from C-band satellite communication systems, IEEE802.11a, and HIPERLAN/2 WLAN systems for example. The antenna is excited by using novel common direction rectangular complementary split-ring resonators (CSRR) fabricated on radiating patch of the dielectric substrate with coplanar waveguide (CPW) feed strip line. The voltage standing wave ratio (VSWR) of the proposed antenna is less than 2.0 in the frequency band from 2.8 to 12 GHz, while showing a very sharp band-rejection performance at 3.9 GHz, 5.2 GHz, and 5.9 GHz. The measurement results show that the proposed antenna provides good omnidirectional field pattern over its whole frequency band excluding the rejected band, which is suitable for UWB applications.

1. Introduction

Commercial ultrawideband (UWB) systems require small low-cost antennas with omnidirectional radiation pattern and large bandwidth. It is a well-known fact that planar monopole antennas present really appealing physical features, such as simple structure, small size, and low cost. Due to all these interesting characteristics, planar monopoles are extremely attractive to be used in emerging UWB applications, and growing research activity is being focused on them. However, their size and bandwidth should be improved, and also their shapes should have simple structure for easy manufacturing [1]. Recently, many techniques have been examined to enhance the antenna bandwidth including the truncated ground plane with the use of an L-shaped notch in the lower corner and an inverted T-shaped notch in the middle [2]. In this proposed antenna, two new slots are used in the ground plane; by using these notches, an additional two resonances are excited, and hence the bandwidth is increased [3]. For UWB systems, the frequency range is between 3.1 and 10.6 GHz, and hence it can interfere with the existing wireless

communication system such as wireless local area network (WLAN) (5.15–5.35 GHz, 5.725–5.825 GHz), so the UWB antenna with a notch-band performance is required [4]. To generate the band-notch frequency, a planar monopole antenna with an inverted U-slot, small strip bar, and two U-shaped slots in the patch is proposed [5]. In this paper, a base swallow-shaped-patch (SSP) antenna is proposed to cover the UWB range, which has a UWB operating bandwidth with a tunable triple-notched frequency at 3.9 GHz, 5.2 GHz and 5.9 GHz. The band-notched operation is achieved by embedding codirectional modified rectangle CSRR slots on radiated patch. The CSRR is under investigation by researchers to implement left-hand materials the codirectional rectangle complementary split-ring resonator (CSRR) is promising for UWB antennas to ensure multiple notched bands [6]. Both triple-band-notched characteristics and compact size are achieved. The antenna has promising features, including good impedance matching performance over the whole operating frequency band, stable radiation patterns, and flexible frequency-notched function.

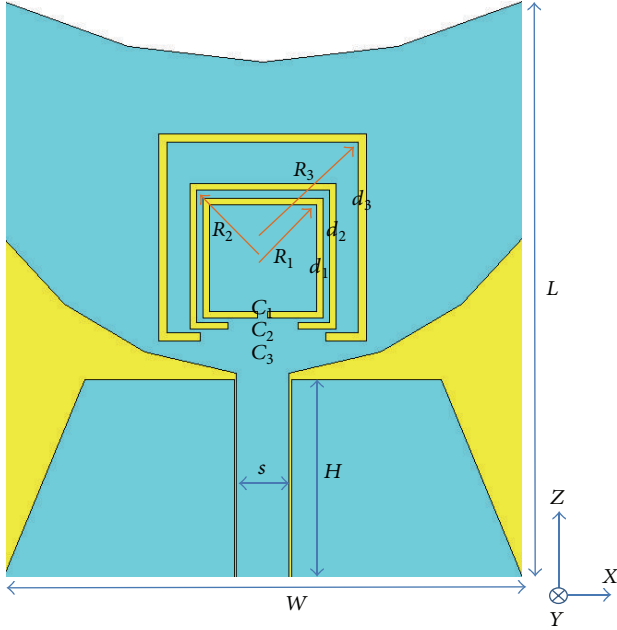


FIGURE 1: Geometry of antenna, with dimensions $R_1 = 3.75$ mm, $R_2 = 4.61$ mm, $R_3 = 6.6$ mm, $C_1 = 0.5$ mm, $C_2 = 3.35$ mm, $C_3 = 6$ mm, $d_1 = 0.3$ mm, $d_2 = 0.3$ mm, $d_3 = 0.4$ mm, $s = 2.5$ mm, $H = 9.8$ mm, $W = 25$ mm, and $L = 27.9$ mm.

2. Antenna Design

Figure 1 shows the configuration of the proposed antenna. It is printed on a 0.508 mm thick RT5880 substrate with the relative permittivity $\epsilon_r = 2.2$ and loss tangent $\tan \delta = 0.0009$. The CPW-fed antenna is composed of a swallow-shaped radiator on the same layer and a trapezoidal ground plane. In designing the antenna, the lowest operating frequency depends on the largest triangle complementary split-ring resonators [7]. Compared with the symmetrical antennas, the radiator is located at an offset distance from the center of the structure to feature an asymmetrical shape, which has the advantage of easing the requirement on the space for placing band-rejected elements. The band-notched performance can be obtained by adding three-quarter-wavelength band-rejected elements. The problem of interference with C-band (3.7–4.2 GHz) satellite communication systems, lower WLAN band (5.15–5.35 GHz), and upper WLAN band (5.725–5.825 GHz) can be settled by rectangle ring3 (R_3), rectangle ring2 (R_2), and rectangle ring1 (R_1), respectively. It is found that, by tuning the length of the codirectional rectangular complementary split-ring resonators ring to be approximately a quarter wavelength at the desired rejected frequency, an additional resonance can be introduced to the antenna response, causing the antenna to be nonresponsive at that frequency. The band-notched performance at 5.15 GHz–5.35 GHz and 5.725 GHz–5.825 GHz can be improved by allocating a combination of rectangle ring2 and rectangle ring1. It is also worthwhile mentioning that, when considering the arrangement of the band-rejected elements, the mutual coupling can be avoided at the notched frequencies by placing rectangle ring3, rectangle

ring2, and rectangle ring1, since the lower WLAN band and the upper WLAN band are close to each other [8]. As a result, the rejected frequency can be easily tuned by changing each rectangle ring independently [9].

Figure 2 shows the current distributions at three center-notched bands. The dimensions of three co-directional rectangle complementary SRRs are corresponding to three notched bands. When the antenna is working at the center of lower-notched band near 3.9 GHz, the outer complementary SRR behaves as a separator in Figure 2(a), which almost has no relation to the other band notches [10]. Similarly, the middle complementary SRR operates as a second separator for the center of middle-notched band near 5.2 GHz in Figure 2(b). From Figure 2(c), the upper-notched band near 5.9 GHz is ensured by the inner complementary SRR [11]. Additionally, as a certain current crowded on the ground plane near the CPW feed line would affect the antenna performance, we find that the dimension of ground plane, especially, has a significant effect on the triple-band-notch performance, as well as impedance bandwidth [12].

3. Results and Discussion

The proposed SSP antenna is successfully fabricated and measured, with the optimized size shown in Figure 3. Figure 4 displays the measured and simulated VSWR for the antenna [13]. It is seen that the proposed antenna exhibits three notched bands of 3.68 GHz–4.20 GHz, 5.05 GHz–5.38 GHz, and 5.72 GHz–6.08 GHz, respectively, covering C-band satellite communication systems and WLAN, while maintaining wideband performance from 2.8 to 12 GHz for VSWR < 2, covering the entire UWB frequency band [14]. The measured VSWR is slightly lower than the simulated result and it may be due to loss tangent $\tan \delta$ of the substrate and the tolerance in manufacturing.

Figures 5 and 6 show the simulated and measured 2D radiation patterns, respectively, at frequencies of 3.5 GHz, 5 GHz, and 7 GHz for the proposed UWB antenna. Measurements of the radiation patterns of the prototype are carried out in an anechoic chamber [15]. It is seen that the radiation patterns in xy -plane (H -plane) are almost omnidirectional and the radiation patterns in yz -plane (E -plane) are monopole alike. Clearly, the triple-notch UWB antenna has a good radiation performance when it operates at 3.5 GHz, 5 GHz, and 7 GHz [16]. By comparing with Figures 5 and 6, the measured radiation patterns show slight deterioration in copolarization and cross-polarization electric field. To some extent, this is because of the measurement environment. Particularly, the SMA feeding connector may have interference with radiation field in the test. Distortions in the E -plane patterns begin to occur at higher frequencies because the radiating elements are no longer small relative to those wavelengths.

Figure 7 reveals its measured peak gain and simulated realized gain versus frequency. As can be seen from Figure 7, the simulation result and measured result fit with each other well. It is observed that the antenna keeps a stable antenna

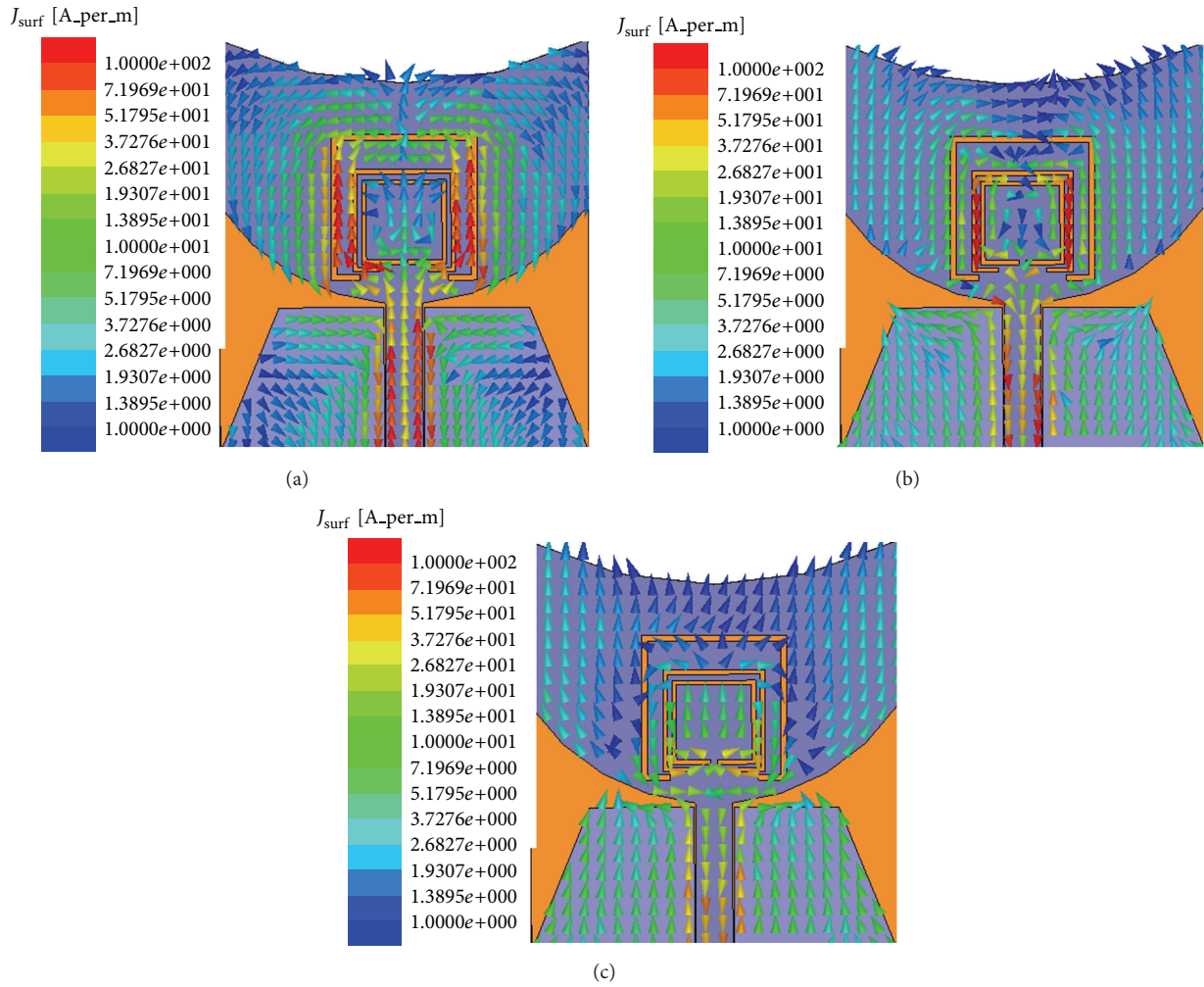


FIGURE 2: The current distribution at different frequencies (a) 3.9 GHz, (b) 5.2 GHz, and (c) 5.9 GHz.

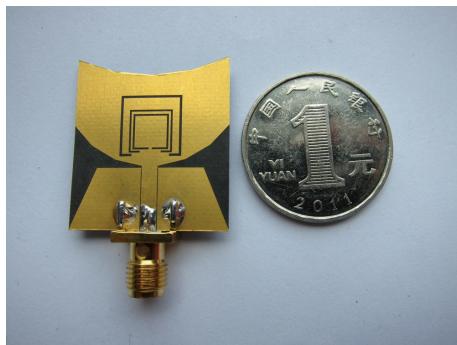


FIGURE 3: Photograph of the proposed antenna.

gain about 3-4 dBi but decreases significantly to about -10 dBi, -6.5 dBi, and -5 dBi at the three notched bands, which demonstrates that the antenna has great triple-band-notched characteristics.

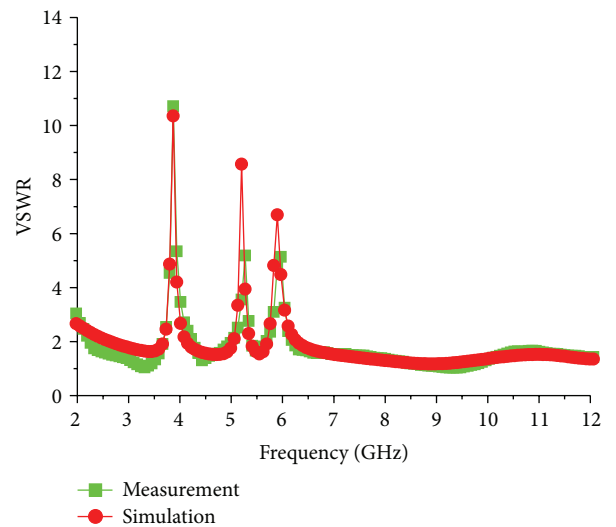


FIGURE 4: Comparison of simulated and measured VSWR of the proposed antenna.

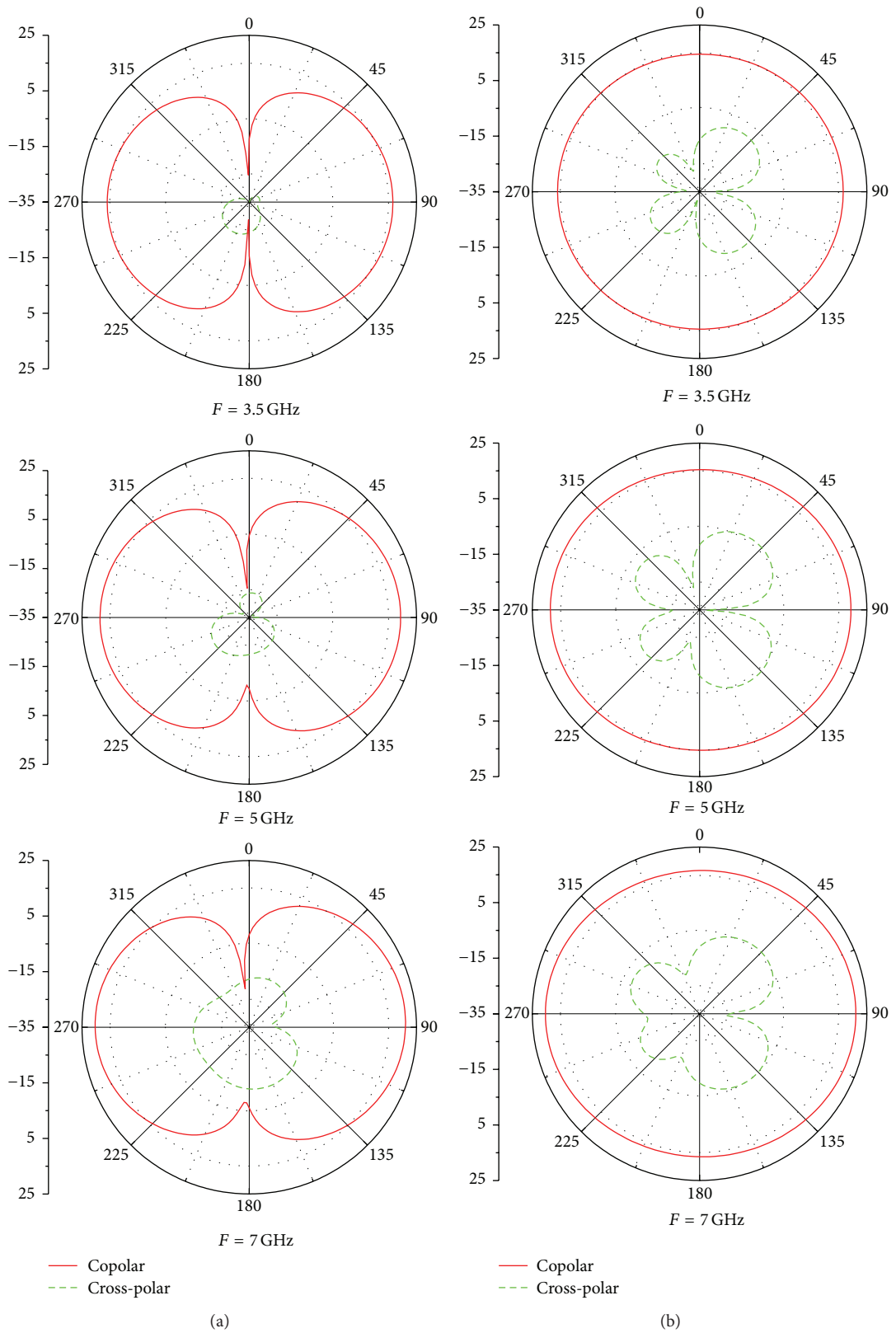


FIGURE 5: Simulated radiation patterns at (a) yz -plane and (b) xy -plane.

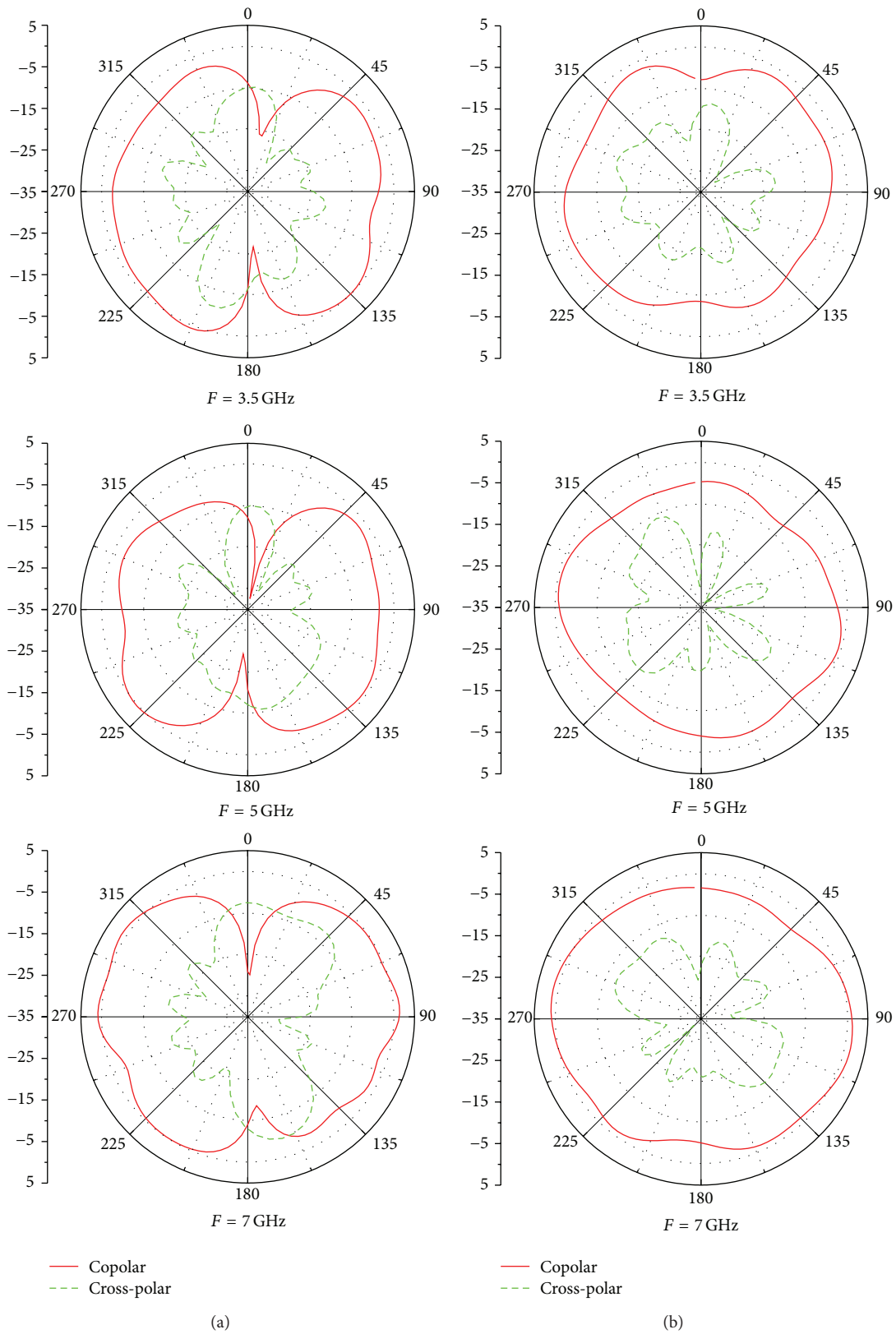


FIGURE 6: Measured radiation patterns at (a) yz -plane and (b) xy -plane.

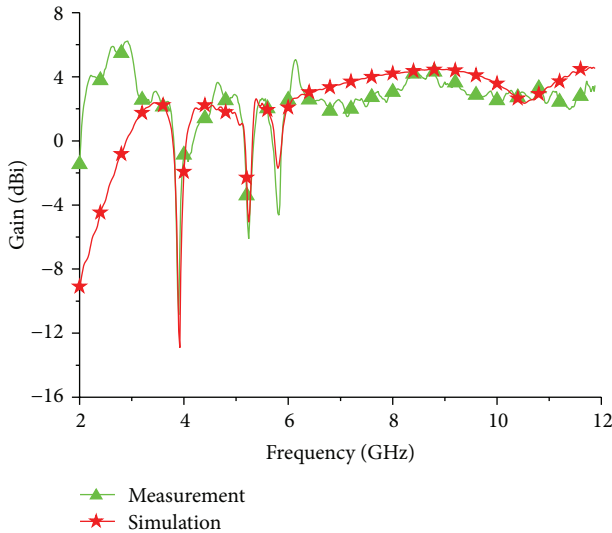


FIGURE 7: Comparison of simulated and measured gains of the proposed antenna.

4. Conclusion

A new printed asymmetrical UWB antenna providing multiple-band-notched function has been presented. The antenna can operate in a wide frequency range and feature improved band-notched performance. The proposed design is validated by the comparison between simulation and measurement. It can be used to avoid interference with other systems operating in the C-band satellite communication systems or WLAN bands.

Acknowledgments

This work is supported by the National Natural Science Foundation of China (Grant no. 61106115) and the Fundamental Research Funds for the Central Universities (ZYGX2011J018).

References

- [1] Z. N. Chen, N. Yang, Y.-X. Guo, and M. Y. W. Chia, "An investigation into measurement of handset antennas," *IEEE Transactions on Instrumentation and Measurement*, vol. 54, no. 3, pp. 1100–1110, 2005.
- [2] L. Liu, Y. Z. Yin, C. Jie, J. P. Xiong, and Z. Cui, "A compact printed antenna using slot-type CSRR for 5.2 GHz/5.8 GHz band-notched UWB application," *Microwave and Optical Technology Letters*, vol. 50, no. 12, pp. 3239–3242, 2008.
- [3] M. Naser-Moghadasi, G. R. Dadashzadeh, A.-A. Kalteh, and B. S. Virdee, "Design of a novel band-notched slot patch antenna for UWB communication systems," *Microwave and Optical Technology Letters*, vol. 52, no. 7, pp. 1599–1603, 2010.
- [4] D. Piazza, P. Mookiah, M. D'Amico, and K. R. Dandekar, "Experimental analysis of pattern and polarization reconfigurable circular patchantennas for MIMO systems," *IEEE Transactions on Vehicular Technology*, vol. 59, no. 5, pp. 2352–2362, 2010.
- [5] S. L. Steven Yang, A. A. Kishk, and K. F. Lee, "Frequency reconfigurable U-slot microstrip patch antenna," *IEEE Antennas and Wireless Propagation Letters*, vol. 7, pp. 127–129, 2008.
- [6] D. Jiang, Y. Xu, R. Xu, and W. Lin, "Compact dual-band-notched UWB planar monopole antenna with modified CSRR," *Electronics Letters*, vol. 48, no. 20, pp. 1250–1252, 2012.
- [7] S. Nikolaou, N. D. Kingsley, G. E. Ponchak, J. Papapolymerou, and M. M. Tentzeris, "UWB elliptical monopoles with a reconfigurable band notch using MEMS switches actuated without bias lines," *IEEE Transactions on Antennas and Propagation*, vol. 57, no. 8, pp. 2242–2251, 2009.
- [8] S. Nikolaou, R. Bairavasubramanian, C. Lugo Jr. et al., "Pattern and frequency reconfigurable annular slot antenna using pin diodes," *IEEE Transactions on Antennas and Propagation*, vol. 54, no. 2, pp. 439–448, 2006.
- [9] Ansoft High Frequency Structure Simulation (HFSS).ver. 10 AnsoftCorp, 2005.
- [10] F. Falcone, T. Lopetegui, M. A. G. Laso et al., "Babinet principle applied to the design of metasurfaces and metamaterials," *Physical Review Letters*, vol. 93, no. 19, Article ID 197401, 2004.
- [11] J. Ding, Z. Lin, Z. Ying, and S. He, "A compact ultra-wideband slot antenna with multiple notch frequency bands," *Microwave and Optical Technology Letters*, vol. 49, no. 12, pp. 3056–3060, 2007.
- [12] Y. D. Dong, W. Hong, Z. Q. Kuai et al., "Development of ultra-wideband antenna with multiple band-notched characteristics using half mode substrate integrated waveguide cavity technology," *IEEE Transactions on Antennas and Propagation*, vol. 56, no. 9, pp. 2894–2902, 2008.
- [13] K. S. Ryu and A. A. Kishk, "UWB antenna with single or dual band-notches for lower WLAN band and upper WLAN band," *IEEE Transactions on Antennas and Propagation*, vol. 57, no. 12, pp. 3942–3950, 2009.
- [14] X. N. Low, Z. N. Chen, and T. S. P. See, "A UWB dipole antenna with enhanced impedance and gain performance," *IEEE Transactions on Antennas and Propagation*, vol. 57, no. 10, pp. 2959–2966, 2009.
- [15] M.-C. Tang, S. Xiao, T. Deng et al., "Compact UWB antenna with multiple band-notches for WiMAX and WLAN," *IEEE Transactions on Antennas and Propagation*, vol. 59, no. 4, pp. 1372–1376, 2011.
- [16] A. Nouri and G. R. Dadashzadeh, "A compact UWB band-notched printed monopole antenna with defected ground structure," *IEEE Antennas and Wireless Propagation Letters*, vol. 10, pp. 1178–1181, 2011.

Research Article

Substrate Integrated Waveguide Fed Cavity Backed Slot Antenna for Circularly Polarized Application

Xiao Hong Zhang, Guo Qing Luo, and Lin Xi Dong

Key Laboratory of RF Circuits & System of Ministry of Education, Microelectronic CAD Center, Hangzhou Dianzi University, Xiasha Higher Education Park, Hangzhou 310018, China

Correspondence should be addressed to Guo Qing Luo; luoguoqing@hdu.edu.cn

Received 13 June 2013; Accepted 28 June 2013

Academic Editor: Bing Liu

Copyright © 2013 Xiao Hong Zhang et al. This is an open access article distributed under the Creative Commons Attribution License, which permits unrestricted use, distribution, and reproduction in any medium, provided the original work is properly cited.

A novel planar low-profile cavity-backed slot antenna for circularly polarized applications is presented in this paper. The low-profile substrate integrated waveguide (SIW) cavity is constructed on a single PCB substrate with two metal layers on the top and the bottom surfaces and metallized via array through the substrate. The SIW cavity is fed by a SIW transmission line. The two orthogonal degenerate cavities resonance TM_{110} mode are successfully stimulated and separated. The circularly polarized radiation has been generated from the crossed-slot structure whose two arms' lengths have slight difference. Its gain is higher than 5.4 dBi, the peak cross-polarization level is lower than -22 dB, and the maximum axial ratio (AR) is about -1.5 dB. Compared with the previous presented low-profile cavity-backed slot antenna work, the spurious radiation from the proposed antenna's feeding element is very low and it has less interference on the following circuits.

1. Introduction

With development of modern wireless communication technology, high-performance antennas become more and more important. Cavity-backed antenna, as one of high gain antennas, has been extensively investigated by many researchers. The conventional cavity-backed antenna is very bulky. Its cavity height is roughly one-quarter wavelength. It is also heavy and expensive because it is fully metallic and is fabricated by mechanical process. Some novel cavity-backed antennas are presented in [1–5], in which the substrate integrated waveguide technique is employed in the cavity design. The backed cavity is fully constructed on a single PCB substrate with metallized via array through the substrate and two metallic layers on the top and the bottom surfaces of the substrate. When some conditions are satisfied, the attenuation constant will be small enough and the leakage from two adjacent vias can be neglected. Then, the novel SIW cavity is equivalent to the conventional metallic cavity. These novel cavity-backed antennas can keep the high radiation performance of conventional cavity-backed antenna, such as high gain, low back lobe, and

low cross-polarization level. They can also retain the advantages of the conventional planar antenna, such as low profile, light weight, good conformability, and seamless integration with planar circuits. They can be easily fabricated by using the low-cost single-layer printed circuit board (PCB) process.

Linearly polarized SIW cavity-backed slot antenna has been presented in [1], in which the antenna is fed by transition between microstrip lines and grounded coplanar waveguides (CPWG). Dual frequency, dual linearly polarized SIW cavity-backed antenna has been investigated in [2], in which a single CPWG feed element is used to stimulate two cavity resonances in the SIW cavity. Circularly polarized SIW cavity-backed antenna also has been discussed in [2], in which a single CPWG is used to excite two orthogonal and degenerate cavity resonances in a circular or square SIW cavity. In order to avoid the spurious radiation generated by the opening feed structures such as microstrip line, coplanar waveguide (CPW), and CPWG, a single probe SIW cavity crossed-slot antenna for circularly polarized application has been proposed in [3]. Even though the spurious radiation of the feeding structure has been eliminated, one drawback of

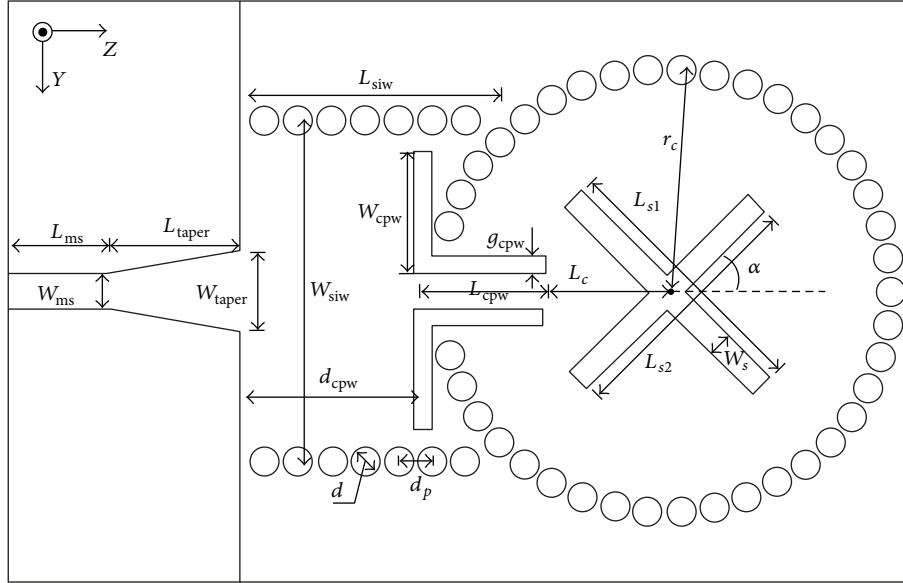


FIGURE 1: Geometry of the proposed antenna.

hardly planar integration has been introduced for the probe feed.

A CPW-fed filtering antenna has been presented in [4], in which its filtering performance is generated by two cascading SIW cavities. Slot etched in the SIW cavity metallic surface not only serves as a radiator but also acts as an equivalent load to the filter. This filtering antenna is fed by a composite structure which comprise CPWG and SIW. A closely spaced array of SIW cavity-backed slot antennas has been investigated in [5], in which a low mutual coupling antenna array has been achieved. The presented antenna array is also fed by a composite structure comprising stripline and SIW, and then a low mutual coupling is achieved by the fully closed feeding structure. Circularly polarized SIW cavity-backed patch antennas with two different feeding transitions are shown in [6], in which the two feeding transitions are constructed by microstrip line to SIW and coax line to SIW. The circularly polarized SIW cavity-backed square ring slot antenna is shown in [7], in which the antenna is fed by coax line to SIW transition.

In this paper, we propose a SIW cavity-backed crossed, slot antenna for circularly polarized application. Its feeding network comprise CPWG and SIW. The whole antenna including its feeding element is a completely closed structure except the crossed-slot radiator. The spurious radiation generated by the feeding element is suppressed and the mutual coupling interference between the proposed antenna and the following circuits is greatly reduced.

2. Antenna Design

Geometrical configuration of the proposed circularly polarized SIW cavity-backed crossed-slot antenna is shown in Figure 1. Its circular backed cavity is constructed by metalized vias' arrays on a single substrate. Crossed slot etched on the bottom metallic surface is used as radiator, whose

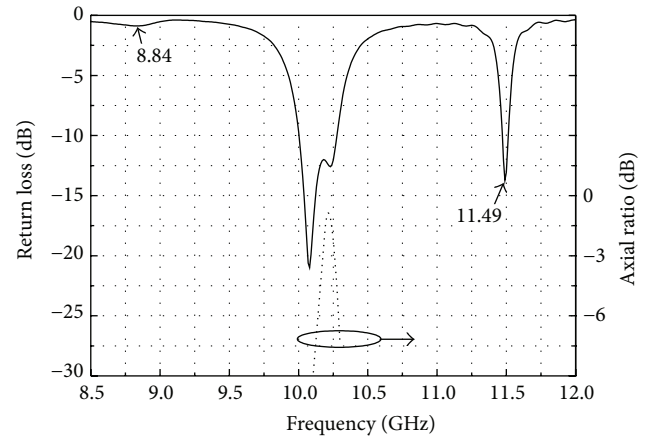


FIGURE 2: Simulated return loss and axial ratio of the proposed antenna.

two arms are orthogonal and has the same width W_s and different lengths of L_{s1} and L_{s2} . A composite feeding element, comprising SIW and CPWG, is located at the angular bisector of the crossed slot and adopted to excite the circular SIW cavity. A transition between microstrip and SIW is introduced for convenience measurement. A sample of the proposed antenna has been discussed, and its detailed geometrical parameters are listed in Table 1.

Full wave simulations of the proposed antenna have been carried out by using commercial software, and its simulated return loss and the axial ratio (AR) are plotted in Figure 2. Frequency ranges of its return loss less than -10 dB are $10.04\sim 10.28$ GHz and $11.47\sim 11.52$ GHz and the measured AR more than -3 dB is $10.16\sim 10.26$ GHz, respectively. Frequency response of the proposed antenna is caused by some different cavity resonances generated in the SIW cavity. From Figures 3(a) and 3(b), it can be found that two cavity resonances

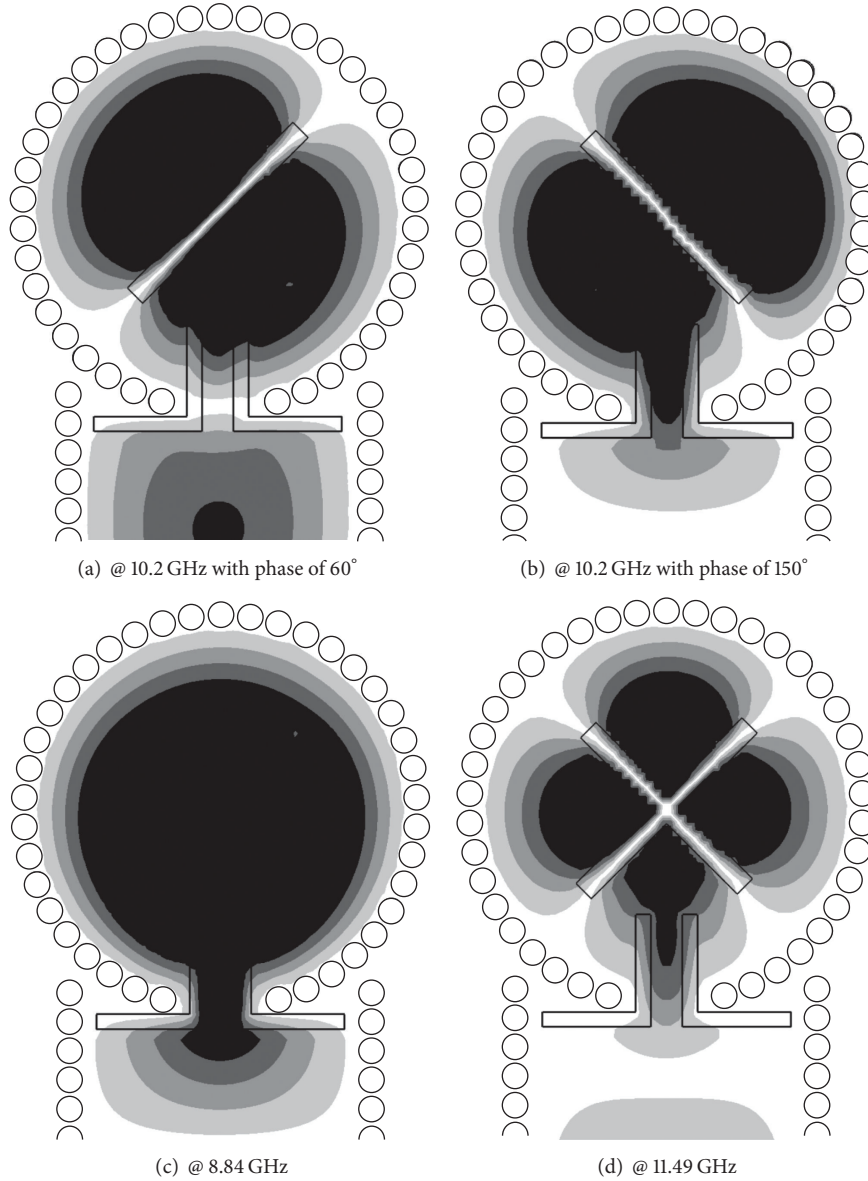


FIGURE 3: Electric field profiles of the proposed antenna.

TM_{110} have been generated in the circular SIW cavity at the frequency range of 10.04~10.28 GHz. These two orthogonal and degenerate cavity resonances TM_{110} can be successfully stimulated by tuning the two arms' lengths of the crossed slot with a slight difference.

The dominant electric field at the two sides of the crossed slot's two arms has opposite phase. There are transverse electric fields across the slot arms; thus, energy can be radiated into outer space by the crossed slot. Radiations from the two orthogonal arms have equal magnitude for the two orthogonal and degenerate resonances TM_{110} . A 90° phase difference has been achieved by tuning the length difference between the crossed-slot two arms. Then, circular polarization is produced in the far field. The simulated AR of the proposed antenna plotted in Figure 2 shows that the circularly polarized radiation has been generated at 10.16~10.26 GHz.

From Figures 2 and 3(c), it can be found that a weak TM_{010} cavity resonance has been stimulated at 8.84 GHz but no radiation can be generated for its field distribution. The TM_{210} cavity mode resonating at 11.49 GHz is a quadrupole mode. The electric field across the crossed-slot two arms has opposite polarity at its half two ends of each arm, and thus only a very weak radiation is produced.

3. Antenna Performance

A prototype of the proposed antenna is shown in Figure 4, which is fabricated by using low-cost PCB process. The whole antenna is constructed on a single-layer Rogers Duroid 5880 substrate with two copper films on its top and bottom surfaces, with permittivity ϵ_r of 2.2, loss tangent of 0.001, and thickness h of 0.5 mm.

TABLE I: Geometrical parameters of the proposed antenna.

| | |
|------------------|------|
| L_{ms} (mm) | 4.0 |
| L_{taper} (mm) | 5.4 |
| L_{siw} (mm) | 8.0 |
| L_{cpw} (mm) | 4.2 |
| g_{cpw} (mm) | 0.7 |
| L_{s1} (mm) | 10.8 |
| W_s (mm) | 1.0 |
| r_c (mm) | 9.1 |
| r (mm) | 0.5 |
| W_{ms} (mm) | 1.45 |
| W_{taper} (mm) | 3.2 |
| W_{siw} (mm) | 14 |
| W_{cpw} (mm) | 5.0 |
| d_{cpw} (mm) | 7.0 |
| L_{s2} (mm) | 10.2 |
| L_c (mm) | 4.9 |
| d_p (mm) | 1.35 |
| α (deg) | 45 |

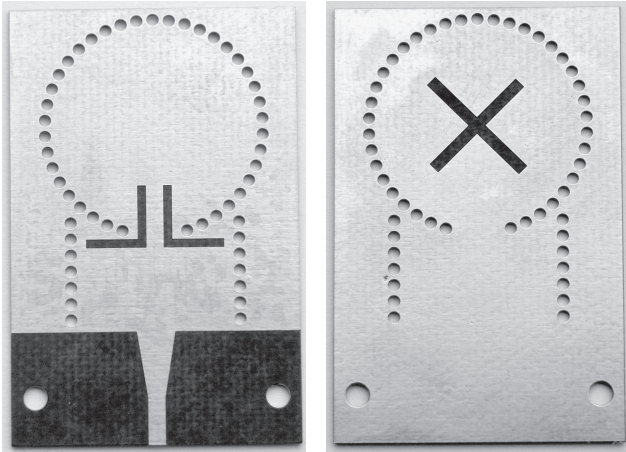


FIGURE 4: Photographs of the fabricated antenna.

Return loss measurements were carried out by an Agilent vector network analyzer. As shown in Figure 5, the measured return loss has a slight discrepancy compared with the simulated one, which is mainly caused by additional transition between microstrip line and SMA connector and slightly caused by fabrication error of the arm length.

Measured gain of the proposed antenna at the boresight direction is shown in Figure 6, in which there is a slight frequency shift between the measured result and the simulated one. The measured gain is slightly smaller than the simulated one. But all of them are more than 5.3 dBi and they are obviously more than that of the conventional planar patch or slot antennas with the same profile.

The measured AR of the proposed antenna at the boresight direction versus frequency has been plotted in Figure 7, in which the AR is defined as a ratio of the minor axis to the major axis of the polarization ellipse. The measured AR

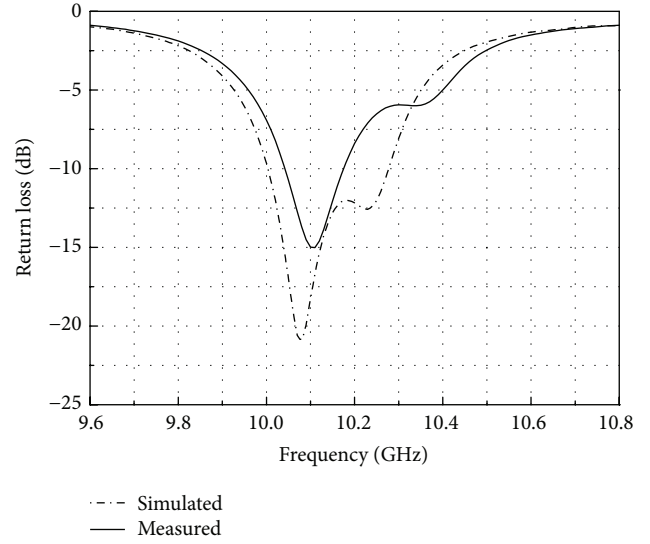


FIGURE 5: Measured return loss of the fabricated antenna compared with its simulated result.

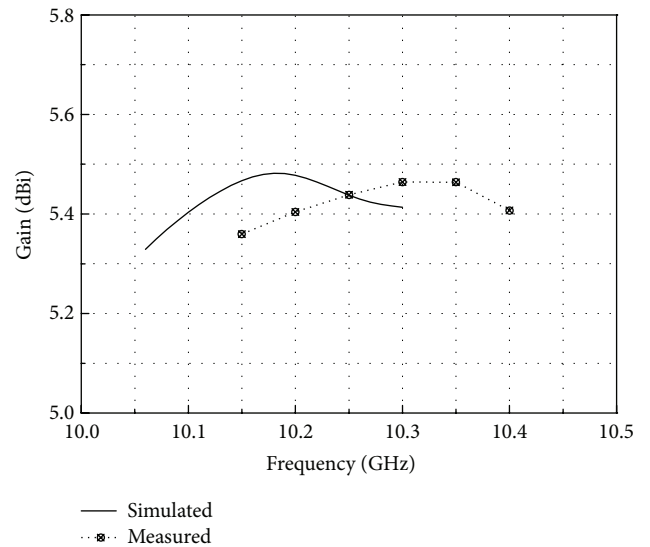


FIGURE 6: Gain of the fabricated antenna at the boresight direction.

curve is in agreement with the simulated curve. There is also a slight frequency shift of 0.1 GHz between the measured peak AR and the simulated peak AR. This slight discrepancy may be caused by the fabrication error of the crossed-slot arm length. The phase difference between the radiations generated by the two arms' length difference, which affects the AR directly. Both the measured AR and the simulated one change rapidly with frequency. It is an inherently characteristic of a single-feed low-profile circularly polarized antenna. The phase variations with frequencies are more rapid than that of the magnitudes. The phase error has stronger influence on the AR than that of the magnitude error. The 3 dB AR bandwidth is the limiting factor in the operating bandwidth of the proposed antenna.

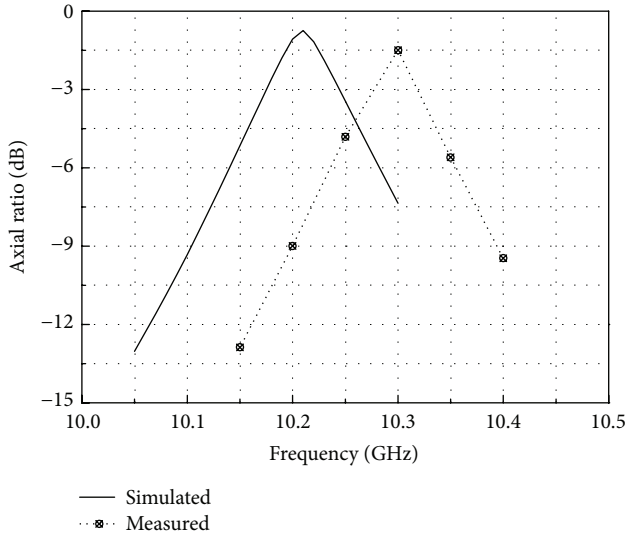


FIGURE 7: AR of the fabricated antenna at the boresight direction.

In order to improve the AR bandwidth, multi-feed configurations such as series feed and parallel feed can be adopted.

Radiation patterns at 10.3 GHz of the fabricated antenna in its two orthogonal cut planes have been plotted in Figure 8. From the figure, it can be found that a left-hand circular polarization (LHCP) radiation is generated from the fabricated antenna because its L_{s1} is more than L_{s2} . Right-hand circular polarization (RHCP) radiation can be easily achieved by setting the arm length L_{s1} less than L_{s2} .

In the x - y cut plane, measured half-power bandwidth (HPBW) of LHCP is 105° ($135^\circ \sim 240^\circ$). Measured cross-polarization level within HPBW in this plane is lower than -16 dB. Circular polarization operating angle θ_{cp} , characterized as the angle off boresight direction for which AR is more than -3 dB, is about 105° ($120^\circ \sim 225^\circ$). In the x - z cut plane, measured HPBW of LHCP is 105° ($135^\circ \sim 240^\circ$). Cross-polarization performance in this plane is better, whose measured result is lower than -18 dB within the HPBW. The measured θ_{cp} is about 105° ($135^\circ \sim 240^\circ$). The measured peak cross-polarization level and the back lobe level are about -22.7 dB and -15.8 dB, respectively. From the measured results, it can be found that the fabricated antenna presents a satisfactory circularly polarized radiation performance.

4. Conclusions

A single SIW-fed cavity-backed crossed-slot antenna is presented in this paper. Its circularly polarized radiation is obtained by tuning the length difference between two arms of its cross slot. The whole antenna including its SIW feed and SIW backed cavity is constructed by metallized via array on a single substrate. The proposed antenna has low profile and can be conveniently manufactured. Single SIW is adopted to stimulate the circular SIW cavity and excite the two orthogonal and degenerate TM_{110} cavity resonances. The presented antenna provides promising circularly polarized radiation performance, which has been validated by the measurements.

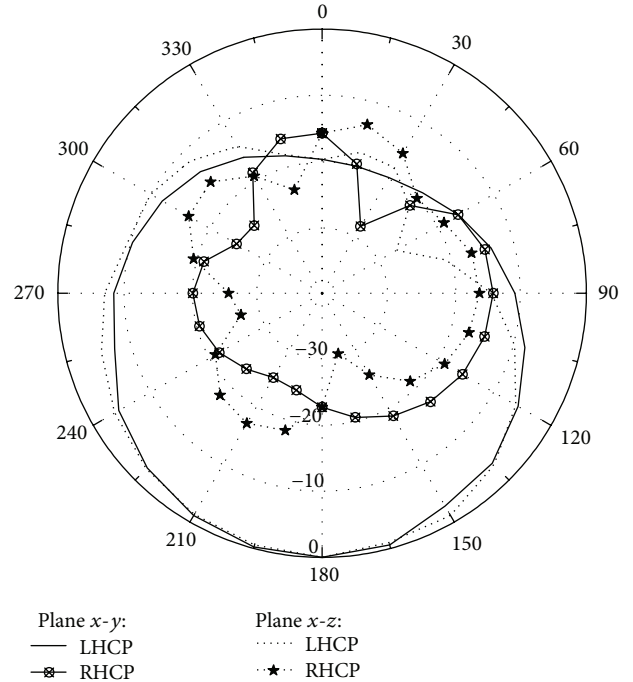


FIGURE 8: Radiation patterns of the fabricated antenna at 10.3 GHz.

Its measured gain is higher than 5.3 dBi, the maximum AR is -1.5 dB, and the peak cross-polarization level and the back lobe level are lower than -22.7 dB and -15.8 dB, respectively.

Acknowledgments

This work was supported in part by the National Natural Science Foundation of China under Contract no. 60801013, the Program for New Century Excellent Talents in University under Contract no. 09-0910, the Foundation for the Author of National Excellent Doctoral Dissertation of China under Contract no. 201045, and the Zhejiang Provincial Natural Science Foundation of China under Contract no. R1110003.

References

- [1] G. Q. Luo, Z. F. Hu, L. X. Dong, and L. L. Sun, "Planar slot antenna backed by substrate integrated waveguide cavity," *IEEE Antennas and Wireless Propagation Letters*, vol. 7, pp. 236–239, 2008.
- [2] G. Q. Luo, Z. F. Hu, Y. Liang, L. Y. Yu, and L. L. Sun, "Development of low profile cavity backed crossed slot antennas for planar integration," *IEEE Transactions on Antennas and Propagation*, vol. 57, no. 10, pp. 2972–2979, 2009.
- [3] G. Q. Luo, L. L. Sun, and L. X. Dong, "Single probe fed cavity backed circularly polarized antenna," *Microwave and Optical Technology Letters*, vol. 50, no. 11, pp. 2996–2998, 2008.
- [4] Y. Yusuf, H. Cheng, and X. Gong, "A seamless integration of 3-D vertical filters with highly efficient slot antennas," *IEEE Transactions on Antennas and Propagation*, vol. 59, no. 11, pp. 4016–4022, 2011.
- [5] S. Dumanli, C. J. Railton, D. L. Paul, and G. S. Hilton, "Closely spaced array of cavity backed slot antennas with pin curtains

walls," *IET Microwaves, Antennas and Propagation*, vol. 5, no. 1, pp. 38–47, 2011.

- [6] D. Kim, J. W. Lee, T. K. Lee, and C. S. Cho, "Design of SIW cavity-backed circular-polarized antennas using two different feeding transitions," *IEEE Transactions on Antennas and Propagation*, vol. 59, no. 4, pp. 1398–1403, 2011.
- [7] J. Lacik, "Circularly polarized SIW square ring-slot antenna for X-band applications," *Microwave and Optical Technology Letters*, vol. 54, no. 11, pp. 2590–2594, 2012.